

NASA/CR—1998-208537



The Real-Time Wall Interference Correction System of the NASA Ames 12-Foot Pressure Wind Tunnel

*Norbert Ulbrich
VERIDIAN/Calspan Operations
NASA Ames Research Center
P.O. Box 7
Moffett Field, California 94035-0007*

National Aeronautics and
Space Administration

Ames Research Center
Moffett Field, California 94035-1000

Prepared for Ames Research Center
under Contract NAS2-13605

July 1998

Available from:

NASA Center for AeroSpace Information
7121 Standard Drive
Hanover, MD 21076-1320
(301) 621-0390

National Technical Information Service
5285 Port Royal Road
Springfield, VA 22161
(703) 487-4650

PREFACE

During the past two years, substantial progress was made in the procedure and software development of a real-time Wall Interference Corrections System (WICS) for the NASA Ames 12ft Pressure Wind Tunnel. Experimental data became available to verify the WICS procedures. Expert System-like diagnostic features were added to the software to allow a reliable real-time operation. Wall interference corrections were successfully computed for a wide variety of wind tunnel models.

I hope that the promising results obtained during the development of WICS will benefit attempts to improve data quality and efficiency of subsonic wind tunnel tests in the NASA Ames 12ft Pressure Wind Tunnel.

I wish to express my appreciation to Alan Boone, test engineer at NASA Ames Research Center. His dedication, his extensive experience in wind tunnel testing, and his helpful comments were critical during the facility prototype development of WICS. Recent progress would not have been possible without his knowledge of classical wall interference corrections and pressure measurement techniques.

I want to thank John Day and Sylvie Faisant for their contributions. Thanks also go to Pat Whittaker, Larry Erickson, Jules Gustie, Darrell Kirk, Bob Gisler, Morgan Wright, Jon Bader, Karlin Roth, Kevin James, Dan Petroff, Dan Clasen, Dianne Butler, Norm Struzynski, Steve Culp, Richard Millington, Tom Bridge, Amit Ghosh, Linda Thompson, and the staff of the Aeronautical Test and Simulation Division at NASA Ames Research Center. I would also like to acknowledge the support from Mat Rueger, Abdi Khodadoust, Pat Driscoll, Pete Minor, and Don Leopold of the Boeing Company.

Moffett Field, California

Norbert Ulbrich

May 1998

ABSTRACT

An improved version of the Wall Signature Method was developed to compute wall interference effects in three-dimensional subsonic wind tunnel testing of aircraft models in real-time. The method may be applied to a fullspan or a semispan model.

A simplified singularity representation of the aircraft model is used. Fuselage, support system, propulsion simulator, and separation wake volume blockage effects are represented by point sources and sinks. Lifting effects are represented by semi-infinite line doublets. The singularity representation of the test article is combined with the measurement of wind tunnel test reference conditions, wall pressure, lift force, thrust force, pitching moment, rolling moment, and precomputed solutions of the subsonic potential equation to determine first order wall interference corrections.

Second order wall interference corrections for pitching and rolling moment coefficient are also determined. A new procedure is presented that estimates a rolling moment coefficient correction for wings with non-symmetric lift distribution.

Experimental data obtained during the calibration of the Ames Bipod model support system and during tests of two semispan models mounted on an image plane in the NASA Ames 12ft Pressure Wind Tunnel are used to demonstrate the application of the wall interference correction method.

TABLE OF CONTENTS

CHAPTER	PAGE
1. INTRODUCTION	1
2. WALL INTERFERENCE CORRECTION PREDICTION	5
2.1 Definition of Interference Corrections	5
2.2 Panel Method Code Solution	8
2.3 Fullspan Model	10
2.3.1 Test Article Wall Interference Correction	10
2.3.2 Support System Wall Interference Correction	14
2.4 Semispan Model	15
2.5 Compressibility Effects	16
2.6 Normalized Perturbation Velocity Definition	18
3. APPLICATION OF THE METHOD TO WIND TUNNEL TESTS	23
3.1 Real-Time Wall Interference Calculation	23
3.2 Matching Conditions	24
3.3 Application of the Method to Semispan Models	26
3.4 Application of the Method to the Ames Bipod	30
4. CONCLUSION AND REMARKS	33
REFERENCES	35
APPENDICES	39
1. Higher Order Correction Formulae	39
2. Panel Method Code Modifications	43
3. Point Source Velocity Vector	49
4. Line Doublet Velocity Vector	51
5. Calculation of the Line Doublet Strength	57
6. Tri-linear Interpolation	61
7. Parabolic Interpolation	63
8. Optimization of the Singularity Location	65
9. Selection of the Singularity / Reference Point Location	67
10. Blockage Effects of a Powered Wind Tunnel Model	71

CHAPTER	PAGE
11. Quality Check of the Least Squares Fit	73
12. Linear Interpolation of Wall Pressure Port Calibration	75
13. Singular Value Decomposition	77
14. Support System Kinematics	79
15. High Angle of Attack Sting Kinematics	83
16. Pitching Moment Lever Arm	87
17. Inclination of Force and Moment Vectors	91
18. Pitching Moment Coefficient Correction	95
19. Rolling Moment Coefficient Correction	101
20. Scale Factor Law	111
FIGURES	113

LIST OF SYMBOLS

A	cross-sectional area of the wind tunnel
a	speed of sound
b	wing span
C	wall pressure port calibration
\bar{C}	interpolated wall pressure port calibration
c	wing chord
c'	mean aerodynamic chord ($2/\bar{S} \cdot \int_0^{b/2} c^2 dy$)
\bar{c}	mean geometric chord (\bar{S}/b)
c_D	drag coefficient
c'_D	uncorrected drag coefficient
Δc_D	drag coefficient correction due to inclination of lift and drag force
c_l	rolling moment coefficient
$c_{l,c}$	corrected rolling moment coefficient
$c_{l,unc}$	uncorrected rolling moment coefficient
Δc_l	rolling moment coefficient correction (non-symmetric lift distribution)
$\Delta \bar{c}_l$	rolling moment coefficient correction (inclination of moment vectors)
c_L	lift coefficient
$c_L(y)$	local lift coefficient
c'_L	uncorrected lift coefficient
Δc_L	lift coefficient correction due to inclination of lift and drag force
c_M	pitching moment coefficient
$c_{M,c}$	corrected pitching moment coefficient
$c_{M,unc}$	uncorrected pitching moment coefficient
Δc_{M1}	pitching moment coefficient correction due to difference between mean and local wall interference corrections along the 3/4-chord of the wing and tail
Δc_{M2}	pitching moment coefficient correction due to streamline curvature
c_n	yawing moment coefficient
$c_{n,c}$	corrected yawing moment coefficient
$c_{n,unc}$	uncorrected yawing moment coefficient

$\Delta \bar{c}_n$	yawing moment coefficient correction (inclination of moment vectors)
c_p	specific heat ; pressure coefficient
D	drag force
D'	uncorrected drag force
f/c	camber of circularly cambered airfoil
k	singularity index
L	lift force
L'	uncorrected lift force
L_t	lift force of a line doublet of the tail
L_w	lift force of a line doublet of the wing
l	length of a Rankine body
M	Mach number or number of reference points
M_e	calibrated Mach number
M_{ref}	test section reference Mach number
M_∞	free-stream Mach number
m	number of wall pressure orifices
N	number of reference points
n	number of singularities
n_t	number of line doublets of the tail
n_w	number of line doublets of the wing
P	pitching moment
p	static pressure
p_{emp}	static pressure at a wall orifice ; empty tunnel calibration
p_{sup}	static pressure at a wall orifice ; support system calibration
p_{tun}	static pressure at a wall orifice ; real-time wind tunnel test
p_T	total pressure in the settling chamber
q	dynamic pressure
q_e	calibrated dynamic pressure
q_{ref}	test section reference dynamic pressure
q_∞	free-stream dynamic pressure
R	gas constant or rolling moment

R'	uncorrected rolling moment
r_1, r_2	polar coordinate
r_o	radius of a halfbody
S	area of the propeller disc of a propulsion simulator
\bar{S}	reference area of test article
s	span of a rectangular wing
Δs	span of a horseshoe vortex
Δs_t	discrete span of a line doublet of the tail
Δs_w	discrete span of a line doublet of the wing
T	temperature
T_P	propulsion simulator thrust
T_T	total temperature in the settling chamber
U	velocity in the x-direction
U_e	calibrated axial velocity; empty tunnel or image plane
U_e^*	calculated value of u_e
U_{ref}	test section reference velocity
U_∞	free-stream velocity
u	perturbation velocity in the x-direction
u_i	streamwise velocity correction
\bar{u}_i	normalized perturbation velocity of the wall interference flow field ; x-component
u_m	axial perturbation velocity; model in free-air
u_m^*	calculated value of u_m
u_s^*	axial perturbation velocity; support system in free-air
\bar{u}_t	normalized perturbation velocity of the wind tunnel flow field ; x-axis
u_t	axial perturbation velocity; wind tunnel flow field
u_t^*	calculated value of u_t
u_{tm}^*	axial perturbation velocity of a model in the wind tunnel flow field
u_{ts}^*	axial perturbation velocity of a support system in the wind tunnel flow field
u'	x' -axis component of the velocity vector
v	flow velocity in the y-direction
v_i	velocity correction in the y-direction

\bar{v}_i	normalized perturbation velocity of the wall interference flow field ; y-axis
v_e^*	y-component of the velocity; empty tunnel or image plane calibration
v_m^*	y-component of the perturbation velocity; model in free-air
v_s^*	y-component of the perturbation velocity; support system in free-air
v_{tm}^*	y-component of the perturbation velocity; model in wind tunnel flow field
v_{ts}^*	y-component of the perturbation velocity; support system in wind tunnel flow field
v'	y' -axis component of the velocity vector
w	flow velocity in the z-direction ; reference point weight
w_i	velocity correction in the z-direction
\bar{w}_i	normalized perturbation velocity of the wall interference flow field ; z-axis
w_e^*	z-component of the velocity; empty tunnel or image plane calibration
w_m^*	z-component of the perturbation velocity; model in free-air
w_s^*	z-component of the perturbation velocity; support system in free-air
w_{tm}^*	z-component of the perturbation velocity; model in wind tunnel flow field
w_{ts}^*	z-component of the perturbation velocity; support system in wind tunnel flow field
w_t	weight of a line doublet of the tail
w_j	weight of a singularity
w_w	weight of a line doublet of the wing (symmetric lift distribution)
\bar{w}_w	weight of a line doublet of the wing (non-symmetric lift distribution)
w'	z' -axis component of the velocity vector
X	value of first calibration variable during calibration
X^*	value of first calibration variable during real-time test
x	x-coordinate; roll axis; line doublet starting point
Δx	pitching moment arm
\bar{x}	incompressible x-coordinate
x_{mr}	x-coordinate of the pitching moment reference axis
x_S	x-coordinate of a point source
x_t	x-coordinate of a line doublet of the tail
x_w	x-coordinate of a line doublet of the wing
x_1	x-coordinate of a point source or line doublet starting point
x_2	x-coordinate of a point sink

x_*	x-coordinate of axis of rotation
x_0	stagnation point distance ; initial x-coordinate of singularity
x'	x-coordinate of the reference coordinate system
Y	value of second calibration variable during calibration or yawing moment
Y'	uncorrected yawing moment
Y^*	value of second calibration variable during real-time test
y	y-coordinate; pitch axis
\bar{y}	incompressible y-coordinate
y_1	y-coordinate of a line doublet starting point
y_S	y-coordinate of a point source
y'	y-coordinate of the reference coordinate system
z	z-coordinate; yaw axis
\bar{z}	incompressible z-coordinate
z_1	z-coordinate of a line doublet starting point
z_S	z-coordinate of a point source
z'	z-coordinate of the reference coordinate system
α	angle of attack of test article
α_i	angle of attack correction
$\hat{\alpha}_i$	mean angle of attack correction along 1/4-chord line of wing
$\bar{\alpha}_i$	mean angle of attack correction along 3/4-chord line of wing
α_m	angle of attack correction caused by the model
α_s	angle of attack correction caused by the support system
α_t	geometric angle of attack
α_*	pitch angle of High Angle of Attack Sting
α_∞	free-stream angle of attack
β	$\sqrt{1 - M^2}$ or sideslip angle of test article
β_*	yaw angle of High Angle of Attack Sting
Γ	circulation of a horseshoe vortex in [m^2/sec] or [ft^2/sec]
Γ_t	circulation constant of the tail in [m^2/sec] or [ft^2/sec]
Γ_w	circulation constant of the wing in [m^2/sec] or [ft^2/sec]

Γ^*	circulation of symmetric lift distribution in $[m^2/sec]$ or $[ft^2/sec]$
Γ^{**}	circulation of non-symmetric lift distribution in $[m^2/sec]$ or $[ft^2/sec]$
γ	isentropic exponent
δ	wall pressure orifice index
ϵ	blockage factor
$\bar{\epsilon}$	mean blockage factor
ϵ_{min}	minimum of blockage factor
ϵ_m	blockage factor caused by a model
ϵ_s	blockage factor caused by a support system
η	number of source / sink pairs ; solid volume blockage
θ	test section reference point
Λ	aspect ratio of wing
ν	model reference point index
ξ	number of sources and sinks
ρ	density
ρ_{ref}	test section reference density
ρ_T	total density in the settling chamber
ρ_{∞}	free-stream density
σ	singularity strength in $[m^3/sec]$ or $[ft^3/sec]$
σ_k	singularity strength divided by reference velocity ; $[m^2]$ or $[ft^2]$
σ_p	sink strength of the propulsion simulator divided by reference velocity
σ_p^*	sink strength of the propulsion simulator in $[m^3/sec]$ or $[ft^3/sec]$
σ_t	strength of a line doublet of tail divided by reference velocity
σ_t^*	strength of a line doublet of the tail in $[m^3/sec]$ or $[ft^3/sec]$
σ_w	wake source strength or strength of a line doublet divided by reference velocity
σ_w^*	wake source strength or strength of a line doublet in $[m^3/sec]$ or $[ft^3/sec]$
σ_w^{**}	strength of a line doublet in $[m^3/sec]$ or $[ft^3/sec]$
σ_1, σ_2	singularity strength of a point source or sink
τ	line doublet orientation angle ; identical with φ_*
φ	roll angle of test article ; sweep angle of wing
$\varphi_{0.25}$	sweep angle of 1/4-chord line of wing

$\varphi_{0.50}$	sweep angle of 1/2-chord line of wing
φ_*	line doublet orientation angle ; identical with τ
φ_1, φ_2	polar coordinate
ϕ_L	line doublet potential
ϕ_{PD}	point doublet potential
ϕ_S	point source potential
ϕ_w	wall / support system potential
ϕ_t	wind tunnel potential
ϕ_σ	singularity potential
ϕ_∞	free-stream potential
ψ_1, ψ_2	length scale of wind tunnel model
n	normal vector at a panel centroid
u_∞	free-stream velocity vector
$\overrightarrow{W_\infty}$	unit wind vector in model coordinate system

LIST OF WALL INTERFERENCE CORRECTIONS

1. FIRST ORDER CORRECTIONS

Correction	Reference	Symbol	Equation
Blockage Factor	Chapter 2	$\epsilon, \epsilon_m, \epsilon_s$	(4),(9a),(15a),(17)
Mach Number	Appendix 1	—	(1.8)
Dynamic Pressure	Appendix 1	—	(1.15)
Angle of Attack	Chapter 2	$\alpha_i, \alpha_m, \alpha_s$	(7),(9b),(15b),(18b)

2. SECOND ORDER CORRECTIONS

Correction	Reference	Symbol	Equation
Lift Coefficient (Inclination of Force Vectors)	Appendix 17	Δc_L	(17.7a)
Drag Coefficient (Inclination of Force Vectors)	Appendix 17	Δc_D	(17.7b)
Pitching Moment Coefficient (Lateral Shift of Center of Pressure)	Appendix 18	Δc_{M1}	(18.4)
Pitching Moment Coefficient (Streamline Curvature)	Appendix 18	Δc_{M2}	(18.21a) (18.21b)
Rolling Moment Coefficient (Inclination of Moment Vectors)	Appendix 17	$\Delta \bar{c}_l$	(17.13a)
Rolling Moment Coefficient (Non-Symmetric Lift Distribution)	Appendix 19	Δc_l	(19.27)
Yawing Moment Coefficient (Inclination of Moment Vectors)	Appendix 17	$\Delta \bar{c}_n$	(17.13b)

CHAPTER 1

INTRODUCTION

Wind tunnel tests have always played an important role in the development of modern aircraft. These tests are used to simulate atmospheric conditions experienced by an aircraft or spacecraft in free-flight. Aerodynamic forces and moments are measured and related to corresponding free flight values using Mach and Reynolds numbers. These measurements provide valuable information about expected performance, stability, and control characteristics of a new aircraft design.

Large wind tunnel models, i.e. wing span on the order of 80% of the wind tunnel width, are often preferred in order to achieve a good simulation of viscous phenomena of the flow field. In this case, however, the presence of the wind tunnel wall and model support system change the free-air flow field experienced by the aircraft model. These flow field interference effects have to be considered to allow a reasonable comparison between wind tunnel test and free flight condition. Therefore, interference corrections to Mach number, dynamic pressure, and angle of attack have to be determined to improve test data quality.

In the 1970s and 1980s, techniques were developed that use boundary measurements during a wind tunnel test to predict wall interference corrections. The Wall Signature Method introduced by *Hackett et al.* [1],[2],[3] and the Two-Variable Method introduced by *Ashill* [4],[5] were used extensively in 3-dimensional wind tunnel testing. *Ashill* [5] gives a detailed discussion and comparison of these techniques.

The Wall Signature Method and Two-Variable Method are both based on potential flow theory. Computed wall interference corrections agree if each method is applied correctly. However, a few differences exist between these two methods. Each method has its advantages and disadvantages. Table 1 compares important features of the Wall Signature Method and the Two-Variable Method.

The Two-Variable Method does not require a singularity representation of the wind tunnel model to determine wall interference corrections. However, the wall interference correction calculation depends on an integration of the measured and interpolated surface pressure distribution on the wind tunnel wall.

The Wall Signature Method uses a singularity representation of test article, wall pressure measurements, precomputed perturbation velocities, and the principle of superposition to compute wall interference correction. No integration and interpolation of the surface pressure distribution is required. Therefore, the Wall Signature Method is more flexible in the selection of wall pressure port measurements required for the wall interference calculation. Computed corrections are relatively insensitive to the number and the location of wall pressure ports used for the least squares fit.

Table 1 : Comparison Wall Signature Method / Two-Variable Method

	Wall Signature Method (<i>Hackett et al.</i>)	Two-Variable Method (<i>Ashill et al.</i>)
Singularity Representation of the Wind Tunnel Model	YES	NO
Measurement of the Flow Velocity at the Wind Tunnel Wall	YES	YES
Number of Wall Pressure Port Measurements	≥ 2	≥ 100
Wall Interference Correction Calculation based on a Perturbation Velocity Flow Field and the Principle of Superposition	YES	NO
Wall Interference Correction Calculation based on an Integration of the Surface Pressure Distribution at the Wind Tunnel Wall	NO	YES
Sensitivity of Computed Corrections to the Number and the Location of Wall Pressure Port Measurements	LOW	HIGH

The Wall Signature Method was selected for use in the real-time Wall Interference Correction System (WICS) of the NASA Ames 12ft Pressure Wind Tunnel, because it is fast and does not depend on an integration of a measured surface pressure distribution. The Wall Signature method will still provide corrections even if a large number of wall pressure ports do not provide a useful measurement.

In general, the Wall Signature Method computes wind tunnel wall interference cor-

rections by introducing a simplified representation of the test article expressed in terms of singularities. Sources and sinks represent the fuselage volume and viscous separation wake blockage effects and horseshoe vortices or line doublets represent the lifting effects. In addition, power simulator blockage effects can be represented by a sink [6] . This singularity representation is combined with a least squares fit of wall pressure measurements, data from calibration tests, and solutions of the subsonic potential equation, in the form of normalized perturbation velocities, to predict Mach number, dynamic pressure, and angle of attack corrections.

During the past decade significant advances in the development of low-order panel method codes and computer hardware have made a fast calculation of complex three-dimensional internal flow field problems on workstation type computers possible. Panel method codes allow application of the Laplace Equation to realistic three-dimensional wind tunnel geometries which is important if the methodology of the Wall Signature Method is applied to the quasi-octogonal cross-section of the 12ft Pressure Wind Tunnel (PWT) at NASA Ames Research Center. It was shown by *Ulbrich and Steinle* [7],[8] that normalized panel method code solutions of the wind tunnel flow field combined with the Wall Signature Method can be used to predict subsonic wall interference corrections close to real-time.

The revised formulation of the Wall Signature Method developed for the 12ft PWT is described in detail in this report. Figure 1 shows principle elements of the modified Wall Signature Method. Improvements of the Wall Signature Method were introduced to allow an application of the Wall Signature Method in real-time and to deal efficiently with a wide range of model and support system geometries.

Originally, *Hackett et al.* [1] based their formulation of the Wall Signature Method on a "local" least squares fit procedure. They introduced a piecewise approximation of the wall signature using a parabola for its maximum and a tanh - function for its downstream asymptote. The location of singularities was found by matching the location of the maximum of the parabola with the inflection point of the tanh - function. Unfortunately, this feature of the original formulation of the Wall Signature Method is difficult to use in a real-time correction system, as it requires the selection of wall pressure ports used for the "local" least squares fit of the maximum of the real-time wall signature.

Ulbrich [9] introduced improvements to the Wall Signature Method to overcome the

limitations of a "local" least squares fit of the wall pressure signature. He suggested a "global" least squares fit procedure which matches the wall signature on all wall pressure ports using panel method code solutions of singularities placed inside the wind tunnel test section. In his approach, a "best" singularity location is found by minimizing the standard deviation of the least squares fit of the wall signature as a function of the singularity location.

Support system wall interference corrections for fullspan model tests can also be found by applying the Wall Signature Method. In this case the Wall Signature Method has to be applied to the difference between the support system and the empty tunnel calibration at the wall pressure ports. Support system wall interference effects can be computed off-line and stored in a database.

In the first part of this report, basic relationships of the proposed Wall Signature Method are derived for a fullspan and a semispan model.

The second part of this report discusses the integration of the method into a wind tunnel facility. Experimental data, obtained during tests of two different size semispan models mounted on an image plane in the NASA Ames 12ft Pressure Wind Tunnel (PWT), are applied to the modified Wall Signature Method to verify computed corrections. Experimental data recorded during the calibration of the Ames Bipod are also applied to the method.

CHAPTER 2

WALL INTERFERENCE CORRECTION PREDICTION

2.1 Definition of Interference Correction

Wind tunnel tests allow the prediction of aerodynamic forces and moments acting on an aircraft model in atmospheric free-flight. Unfortunately, the wind tunnel wall and the model support system change the flow field experienced by the aircraft. Many of these changes can be ignored if the aircraft model is small compared to the wind tunnel height and width. However, if the span of the test article is large or if substantial flow separation occurs, wall and model support system interference effects cannot be neglected. Then, reliable estimates of interference corrections to Mach number, dynamic pressure, and angle of attack are necessary so that wind tunnel test data may be compared with free-flight conditions.

In general, wall and support system interference corrections are defined as the difference between the wind tunnel flow field and the free-air flow field experienced by the model (see Fig.2a) . Corrections are described in terms of a blockage factor ϵ and an angle of attack correction α_i . Mach number and dynamic pressure corrections are related to the blockage factor computed at some reference point in the wind tunnel. For more detail on classical subsonic wall interference corrections, see AGARDograph 109, [10] . The blockage correction relates the free-stream velocity U_∞ to a calibrated empty tunnel velocity U_e at a model reference point ν (see Fig. 2b) . The calibrated empty tunnel velocity U_e captures the effects of the wind tunnel wall boundary layer growth, wall divergence, and orifice error. It is still necessary to correct for the wall interference effect of the test article, its separation wake, and the influence of the support system.

The ratio between free-stream velocity U_∞ and the calibrated empty tunnel velocity U_e is expressed as a function of the blockage factor ϵ , [10] :

$$\frac{U_\infty(\nu)}{U_e(\nu)} = 1 + \frac{u_i(\nu)}{U_e(\nu)} = 1 + \epsilon(\nu) \quad (1)$$

where u_i is the axial velocity correction at the model reference point ν caused by the model and support system interference effects relative to the calibrated empty tunnel velocity U_e .

For small changes in velocity, second order approximations of Mach number and dynamic pressure correction can be expressed as a function of the blockage factor $\epsilon(\nu)$ using a Taylor series expansion. These second order approximations are used if a large blockage factor is expected, e.g. during high angle of attack tests of aircraft models. We get (see Appendix 1) :

$$\frac{M_\infty - M_e(\nu)}{M_e(\nu)} = \left[1 + \frac{\gamma - 1}{2} \cdot M_e^2(\nu) \right] \cdot \left[\epsilon(\nu) + \frac{3(\gamma - 1)M_e^2(\nu)}{4} \cdot \epsilon(\nu)^2 \right] \quad (2a)$$

$$\frac{q_\infty - q_e(\nu)}{q_e(\nu)} = \left[2 - M_e^2(\nu) \right] \cdot \epsilon(\nu) + \left[1 - \frac{5}{2}M_e^2(\nu) + \frac{2-\gamma}{2}M_e^4(\nu) \right] \cdot \epsilon(\nu)^2 \quad (2b)$$

The calculation of wall interference corrections based on the ideas of the Wall Signature Method requires the formulation of a blockage factor ϵ and an angle of attack correction α ; such that a direct connection between experiment and the panel method code computation is possible [7],[8].

Studies by the author have shown that differences of the panel method code solutions can be used in combination with the Wall Signature Method to predict interference corrections. Figure 2b shows the relationship between the empty tunnel calibration, support system calibration, wind tunnel test, free-air flow field, and the corresponding panel method code calculations using a simplified representation of the test article and support system in terms of singularities. This representation is uniquely defined if type, location, and strength of the singularities is known. The type and location of singularities must be specified by a test engineer. The Wall Signature Method is used to compute the strength of the singularities. The Principle of Superposition and panel method code solutions of the wall interference flow field are used to determine wall interference corrections.

It is assumed that singularities of the test article and support system are located inside a tunnel of constant cross-sectional area as effects of wall divergence and boundary layer growth are already included in the calibrated empty tunnel velocity U_e . The calibrated velocity U_e corresponds to a constant reference velocity U_e^* of a constant cross-section wind tunnel.

Comparing the flow fields depicted in Fig. 2b we can make the following approximation

of the velocity ratio $U_\infty(\nu)/U_e(\nu)$ defined in Eq. (1) :

$$\begin{aligned} \frac{U_\infty(\nu)}{U_e(\nu)} &\approx \frac{U_e^* + [(U_e^* + u_i^*(\nu)) - (U_e^* + u_m^*(\nu))]}{U_e^*} \\ &= 1 + \left[\frac{u_i^*(\nu) - u_m^*(\nu)}{U_e^*} \right] \end{aligned} \quad (3a)$$

The total perturbation velocity u_i^* of the wind tunnel flow field caused by the test article and support system is expressed as the sum of the perturbation velocity contribution u_{tm}^* of the test article and the perturbation velocity contribution u_{ts}^* of the support system (see Fig. 2c) . The perturbation velocity component u_{ts}^* of the support system perturbation velocity flow field can further be represented as the sum of the perturbation velocity component $u_{ts}^* - u_s^*$ due to the wall interference of the support system and the perturbation velocity component u_s^* due to the direct influence of the support system (see Fig. 2d). Finally we can write :

$$\begin{aligned} \frac{U_\infty(\nu)}{U_e(\nu)} &= 1 + \left[\frac{u_{tm}^*(\nu) - u_m^*(\nu) + u_{ts}^*(\nu) - u_s^*(\nu) + u_s^*(\nu)}{U_e^*} \right] \\ &= 1 + \left[\frac{u_{tm}^*(\nu) - u_m^*(\nu)}{U_e^*} \right] + \left[\frac{u_{ts}^*(\nu) - u_s^*(\nu)}{U_e^*} \right] + \frac{u_s^*(\nu)}{U_e^*} \end{aligned} \quad (3b)$$

It is difficult to predict the direct influence of the support system on the model flow field in terms of a perturbation velocity component u_s^* . The Wall Signature Method cannot be used to determine the direct influence of the support system on the model as this technique has been developed for wind tunnel wall interference studies. Experimental or CFD studies have to be used to estimate the direct influence u_s^* .

For the present study it is assumed that the direct interference between support system and wind tunnel model is small, i.e. $u_s^* \approx 0$. Then, comparing Eqs. (1) and (3b), we get for $\epsilon(\nu)$:

$$\epsilon(\nu) \approx \left[\frac{u_{tm}^*(\nu) - u_m^*(\nu)}{U_e^*} \right] + \left[\frac{u_{ts}^*(\nu) - u_s^*(\nu)}{U_e^*} \right] = \epsilon_m(\nu) + \epsilon_s(\nu) \quad (4)$$

Interference velocity components in pitch and yaw axis direction can be expressed in forms similar to Eq. (4) if direct influence of the support system is neglected, i.e., $v_s^* \approx 0$ and $w_s^* \approx 0$. We get :

$$\frac{v_i(\nu)}{U_e(\nu)} \approx \left[\frac{v_{tm}^*(\nu) - v_m^*(\nu)}{U_e^*} \right] + \left[\frac{v_{ts}^*(\nu) - v_s^*(\nu)}{U_e^*} \right] \quad (5a)$$

$$\frac{w_i(\nu)}{U_e(\nu)} \approx \left[\frac{w_{tm}^*(\nu) - w_m^*(\nu)}{U_e^*} \right] + \left[\frac{w_{ts}^*(\nu) - w_s^*(\nu)}{U_e^*} \right] = \alpha_m + \alpha_s \quad (5b)$$

The velocity ratios α_m and α_s are angle of attack corrections due to the model and support system wall interference effects.

The interference velocity component in the z-axis direction is related to the free-stream angle of attack α_∞ experienced by the test article at the model reference point. Therefore we get :

$$\alpha_\infty(\nu) = \alpha_t(\nu) + \alpha_i(\nu) \quad (6)$$

where α_t is the geometric angle of attack measured relative to the wind tunnel centerline and α_i is the angle of attack correction due to lift interference of the test article and due to the change of the flow field angle caused by the interference flow field of the model support system. The total angle of attack correction of a fullspan model is then :

$$\alpha_i(\nu) = \frac{w_i(\nu)}{U_\infty(\nu)} = \frac{U_e(\nu)}{U_\infty(\nu)} \cdot \frac{w_i(\nu)}{U_e(\nu)} = \frac{U_e(\nu)}{U_\infty(\nu)} \cdot \left[\alpha_m + \alpha_s \right] \quad (7)$$

where $U_e(\nu)/U_\infty(\nu)$ and $w_i(\nu)/U_e(\nu)$ are given by Eqs. (3b), (5b) . The angle of attack correction for the semispan model is obtained by replacing $w_i(\nu)$ by $v_i(\nu)$ in Eq. (7) .

The calculation of the Mach number, dynamic pressure, and angle of attack correction using Eqs. (2a), (2b), (4), (7) is reduced to finding blockage corrections ϵ_m and ϵ_s and angle of attack corrections α_m and α_s .

Model corrections ϵ_m and α_m , i.e. velocity differences $[u_{tm}^* - u_m^*]/U_e^*$, $[v_{tm}^* - v_m^*]/U_e^*$ or $[w_{tm}^* - w_m^*]/U_e^*$, and support system corrections ϵ_s and α_s , i.e. velocity differences $[u_{ts}^* - u_s^*]/U_e^*$, $[v_{ts}^* - v_s^*]/U_e^*$ or $[w_{ts}^* - w_s^*]/U_e^*$, can be computed by using the modified Wall Signature Method. This is possible because the wall interference flow field caused by the wind tunnel model and support system can be treated as a far field effect. This will be explained in detail in the following sections.

2.2 Panel Method Code Solution

In the previous section, it was demonstrated that wall interference effects of a test article and support system , i.e. ϵ_m , ϵ_s , α_m , and α_s , can be found by calculating dimensionless velocities $[u_{tm}^* - u_m^*]/U_e^*$, $[v_{tm}^* - v_m^*]/U_e^*$, $[w_{tm}^* - w_m^*]/U_e^*$, $[u_{ts}^* - u_s^*]/U_e^*$, $[v_{ts}^* - v_s^*]/U_e^*$,

and $[w_{i,s}^* - w_s^*]/U_e^*$ at a selected test article reference point ν . These dimensionless velocities are computed by superimposing panel method code solutions and applying the Wall Signature Method. In real-time operation, the Wall Signature Method uses a singularity representation of the test article in combination with the measurement of wall pressure, lift force, propulsion simulator thrust force, pitching moment, and precalculated normalized perturbation velocities to predict model wall interference corrections. The Wall Signature Method may also be used to predict support system wall interference corrections by taking the difference between the wall pressure port calibration of the support system and empty tunnel. However, the application of the Wall Signature Method is only possible, if precalculated solutions of the subsonic potential equation in the form of normalized perturbation velocities are linear with respect to singularity strength.

In general, the perturbation flow field of a singularity placed inside a wind tunnel of constant cross-sectional area is a linear function of the singularity strength. Figure 3 depicts a singularity of strength σ_0 located inside a selected wind tunnel configuration of constant cross-sectional area A . The corresponding flow field solution is obtained by using a modified panel method code as a boundary value problem solver (see Appendix 2 for a detailed description of these modifications). Figure 3 also shows a singularity of the same type and location but with different singularity strength σ_1 . The strength σ_0 and σ_1 of these two singularities are related as follows :

$$\sigma_1 = \lambda \cdot \sigma_0 \quad (8a)$$

We know for the corresponding panel method code solutions in terms of the perturbation velocities :

$$u_1^* = \lambda \cdot u_0^* \quad (8b)$$

Equation (8b) is valid as long as the cross-section of the selected panel geometry of the wind tunnel test section is constant. This relationship allows the user to find all wind tunnel flow field solutions of $\sigma_1 \neq 1.0$ [ft^3/sec] by simply multiplying the flow field solution of $\sigma_0 = 1.0$ [ft^3/sec] with the factor $\lambda = \sigma_1/\sigma_0$.

In the following section, details will be developed as to how the Wall Signature Method can be combined with the linear property of panel method solutions defined by

Eqs. (8a),(8b) to obtain test article and support system wall interference corrections for a fullspan or semispan model.

2.3 Fullspan Model

2.3.1 Test Article Wall Interference Correction

The Wall Signature Method can be applied to compute the blockage factor ϵ_m and angle of attack correction α_m caused by test article wall interference effects at a reference point “ ν ” .

The Wall Signature Method uses a simplified representation of the test article in terms of point sources, point sinks, and line doublets in combination with measurement of wall pressure, lift force, propulsion simulator thrust, pitching moment, and precalculated normalized perturbation velocities to obtain the blockage factor and angle of attack correction. The blockage factor, ϵ_m , and angle of attack correction, α_m , are linear functions of the singularity representation of the test article (see previous section). The principle of superposition allows ϵ_m and α_m to be expressed as the sum of contributions of “ n ” singularities that represent the test article. Figure 4 shows, as an example, how the principle of superposition can be applied to a simplified representation of a test article using three singularities. Knowing that ϵ_m and α_m are a linear function of the singularity strength σ , we get for “ n ” singularities :

$$\epsilon_m(\nu) = \sum_{k=1}^n \sigma_k \cdot \overline{u}_i(\nu, k) \quad (9a)$$

$$\alpha_m(\nu) = \sum_{k=1}^n \sigma_k \cdot \overline{w}_i(\nu, k) \quad (9b)$$

where $\overline{u}_i(\nu, k)$ and $\overline{w}_i(\nu, k)$ are normalized perturbation velocities of the wall interference flow field. These normalized velocities are dimensionless perturbation velocities divided by unit singularity strength per unit velocity. Perturbation velocity $\overline{u}_i(\nu, k)$ is the normalized axial perturbation velocity component of the wall interference flow field and $\overline{w}_i(\nu, k)$ is the normalized perturbation velocity component perpendicular to the wing plane of the test article. Normalized perturbation velocities have the unit $[1/m^2]$ or $[1/ft^2]$. Singularity strength σ_k has the unit $[m^2]$ or $[ft^2]$ and is compatible with these normalized perturbation

velocities. Singularity strength σ_k is defined as singularity strength σ in $[m^3/sec]$ or $[ft^3/sec]$ (see also App. 3,4) divided by reference velocity U_e^* or U_{ref} :

$$\sigma_k = \frac{\sigma}{U_e^*} = \frac{\sigma}{U_{ref}} \quad (10)$$

The strength of the singularities is computed similar to the procedures outlined by *Ulbrich and Steinle* [7],[8], and *Koning* [6], using the measurement of lift force, thrust force, pitching moment, and a least squares fit of wall pressure signature. Figure 5a summarizes the basic steps in the application of the Wall Signature Method to a fullspan model configuration. Rectangular boxes in Fig. 5a symbolize real-time measurements, rounded boxes symbolize information stored in database files, and elliptical boxes symbolize computational procedures.

Fuselage volume blockage effects are represented by point sources and point sinks. The location of these sources and sinks has been selected by the user such that pairs of sources and sinks are related to Rankine bodies describing the fuselage volume of the test article. Strengths $\sigma_1, \dots, \sigma_\eta$ of point sources and strengths $\sigma_{\eta+1}, \dots, \sigma_{2\eta}$ of point sinks are reduced to a single variable σ_* if weighting factors $w_1, \dots, w_{2\eta}$ are introduced. These weighting factors must be defined by the user. We then obtain :

$$\frac{\sigma_j}{\sigma_*} = w_j \quad ; \quad 1 \leq j \leq 2\eta \quad (11a)$$

where

$$w_j = -w_{j-\eta} \quad ; \quad \eta+1 \leq j \leq 2\eta \quad (11b)$$

Separation wake blockage effects are represented by a set of sources, $\sigma_{2\eta+1}, \dots, \sigma_\xi$. Again, weighting factors are introduced to reduce the number of independent variables. Assuming that the strength σ_{**} is a common reference strength of sources related to the separation wake we get :

$$\frac{\sigma_j}{\sigma_{**}} = w_j \quad ; \quad 2\eta+1 \leq j \leq \xi \quad (12)$$

The weighting factors $w_{2\eta+1}, \dots, w_\xi$ are, by definition, greater than zero since separation wake blockage effects are modeled as sources. The calculation of the strength of a total

number of “ ξ ” point sources and sinks representing fuselage volume and wake blockage effects is then reduced to finding the values of σ_* and σ_{**} using the Wall Signature Method.

A least squares fit of velocities derived from wall pressure measurements is used to calculate σ_* and σ_{**} (see Fig. 5b) . It is assumed that a total number of “ n ” singularities has been selected to represent the test article. Axial velocities are derived from pressure measurements at “ m ” wall pressure orifices. The measured real-time wall signature, $U_e(\delta) + u_t(\delta)$, is corrected for orifice error, wall divergence, and wall boundary layer growth by subtracting the measured velocity, $U_e(\delta) + u_{ts}(\delta)$, of the support system calibration at each wall orifice location “ δ ” . The computational equivalent, U_e^* , to the calibrated velocity, U_e or U_{ref} , at the wall pressure orifice “ δ ” is constant everywhere inside of the test section as it is computed using a constant cross-section wind tunnel. Normalized perturbation velocities of the wind tunnel flow field at wall pressure orifice locations, “ δ ”, have to be introduced to compute the strength of singularities representing the test article. They relate the strength of point sources, sinks, and line doublets to the perturbation velocity components at the wall pressure orifices. The strengths, $\sigma_{\xi+1}, \dots, \sigma_\mu$, of line doublets representing lifting effects of the test article are estimated by combining lift force, pitching moment, and rolling moment measurements with the *Kutta/Joukowski* formula (see Appendix 5 and Appendix 19) . The strengths, $\sigma_{\mu+1}, \dots, \sigma_n$, of point sinks representing blockage effects of propulsion simulators are estimated using thrust measurements and *Koning’s* formula (see Appendix 10) . The normal equation of the modified linear least squares problem depicted in Fig. 5b is given as, [11] :

$$[\mathbf{A}^T_{2 \times m} \cdot \mathbf{A}_{m \times 2}] \cdot \mathbf{X}_{2 \times 1} = \mathbf{A}^T_{2 \times m} \cdot \mathbf{B}_{m \times 1} \quad (13a)$$

$$\mathbf{X}_{2 \times 1} = \begin{pmatrix} \sigma_* \\ \sigma_{**} \end{pmatrix} \quad (13b)$$

$$\mathbf{A}_{m \times 2} = \begin{pmatrix} a_{1,1} & a_{1,2} \\ \vdots & \vdots \\ a_{m,1} & a_{m,2} \end{pmatrix} \quad (13c)$$

$$a_{\delta,1} = \sum_{k=1}^{2\eta} w_k \cdot \bar{u}_t(\delta, k) \quad (13d)$$

$$a_{\delta,2} = \sum_{k=2\eta+1}^{\xi} w_k \cdot \bar{u}_t(\delta, k) \quad (13e)$$

$$\mathbf{B}_{m \times 1} = \begin{pmatrix} b_1 \\ \vdots \\ b_m \end{pmatrix} \quad (13f)$$

$$b_\delta = \frac{[U_e(\delta) + u_t(\delta)] - [U_e(\delta) + u_{ts}(\delta)]}{U_{ref}} - \sum_{k=\xi+1}^n \sigma_k \cdot \bar{u}_t(\delta, k) \quad (13g)$$

The vector \mathbf{X} contains the strength of singularities modeling the fuselage volume and wake blockage effects. The matrix \mathbf{A} contains normalized perturbation velocities of the wind tunnel flow field. The vector \mathbf{B} contains residual perturbation velocity components caused by the fuselage volume and separation wake. Line doublet and propulsion simulator contributions, $k = \xi + 1, \dots, n$, are subtracted from the measured wall signature difference between the wind tunnel flow field and the support system calibration at the wall pressure ports “ δ ” (see Fig. 5b).

Perturbation velocity, $\bar{u}_t(\delta, k)$, is the normalized perturbation velocity of the wind tunnel flow field of singularity “ k ” at wall pressure orifice “ δ ”. It is defined as the dimensionless perturbation velocity divided by unit singularity strength per unit velocity at wall pressure orifice “ δ ” due to a singularity “ k ” located inside the test section.

In general, it is required that the measured velocity, $U_e(\delta) + u_t(\delta)$, at wall pressure port “ δ ” can be approximated by its component in the streamwise direction. In practical applications, however, a least squares fit can tolerate a few wall pressure measurements that do not fulfill this condition as the normal equation of the least squares fit, Eq. (13a), assigns equal weight to all wall pressure port measurements.

The solution of the two variable linear least squares problem defined in Eq. (13a) can be written in explicit form as :

$$\mathbf{X}_{2 \times 1} = [\mathbf{A}^T \cdot \mathbf{A}]_{2 \times 2}^{-1} \cdot [\mathbf{A}^T \cdot \mathbf{B}]_{2 \times 1} \quad (14)$$

The solution vector \mathbf{X} is computed by using the Singular Value Decomposition technique [12], which is the numerical method of choice for linear least squares problems.

It is now possible to compute the blockage correction, $\epsilon_m(\nu)$, and the angle of attack correction, $\alpha_m(\nu)$, at reference point “ ν ” as the strength and location of all singularities representing the test article and wake are known.

2.3.2 Support System Wall Interference Correction

The Wall Signature Method can also be used to find the blockage factor, ϵ_s , and the angle of attack correction, α_s , caused by support system wall interference effects. The application of the Wall Signature Method to the support system wall interference problem closely follows procedures discussed in the previous section. Figure 6a summarizes basic elements in the application of the Wall Signature Method to the support system wall interference problem.

Support system wall interference effects have been defined in Eqs. (4) and (5b). Similar to Eqs. (9a),(9b), ϵ_s and α_s are a linear function of the singularity strength. It is assumed that a total number of “ ξ ” sources and sinks of unknown strength are used to represent blockage effects of the support system. We then get :

$$\epsilon_s(\nu) = \sum_{k=1}^{\xi} \sigma_k \cdot \bar{u}_i(\nu, k) \quad (15a)$$

$$\alpha_s(\nu) = \sum_{k=1}^{\xi} \sigma_k \cdot \bar{w}_i(\nu, k) \quad (15b)$$

where $\bar{u}_i(\nu, k)$ and $\bar{w}_i(\nu, k)$ are normalized perturbation velocities of the wall interference flow field.

Again, positions of sources and sinks modeling solid volume blockage effects are selected such that pairs of sources and sinks are related to Rankine bodies describing the volume of the support system (see Eq. (11a),(11b)). Sources related to wake blockage effects of the support system are placed where a wake separation on the support system is expected (see Eq. (12)). Introducing weighting factors it is possible to reduce the number of unknown singularity strength values to two, i.e. σ_* and σ_{**} .

Assuming that “ m ” wall pressure measurements are taken during the support system calibration and that “ ξ ” singularities are used to represent the support system, we get the following normal equation of the least squares problem, [11] :

$$[\mathbf{A}^T_{2 \times m} \cdot \mathbf{A}_{m \times 2}] \cdot \mathbf{X}_{2 \times 1} = \mathbf{A}^T_{2 \times m} \cdot \mathbf{B}_{m \times 1} \quad (16a)$$

where

$$\mathbf{B}_{m \times 1} = \begin{pmatrix} b_1 \\ \vdots \\ b_m \end{pmatrix} \quad (16b)$$

$$b_\delta = \frac{[U_e(\delta) + u_{ts}(\delta)] - U_e(\delta)}{U_{ref}} \quad (16c)$$

The vector \mathbf{X} contains the strength of singularities describing the support system volume and wake blockage effects (see also Eq. 13b) . The matrix \mathbf{A} is given by Eqs. (13c), (13d), and (13e) using the perturbation velocities $\bar{u}_t(\delta, k)$ of the singularities $1 \leq k \leq \xi$ representing the support system. The vector \mathbf{B} contains perturbation velocity components caused by support system volume and separation wake. These perturbation velocity components are the measured wall signature difference between the support system calibration and the empty tunnel calibration at wall pressure ports “ δ ” (see Fig. 6b).

2.4 Semispan Model

In general, blockage and angle of attack corrections are computed using Eqs. (4) and (5b) if the modified Wall Signature Method is applied to a semispan model. Studies by the author have shown that a semispan model mounted on a finite length image plane may be treated similar to the fullspan model configuration. It is only necessary to select the proper geometry of the wind tunnel, i.e. the cross-section of the wind tunnel channel above the image plane surface plus its reflected image, for the calculation of normalized perturbation velocities (see Fig. 7) . However, a new calibration of the empty tunnel velocities, $U_e(\delta)$ and U_{ref} , must be conducted because the installation of the image plane changes the empty tunnel geometry.

Semispan models normally consist of half of the fuselage mounted on the image plane. It is therefore necessary to place singularities representing the fuselage volume on the surface of the image plane. This requires further modification of a panel method code to compute normalized perturbation velocities (for more detail see Appendix 2) .

No support system is present in the test section, i.e. $u_t = u_{tm}$, $u_{ts} = 0.0$, and $u_s = 0.0$ (see boundary value problems depicted in Fig. 8) . Thus Eq. (4), (5b), (7) are replaced by the following expressions :

$$\epsilon(\nu) \approx \left[\frac{u_{tm}^*(\nu) - u_m^*(\nu)}{U_e^*(\nu)} \right] = \epsilon_m(\nu) \quad (17)$$

$$\frac{v_i(\nu)}{U_e(\nu)} \approx \left[\frac{v_{tm}^*(\nu) - v_m^*(\nu)}{U_e^*(\nu)} \right] = \alpha_m(\nu) \quad (18a)$$

$$\alpha_i(\nu) = \frac{v_i(\nu)}{u_\infty(\nu)} = \frac{U_e(\nu)}{u_\infty(\nu)} \cdot \frac{v_i(\nu)}{U_e(\nu)} = \frac{U_e(\nu)}{u_\infty(\nu)} \cdot \alpha_m(\nu) \quad (18b)$$

Normalized perturbation velocities, \bar{u}_i , \bar{v}_i , and \bar{w}_i , of the interference and wind tunnel flow field are computed using a panel method code. These perturbation velocities are required for the least squares fit of the wall signature and the calculation of wall interference corrections. The user has to make sure that the orientation angle of the line doublets is changed for semispan tests (see Appendix 4).

Figure 9a summarizes the basic elements of the Wall Signature Method for semispan model tests. The least squares fit of the wall signature, defined in Eqs. (13a) to (13f), still applies. Again, it is necessary to subtract the contribution of the wing line doublets and the contribution of the propulsion simulator point sinks from the wall signature difference. However, the image plane is calibrated as a part of the wind tunnel wall and no support system is present in the tunnel. Therefore, the wall signature difference is defined as the difference between the wind tunnel measurement, $U_e(\delta) + u_t(\delta)$, and the image plane calibration, $U_e(\delta)$, (see Fig. 9b). Equation (13g) is replaced by

$$b_\delta = \frac{[U_e(\delta) + u_t(\delta)] - U_e(\delta)}{U_{ref}} - \sum_{k=\xi+1}^n \sigma_k \cdot \bar{u}_t(\delta, k) \quad (19)$$

For a semispan model configuration the lift force measurement and the *Kutta/Joukowski* formula are needed to determine the strength of the line doublets of the wing (see Appendix 5).

2.5 Compressibility Effects

Compressibility effects have to be taken into account if the modified formulation of the Wall Signature Method is applied to a subsonic wind tunnel flow field.

In general, the Prandtl/Glauert transformation may be used to approximate the effects of compressibility in a flow field. This transformation requires a coordinate stretching of the wind tunnel geometry, singularity location, singularity strength, and reference point location when normalized perturbation velocities are being computed as outlined in the previous sections (for more detail on the transformation see Ref. [13] and [14]).

The application of the Prandtl/Glauert rule to the flow field of a singularity located inside of a wind tunnel requires several steps. First, coordinates (x, y, z) of the tunnel

geometry and of the singularity position are transformed to corresponding incompressible coordinates $(\bar{x}, \bar{y}, \bar{z})$ using the Prandtl/Glauert transformation :

$$\bar{x} = x \quad (20a)$$

$$\bar{y} = y \cdot \sqrt{1 - M^2} = y \cdot \beta \quad (20b)$$

$$\bar{z} = z \cdot \sqrt{1 - M^2} = z \cdot \beta \quad (20c)$$

It is necessary to stretch the strength of the singularity as well. The strength of a source is related to the cross-sectional area of a corresponding halfbody, [13], as

$$\sigma = \pi \cdot R^2 \cdot U_\infty = \pi \cdot [y^2 + z^2] \cdot U_\infty \quad (21)$$

where R equals the radius of a halfbody far downstream of the source location. Singularity strength σ has the units $[m^3/sec]$ or $[ft^3/sec]$. Comparing Eqs. (20b),(20c),(21) we see that the singularity strength is proportional to β^2 . The strength of a line doublet is related to a corresponding wing span increment, i.e. Δy , and angle of attack, i.e. w/U_∞ or $d z/d x$. Considering Eqs.(20b) and (20c) we see that the line doublet strength has to be proportional to β^2 . Finally, we get for the incompressible singularity strength :

$$\bar{\sigma} = \sigma \cdot [1 - M^2] = \sigma \cdot \beta^2 \quad (22)$$

A Mach number, M , derived from the calibrated velocity, U_{ref} , at a test section reference point should be used for the coordinate and singularity strength stretching.

Next, the incompressible flow field is obtained by using the modified version of the panel method code PMARC,[15] as a boundary value problem solver. Finally, perturbation velocities calculated relative to the inlet velocity are transformed from the incompressible flow field, $(\bar{u}, \bar{v}, \bar{w})$, to the compressible flow field, (u, v, w) . We then get :

$$u = \frac{\bar{u}}{\beta^2} \quad (23a)$$

$$v = \frac{\bar{v}}{\beta} \quad (23b)$$

$$w = \frac{\bar{w}}{\beta} \quad (23c)$$

A quantitative check of compressibility effects is possible if we place a point source of unit strength inside the geometry of the 12ft PWT and use a modified panel method code and the Prandtl/Glauert transformation described above to solve the flow field. Far downstream of the point source the flow field is essentially one-dimensional and asymptotes of perturbation velocities for different Mach numbers can be calculated. The results of the panel method code calculations on Row 1 (see Fig. 17b for location of Row 1) for Mach numbers $M = 0.0, 0.3, 0.6$ are plotted in Fig. 10 . Asymptotic values of perturbation velocities can be found in Table 2 .

Independent of the panel method code calculation it is also possible to apply the Area-Velocity-Relation of compressible flow, [16] . We can write :

$$\frac{d u}{U_{\infty}} = \frac{1}{1 - M^2} \cdot \frac{-d A}{A} \quad (24)$$

The 12ft PWT has a cross-sectional area $A = 109.74 [ft^2]$. A point source of strength $\sigma/U_{\infty} = 1.0 [ft^2]$ corresponds to a change of cross-sectional area of $-dA = 1.0 [ft^2]$ (see also Eq. (21)). Equation (24) is applied to Mach numbers $M = 0.0, 0.3, 0.6$. Results are shown in the table below.

Table 2 : Calculated Asymptotes of Perturbation Velocity

Mach Number	Panel Method Code	Equation (24) ; du/U_{∞}
0.0	0.0091	0.0091
0.3	0.0100	0.0100
0.6	0.0140	0.0142

Comparing the results of the panel method code calculation and the Area-Velocity-Relation, we get excellent agreement to verify application of the Prandtl/Glauert transformation.

2.6 Normalized Perturbation Velocity Definition

In general, normalized perturbation velocities can be defined as dimensionless perturbation velocities divided by unit singularity strength per unit velocity caused by some singularity. For example, the normalized perturbation velocity, $\overline{u}_f(\delta, k)$, at a point, $(x_{\delta}, y_{\delta}, z_{\delta})$,

in the free-air flow field of a unit strength source located at (x_k, y_k, z_k) can be defined as (see also Eq. (3.2a) in Appendix 3) :

$$\begin{aligned} \overline{u}_f(\delta, k) &= \frac{u(\delta, k)}{U_{ref}} \cdot \frac{U_{ref}}{\sigma} = \frac{u(\delta, k)}{U_{ref}} \cdot \frac{1}{\sigma_k} \\ &= \frac{1}{4 \pi} \cdot \frac{x_\delta - x_k}{\left[(x_\delta - x_k)^2 + (y_\delta - y_k)^2 + (z_\delta - z_k)^2 \right]^{3/2}} \end{aligned} \quad (25)$$

Two different sets of normalized perturbation velocities for a given singularity type, location, and specified model reference point location have to be computed if the Wall Signature Method is applied. The first set is related to the wind tunnel flow field of a singularity. The second set is related to the wall interference flow field of a singularity.

Normalized perturbation velocities, $\overline{u}_i(\delta, k)$, of the wind tunnel flow field of a singularity are required for the least squares fitting of the wall signature on wall pressure orifices “ δ ” (see Eqs. (13d), (13e), (13g), (19)) . Each normalized perturbation velocity can be interpreted as a dimensionless streamwise perturbation velocity divided by unit singularity strength per unit velocity at wall pressure orifice “ δ ” caused by the wind tunnel flow field of a singularity located at position “ k ” .

Normalized perturbation velocities, $\overline{u}_i(\nu, k)$ and $\overline{w}_i(\nu, k)$, of the wall interference flow field are required to determine wall interference corrections at reference point “ ν ” (see Eqs. (9a), (9b), (15a), (15b)) . Each of these perturbation velocities can be interpreted as a dimensionless perturbation velocity component divided by unit singularity strength per unit velocity at flow field reference point “ ν ” caused by the wall interference flow field of a singularity located at position “ k ” . Normalized perturbation velocity $\overline{u}_i(\nu, k)$ is the streamwise perturbation velocity component and normalized perturbation velocity $\overline{w}_i(\nu, k)$ is the perturbation velocity component perpendicular to the wing plane.

Explicit equations of these normalized perturbation velocities can be derived in the case of a wind tunnel with rectangular cross-section using the Method of Images. However, normalized perturbation velocities of a wind tunnel with non-rectangular cross-section have to be computed using a panel method code as a boundary value problem solver (see Ref. [15],[17], and Appendix 2 for more detail) .

Exact Bessel Function solutions of the angle of attack correction of a line doublet located in plane $z = 0.0$ inside of a wind tunnel with circular cross-section are available.

NACA TN 2454, [18] lists these corrections in the form of upwash factor tables. Tables can be compared with the normalized perturbation velocities of the wall interference flow field that were computed using a modified panel method code [15],[17] .

At first, an upwash factor table used for fullspan model tests (Table I on p.32 of NACA TN 2454, [18]) is compared with the corresponding panel method code solution. Figs. 11a and 11b compare upwash factor F as a function of the dimensionless streamwise coordinate and the dimensionless line doublet location (lateral coordinate $\eta = 0.7$). The exact Bessel Function solution and the numerical panel method code solution of the upwash factor F show reasonable agreement verifying the normalized perturbation velocity definition of the fullspan configuration.

Table 3 compares the input and accuracy characteristics of NACA TN 2454 and the panel method code solution of the normalized perturbation velocities.

Table 3 : Comparison NACA TN 2454 / Panel Method Code

	NACA TN 2454	Panel Method Code
Tunnel Geometry	Circular Tunnel One Bipolar Tunnel	Any Tunnel Geometry
Solution Type	Exact (Circular) Approximation (Bipolar)	Numerical Solution
Singularity Type	Line Doublet	Point Source, Point Doublet, Line Doublet
Singularity Location	Z=0.0 (Circular) Y=0.0 (Bipolar)	Minimum distance from wall panels $\approx 0.2 \times$ tunnel radius
Reference Point Location	Z=0.0 (Circular) Y=0.0 (Bipolar)	Minimum distance from wall panels $\approx 0.2 \times$ tunnel radius

Unfortunately, no rigorous solution of the upwash factor F , i.e. angle of attack correction, of a line doublet located inside of a bipolar wind tunnel (image plane / semispan configuration) is available. However, NACA TN 2454 provides an approximation of the upwash factor F for a bipolar wind tunnel that can be compared with the results obtained by applying a panel method code. Fig. 11c compares this approximation of upwash factor F (Fig. 5(c) on p.56 of NACA TN 2454, [18]) with the panel method code solution. Both approximations show reasonable agreement verifying the normalized perturbation velocity

definition of the semispan model configuration.

A panel method code allows the user to compute normalized perturbation velocities for any type of constant cross-section wind tunnel geometry that can be paneled. Singularities and reference points can also be placed anywhere inside of the wind tunnel as long as the minimum distance of the singularity or reference point from the paneled wind tunnel wall (60 panels used to represent tunnel cross-section) is greater than $0.2 \times$ tunnel radius.

CHAPTER 3

APPLICATION OF THE METHOD TO WIND TUNNEL TESTS

3.1 Real-Time Wall Interference Calculation

The revised and improved version of the Wall Signature Method presented in this report can be used to predict the Mach number, dynamic pressure, and angle of attack correction at a test article reference point due to the subsonic wind tunnel wall interference effects. Post-test analysis of subsonic wall interference effects is also possible as long as the exact position of the test article in the wind tunnel is known for a specific angle of attack setting. The location of singularities representing the test article is directly related to this position. Perturbation velocities of the wind tunnel and interference flow field can be computed as outlined in the previous chapters.

The real-time calculation of wall interference corrections is fast because the Wall Signature Method only requires superposition of the perturbation velocities, application of the *Kutta/Joukowski* formula (Appendix 5), *Koning's* formula (Appendix 10), and the solution of a 2×2 linear system of equations related to the least squares fit of the wall signature.

The precalculation of normalized perturbation velocities used for the real-time least squares fit of the wall signatures and for the calculation of corrections has to be done on a mainframe computer or fast workstation since a realistic implementation of the proposed Wall Signature Method requires the calculation of perturbation velocities for many different singularity types, locations, and Mach numbers. Figures 12a,12b depict geometries of the NASA 12ft Pressure Wind Tunnel test section that are selected for the calculation of the perturbation velocities of the wind tunnel and interference flow field using a panel method code as a boundary value problem solver. Precomputed normalized perturbation velocities have to be stored in a database that is accessed during a wind tunnel test.

A singularity and reference point grid has to be used for the calculation of the perturbation velocity database. These two grids should be selected such that they allow for a real-time interpolation of all conceivable singularity and reference point locations in the wind tunnel test section. Perturbation velocities required for singularities representing the

test article change as a function of test article geometry and position in the wind tunnel test section. Size, complexity, and accuracy requirements of the perturbation velocity database have to be balanced to guarantee best real-time performance. Thus, perturbation velocities of the wind tunnel and interference flow field for a given test article location are found in real-time by applying a tri-linear interpolation (real-time singularity position; Appendix 6) and parabolic interpolation (real-time Mach number; Appendix 7) to the precomputed perturbation velocity database.

Blockage effects of the support system can be computed off-line by applying the Wall Signature Method to the difference between the support system and the empty tunnel calibration. Computed support system wall interference corrections on the reference point grid have to be stored in a database as a function of the support system calibration variables. The support system wall interference corrections are added in real-time to the wall interference corrections caused by the test article.

Post-test analysis of the interference effects is based on minimizing the standard deviation of the least squares fit of the wall signature as a function of the location of the test article singularities (see Appendix 8). This procedure provides an optimal singularity representation of the test article.

Studies of the author have shown that the real-time speed of the wall interference calculation is governed by the efficiency of the interpolation of the perturbation velocities using the precomputed perturbation velocity database.

Figures 13a,13b depict basic elements of the real-time Wall Signature Method for a fullspan and a semispan model configuration. The empty tunnel calibration, support system calibration, real-time wall pressures, lift force, propulsion simulator thrust, and pitching moment measurements are the critical link between experiment and the panel method code calculation. Matching conditions between the wind tunnel test and the panel method code calculation will be discussed in detail in the following section.

3.2 Matching Conditions

The least squares fit proposed for a fullspan and semispan model configuration relates experimental data, i.e. wall pressure measurements, to precomputed normalized perturba-

tion velocities. Therefore suitable equations have to be found to convert the wall pressure measurements to perturbation velocities.

Perturbation velocity differences $[U_e + u_t] - [U_e + u_{ts}]$, $[U_e + u_{ts}] - U_e$, and $[U_e + u_t] - U_e$ defined in Eqs. (13g), (16c), and (19) can be related to the wall pressure measurements taken during calibration and real-time wind tunnel test by applying the energy equation and the isentropic flow assumption. Assuming that the total temperature T_T and total pressure p_T in the tunnel settling chamber, and the static pressure p at wall pressure orifice δ are known, we get for the flow velocity (see Fig. 14a) :

$$U(p(\delta)) = \sqrt{\frac{2 \gamma R T_T}{\gamma - 1} \cdot \left[1 - \left[1 - \frac{p_T - p(\delta)}{p_T} \right]^{(\gamma-1)/\gamma} \right]} \quad (26)$$

Dimensionless perturbation velocities can then be written as :

$$\frac{[U_e(\delta) + u_t(\delta)] - [U_e(\delta) + u_{ts}(\delta)]}{U_{ref}} = \frac{U(p_{tun}(\delta)) - U(p_{sup}(\delta))}{U_{ref}} \quad (27a)$$

$$\frac{[U_e(\delta) + u_{ts}(\delta)] - U_e(\delta)}{U_{ref}} = \frac{U(p_{sup}(\delta)) - U(p_{emp}(\delta))}{U_{ref}} \quad (27b)$$

$$\frac{[U_e(\delta) + u_t(\delta)] - U_e(\delta)}{U_{ref}} = \frac{U(p_{tun}(\delta)) - U(p_{emp}(\delta))}{U_{ref}} \quad (27c)$$

The flow velocity $U(p(\delta))$ in Eq. (26) is written as a function of the pressure difference $p_T - p(\delta)$ as it is easier to measure a pressure difference at a wall pressure port. Real-time static pressure p_{tun} , support system static pressure p_{sup} , and empty tunnel calibration static pressure p_{emp} are recorded at each wall pressure port “ δ ”. Measured velocity $U_e(\delta) = U(p_{emp}(\delta))$ at a wall pressure port “ δ ” is the first matching condition. It is required to obtain the perturbation velocities defined in Eqs. (27b),(27c) .

The velocity U_{ref} in Eqs. (13g), (16c), and (19) is the second matching condition between the wind tunnel flow field and the corresponding dimensionless panel method code calculation. It is required to non-dimensionalize the perturbation velocities defined in Eqs. (27a),(27b),(27c) . It can be considered as the constant flow velocity inside of a hypothetical constant cross-sectional test section. This velocity should be measured during the empty tunnel calibration at a specific model reference point θ (see Fig. 14b; this point has the coordinates $X=120.71$ [ft], $Y=0.0$ [ft], $Z=0.0$ [ft] in the 12ft PWT). The

velocity U_{ref} can be measured by using, e.g., a static pipe installed in the wind tunnel during the calibration. We then get :

$$U_{ref} = \sqrt{\frac{2 \gamma R T_T}{\gamma - 1} \cdot \left[1 - \left[1 - \frac{p_T - p_{emp}(\theta)}{p_T} \right]^{(\gamma-1)/\gamma} \right]} \quad (28)$$

The real-time lift force and pitching moment measurements are related to the strength of the corresponding line doublets using the *Kutta/Joukowski* formula. Its application requires knowledge of velocity U_{ref} and density $\rho_{ref}(\theta)$ at a model reference point θ measured during the calibration of the wind tunnel. This velocity and fluid density connect lift force and pitching moment measured in $[lbf],[ft * lbf]$ or $[N],[N * m]$ to the definition of the line doublet strength in $[ft^2]$ or $[m^2]$ (see Appendix 5). The fluid density is also required to relate the propulsion simulator thrust measurement to the sink strength if *Koning's* formula is applied (see Appendix 10). The density $\rho_{ref}(\theta)$ is the third matching condition. It is found by applying the ideal gas and the isentropic flow relationship at a test section reference station θ . We get :

$$\rho_{ref}(\theta) = \frac{p_T}{R T_T} \cdot \left[\frac{p_{emp}(\theta)}{p_T} \right]^{1/\gamma} \quad (29)$$

where $p_{emp}(\theta)$ is the static pressure measured at the model reference point θ .

It is interesting to note that the perturbation velocity differences $[U_e(\delta) + u_t(\delta)] - [U_e(\delta) + u_{ts}(\delta)]$, $[U_e(\delta) + u_{ts}(\delta)] - U_e(\delta)$, and $[U_e(\delta) + u_t(\delta)] - U_e(\delta)$ remove the influence of the wall boundary layer growth, orifice error, image plane, and wall divergence from the least squares fit. Therefore it is possible to use the geometry of an equivalent wind tunnel with constant cross-sectional area for the calculation of normalized perturbation velocities of the wind tunnel and interference flow field.

Three matching conditions, i.e. $U_e(\delta)$, U_{ref} , and ρ_{ref} , establish a link between the measurement of wall pressures, forces, moments and the panel code solutions of the wind tunnel and interference flow field expressed as normalized perturbation velocities. Figure 14c summarizes the importance of these matching conditions.

3.3 Application of the Method to Semispan Models

In the summer of 1996, two different sized semispan models were tested in the NASA Ames 12ft Pressure Wind Tunnel (PWT). Both models, i.e. the 8 % and 14 % scale 7J7

semispan models, were provided by the Boeing Corporation. Each model was mounted on the image plane in the 12ft PWT. Figure 15 shows a similar test configuration.

Both models were tested over a wide range of angle of attack, total pressure, and Mach number settings. For the present study, two runs were selected. During Run No. 154 the 8 % scale model was tested from -20.28° to 19.82° uncorrected angle of attack at a total pressure of 2.0 [atm] and a Mach number of 0.25 . During Run No. 219 the 14 % scale model was tested from -4.03° to 9.98° uncorrected angle of attack at a total pressure of 2.0 [atm] and a Mach number of 0.30 .

The application of the present wall interference correction method was done in several steps. At first, type and initial location of the singularities representing each model were specified. Rules of thumb given in Appendix 9 were used to select type, location, and weighting factors for these singularities. A total of 11 singularities were selected for each model. A source and a sink were selected to represent fuselage blockage, two sources were selected to model the separation wake blockage effects. Seven line doublets, located along the 1/4 chord line of the wing, were chosen to represent lifting effects. Weighting factors for the line doublets were selected to model an elliptic lift distribution for the wing. Figures 16a,16b give the singularity representation of each semispan model for 0° angle of attack. The real-time coordinates of these singularities as a function of the pitch angle were computed using the known kinematics of a semispan model mounted on the image plane (for more detail see Eqs. (14.19a),(14.19b) in Appendix 14) .

In the next step, measured lift force in combination with the *Kutta-Joukowski* formula was used to determine the strength of line doublets for the wing for each data point.

The strength of the remaining singularities was computed using a least squares fit of the wall pressure measurements on 180 wall pressure ports that were arranged in six rows above the image plane. The least squares fit used wall pressure port rows 1,2,3,6,7,8 depicted in Fig. 17a,17b . For more detail on the least squares fit procedure see Section 2.4 .

The standard deviation of the least squares fit of the wall signature was computed for each data point of Runs 154 and 219 (see Figs. 18a,18b) . The standard deviation of the 8 % scale model was on the order of 0.002 in units of the dimensionless perturbation velocity. This agrees with the standard deviation of a wall signature obtained by *Rueger et al.*, [19] who reported a value of 0.005 in units of pressure coefficient, i.e. 0.0025 in units of

the dimensionless perturbation velocity. The standard deviation of the 14 % scale model was on the order of 0.003 to 0.006 in units of the dimensionless perturbation velocity.

Figures 19a to 19f show the result of the least squares fit of the wall signature for the 8 % semispan model at 19.82° uncorrected angle of attack. Figures 20a to 20f show the result of the least squares fit of the wall signature for the 14 % semispan model at 9.98° uncorrected angle of attack. Figures 21a, 21b depict the wall signature for both models at approximately 0.0° angle of attack at wall pressure port Row 6 . The large difference in solid volume blockage of both models can clearly be detected in the wall signature. The measured wall signature difference “ u ” depicted in Figs. (19a) to (21b), i.e. the velocity difference $[U_e + u_t] - U_e$ in Fig. 9b, shows excellent agreement with its least squares fit.

The present method (WICS), the two-variable method, and the classical method were used to compute wall interference corrections. Two-variable method results were provided by Mat Rueger of Boeing St. Louis. Classical corrections were provided by Alan Boone of NASA ARC who used NACA Rep. No. 995 (solid volume blockage), [20], R.A.E. Rep. No. 3400, [21] (separation wake blockage), and NACA TN 2454, [18] , to determine wall interference corrections. Mean wall interference corrections for each model were computed using flow field reference points located along the 3/4 chord line of the wing. Corresponding results are compared below.

As expected, wall interference corrections computed by WICS and the two-variable method show excellent agreement because both methods are based on potential flow theory and boundary flow measurements. Angle of attack corrections agree well in all three cases (see Figs. 22a,22b) . The solid volume blockage factor contribution depicted in Fig. 23a agrees well for the 8 % scale model in all three cases. A comparison of the solid volume blockage factor contribution of the 14 % scale model depicted in Fig. 23b shows larger differences between classical corrections and WICS. This can be explained by the fact that the calculation of the solid volume blockage using the classical method (NACA Rep. No. 995) assumes that a wind tunnel of constant cross-section extends to far upstream and downstream of the semispan model. This assumption, however, cannot be justified anymore in the case of the 14 % scale model as the fuselage length is 16.69 [ft] and the length of the image plane is ≈ 20.0 [ft] . The classical method will therefore overpredict the solid volume blockage effect for the 14 % scale model. The separation wake blockage

factor contribution for the 8 % scale model determined based on the classical method [21] is larger than the blockage factor computed using WICS or the two-variable method (see Figs. 23a) . This agrees with observations reported in the literature, [5],[19] .

The 8 % and 14 % scale model have identical geometry. Therefore it is possible to compare the minimum of the blockage factor of both models by using a scale factor law (for more detail see Appendix 20). Results discussed in Appendix 20 demonstrate that blockage corrections computed with the present method (WICS) satisfy this scale factor law. Thus, wall pressure measurement accuracy and the solid volume description used by the present method are sufficiently accurate for computing blockage effects.

In general, the ratio between measurements and unknowns of a least squares fit has to be large to take full advantage of its smoothing characteristics. In our application the number of unknowns of the least squares fit is two (see Eqs. (13a),(16a)). Figures 23c, 23d compare the computed dynamic pressure correction for the 8 % scale model with 180 or 30 wall pressure ports used for the least squares fit of the wall signature. The differences in the computed corrections depicted in Figs. 23c, 23d are small. This demonstrates a key operational advantage of the Wall Signature Method : the calculation of the corrections is relatively insensitive to the number and location of the wall pressure ports (see also Table 1 in Chapter 1) . Comparison of the data scatter in the computed dynamic pressure correction depicted in Figs. 23c,23d shows that an increase in the number of wall pressure measurements used in the least squares fit reduces the data scatter of the computed blockage corrections.

The local dynamic pressure correction for the 8 % model at 19.82° angle of attack and for the 14 % model at 9.98° angle of attack are computed in the plane $Y=0.0$ [ft] (cut through test section parallel to side wall). The dynamic pressure correction for the 8 % model at 19.82° increases gradually as an observer moves from upstream to downstream of the model (see Fig. 24a) . The separation wake blockage effects dominate the dynamic pressure correction downstream of the model at an angle of attack of 19.82° . The contour lines are nearly parallel to the z -axis. We conclude that the dynamic pressure correction for the 8 % model is almost exclusively a function of the streamwise coordinate.

The dynamic pressure correction for the 14 % model at 9.98° has a saddle point at the streamwise coordinate 120.0 [ft] (see Fig. 24b) . The correction decreases as an observer

moves downstream of the model. Therefore, it can be concluded that the solid volume blockage effects dominate the correction at an angle of attack of 9.98° .

In both contour plots, it can be seen that the minimum of the dynamic pressure correction for a constant streamwise coordinate is about 4.0 [ft] above the image plane. This is caused by the fact that the tunnel width increases as an observer moves from the image plane surface to the tunnel centerline (see also Fig. 15).

The local angle of attack corrections for 19.82° and 9.98° for each model are computed in the plane $Y=0.0$ [ft] (cut through test section parallel to side wall). The contour plots of the results are depicted in Figs. 24c,24d. The angle of attack correction variation along the 3/4 chord line of the 8 % model at 19.82° , i.e. from wing root to tip, is on the order of 0.05° . The aerodynamic twist is insignificant in this case. However, the angle of attack correction variation along the 3/4 chord line of the 14 % model at 9.98° is on the order of 1.0° and cannot be ignored anymore.

3.4 Application of the Method to the Ames Bipod

In 1995 the Ames Bipod, a floor-mounted support system, was tested in the NASA Ames 12ft Pressure Wind Tunnel (PWT). Blockage corrections due to support system wall interference effects were computed using the Wall Signature Method (WICS) as outlined in Section 2.3.2.

The application of the Wall Signature Method to the Ames Bipod was done in several steps. At first, type, initial location, and weight of singularities representing the Ames Bipod were specified. Figure 25a shows the Ames Bipod geometry and lists type, initial location, and weight of these singularities. A total number of 27 singularities was selected for the support system. Singularities No. 1 to No. 18, i.e. 9 source/sink pairs, were chosen to represent solid volume blockage effects of the support system. Singularities No. 19 to No. 27 were chosen to model separation wake blockage effects.

In a second step, strength values of these singularities were computed using a least squares fit of the wall pressure measurements. Wall pressures on Row 1 to Row 8 (see Figs. 17a,17b) were measured during the support system calibration as a function of the total pressure in the settling chamber and the Mach number at a test section reference

point. Wall pressure measurements obtained during an empty tunnel calibration were also available. The least squares fit was applied to the difference between the wall signature measured during the support system calibration and the wall signature measured during the empty tunnel calibration. Figures 25b,25c show the result of the least squares fit on Row 2 and Row 4 . Measured wall signature difference and least squares fit show reasonable agreement. Larger differences between the measured wall signature and the least squares fit on Row 4 are caused by the fact that singularities cannot be placed too close to the floor for numerical reasons (see also Chapter 2.6). Finally, the blockage factor was computed on planes $Y=0.0$ [ft] (parallel to test section side wall), $X=120.71$ [ft] (parallel to test section inlet), and $Z=0.0$ [ft] (parallel to test section floor) .

Figure 25d shows the blockage factor on plane $Y=0.0$ [ft] that was computed using the initial singularity location given in Fig. 25a . Figure 25e shows the blockage factor on plane $Y=0.0$ [ft] that was computed after the standard deviation of the least squares fit was minimized as a function of the singularity location (see Appendix 8). Comparing both contour plots it can be recognized that differences in the computed blockage factor are small, i.e. computed corrections are not very sensitive to the location of singularities as long as they are placed at the location of the support system. Comparing singularity locations before and after the minimization it can be noticed that sources No. 1 to No. 9 and sources No. 19 to No. 27 have moved closer together. The minimization procedure has correctly deduced from the wall signature difference that the front post of the Ames Bipod has a significantly larger diameter than the pitch strut, i.e. most of the separation wake of the Ames Bipod is caused by the front post.

Figure 25f shows the blockage factor on plane $X=120.71$ [ft] . In this contour plot it can be seen that the blockage factor increases in any direction if an observer moves closer to the test section wall. A minimum of the blockage factor is located ≈ 1.0 [ft] above the tunnel centerline. The blockage factor increases significantly if an observer moves closer to the test section floor.

Figure 25g shows the blockage factor on plane $Z=0.0$ [ft] . As expected, the blockage factor increases if an observer moves from an upstream position to a downstream position. This observation is caused by the fact that the separation wake blockage dominates blockage corrections downstream of the Ames Bipod.

CHAPTER 4

CONCLUSION AND REMARKS

A revised version of the Wall Signature Method was developed which allows the user to predict Mach number, dynamic pressure, and angle of attack correction due to wall interference effects in three-dimensional subsonic wind tunnel testing of aircraft models. This improved formulation of the Wall Signature Method uses lift force, propulsion simulator thrust force, pitching moment, wall pressure measurements, empty tunnel calibration, support system calibration, a simplified representation of the test article and support system in terms of singularities, and precalculated normalized solutions of the subsonic potential equation expressed as normalized perturbation velocities to predict wall interference corrections at a model reference point in real-time.

The method is applicable to complex wind tunnel and support system configurations. Wall interference corrections are found by taking the difference between a simplified representation of the wind tunnel flow field in terms of singularities and the corresponding free-air solution. Computational procedures were developed to predict solid body blockage, separation wake blockage, propulsion simulator blockage, and lift interference correction if a fullspan model or a semispan model is tested.

The definition of normalized perturbation velocities used by the method has been improved to allow the user to take full advantage of the geometry modeling capabilities of a three-dimensional panel method code. A "global" least squares fit procedure of the wall signature was also introduced to improve the application of the Wall Signature Method in real-time. Optimal locations of singularities are defined by minimizing the standard deviation of the least squares fit of the wall signature.

Experimental data obtained during tests of two semispan models mounted on an image plane in the NASA 12ft Pressure Wind Tunnel were applied to the modified Wall Signature Method. Blockage and angle of attack corrections were computed for different angle of attack settings. In all cases, computed angle of attack corrections show good agreement with corresponding classical corrections. Computed blockage corrections are smaller than corresponding classical corrections. This result agrees with observations reported in

literature, [5],[19] .

Experimental data recorded during the calibration of the Ames Bipod was also successfully applied to the method.

Further experimental studies have to be conducted in the future to gain confidence in the method.

LIST OF REFERENCES

- [1] Hackett, J. E., Wilsden, D. J. and Lilley, D. E., "Estimation of Tunnel Blockage from Wall Pressure Signatures: a Review and Data Correlation," NASA CR-152241, Lockheed-Georgia Company, Marietta, Georgia, March 1979 .
- [2] Hackett, J. E., Wilsden, D. J. and Stevens, W. A. , "A Review of the Wall Pressure Signature and other Tunnel Constraint Correction Methods for High Angle-of-Attack Tests," AGARD-R-692, Munich, May 1980.
- [3] Hackett, J. E., "Living with Solid-Walled Wind Tunnels," AIAA 82-0583, presented at the AIAA 12th Aerodynamic Testing Conference, March 22-24, 1982/Williamsburg, Virginia.
- [4] Ashill, P. R., Keating, R. F. A., "Calculation of Tunnel Wall Interference from Wall Pressure Measurements," The Aeronautical Journal, Vol. 92, No. 911, January 1988, p.36 to p.53 .
- [5] Ashill, P. R., "Boundary-Flow Measurement Methods for Wall Interference Assessment and Correction; Classification and Review," Proceedings, 73rd AGARD Fluid Dynamics Panel Meeting and Symposium on Wall Interference, Support Interference and Flowfield Measurements, Oct. 4-7, 1993, p.12-1 to p.12-21 .
- [6] Koning, C., "Influence of the Propeller on other Parts of the Airplane Structure," in "Aerodynamic Theory," edited by Durand, W. F., Springer Verlag, Berlin, 1935, Volume IV, Division M, Section 5, p.367/368 .
- [7] Ulbrich, N. and Steinle, F. W., "Real-Time Wall Interference Calculation in Three-Dimensional Subsonic Wind Tunnel Testing," AIAA 94-0771, presented at the 32nd Aerospace Sciences Meeting, Reno, Nevada, January 10-13, 1994 .

- [8] Ulbrich, N. and Steinle, F. W., "Semispan Model Wall Interference Prediction Based on the Wall Signature Method," AIAA 95-0793, presented at the 33rd Aerospace Sciences Meeting, Reno, Nevada, January 9-12, 1995 .
- [9] Ulbrich, N., "Real-Time Wind Tunnel Wall Interference Prediction Based on Linearized Panel Method Code Solutions," final report of National Research Council tenure, presented to the Aeronautical Test and Simulation Division at NASA Ames Research Center, Moffett Field, California, December 1994 .
- [10] Garner, H. C., Rogers, E. W. E., Acum, W. E. A. and Maskell, E. C., "Subsonic Wind Tunnel Wall Corrections," AGARDograph 109, North Atlantic Treaty Organization, October 1966 .
- [11] Strang, G., "Introduction to Applied Mathematics, " Wellesley-Cambridge Press, Wellesley, Massachusetts, 1986, p.35-39 .
- [12] Press, W. H., Teukolsky, S. A., Vetterling, W. T., Flannery, B. P., "Numerical Recipes in FORTRAN 77," Cambridge University Press, reprint of second edition with corrections, 1996, p.51-63, p.670-673 .
- [13] Schlichting, H. and Truckenbroth, E., "Aerodynamik des Flugzeuges," Vol. 2, 2nd Ed., Springer-Verlag, Berlin, Heidelberg, New York, 1967, p.159-164 .
- [14] Kuethe, A. M. and Chow, C., "Foundations of Aerodynamics," 4th Ed., John Wiley & Sons, New York, 1986, p.271-272 .
- [15] Ashby, D. L., Dudley, M. R., Iguchi, S. K., Browne, L., Katz, J., "Potential Flow Theory and Operation Guide for the Panel Code PMARC," NASA TM 102851, NASA Ames Research Center, Moffett Field, California, January 1991 .

- [16] Liepmann, H. W. and Roshko, A., "Elements of Gasdynamics," 1st Ed., John Wiley & Sons Inc., New York, 1957, p.52 .
- [17] Lo, C. F., Xian, X. and Ulbrich, N., "Wind Tunnel Interference Calculated By a Panel Method," AIAA 95-0794, presented at the 33rd Aerospace Sciences Meeting, Reno, Nevada, January 9-12, 1995 .
- [18] Sivells, J. C. and Salmi, R. M., "Jet-Boundary Corrections for Complete and Semispan Swept Wings in Closed Circular Wind Tunnels," NACA TN 2454, 1951, p.8, p.17, p.18 .
- [19] Rueger, M., Crites, R., Weirich, R., "Comparison of Conventional and Emerging (Measured Variable) Wall Correction Techniques for Tactical Aircraft in Subsonic Wind Tunnels," AIAA 95-0108, presented at the 33rd Aerospace Sciences Meeting and Exhibit, January 9-12, 1995, Reno, Nevada.
- [20] Herriot, J. G., "Blockage Corrections for Three-Dimensional-Flow Closed-Throat Wind Tunnels, with Consideration of the Effect of Compressibility," NACA Report No. 995, Ames Aeronautical Laboratory, Moffett Field, California, 1951.
- [21] Maskell, E. C., "A Theory of the Blockage Effects on Bluff Bodies and Stalled Wings in a Closed Wind Tunnel," R.A.E. Report No. 3400, November 1963 .
- [22] Katz, J. and Plotkin, A., "Low-Speed Aerodynamics: From Wing Theory to Panel Methods," McGraw-Hill Series in Aeronautical and Aerospace Engineering, New York, 1991, p.60, p.63, p.378-420 .
- [23] Schlichting, H. and Truckenbroth, E., "Aerodynamik des Flugzeuges," Vol. 1, 2nd Ed., Springer-Verlag, Berlin, Heidelberg, New York, 1967, p.62-63 .

- [24] Ashley, H. and Landahl, M., "Aerodynamics of Wings and Bodies," Addison-Wesley Publishing Company, Inc., Reading, Massachusetts, 1965, p.87 .
- [25] DeYoung, J. and Harper, C. W., "Theoretical Symmetric Span Loading at Subsonic Speeds for Wings having Arbitrary Plan Form," NACA Report No. 921, Ames Aeronautical Laboratory, Moffett Field, California, 1948 .
- [26] Burden, R. L. and Faires, J. D., "Numerical Analysis," 3rd Ed., PWS-Kent Publishing Company, Boston, Massachusetts, 1985, p.514 .
- [27] Heyson, H. H., "Jet-Boundary Corrections for Lifting Rotors Centered in Rectangular Wind Tunnels," NASA Technical Report R-71, Langley Research Center, Langley Field, VA, 1960 .
- [28] Pope, A., "Basic Wing and Airfoil Theory," 1st Ed., McGraw-Hill Book Company, Inc., 1951, p.91 .
- [29] Schlichting, H. and Truckenbroth, E., "Aerodynamics of the Airplane," translated by H.J. Ramm, McGraw-Hill International Book Company, 1979, p.162/163 .

APPENDIX 1

HIGHER ORDER CORRECTION FORMULAE

The testing of an aircraft model at a high angle of attack in a three-dimensional subsonic wind tunnel can create large separation wake blockage effects. In this case, first order approximations of the Mach number and dynamic pressure correction as a function of the blockage factor ϵ are no longer sufficient. Second order approximations have to be derived.

A second order approximation of the Mach number correction can be found using a Taylor series expansion. The Mach number is expressed as a function of a small change in the fluid velocity. Assuming that this velocity change ΔU is related to the flow velocity U and blockage factor ϵ as :

$$\Delta U = \epsilon \cdot U \quad (1.1)$$

we get the following Taylor series expansion of the Mach number :

$$M(U + \epsilon U) = M(U) + \frac{d M(U)}{d U} \cdot \frac{(\epsilon U)}{1!} + \frac{d^2 M(U)}{d U^2} \cdot \frac{(\epsilon U)^2}{2!} + \dots \quad (1.2)$$

It is necessary to express the Mach number as a function of the fluid velocity U . Applying the energy equation we know :

$$c_p T_T = c_p T + \frac{U^2}{2} \quad (1.3)$$

Combining the energy equation with the definition of the Mach number, i.e.

$$M^2 = \frac{U^2}{a^2} = \frac{U^2}{\gamma R T} \quad (1.4)$$

and with the relationship between specific heat at constant pressure, isentropic exponent, and Gas constant, i.e. $c_p(\gamma - 1) = \gamma R$, we get :

$$M(U) = \frac{U}{\sqrt{\gamma - 1}} \cdot \left[c_p T_T - \frac{U^2}{2} \right]^{-1/2} \quad (1.5)$$

After some algebra we get for the first and second derivative :

$$\frac{d M(U)}{d U} = \frac{M(U)}{U} \cdot \left[1 + \frac{\gamma - 1}{2} \cdot M^2(U) \right] \quad (1.6a)$$

$$\frac{d^2 M(U)}{d U^2} = \frac{3}{2} \cdot (\gamma - 1) \cdot \frac{M^3(U)}{U^2} \cdot \left[1 + \frac{\gamma - 1}{2} \cdot M^2(U) \right] \quad (1.6b)$$

Combining Eqs. (1.2), (1.6a), (1.6b) and rearranging terms we get :

$$\begin{aligned} \frac{M(U + \epsilon U) - M(U)}{M(U)} &= \left[1 + \frac{\gamma - 1}{2} \cdot M^2(U) \right] \cdot \epsilon \\ &+ \frac{3}{4} \cdot (\gamma - 1) \cdot M^2(U) \cdot \left[1 + \frac{\gamma - 1}{2} \cdot M^2(U) \right] \cdot \epsilon^2 \\ &+ \dots \end{aligned} \quad (1.7)$$

Using the nomenclature introduced in Chapter 2.1 and assuming that $M(U + \epsilon U) = M_\infty$ and $M(U) = M_e$, we get the second order approximation :

$$\frac{M_\infty - M_e}{M_e} \approx \left[1 + \frac{\gamma - 1}{2} \cdot M_e^2 \right] \cdot \left[\epsilon + \frac{3}{4} \cdot (\gamma - 1) \cdot M_e^2 \cdot \epsilon^2 \right] \quad (1.8)$$

Similar to the Mach number correction it is necessary to derive a second order approximation of the dynamic pressure correction using a Taylor series expansion.

Assuming that the velocity change ΔU is related to the flow velocity U and blockage factor ϵ according to Eq. (1.1) we get the following Taylor series expansion for the dynamic pressure :

$$q(U + \epsilon U) = q(U) + \frac{d q(U)}{d U} \cdot \frac{(\epsilon U)}{1!} + \frac{d^2 q(U)}{d U^2} \cdot \frac{(\epsilon U)^2}{2!} + \dots \quad (1.9)$$

The dynamic pressure has to be expressed as a function of the fluid velocity U . Applying the energy equation (Eq. (1.3)), the Mach number definition (Eq. (1.4)), the ideal gas law, i.e. :

$$\frac{p}{\rho} = R \cdot T \quad (1.10)$$

and assuming isentropic flow, i.e. :

$$\frac{p}{\rho^\gamma} = \frac{p_T}{\rho_T^\gamma} \quad (1.11)$$

we get :

$$q(U) = \left[\frac{R \rho_T^\gamma}{c_p p_T} \right]^{1/(\gamma-1)} \cdot \left[c_p T_T - \frac{U^2}{2} \right]^{1/(\gamma-1)} \cdot \frac{U^2}{2} \quad (1.12)$$

After some algebra the first and second derivative can be obtained as :

$$\frac{d q(U)}{d U} = \frac{q(U)}{U} \cdot \left[2 - M^2(U) \right] \quad (1.13a)$$

$$\frac{d^2 q(U)}{d U^2} = \frac{q(U)}{U^2} \cdot \left[2 - 5 M^2(U) + (2 - \gamma) \cdot M^4(U) \right] \quad (1.13b)$$

Combining Eqs. (1.9), (1.13a), (1.13b) and rearranging terms, we get :

$$\begin{aligned} \frac{q(U + \epsilon U) - q(U)}{q(U)} &= \left[2 - M^2(U) \right] \cdot \epsilon \\ &+ \left[1 - \frac{5}{2} M^2(U) + \frac{2 - \gamma}{2} \cdot M^4(U) \right] \cdot \epsilon^2 \\ &+ \dots \end{aligned} \quad (1.14)$$

Again, using the nomenclature introduced in Chapter 2.1 and assuming that $q(U + \epsilon U) = q_\infty$, $q(U) = q_e$, and $M(U) = M_e(U)$, we get the approximation :

$$\frac{q_\infty - q_e}{q_e} \approx \left[2 - M_e^2(U) \right] \cdot \epsilon + \left[1 - \frac{5}{2} M_e^2(U) + \frac{2 - \gamma}{2} \cdot M_e^4(U) \right] \cdot \epsilon^2 \quad (1.15)$$

APPENDIX 2

PANEL METHOD CODE MODIFICATIONS

Introduction

In general, it is necessary to use a three-dimensional panel method code to calculate normalized perturbation velocities caused by singularities if the Wall Signature Method is applied to a wind tunnel with a non-rectangular but constant cross-section. Unfortunately, commercially available panel method codes do not allow the calculation of the flow field of a singularity placed inside of a wind tunnel. However, a few modifications to a panel method code can be introduced which make it possible to solve this type of internal flow field problem and to compute perturbation velocities.

A panel method code may be used to find the velocity potential of a given internal flow problem if the corresponding internal flow geometry, e.g. the geometry of the wind tunnel test section of constant cross-sectional area, is paneled. The specification of normal velocities at the wind tunnel inlet is also required (see *Ashby et al.* [15] for more detail on the application of a panel method code to internal flow problems; see *Katz and Plotkin* [22] for a more detailed description of three-dimensional panel method codes).

The boundary value problem of a singularity placed inside a wind tunnel flow field is depicted in Fig. 26. The velocity potential has to fulfill the Laplace equation :

$$\nabla^2 [\phi_\infty + \phi_t] = 0 \quad (2.1)$$

where ϕ_∞ is the free-stream potential and ϕ_t is the wind tunnel potential due to the wind tunnel walls and the singularity. Zero normal flow has to be satisfied across the wind tunnel wall surface and so we get:

$$\frac{\partial}{\partial \mathbf{n}} [\phi_\infty + \phi_t] = 0 \quad (2.2a)$$

The normal velocity vector \mathbf{u}_∞ has to be specified by the user at the test section inlet:

$$\frac{\partial}{\partial \mathbf{n}} [\phi_\infty + \phi_t] = \mathbf{u}_\infty \quad (2.2b)$$

Based on the principle of superposition (see Fig. 26) it is possible to express the wind tunnel potential ϕ_t as the sum of the singularity potential ϕ_σ and the wind tunnel wall potential ϕ_w :

$$\phi_t = \phi_\sigma + \phi_w \quad (2.3)$$

Combining Eqs. (2.1),(2.3) and knowing that the singularity potential itself fullfills Laplace's equation we get:

$$\nabla^2 [\phi_\infty + \phi_w] = 0 \quad (2.4)$$

Combining Eqs. (2.2a), (2.3) and rearranging terms we get the boundary condition across the wind tunnel wall surface:

$$\frac{\partial}{\partial \mathbf{n}} [\phi_\infty + \phi_w] = - \frac{\partial}{\partial \mathbf{n}} [\phi_\sigma] \quad (2.5a)$$

Combining Eqs. (2.2b),(2.3) and rearranging terms we get the boundary condition at the test section inlet:

$$\frac{\partial}{\partial \mathbf{n}} [\phi_\infty + \phi_w] = \mathbf{u}_\infty - \frac{\partial}{\partial \mathbf{n}} [\phi_\sigma] \quad (2.5b)$$

The velocity vector \mathbf{u}_∞ and the singularity potential ϕ_σ are known and so the boundary value problem given by Eqs. (2.4),(2.5a),(2.5b) can be solved. This requires the modification of the original panel method code such that the boundary conditions given by Eqs. (2.2a),(2.2b) are replaced by the boundary conditions given by Eqs. (2.5a),(2.5b) . Only the normal velocity component due to the singularity, i.e.

$$- \frac{\partial}{\partial \mathbf{n}} [\phi_\sigma]$$

has to be added to prescribed normal velocities at panel centroids.

Finally, the flow field solution of a singularity placed inside a wind tunnel test section can be found by superimposing the solution of the boundary value problem given by Eqs. (2.4),(2.5a),(2.5b), i.e. $\phi_\infty + \phi_w$, computed using the modified panel method code with the known analytic solution of the singularity potential ϕ_σ .

The modification of the boundary conditions based on Eqs.(2.5a),(2.5b) does not cause numerical difficulties if a singularity like a point source, point sink, or point doublet is selected. In these cases, the singularity potential ϕ_σ vanishes if the distance between

singularity and panel centroid is large and therefore normalized perturbation velocities can be computed with no restrictions. However, the boundary conditions have to be modified carefully if a horseshoe vortex or a semi-infinite line doublet is selected as a singularity. Panel method code PMARC, [15] models the internal flow geometry as a closed box and a horseshoe vortex or a semi-infinite line doublet will intersect panels defining the outflow conditions. Therefore, the flow field of a line doublet has to be computed by solving the flow field of a point doublet and this solution has to be made perfectly symmetric or anti-symmetric relative to the streamwise coordinate of the point doublet. Finally, a numerical integration is applied in the streamwise direction to obtain the flow field of a line doublet (for more detail see Appendix 4).

Modifications of a panel method code for semispan test are similar to the procedures described above. The user only has to make sure that normal velocities induced on the image plane surface by a singularity located on the image plane surface, i.e. point sources and sinks representing the semispan model fuselage volume, are zero.

Numerical Verification

A slender Rankine body ($l/2r_0 \approx 10$) is selected to verify the proposed panel method code modification if a source or sink is selected as a singularity (see Fig. 27a for a detailed description of the Rankine body geometry). A point source of strength $+1.0 [ft^2]$ is located at $X=116.0 [ft]$, $Y=2.0 [ft]$, $Z=-3.0 [ft]$ and a point sink of strength $-1.0 [ft^2]$ is located at $X=126.0 [ft]$, $Y=2.0 [ft]$, $Z=-3.0 [ft]$. The shape and surface pressure coefficient distribution of the corresponding Rankine body can be described in analytic form using polar coordinates, [23].

Assuming $x_1 - x_0 \leq x \leq x_1 + (x_2 - x_1)/2$, we obtain :

$$r_1 = r_0 \cdot \frac{\sin \varphi_1/2}{\sin \varphi_1} \quad (2.6a)$$

$$\cos \varphi_1 = \frac{x_1 - x}{r_1} \quad (2.6b)$$

$$c_p = 1 - 4 \sin^2 \frac{\varphi_1}{2} + 3 \sin^4 \frac{\varphi_1}{2} \quad (2.6c)$$

Assuming $x_1 + (x_2 - x_1)/2 \leq x \leq x_2 + x_0$, we obtain :

$$r_2 = r_0 \cdot \frac{\sin \varphi_2/2}{\sin \varphi_2} \quad (2.7a)$$

$$\cos \varphi_2 = \frac{x - x_2}{r_2} \quad (2.7b)$$

$$c_p = 1 - 4 \sin^2 \frac{\varphi_2}{2} + 3 \sin^4 \frac{\varphi_2}{2} \quad (2.7c)$$

where the stagnation point distance x_0 and the halfbody radius r_0 for a point source strength σ of +1.0 are given as:

$$x_0 = \sqrt{\frac{1}{4\pi}} \quad (2.8a)$$

$$r_0 = \sqrt{\frac{1}{\pi}} \quad (2.8b)$$

In a first step it is necessary to panel the selected Rankine body using the known description of its shape in polar coordinates (see Fig. 27b). The free-air solution of the surface pressure coefficient distribution of this geometry is calculated using panel method code PMARC, [15]. The result of this panel method code calculation is compared with the corresponding analytic solution given by Eqs. (2.6c),(2.7c). Figure 28 shows excellent agreement between the panel method and corresponding analytic solution of the surface pressure coefficient distribution of a Rankine body.

In the second step the Rankine body is placed inside a wind tunnel test section. The chosen wind tunnel geometry is similar to a test section configuration of the NASA Ames 12ft Pressure Wind Tunnel which will be used for semispan model tests. Figure 29 shows the corresponding wind tunnel wall, support system and Rankine body paneling. Velocities are computed along eight rows on the wind tunnel wall using the original version of panel method code PMARC, [15].

Then, panel method code PMARC, [15] was modified to solve the boundary value problem given by Eqs. (2.4),(2.5a),(2.5b). The velocity field due to a point source and point sink is used to represent the Rankine body (see also Appendix 3). The Rankine body is replaced by corresponding point source and sink of strength +1.0 [ft^2] at X=116.0 [ft], Y=2.0 [ft], Z=-3.0 [ft] and -1.0 [ft^2] located at X=126.0 [ft], Y=2.0 [ft], Z=-3.0 [ft] and velocities are again computed on eight rows using the modified version of the panel method code.

Figure 30 compares dimensionless velocities of both calculations on Row 4. Velocities show excellent agreement to verify the proposed panel method code modifications if point sources or point sinks are used to represent volume effects of a test article.

A rectangular wing ($s/c = 3.56$) with a NACA 0012 airfoil section at an angle of attack of 5° is selected to verify the proposed panel method code modification if a semi-infinite line doublet is selected as a singularity (see Fig. 31 for a detailed description of the wing geometry).

The rectangular wing is placed inside a wind tunnel test section. Figure 32 shows the corresponding wind tunnel wall, support system and wing paneling. Lift coefficient of the wing and velocities along eight rows on the wind tunnel wall are computed using the original version of panel method code PMARC, [15]. Panel method code PMARC was also used to compute the wall signature at angle of attack 0° . This wall signature is due to the thickness of the wing and was therefore subtracted from the wall signature calculated for 5° to obtain the wall signature due to lift only.

Then, panel method code PMARC, [15] was modified to solve the boundary value problem given by Eqs. (2.4),(2.5a),(2.5b). The velocity field of four line doublets is used to represent lifting effects of the wing at 5° angle of attack (see also Appendix 4). The location of these line doublets is depicted in Fig. 33. The computed lift coefficient of the wing placed inside the wind tunnel test section (see Fig. 32) has to be related to the strength of the semi-infinite line doublets. Using the definition of the lift coefficient and the Kutta/Joukowski formula we get for the lift force :

$$L = c_L \cdot \rho \cdot \frac{U^2}{2} \cdot s \cdot c = \rho \cdot U \cdot \Gamma \cdot s \quad (2.9)$$

So we get for the circulation Γ :

$$\Gamma = c_L \cdot \frac{U}{2} \cdot c \quad (2.10)$$

The line doublet strength σ of each of the four line doublets is then given as (see Appendix 4) :

$$\sigma = \Gamma \cdot \frac{s}{4} = c_L \cdot \frac{U}{2} \cdot c \cdot \frac{s}{4} \quad (2.11a)$$

or

$$\frac{\sigma}{U} = c_L \cdot \frac{c}{2} \cdot \frac{s}{4} \quad (2.11b)$$

Knowing that $c_L = 0.3556$, $c = 1.5$ [ft], and $s/4 = 1.3334$ [ft] for the selected wing we get for the singularity strength per unit velocity of each of the four line doublets $\sigma/U = 0.3556$ [ft²].

The wing can now be replaced by four line doublets of strength $0.3556 [ft^2]$ and velocities are again computed on eight rows using the modified version of the panel method code.

Figure 34 compares dimensionless velocities on the wind tunnel wall of both calculations at Row 8. Velocities due to lift effects show excellent agreement to verify the proposed panel method code modifications if semi-infinite line doublets are used to represent lift of a wing.

Summary

A three-dimensional panel method code was modified to calculate the flow field of a singularity placed inside a wind tunnel test section. The modification was verified by replacing a Rankine body by a point source and point sink and by replacing a rectangular wing at 5° angle of attack by four line doublets. Corresponding flow field solutions compare favorably in both cases. The panel method code modification will work with no restrictions if a point source or point sink is selected as a singularity. However, boundary conditions have to be modified carefully if a horseshoe vortex or semi-infinite line doublet is selected as this type of singularity intersects outflow panels of the internal flow geometry and therefore requires a numerical integration of the corresponding point doublet solution.

APPENDIX 3

POINT SOURCE VELOCITY VECTOR

The velocity vector of a three-dimensional point source is required if a panel method code is modified to compute the flow field of a source or sink placed inside a wind tunnel. The potential of a point source at location (x_S, y_S, z_S) is given as, [22] :

$$\phi_S(x, y, z) = \frac{-\sigma}{4 \cdot \pi \cdot [(x - x_S)^2 + (y - y_S)^2 + (z - z_S)^2]^{1/2}} \quad (3.1)$$

The velocity components of this point source are :

$$u(x, y, z) = \frac{\partial \phi_S}{\partial x} = \frac{\sigma}{4 \pi} \cdot \frac{x - x_S}{[(x - x_S)^2 + (y - y_S)^2 + (z - z_S)^2]^{3/2}} \quad (3.2a)$$

$$v(x, y, z) = \frac{\partial \phi_S}{\partial y} = \frac{\sigma}{4 \pi} \cdot \frac{y - y_S}{[(x - x_S)^2 + (y - y_S)^2 + (z - z_S)^2]^{3/2}} \quad (3.2b)$$

$$w(x, y, z) = \frac{\partial \phi_S}{\partial z} = \frac{\sigma}{4 \pi} \cdot \frac{z - z_S}{[(x - x_S)^2 + (y - y_S)^2 + (z - z_S)^2]^{3/2}} \quad (3.2c)$$

The singularity strength σ has the unit $[ft^3/sec]$ or $[m^3/sec]$. The perturbation velocity field given in Eqs. (3.2a),(3.2b),(3.2c) could be used to change a panel method code as outlined in Appendix 2 .

APPENDIX 4

LINE DOUBLET VELOCITY VECTOR

The velocity vector of a three-dimensional semi-infinite line doublet is required if a panel method code is modified to compute the flow field of a line doublet placed inside a wind tunnel.

In general, a semi-infinite line doublet can be considered as an elementary horseshoe vortex ([22], see also Fig. 35). The potential of a line doublet can be obtained by integrating the solution for a point doublet in the x-direction, [24]. A point doublet does not have a radial symmetry as in case of a point source and therefore the line doublet potential will be a function of the orientation of the point doublet. For lift force acting in the positive z-direction (see Fig. 35) it is necessary that point doublets point in the negative z-direction. The potential of a finite length line doublet with starting point at (x_1, y_1, z_1) and end point at (x_N, y_1, z_1) is then given as, [22] :

$$\phi(x, y, z) = \frac{\sigma}{4\pi} \cdot \int_{x_1}^{x_N} \frac{[z - z_1] d\xi}{\left[[x - \xi]^2 + [y - y_1]^2 + [z - z_1]^2 \right]^{3/2}} \quad (4.1)$$

or

$$\phi(x, y, z) = \frac{-\sigma}{4\pi} \cdot \frac{z - z_1}{[y - y_1]^2 + [z - z_1]^2} \cdot A \quad (4.2a)$$

$$A = \frac{x - x_N}{\left[[x - x_N]^2 + [y - y_1]^2 + [z - z_1]^2 \right]^{1/2}} - \frac{x - x_1}{\left[[x - x_1]^2 + [y - y_1]^2 + [z - z_1]^2 \right]^{1/2}} \quad (4.2b)$$

Taking the limit $x_N \rightarrow \infty$ we get the potential for the semi-infinite line doublet :

$$\phi_L(x, y, z) = \lim_{x_N \rightarrow \infty} \phi(x, y, z) = \frac{\sigma}{4\pi} \cdot \frac{z - z_1}{[y - y_1]^2 + [z - z_1]^2} \cdot B \quad (4.3a)$$

$$B = 1 + \frac{x - x_1}{\left[[x - x_1]^2 + [y - y_1]^2 + [z - z_1]^2 \right]^{1/2}} \quad (4.3b)$$

This equation agrees with equation (5-35) in Ref. [24], if the starting point of the line doublet is located at $(x_1 = 0, y_1 = 0, z_1 = 0)$. The velocity components can now be obtained by taking derivatives of the velocity potential ϕ_L .

In the x-direction we get :

$$u(x, y, z) = \frac{\partial \phi_L}{\partial x} = \frac{\sigma}{4 \pi} \cdot \frac{z - z_1}{[(x - x_1)^2 + (y - y_1)^2 + (z - z_1)^2]^{3/2}} \quad (4.4)$$

In the y-direction we get :

$$v(x, y, z) = \frac{\partial \phi_L}{\partial y} = \frac{-\sigma}{4 \pi} \cdot \frac{(y - y_1) \cdot (z - z_1)}{[(y - y_1)^2 + (z - z_1)^2]} \cdot C \quad (4.5a)$$

$$C = \frac{2 \cdot B}{[(y - y_1)^2 + (z - z_1)^2]} + \frac{x - x_1}{[(x - x_1)^2 + (y - y_1)^2 + (z - z_1)^2]^{3/2}} \quad (4.5b)$$

In the z-direction we get :

$$w(x, y, z) = \frac{\partial \phi_L}{\partial z} = \frac{\sigma}{4 \pi} \cdot \frac{1}{[(y - y_1)^2 + (z - z_1)^2]} \cdot D \quad (4.6a)$$

$$D = \frac{[(y - y_1)^2 - (z - z_1)^2]}{[(y - y_1)^2 + (z - z_1)^2]} \cdot B - \frac{[(x - x_1) \cdot (z - z_1)^2]}{[(x - x_1)^2 + (y - y_1)^2 + (z - z_1)^2]^{3/2}} \quad (4.6b)$$

The calculation of the flow field of a semi-infinite line doublet located inside a wind tunnel of constant cross-sectional area is difficult if a modified version of panel method code PMARC is used (see Appendix 2) . The line doublet intersects the exit plane of the paneled wind tunnel geometry and can cause convergence and accuracy problems.

Fortunately, it is possible to calculate the flow field of a line doublet in a wind tunnel of constant cross-sectional area by integrating the flow field of the panel method code solution of a point doublet in the streamwise direction. The line doublet flow field solution is obtained by shifting and superimposing corresponding point doublet solutions (see Fig. 36a) .

In general, the potential of a semi-infinite line doublet (Eq. (4.1) ; $x_N \gg x_1$) can be approximated using numerical integration. We get then :

$$\phi_L(x, y, z) \approx \sum_{k=1}^N \phi_{PD}(x, y, z; x_k) \cdot \Delta x \quad (4.7a)$$

$$\phi_{PD}(x, y, z; x_k) = \frac{\sigma}{4 \pi} \cdot \frac{z - z_1}{[(x - x_k)^2 + (y - y_1)^2 + (z - z_1)^2]^{3/2}} \quad (4.7b)$$

$$x_k = x_1 + (k - 1) \cdot \Delta x \quad ; \quad x_N \gg x_1$$

where Δx is the step size of the integration. The perturbation velocities of the line doublet can now be approximated as :

$$u(x, y, z) \approx \Delta x \cdot \sum_{k=1}^N \frac{\partial}{\partial x} \phi_{PD}(x, y, z; x_k) \quad (4.8a)$$

$$v(x, y, z) \approx \Delta x \cdot \sum_{k=1}^N \frac{\partial}{\partial y} \phi_{PD}(x, y, z; x_k) \quad (4.8b)$$

$$w(x, y, z) \approx \Delta x \cdot \sum_{k=1}^N \frac{\partial}{\partial z} \phi_{PD}(x, y, z; x_k) \quad (4.8c)$$

where

$$\frac{\partial}{\partial x} \phi_{PD}(x, y, z; x_k) = \frac{\sigma}{4 \pi} \cdot \frac{(-3) \cdot [x - x_k] \cdot [z - z_1]}{[[x - x_k]^2 + [y - y_1]^2 + [z - z_1]^2]^{5/2}} \quad (4.9a)$$

$$\frac{\partial}{\partial y} \phi_{PD}(x, y, z; x_k) = \frac{\sigma}{4 \pi} \cdot \frac{(-3) \cdot [y - y_1] \cdot [z - z_1]}{[[x - x_k]^2 + [y - y_1]^2 + [z - z_1]^2]^{5/2}} \quad (4.9b)$$

$$\frac{\partial}{\partial z} \phi_{PD}(x, y, z; x_k) = \frac{\sigma}{4 \pi} \cdot \frac{[x - x_k]^2 + [y - y_1]^2 - 2 \cdot [z - z_1]^2}{[[x - x_k]^2 + [y - y_1]^2 + [z - z_1]^2]^{5/2}} \quad (4.9c)$$

For a wind tunnel of constant cross-sectional area a streamwise shift of the flow field solution of a point doublet located at (x_1, y_1, z_1) is possible (see Fig. 36b) . Therefore Eqs. (4.8a), (4.8b), (4.8c) only require the calculation of $\phi_{PD}(x, y, z; x_1)$ as the following relationships apply :

$$\frac{\partial}{\partial x} \phi_{PD}(x, y, z; x_k) = \frac{\partial}{\partial x} \phi_{PD}(x - [k - 1]\Delta x, y, z; x_1) \quad (4.10a)$$

$$\frac{\partial}{\partial y} \phi_{PD}(x, y, z; x_k) = \frac{\partial}{\partial y} \phi_{PD}(x - [k - 1]\Delta x, y, z; x_1) \quad (4.10b)$$

$$\frac{\partial}{\partial z} \phi_{PD}(x, y, z; x_k) = \frac{\partial}{\partial z} \phi_{PD}(x - [k - 1]\Delta x, y, z; x_1) \quad (4.10c)$$

The numerical integration defined by Eqs. (4.8a), (4.8b), (4.8c) has to be done carefully. Integration error due to the fact that the numerical solution of a point doublet flow field is not perfectly antisymmetric (see Eq. (4.9a)) or symmetric (see Eqs. (4.9b),(4.9c))

relative to its x-coordinate x_k has to be avoided. This can be done by considering, e.g., the numerical solution upstream ($x < x_k$) of the point doublet as exact and imposing the following conditions on the downstream part ($x > x_k$) of the perturbation velocities :

$$u(x, y, z) = -u(x_k - [x - x_k], y, z) ; \quad x > x_k \quad (4.11a)$$

$$v(x, y, z) = v(x_k - [x - x_k], y, z) ; \quad x > x_k \quad (4.11b)$$

$$w(x, y, z) = w(x_k - [x - x_k], y, z) ; \quad x > x_k \quad (4.11c)$$

Unfortunately, the point doublet and therefore also the semi-infinite line doublet does not have a radial symmetry. However, the velocity vector of a point or line doublet not pointing in the negative z-axis direction can easily be found by applying a coordinate system rotation. A rotation angle τ related to the directional property of the line doublet is introduced as depicted in Fig. 37 .

The relationship of coordinates and velocities between the line doublet fixed coordinate system (x, y, z) and reference coordinate system (x', y', z') is depicted in Fig. 37 . The rotation angle direction is defined such that the lift force caused by the semi-infinite line doublet points in the positive y' -axis if the line doublet is rotated by $+90^\circ$. In this case we get for the transformation of coordinates from the reference coordinate system, i.e. (x', y', z') , to coordinates in the line doublet fixed coordinate system (x, y, z) :

$$x = x' \quad (4.12a)$$

$$y = y' \cdot \cos \tau - z' \cdot \sin \tau \quad (4.12b)$$

$$z = y' \cdot \sin \tau + z' \cdot \cos \tau \quad (4.12c)$$

The velocities components (u, v, w) are computed in the line doublet fixed coordinate system. Finally it is necessary to back-transform these velocity components to the reference coordinate system. We get then :

$$u' = u \quad (4.13a)$$

$$v' = v \cdot \cos \tau + w \cdot \sin \tau \quad (4.13b)$$

$$w' = -v \cdot \sin \tau + w \cdot \cos \tau \quad (4.13c)$$

The singularity strength σ has the unit [ft^3/sec] or [m^3/sec]. The perturbation velocity field given in Eqs. (4.8a),(4.8b),(4.8c) could be used to change a panel method code as outlined in Appendix 2 .

APPENDIX 5

CALCULATION OF THE LINE DOUBLET STRENGTH

In general, it is possible to compute the strength of line doublets representing lifting effects of an aircraft by using lift and pitching moment measurements recorded during a wind tunnel test (see *Ulbrich and Steinle*, [7]).

Assuming that the lifting surfaces of the wing and tail of an aircraft model are discretized by using equally spaced line doublets along the 1/4-chord line of the wing and tail we get for the total lift and pitching moment (see also Fig. 38) :

$$L = \sum_{i=1}^{n_w} L_w(i) + \sum_{j=1}^{n_t} L_t(j) \quad (5.1)$$

$$P = \sum_{i=1}^{n_w} \left[L_w(i) \cdot [x_{mr} - x_w(i)] \right] + \sum_{j=1}^{n_t} \left[L_t(j) \cdot [x_{mr} - x_t(j)] \right] \quad (5.2)$$

where $L_w(i)$ and $L_t(j)$ are the lift contributions of the line doublets of the wing and tail.

Similar to Eqs. (2.9) and (2.11), the Kutta/Joukowski formula may be used to connect a lift force to a line doublet strength. The application of the Kutta/Joukowski formula in a wind tunnel requires the calculation of the product $\rho_\infty \cdot U_\infty$ where ρ_∞ is the free-stream density and U_∞ is the free-stream velocity at the location of the aircraft model. A first order approximation of the product $\rho_\infty \cdot U_\infty$ may be obtained by applying wall interference corrections to the measured reference density ρ_{ref} and reference velocity U_{ref} at a model reference station (see Eqs. (5.78) and (5.82) in Ref. [10]) . We then get :

$$\rho_\infty \cdot U_\infty \approx \rho_{ref} \cdot U_{ref} \cdot \left[1 + \epsilon \cdot (1 - M_{ref}^2) \right] \quad (5.3a)$$

The Kutta/Joukowski formula may now be written as :

$$L_w(i) = \rho_\infty \cdot U_\infty \cdot \sigma_w^*(i) \approx \rho_{ref} \cdot U_{ref} \cdot \left[1 + \epsilon \cdot (1 - M_{ref}^2) \right] \cdot \sigma_w^*(i) \quad (5.3b)$$

$$L_t(j) = \rho_\infty \cdot U_\infty \cdot \sigma_t^*(j) \approx \rho_{ref} \cdot U_{ref} \cdot \left[1 + \epsilon \cdot (1 - M_{ref}^2) \right] \cdot \sigma_t^*(j) \quad (5.3c)$$

Introducing singularity weights $w_w(i)$, $w_t(j)$, and discrete line doublet span Δs_w , Δs_t on the wing and tail we get for the singularity strength :

$$\sigma_w^*(i) = \Gamma_w \cdot \Delta s_w \cdot w_w(i) \quad (5.4a)$$

$$\sigma_t^*(j) = \Gamma_t \cdot \Delta s_t \cdot w_t(j) \quad (5.4b)$$

The circulation Γ_w and Γ_t are the only unknowns in Eqs. (5.1) and (5.2) if line doublets weights are specified by the user. The weights may represent, e.g., elliptic lift distribution along the wing and tail of an aircraft model. Experimental or CFD solutions of the true lift distribution may also be used to determine weights (see also NACA Report No. 921, [25]). Combining Eqs. (5.1) to (5.4b) we get :

$$\frac{L}{\rho_{ref} \cdot U_{ref} \cdot \left[1 + \epsilon \cdot (1 - M_{ref}^2) \right]} = \Gamma_w \cdot \alpha_1 + \Gamma_t \cdot \alpha_2 \quad (5.5a)$$

$$\frac{P}{\rho_{ref} \cdot U_{ref} \cdot \left[1 + \epsilon \cdot (1 - M_{ref}^2) \right]} = \Gamma_w \cdot \beta_1 + \Gamma_t \cdot \beta_2 \quad (5.5b)$$

where

$$\alpha_1 = \Delta s_w \cdot \sum_{i=1}^{n_w} w_w(i) \quad (5.6a)$$

$$\alpha_2 = \Delta s_t \cdot \sum_{j=1}^{n_t} w_t(j) \quad (5.6b)$$

$$\beta_1 = \Delta s_w \cdot \sum_{i=1}^{n_w} \left[w_w(i) \cdot [x_{mr} - x_w(i)] \right] \quad (5.7a)$$

$$\beta_2 = \Delta s_t \cdot \sum_{j=1}^{n_t} \left[w_t(j) \cdot [x_{mr} - x_t(j)] \right] \quad (5.7b)$$

Equations (5.5a) and (5.5b) are a 2×2 linear system of equations which can be solved easily for Γ_w and Γ_t :

$$\Gamma_w = \frac{1}{\rho_{ref} \cdot U_{ref} \cdot \left[1 + \epsilon \cdot (1 - M_{ref}^2) \right]} \cdot \frac{L \cdot \beta_2 - P \cdot \alpha_2}{\alpha_1 \cdot \beta_2 - \alpha_2 \cdot \beta_1} \quad (5.8a)$$

$$\Gamma_t = \frac{1}{\rho_{ref} \cdot U_{ref} \cdot \left[1 + \epsilon \cdot (1 - M_{ref}^2) \right]} \cdot \frac{(-L) \cdot \beta_1 + P \cdot \alpha_1}{\alpha_1 \cdot \beta_2 - \alpha_2 \cdot \beta_1} \quad (5.8b)$$

Finally, the singularity strength is obtained by applying Eqs. (5.4a) and (5.4b) .

The line doublet strength has to be compatible with non-dimensionalized perturbation velocities used in the panel method code computation of the wind tunnel and wall interference flow field (see Eq. (25) and Appendix 2). Correct units for velocity, density,

force, and pitching moment have to be selected if Eqs. (5.4a), (5.4b) are used. Table 4 lists units :

Table 4: Units for Singularity Strength Calculation

Quantity	SI unit	non-SI unit
Velocity	m / sec	ft / sec
Density	kg / m^3	$Slug / ft^3$
Force	$N \equiv kg \cdot m / sec^2$	$lbf \equiv Slug \cdot ft / sec^2$
Moment	$N \cdot m$	$ft \cdot lbf$

The singularity strength as defined in Eqs. (5.3b),(5.3c) has the unit $[m^3/sec]$ or $[ft^3/sec]$. Similar to Eq. (25), it is necessary to divide the strength by the reference velocity U_{ref} . Therefore we get for the normalized strength in units $[m^2]$ or $[ft^2]$:

$$\sigma_w(i) = \frac{\sigma_w^*(i)}{U_{ref}} \quad (5.9a)$$

$$\sigma_t(j) = \frac{\sigma_t^*(j)}{U_{ref}} \quad (5.9b)$$

Semispan model tests are often conducted using only the wing and fuselage of an aircraft model. In this case the circulation Γ_t is zero and only the lift force measurement will be used to calculate the strength of line doublets representing lifting effects of the wing. Using Eqs. (5.5a) we get for Γ_w :

$$\Gamma_w = \frac{L}{\rho_{ref} \cdot U_{ref} \cdot \left[1 + \epsilon \cdot (1 - M_{ref}^2) \right] \cdot \alpha_1} \quad (5.10)$$

In general, the application of Eqs. (5.8a), (5.8b), (5.10) to the Wall Signature Method requires at least a one step iteration as blockage factor ϵ can only be estimated after a successful least squares fit of the wall signature. Zero may be selected as an initial approximation of blockage factor ϵ in Eqs. (5.8a), (5.8b), and (5.10).

APPENDIX 6

TRI-LINEAR INTERPOLATION

In general, tri-linear interpolation can be used to find the value of a scalar function $f(x_p, y_p, z_p)$ using known values $f(x_i, y_j, z_k), f(x_{i+1}, y_j, z_k), \dots$, at corresponding eight grid cell corner points (see Fig. 39).

Tri-linear interpolation requires several steps. At first we have to find grid cell indices (i, j, k) such that $x_i \leq x_p \leq x_{i+1}; y_j \leq y_p \leq y_{j+1}; z_k \leq z_p \leq z_{k+1}$. For a constant grid cell size $\Delta x, \Delta y, \Delta z$, indices (i, j, k) can be computed as :

$$i = INT\left[\frac{x_p - x_1}{\Delta x}\right] + 1 \quad (6.1a)$$

$$j = INT\left[\frac{y_p - y_1}{\Delta y}\right] + 1 \quad (6.1b)$$

$$k = INT\left[\frac{z_p - z_1}{\Delta z}\right] + 1 \quad (6.1c)$$

where x_1, y_1, z_1 are the starting coordinates of the entire grid.

In the next step, weighting factors of each grid cell corner point have to be found. The line connecting a corner point with its opposite corner point is assumed to be a spacial diagonal of the grid cell. Then, the weighting factor of a grid cell corner point is computed by dividing the volume of the rectangular prism defined by point (x_p, y_p, z_p) and the opposite corner point by the total volume of the grid cell. For example, the weighting factor of grid cell corner point (x_{i+1}, y_j, z_k) is :

$$w_{i+1,j,k} = \frac{V_{i,j+1,k+1}}{V_{cell}} \quad (6.2a)$$

where

$$V_{i,j+1,k+1} = ABS\left[[x_p - x_i] \cdot [y_p - y_{j+1}] \cdot [z_p - z_{k+1}] \right] \quad (6.2b)$$

$$V_{cell} = ABS\left[[x_{i+1} - x_i] \cdot [y_{j+1} - y_j] \cdot [z_{k+1} - z_k] \right] = \Delta x \cdot \Delta y \cdot \Delta z \quad (6.2c)$$

Finally, the functional value $f(x_p, y_p, z_p)$ can be interpolated as :

$$f(x_p, y_p, z_p) = \sum_{\alpha=i}^{i+1} \sum_{\beta=j}^{j+1} \sum_{\gamma=k}^{k+1} f(x_\alpha, y_\beta, z_\gamma) \cdot w_{\alpha,\beta,\gamma} \quad (6.3)$$

Table 5 lists grid cell corner points and corresponding opposite corner points.

Table 5: Grid Cell Indices

<i>No.</i>	<i>Corner Point</i>	<i>Opposite Corner Point</i>
1	i, j, k	$i + 1, j + 1, k + 1$
2	$i, j + 1, k$	$i + 1, j, k + 1$
3	$i + 1, j, k$	$i, j + 1, k + 1$
4	$i + 1, j + 1, k$	$i, j, k + 1$
5	$i, j, k + 1$	$i + 1, j + 1, k$
6	$i, j + 1, k + 1$	$i + 1, j, k$
7	$i + 1, j, k + 1$	$i, j + 1, k$
8	$i + 1, j + 1, k + 1$	i, j, k

Tri-linear interpolation is applied to calculate normalized perturbation velocities of a singularity located at a point (x_p, y_p, z_p) assuming that perturbation velocities are known for singularities located on eight corner points of a singularity grid cell.

APPENDIX 7

PARABOLIC INTERPOLATION

A parabola is used to interpolate normalized perturbation velocities $y(M)$ as a function of the real-time Mach number M . The parabola has the following form :

$$y(M) = a \cdot M^2 + b \cdot M + c \quad (7.1)$$

Three coefficients a, b, c of the parabola have to be calculated. Therefore it is necessary to compute the perturbation velocity database for three discrete Mach numbers.

Three discrete Mach numbers $M_1 = 0.0, M_2 = 0.3, M_3 = 0.6$ are selected and corresponding normalized perturbation velocities $y(M_1), y(M_2), y(M_3)$ are known. Then we get for the coefficients of the parabola :

$$a = \frac{1}{M_3 - M_2} \cdot \left[\frac{y(M_3) - y(M_1)}{M_3 - M_1} - \frac{y(M_2) - y(M_1)}{M_2 - M_1} \right] \quad (7.2a)$$

$$b = \frac{y(M_2) - y(M_1)}{M_2 - M_1} - a \cdot (M_1 + M_2) \quad (7.2b)$$

$$c = y(M_1) - a \cdot M_1^2 - b \cdot M_1 \quad (7.2c)$$

Coefficients a, b, c have to be computed for $n_1 \cdot (n_2 + n_3)$ parabolas in real-time if, e.g., a test article and support system are represented by n_1 singularities, wall signatures are measured at a total number of n_2 wall pressure ports, and a reference point grid of n_3 points is selected.

APPENDIX 8

OPTIMIZATION OF THE SINGULARITY LOCATION

The wall signature method calculates wall interference corrections based on a singularity representation of the test article and the support system. The wind tunnel test engineer has to specify the initial location of these singularities using simple rules. For example, sources and sinks representing the fuselage volume should be located along the fuselage axis such that they represent a Rankine body approximation of fuselage volume effects, line doublets should be distributed along the 1/4-chord line of lifting surfaces, and sources related to separation wake effects should be located at points where separation is likely to occur during a test.

The initial singularity representation is not unique as the test engineer has to specify the singularity location. However, it is possible to make the singularity location unique by minimizing the standard deviation of the least squares fit as a function of the singularity location.

An efficient optimization can only be achieved if the total number of independent variables of the minimization, i.e. the coordinates of each singularity, is reduced to a reasonable limit. It is also necessary to restrict the direction of change of the singularity coordinates.

During the support system calibration three groups of singularities exist, i.e., sources of the support system volume, sinks of the support system volume, and sources of the support system wake. Therefore it is possible to reduce the number of independent variables down to three, if the relative distances of the singularities of each group is kept constant during the optimization. The direction of change of the optimization is defined by the line connecting the first source and the first sink of singularities representing the support system volume.

Similarly, during the wind tunnel test of a test article five groups of singularities exist, i.e., sources of the fuselage volume, sinks of the fuselage volume, and sources of the wing separation wake, line doublets of the wing, and line doublets of the tail. Therefore the number of independent variables can be reduced to five, if the relative distances of

the singularities of each group is kept constant during the optimization. In this case the direction of change of the optimization is defined by the line connecting the first source and the first sink of singularities representing the fuselage volume. Assuming that the 1/4-chord line of the wing and tail are ideal locations for line doublets of the wing and tail it is even possible to reduce the number of independent variables to three.

An optimization algorithm based on the Method of Steepest Decent has been included in the real-time software package of WICS (see also Ref. [26]) .

APPENDIX 9

SELECTION OF THE SINGULARITY / REFERENCE POINT LOCATION

The Wall Signature Method uses a singularity representation of the wind tunnel model to predict wall interference corrections. The singularity representation of the model is uniquely defined if TYPE, LOCATION, and STRENGTH of each singularity are known.

The STRENGTH of each singularity is derived from real-time measurements of wall signature, lift force, and pitching moment. If a propulsion simulator is used during a test it is also necessary to measure the propulsion simulator thrust and the propeller disk area.

The TYPE of each singularity is chosen by the wind tunnel test engineer. A singularity TYPE should be selected such that it represents a blockage or lifting effect of the wind tunnel model. Sources and sinks are used to represent volume and wake blockage effects of the wind tunnel model. Line doublets are used to represent lifting effects of the wind tunnel model. A sink is used to model blockage effects of a propulsion simulator in wind tunnel testing.

The LOCATION of each singularity has to be specified by wind tunnel test engineer. LOCATIONS should be selected based on geometry of wind tunnel model. All singularity coordinates have to be provided in tunnel coordinates.

The following empirical rules will help the test engineer to make reasonable selections of the singularity TYPE and LOCATION :

(1) FULLSPAN WIND TUNNEL MODEL :

(1.1) Fuselage Volume : A source of weighting factor "+1.0" has to be placed on the fuselage axis approximately one mean fuselage radius downstream of the nose of the fuselage. A source of weighting factor "-1.0" , i.e. a sink, has to be placed on the fuselage axis approximately one mean fuselage radius upstream of the tail end of the fuselage.

(1.2) Wake Separation : Sources with positive weighting factors have to be placed on the wind tunnel model at locations where flow separation occurs. If a wind tunnel model is tested, e.g., in landing configuration sources of equal strength should be placed at the location of the wing flaps.

(1.3) Wing : The wing span is divided into equal size wing span increments. One line doublet is assigned to each wing span increment. Line doublet starting points are placed where the 1/4 chord line of the wing and the middle of each wing span increment intersect.

(1.4) Tail : The tail span is divided into equal size tail span increments. One line doublet is assigned to each tail span increment. Line doublet starting points are placed where the 1/4 chord line of the tail and the middle of each tail span increment intersect.

(1.5) Propulsion Simulator : A source of weighting factor “-1.0” , i.e. a sink, is placed at the center of the propeller if a turboprop engine is simulated; a sink is placed halfway between the compressor and turbine if a turbojet or turbofan engine is simulated.

(2) SEMISPAN WIND TUNNEL MODEL :

(2.1) Fuselage Volume : A source of weighting factor “+1.0” has to be placed on the fuselage axis approximately one mean fuselage radius downstream of the nose of the fuselage. A source of weighting factor “-1.0” , i.e. a sink, has to be placed on the fuselage axis approximately one mean fuselage radius upstream of the tail end of the fuselage. The z-coordinate of the source and sink of the semispan model fuselage does not have to be specified. The Wall Interference Correction System (WICS) of the NASA Ames 12ft Pressure Wind Tunnel (PWT) implicitly assumes that their z-coordinate is identical with the z-coordinate of the image plane surface.

(2.2) Wake Separation : Sources with positive weighting factors have to be placed on the wind tunnel model at locations where flow separation occurs. If a wind tunnel model is tested, e.g., in landing configuration sources of equal strength should be placed at the location of the wing flaps.

(2.3) Wing : The wing semispan is divided into equal size wing span increments. One line doublet is assigned to each wing span increment. Line doublet starting points are placed where the 1/4 chord line of the semispan wing and the middle of each wing span increment intersect.

(2.4) Propulsion Simulator : A source of weighting factor “-1.0” , i.e. a sink, is placed at the center of the propeller if a turboprop engine is simulated; a sink is placed halfway between the compressor and turbine if a turbojet or turbofan engine is simulated.

(3) REFERENCE POINTS :

WICS computes mean wall interference corrections for sets of reference points. The test engineer has to specify these sets of reference points in the tunnel coordinate system. WICS allows the test engineer to specify up to 10 independent sets of reference points. Sets of reference points can be specified along the fuselage axis and along the 3/4 chord line of the wing or tail.

A simple Expert System should be designed in the future that assists the test engineer in the selection of the singularity location and weighting factors.

APPENDIX 10

BLOCKAGE EFFECT OF A POWERED WIND TUNNEL MODEL

The correct simulation of flow interference effects between the aircraft fuselage, the wing, and the engine cowling during a wind tunnel test requires the installation of a propulsion simulator in a wind tunnel model. The blockage correction caused by a propulsion simulator has to be estimated if a significant amount of thrust is produced.

In general, a propulsion simulator is operated as a small propeller. A point doublet pointing in the streamwise direction may be used to estimate propulsion simulator blockage effects during a wind tunnel test, [22]. A more accurate modeling of blockage effects may be obtained if a semi-infinite line doublet pointing in the streamwise direction is used, [27]. The velocity potential of a semi-infinite line doublet with a starting point at (x_1, y_1, z_1) is given as, [22]:

$$\phi_{LD}(x, y, z) = \frac{-\sigma}{4\pi} \cdot \lim_{x_2 \rightarrow \infty} \int_{x_1}^{x_2} \frac{[x - \xi] d\xi}{\left[[x - \xi]^2 + [y - y_1]^2 + [z - z_1]^2 \right]^{3/2}} \quad (10.1)$$

It can be shown that the velocity potential defined in Eq. (10.1) is identical with the velocity potential of a sink located at (x_1, y_1, z_1) (see Eq. 3.1):

$$\phi_{LD}(x, y, z) = -\phi_S(x, y, z) = \frac{\sigma}{4\pi} \cdot \frac{1}{\left[[x - x_1]^2 + [y - y_1]^2 + [z - z_1]^2 \right]^{1/2}} \quad (10.2)$$

Location and strength of this sink have to be specified. It is reasonable to place the sink at the center of the propeller or compressor disk of the propulsion simulator. The sink strength σ may be related to the propulsion simulator thrust T_P , propeller disk area S , free-stream velocity U_∞ , and free-stream density ρ_∞ by applying an approximate solution of the flow around the ideal propeller given by *Koning*, [6]. In wind tunnel testing, free-stream velocity and density have to be estimated by applying blockage corrections to the measured reference velocity U_{ref} and reference density ρ_{ref} , i.e. $U_\infty \approx U_{ref} (1 + \epsilon)$ and $\rho_\infty \approx \rho_{ref} (1 - \epsilon M_{ref}^2)$ (see Eqs. (5.78) and (5.82) in Ref.[10]). Then, we get for the propulsion simulator sink strength:

$$\sigma_p^* = S \cdot \left[\sqrt{U_{ref}^2 \cdot (1 + \epsilon)^2 + \frac{2 \cdot T_P}{\rho_{ref} \cdot (1 - \epsilon M_{ref}^2) \cdot S}} - U_{ref} \cdot (1 + \epsilon) \right] \quad (10.3)$$

Equations (10.3), i.e. *Koning's* formula, may also be obtained by considering blockage effects of a lifting rotor in subsonic wind tunnel testing, [27] .

Effects of a propulsion simulator on wind tunnel blockage effects can easily be included in the least squares fit of the wall signature required for the application of the Wall Signature Method. The strength of the propulsion simulator sink is known from the thrust measurement. It is only necessary to subtract the corresponding wall signature contribution from the total wall signature (see also Eqs. (13g) in Chapter 2) .

The sink strength σ_p^* as defined in Eq. (10.3) has the unit $[m^3/sec]$ or $[ft^3/sec]$. It has to be divided by U_{ref} if normalized perturbation velocities as defined in Chapter 2 are used for the least squares fit of the wall signature. Finally we get :

$$\sigma_p = S \cdot \left[\sqrt{(1 + \epsilon)^2 + \frac{2 \cdot T_P}{\rho_{ref} \cdot U_{ref}^2 \cdot S \cdot (1 - \epsilon M_{ref}^2)}} - (1 + \epsilon) \right] \quad (10.4)$$

The application of Eq. (10.4) to the Wall Signature Method requires at least a one step iteration as blockage factor ϵ can only be estimated after a successful least squares fit of the wall signature (see also Appendix 5).

APPENDIX 11

QUALITY CHECK OF THE LEAST SQUARES FIT

The Wall Signature Method uses a linear least squares fit of the difference between wall signature and corresponding wall pressure port calibration to predict blockage effects of a test article. In practical applications the facility hardware cannot guarantee that good pressure measurements are recorded on all wall pressure ports at all times. However, not all pressure measurements are required to compute a blockage correction of the test article. Therefore an efficient implementation of a wall interference correction system based on the Wall Signature Method has to check measurements on each wall pressure port.

Studies using experimental data have shown that a four-step quality check of the least squares fit is sufficient to identify unacceptable wall signature measurements without rejecting too many data points. Wall signatures obtained during the empty tunnel or support system calibration have to be inspected separately. They are used to remove orifice error, wall divergence, and wall boundary layer displacement effects.

The proposed quality check of the difference between the real-time and calibrated wall signature is done as follows (see also Fig. 40) :

CHECK 1 : WALL SIGNATURE DIFFERENCE MAGNITUDE

The absolute value of the wall signature difference is computed for each wall pressure port. A port is rejected, i.e. its port flag is set to zero, if the wall signature difference is larger than a specified upper bound. This bound is a function of the wind tunnel facility configuration and data acquisition hardware. An upper bound of 0.1 has been selected for the NASA Ames 12ft Pressure Wind Tunnel.

CHECK 2 : OUTLIER IDENTIFICATION

The absolute value of the difference between the wall signature difference and its least squares fit is computed for each wall pressure port. A port is rejected, i.e. its port flag is set to zero, if this difference is larger than three times the standard deviation of the least squares fit.

CHECK 3 : STANDARD DEVIATION OF EACH ROW

The standard deviation of each wall pressure port row is computed. A wall pressure

port row is rejected, i.e. its wall pressure port flags are set to zero, if the standard deviation is larger than a specified upper bound. This bound is a function of the wind tunnel facility configuration and data acquisition hardware. An upper bound of 0.01 (perturbation velocity) has been selected for the NASA Ames 12ft Pressure Wind Tunnel.

CHECK 4 : WALL PRESSURE PORT NUMBER

The total number of wall pressure ports used for the least squares fit of the wall signature difference is computed after CHECKS 1 TO 3 are applied. No wall interference corrections are computed if the total number of wall pressure ports is smaller than a specified lower limit. The lower limit of wall pressure ports is a function of the wind tunnel facility. A number of 60 wall pressure ports has been selected as the lower limit of the NASA Ames 12ft Pressure Wind Tunnel.

APPENDIX 12

LINEAR INTERPOLATION OF WALL PRESSURE PORT CALIBRATION

The Wall Signature Method uses a linear least squares fit of the difference between real-time wall signature and corresponding wall pressure port calibration to determine blockage effects of a test article. A value of the wall pressure port calibration has to be found that matches real-time test conditions.

The wall pressure port calibration is usually a function of several independent calibration variables. It can be a function of the total pressure p_T and Mach number M at some wind tunnel reference station. The wall pressure port calibration can also be a function of the support system kinematics. In this case calibration variables describing the position of the support system during the calibration have to be introduced.

An interpolation algorithm has been developed for the WICS software package that uses linear interpolation to determine the wall pressure port calibration as a function of real-time test conditions. This algorithm fulfills reliability, performance, and accuracy requirements of WICS.

The interpolation algorithm is applicable to up to four independent calibration variables. As an example, a detailed description of this interpolation algorithm for two independent calibration variables will be presented below. A detailed description of the algorithm for three and four independent variables is beyond the scope of the WICS Theory Guide.

In general, a value of the wall pressure port calibration $C(X^*, Y^*)$ has to be found for real-time test conditions defined by, e.g., two independent variables X^*, Y^* . It is assumed that wall pressure ports are calibrated for discrete combinations of these variables. A total of “ n ” discrete values of the first calibration variable X_i were selected. The second calibration variable $Y_{i,j}$ was changed by keeping the first calibration variable X_i constant. A total of “ $m(i)$ ” discrete values of the second calibration variable $Y_{i,j}$ were selected. Therefore we get the following set of discrete wall pressure port calibrations : $C(X_i, Y_{i,j})$ for $1 \leq i \leq n$ and $1 \leq j \leq m(i)$.

The interpolation of the calibration is done in two steps. At first, calibrations are interpolated for the second calibration variable Y^* . The first calibration variable X_i

is kept constant. Comparing Y^* and $Y_{i,j}$ only one of three possible cases applies (see Fig. 41a) :

Case 1 : $Y^* < Y_{i,1}$

$$\bar{C}(X_i) = C(X_i, Y_{i,1}) \quad (12.1)$$

Case 2 : $Y_{i,j} \leq Y^* \leq Y_{i,j+1}$

$$\bar{C}(X_i) = C(X_i, Y_{i,j}) + \frac{C(X_i, Y_{i,j+1}) - C(X_i, Y_{i,j})}{Y_{i,j+1} - Y_{i,j}} \cdot [Y^* - Y_{i,j}] \quad (12.2)$$

Case 3 : $Y^* > Y_{i,m(i)}$

$$\bar{C}(X_i) = C(X_i, Y_{i,m(i)}) \quad (12.3)$$

Finally, calibrations are interpolated for the calibration variable X^* by using the first calibration variable X_i and interpolated calibrations $\bar{C}(X_i)$. Again, comparing X^* and X_i , only one of three cases applies (see Fig. 41b) :

Case 1 : $X^* < X_1$

$$C(X^*, Y^*) = \bar{C}(X_1) \quad (12.4)$$

Case 2 : $X_i \leq X^* \leq X_{i+1}$

$$C(X^*, Y^*) = \bar{C}(X_i) + \frac{\bar{C}(X_{i+1}) - \bar{C}(X_i)}{X_{i+1} - X_i} \cdot [X^* - X_i] \quad (12.5)$$

Case 3 : $X^* > X_n$

$$C(X^*, Y^*) = \bar{C}(X_n) \quad (12.6)$$

Basic ideas and elements of the interpolation algorithm can easily be extended to three and four independent calibration variables.

Support system wall interference corrections at a reference point grid are required if the Wall Interference Correction System of the 12ft PWT is applied to a fullspan model test configuration (see Fig. 13a) . These corrections are known as a function of calibration variables. A similar linear interpolation algorithm may be used to interpolate the corrections for real-time test conditions.

APPENDIX 13

SINGULAR VALUE DECOMPOSITION

The numerical method of choice for solving linear least-squares problems, i.e. Eq. (13a) or Eq. (16a), is the Singular Value Decomposition (SVD) technique, [12]. This robust numerical technique was selected for the WICS software. The application of the SVD technique to Eqs. (13a), (16a) can be summarized in three steps :

Step 1 : Rewrite Eq. (13a) or Eq. (16a) as an overdetermined linear system :

$$\mathbf{A}_{m \times 2} \cdot \mathbf{X}_{2 \times 1} = \mathbf{B}_{m \times 1} \quad (13.1)$$

Step 2 : Write matrix \mathbf{A} as the product of a column-orthogonal matrix \mathbf{U} , a diagonal matrix \mathbf{W} with positive or zero elements, and the transpose of an orthogonal matrix \mathbf{V} . Matrices \mathbf{U} , \mathbf{W} , and \mathbf{V} are found using the SVD algorithm. We get :

$$\mathbf{A}_{m \times 2} = \mathbf{U}_{m \times 2} \cdot \mathbf{W}_{2 \times 2} \cdot \mathbf{V}_{2 \times 2}^T \quad (13.2)$$

Step 3 : Determine the solution of the least squares problem by computing the following matrix product :

$$\mathbf{X}_{2 \times 1} = \mathbf{V}_{2 \times 2} \cdot \mathbf{W}_{2 \times 2}^{-1} \cdot \mathbf{U}_{2 \times m}^T \cdot \mathbf{B}_{m \times 1} \quad (13.3)$$

It is important to identify elements of the diagonal matrix \mathbf{W} , i.e. singular values of \mathbf{W} , that are small. These singular values and their reciprocal will be set to zero if the least squares problem is ill-conditioned.

APPENDIX 14

SUPPORT SYSTEM KINEMATICS

In general, it is recommended to compute real-time coordinates of singularities that represent the support system or the test article if WICS is used to predict wall interference corrections in the 12ft PWT. This reduces the standard deviation of the least squares fit of the wall pressure signature and improves the accuracy of computed blockage corrections.

The real-time coordinates of singularities are a function of the kinematics, i.e. the movement, of the support system or the test article. Three different types of support systems are presently available for testing in the 12ft PWT, i.e. the Ames Bipod, the High Angle of Attack Sting, and the Image Plane. Equations describing the movement of these support systems and of the test article in the tunnel coordinate system (see Figs. 17a,17b) have to be derived.

Ames Bipod / High Angle of Attack Sting

The kinematics of the Ames Bipod and of the High Angle of Attack Sting in the tunnel coordinate system are essentially identical, if the roll angle of the High Angle of Attack Sting is kept at $\varphi = 0.0^\circ$ (the more complex case of a non-zero roll angle is discussed in Appendix 15). The kinematics may be described by one rotation about the axis $x_* = 120.71 [ft]$, $z = 0.0 [ft]$ and one rotation about the axis $x_* = 120.71 [ft]$, $y = 0.0 [ft]$. Angles α and β depicted in Fig. 42a are independent variables that describe the motion. For a roll angle $\varphi = 0.0^\circ$, angle α may be approximated by the pitch angle of the wind tunnel model and angle β may be approximated by the sideslip angle of the wind tunnel model. Figures 42b and 42c show the connection between angle α , angle β , and singularity coordinates. It is assumed that point $P_1(x_1, y_1, z_1)$ describes the initial location of a singularity. After a first rotation about the axis $x_* = 120.71 [ft]$, $z = 0.0 [ft]$ the singularity moves to point $P_2(x_2, y_2, z_2)$. After a second rotation about the axis $x_* = 120.71 [ft]$, $y = 0.0 [ft]$ the singularity moves to point $P_3(x_3, y_3, z_3)$. The final position of the singularity at point P_3 is known if coordinates x_3, y_3, z_3 are given as a function of initial coordinates x_1, y_1, z_1 , the pitch angle α , and the sideslip angle β .

Coordinates of point P_3 can be derived by considering triangles depicted in Fig. 42b :

$$\cos \gamma = \frac{x_1 - x_*}{R_1} \quad (14.1)$$

$$\sin \gamma = \frac{z_1}{R_1} \quad (14.2)$$

$$\cos (\gamma - \alpha) = \frac{x_2 - x_*}{R_1} \quad (14.3)$$

$$\sin (\gamma - \alpha) = \frac{z_2}{R_1} = \frac{z_3}{R_1} \quad (14.4)$$

The following trigonometric formulas are known :

$$\cos (\gamma - \alpha) = \cos \gamma \cdot \cos \alpha + \sin \gamma \cdot \sin \alpha \quad (14.5)$$

$$\sin (\gamma - \alpha) = \sin \gamma \cdot \cos \alpha - \cos \gamma \cdot \sin \alpha \quad (14.6)$$

Combining Eqs. (14.1),(14.2),(14.3),(14.5) we get :

$$x_2 = x_* + (x_1 - x_*) \cdot \cos \alpha + z_1 \cdot \sin \alpha \quad (14.7a)$$

Combining Eqs. (14.1),(14.2),(14.4),(14.6) we get :

$$z_2 = z_3 = z_1 \cdot \cos \alpha - (x_1 - x_*) \cdot \sin \alpha \quad (14.7b)$$

Considering triangles depicted in Fig. 42c we get :

$$\cos \gamma = \frac{x_2 - x_*}{R_2} \quad (14.8)$$

$$\sin \gamma = \frac{y_1}{R_2} = \frac{y_2}{R_2} \quad (14.9)$$

$$\cos (\gamma + \beta) = \frac{x_3 - x_*}{R_2} \quad (14.10)$$

$$\sin (\gamma + \beta) = \frac{y_3}{R_2} \quad (14.11)$$

The following trigonometric formulas are known :

$$\cos (\gamma + \beta) = \cos \gamma \cdot \cos \beta - \sin \gamma \cdot \sin \beta \quad (14.12)$$

$$\sin (\gamma + \beta) = \sin \gamma \cdot \cos \beta + \cos \gamma \cdot \sin \beta \quad (14.13)$$

Combining Eqs. (14.8),(14.9),(14.10),(14.12) we get :

$$x_3 = x_* + (x_2 - x_*) \cdot \cos \beta - y_1 \cdot \sin \beta \quad (14.14a)$$

Combining Eqs. (14.8),(14.9),(14.11),(14.13) we get :

$$y_3 = y_1 \cdot \cos \beta + (x_2 - x_*) \cdot \sin \beta \quad (14.14b)$$

The calculation of coordinates x_3, y_3, z_3 can be summarized as follows : Calculate x_3 using Eqs. (14.7a) and (14.14a) . Calculate y_3 using Eqs. (14.7a) and (14.14b) . Calculate z_3 using Eq. (14.7b) .

Image Plane

The movement of a semispan model mounted on the Image Plane can be described by a single rotation about the semispan model pitch axis ($x_* = 120.71 [ft]$, $y = 0.0 [ft]$). The pitch angle α is the independent variable that describes the motion (see Fig. 42d). Figures 42e and 42f show the connection between pitch angle and singularity coordinates for a left and right wing semispan model. It is assumed that point $P_1(x_1, y_1, z_1)$ describes the initial location of a singularity. After a rotation about the pitch axis the singularity moves to the final position at point $P_2(x_2, y_2, z_2)$. The coordinate z_1 of the singularity does not change in this case, i.e. $z_2 = z_1$. The final position of the singularity at point P_2 is known if coordinates x_2, y_2 are given as a function of initial coordinates x_1, y_1 and the pitch angle α .

Coordinates of point P_2 can be derived for a left wing semispan model by considering triangles depicted in Fig. 42e :

$$\cos \gamma = \frac{x_1 - x_*}{R} \quad (14.15)$$

$$\sin \gamma = \frac{y_1}{R} \quad (14.16)$$

$$\cos (\gamma - \alpha) = \frac{x_2 - x_*}{R} \quad (14.17)$$

$$\sin (\gamma - \alpha) = \frac{y_2}{R} \quad (14.18)$$

Combining Eqs. (14.5),(14.15),(14.16),(14.17) we get :

$$x_2 = x_* + (x_1 - x_*) \cdot \cos \alpha + y_1 \cdot \sin \alpha \quad (14.19a)$$

Combining Eqs. (14.6),(14.15),(14.16),(14.18) we get :

$$y_2 = y_1 \cdot \cos \alpha - (x_1 - x_*) \cdot \sin \alpha \quad (14.19b)$$

Figure 42f shows initial and final coordinates for a right wing semispan model. In this case coordinates of point P_2 can be derived by simply replacing pitch angle α by $-\alpha$ in Eqs.(14.19a),(14.19b) and noting that $\cos(-\alpha) = \cos(\alpha)$ and $\sin(-\alpha) = -\sin(\alpha)$. We then get :

$$x_2 = x_* + (x_1 - x_*) \cdot \cos \alpha - y_1 \cdot \sin \alpha \quad (14.20a)$$

$$y_2 = y_1 \cdot \cos \alpha + (x_1 - x_*) \cdot \sin \alpha \quad (14.20b)$$

APPENDIX 15

HIGH ANGLE OF ATTACK STING KINEMATICS

The kinematics of the High Angle of Attack Sting (HAA) for a roll angle of $\varphi = 0.0^\circ$ is described in detail in Appendix 14 . In Appendix 14 the reasonable assumption is made that the pitch angle α_* of the HAA may be approximated by the angle of attack α of the test article and that the yaw angle β_* of the HAA may be approximated by the sideslip angle β of the test article. The line doublet orientation angle φ_* of the test article, defined as the angle between the positive z-direction of the test section fixed coordinate system (see Fig. 42a) and the lift force vector, is also equal to 0.0° for a roll angle $\varphi = 0.0^\circ$. These assumptions, however, are invalid if the roll angle φ of the HAA is not equal to 0.0° .

Equations are derived in this Appendix that use the angle of attack α , sideslip angle β , and roll angle φ of the test article to (i) compute the pitch angle α_* and the yaw angle β_* of the HAA, to (ii) compute the location of test article singularities and reference points, and to (iii) compute the orientation angle of test article line doublets.

(i) PITCH ANGLE α_* AND YAW ANGLE β_* OF THE HAA : The pitch and yaw angle of the HAA may be computed in several steps assuming that angle of attack α , sideslip angle β , and roll angle φ of the test article are known. In a first step, the unit wind vector $\overrightarrow{W_\infty}$ is expressed in the model coordinate system defined by unit vectors \overrightarrow{i} , \overrightarrow{j} , and \overrightarrow{k} . Using Fig. 43a it can easily be seen that

$$\overrightarrow{W_\infty} = \begin{pmatrix} \cos \alpha \cdot \cos \beta \\ - \sin \beta \\ \sin \alpha \cdot \cos \beta \end{pmatrix} \quad (15.1)$$

In the second step, it is necessary to reverse the roll angle rotation. Assuming that the roll axis of the test article is identical with unit vector \overrightarrow{i} (see Fig. 43b), we get for the rotated unit vectors \overrightarrow{I} , \overrightarrow{J} , and \overrightarrow{K} :

$$\overrightarrow{I} = \overrightarrow{i} = \begin{pmatrix} 1 \\ 0 \\ 0 \end{pmatrix} \quad (15.2a)$$

$$\overrightarrow{J} = \begin{pmatrix} 0 \\ \cos \varphi \\ \sin \varphi \end{pmatrix} \quad (15.2b)$$

$$\vec{K} = \begin{pmatrix} 0 \\ -\sin \varphi \\ \cos \varphi \end{pmatrix} \quad (15.2c)$$

Now it is possible to compute the yaw angle β_* of the HAA by using a scalar product and a right-angled triangle depicted in Fig. 43c . The yaw angle β_* is defined as the angle between unit wind vector \vec{W}_∞ and the plane spanned by unit vectors \vec{I} and \vec{K} . Using the projection $[\vec{W}_\infty \circ \vec{J}] \vec{J}$ of the unit wind vector \vec{W}_∞ in the direction of unit vector \vec{J} and the sign convention that β_* is positive if the unit wind vector is coming from the right wing, we get :

$$\sin \beta_* = -\vec{W}_\infty \circ \vec{J} \quad (15.3a)$$

or

$$\beta_* = \arcsin \left[-\vec{W}_\infty \circ \vec{J} \right] \quad ; \quad -\frac{\pi}{2} \leq \beta_* \leq \frac{\pi}{2} \quad (15.3b)$$

where the scalar product $\vec{W}_\infty \circ \vec{J}$ is computed by using Eqs. (15.1) and (15.2b) :

$$\vec{W}_\infty \circ \vec{J} = -\sin \beta \cdot \cos \varphi + \sin \alpha \cdot \cos \beta \cdot \sin \varphi \quad (15.3c)$$

Similarly, the pitch angle α_* of the HAA may be computed by using a scalar product and a right-angled triangle depicted in Fig. 43c . The pitch angle α_* is defined as the angle between unit vector \vec{I} and the projection of the wind vector \vec{W}_∞ on the plane spanned by unit vectors \vec{I} and \vec{K} . Using the projection of vector $\vec{W}_\infty - [\vec{W}_\infty \circ \vec{J}] \vec{J}$ in the direction of unit vector \vec{K} we get :

$$\sin \alpha_* = \frac{(\vec{W}_\infty - [\vec{W}_\infty \circ \vec{J}] \vec{J}) \circ \vec{K}}{\sqrt{1 - [\vec{W}_\infty \circ \vec{J}]^2}} \quad (15.4a)$$

Knowing that $\vec{J} \perp \vec{K}$, i.e. $(\vec{W}_\infty - [\vec{W}_\infty \circ \vec{J}] \vec{J}) \circ \vec{K} = \vec{W}_\infty \circ \vec{K}$, we finally get

$$\alpha_* = \arcsin \left[\frac{\vec{W}_\infty \circ \vec{K}}{\sqrt{1 - [\vec{W}_\infty \circ \vec{J}]^2}} \right] \quad ; \quad -\frac{\pi}{2} \leq \alpha_* \leq \frac{\pi}{2} \quad (15.4b)$$

Scalar products in Eq. (15.4b) are computed by using Eqs. (15.1), (15.2b), and (15.2c) .

(ii) SINGULARITY AND REFERENCE POINT COORDINATES : It is now possible to compute the location of singularities and reference points of a test article that is mounted on the HAA by using Eqs. (15.3b), (15.4b) and Eqs. (14.7a), (14.7b), (14.14a), and (14.14b) of Appendix 14 . This is done as follows :

(1.) Apply roll angle φ to the initial singularity or reference point location given by point $P_0(x_0, y_0, z_0)$. Using Fig. 43d it is possible to compute the new location of the singularity or reference point at point $P_1(x_1, y_1, z_1)$ as :

$$x_1 = x_0 \quad (15.5a)$$

$$y_1 = R_0 \cdot \cos [\mu - \varphi] \quad (15.5b)$$

$$z_1 = R_0 \cdot \sin [\mu - \varphi] \quad (15.5c)$$

Combining Eqs. (15.5b), (15.5c), (14.5), (14.6) and knowing that $\cos \mu = y_0/R_0$ and $\sin \mu = z_0/R_0$ we finally get :

$$y_1 = y_0 \cdot \cos \varphi + z_0 \cdot \sin \varphi \quad (15.5d)$$

$$z_1 = z_0 \cdot \cos \varphi - y_0 \cdot \sin \varphi \quad (15.5e)$$

(2.) Rewrite Eqs. (14.7a), (14.7b), (14.14a), (14.14b) by replacing α, β with α_*, β_* :

$$x_2 = x_* + (x_1 - x_*) \cdot \cos \alpha_* + z_1 \cdot \sin \alpha_* \quad (15.6a)$$

$$x_3 = x_* + (x_2 - x_*) \cdot \cos \beta_* - y_1 \cdot \sin \beta_* \quad (15.6b)$$

$$y_3 = y_1 \cdot \cos \beta_* + (x_2 - x_*) \cdot \sin \beta_* \quad (15.6c)$$

$$z_3 = z_1 \cdot \cos \alpha_* - (x_1 - x_*) \cdot \sin \alpha_* \quad (15.6d)$$

The calculation of coordinates x_3, y_3, z_3 may be summarized as follows : Calculate x_3 using Eqs. (15.6a) and (15.6b) . Calculate y_3 using Eqs. (15.6a) and (15.6c) . Calculate z_3 using Eq. (15.6d) .

(iii) LINE DOUBLET ORIENTATION ANGLE φ_* : In general, the line doublet orientation angle φ_* of the test article (identical with angle τ in Appendix 4) is defined as the angle between the positive z-direction of the test section fixed coordinate system (see

Fig. 42a) and the lift force vector. Angle φ_* can easily be computed using a unit vector that is parallel to the positive z-direction of the test section coordinate system and a unit vector that is parallel to the lift force vector.

A unit vector \vec{Z} that is parallel to the positive z-direction of the test section coordinate system may be obtained by rotating unit vector \vec{K} in the $\vec{I} - \vec{K}$ plane (see Figs. 43c, 43e). The selected rotation angle is equal to the pitch angle α_* of the HAA given in Eq. (15.4b). Using Fig. 43e we then get :

$$\vec{Z} = \frac{\vec{K} - \tan \alpha_* \cdot \vec{I}}{\left| \vec{K} - \tan \alpha_* \cdot \vec{I} \right|} \quad (15.7a)$$

where

$$\vec{K} - \tan \alpha_* \cdot \vec{I} = \begin{pmatrix} -\tan \alpha_* \\ -\sin \varphi \\ \cos \varphi \end{pmatrix} \quad (15.7b)$$

$$\left| \vec{K} - \tan \alpha_* \cdot \vec{I} \right| = \sqrt{1 + \tan^2 \alpha_*} \quad (15.7c)$$

A unit vector \vec{W} that is parallel to the lift force vector may be obtained by computing the cross-product $\vec{W}_\infty \times \vec{j}$ using Eqs. (15.1) and knowing that $\vec{j} = (0; 1; 0)$ (see also Fig. 43a). We then get :

$$\vec{W} = \frac{\vec{W}_\infty \times \vec{j}}{\left| \vec{W}_\infty \times \vec{j} \right|} = \begin{pmatrix} -\sin \alpha \\ 0 \\ \cos \alpha \end{pmatrix} \quad (15.8)$$

Finally, the line doublet orientation angle φ_* may be obtained by computing the scalar product of unit vectors \vec{W} and \vec{Z} . We get :

$$\vec{W} \circ \vec{Z} = \cos \varphi_* \quad (15.9)$$

Combining Eqs. (15.7a), (15.7b), (15.7c), (15.8), and (15.9) we obtain :

$$\varphi_* = \arccos \left(\vec{W} \circ \vec{Z} \right) ; \quad \varphi \leq \pi \quad (15.10a)$$

$$\varphi_* = 2\pi - \arccos \left(\vec{W} \circ \vec{Z} \right) ; \quad \varphi > \pi \quad (15.10b)$$

where

$$\vec{W} \circ \vec{Z} = \frac{\sin \alpha \cdot \tan \alpha_* + \cos \alpha \cdot \cos \varphi}{\sqrt{1 + \tan^2 \alpha_*}} \quad (15.10c)$$

APPENDIX 16

PITCHING MOMENT LEVER ARM

In Appendix 5 equations are derived that compute the singularity strength of a line doublet of a wind tunnel model by using the measured lift force and pitching moment. The pitching moment lever arm is approximated in Eq. (5.2) as the difference between the x-coordinate of the pitching moment reference axis and the x-coordinate of the line doublet starting point (see Fig.38) . This approximation, however, is not valid anymore if a wind tunnel model is tested at a high angle of attack. More general equations are derived in this Appendix that use the pitching moment axis and the lift force axis to compute the pitching moment lever arm of a line doublet.

In general, the pitching moment lever arm of a line doublet is defined as the distance between the pitching moment axis and the lift force axis of a line doublet (see Fig. 44) . Therefore a mathematical description of each axis has to be found in order to compute the pitching moment lever arm.

(i) PITCHING MOMENT AXIS EQUATION : The pitching moment axis equation may be found by using the initial coordinates of the balance center in the tunnel coordinate system (see Fig. 17a, 17b). Assuming that x_{mr}, y_{mr}, z_{mr} are the initial coordinates of the balance center (i.e. angle of attack, sideslip angle, and roll angle of the test article are equal to zero), it is possible to introduce an initial unit pitching moment axis vector \vec{A} as follows :

$$\vec{A} = \vec{A}_2 - \vec{A}_1 \quad (16.1a)$$

where

$$\vec{A}_1 = \begin{pmatrix} x_{mr} \\ y_{mr} \\ z_{mr} \end{pmatrix} \quad (16.1b)$$

For a fullspan model point vector \vec{A}_2 is defined as :

$$\vec{A}_2 = \begin{pmatrix} x_{mr} \\ y_{mr} + 1.0 \\ z_{mr} \end{pmatrix} \quad (16.1c)$$

For a left wing semispan model point vector \vec{A}_2 is defined as :

$$\vec{A}_2 = \begin{pmatrix} x_{mr} \\ y_{mr} \\ z_{mr} - 1.0 \end{pmatrix} \quad (16.1d)$$

For a right wing semispan model point vector \vec{A}_2 is defined as :

$$\vec{A}_2 = \begin{pmatrix} x_{mr} \\ y_{mr} \\ z_{mr} + 1.0 \end{pmatrix} \quad (16.1e)$$

In the next step, equations describing the kinematics, i.e. the movement of the model support system, have to be applied to the points described by vector \vec{A}_1 and \vec{A}_2 (see Appendix 14 and 15). Point vector \vec{A}_1 moves to point vector \vec{C} and point vector \vec{A}_2 moves to point vector \vec{C}_* . After points \vec{A}_1 , \vec{A}_2 are moved to their new location, it is possible to describe the unit pitching moment axis vector \vec{D} as :

$$\vec{D} = \vec{C}_* - \vec{C} \quad (16.2)$$

A point \vec{P} on the pitching moment axis may now be described by using vectors \vec{C} , \vec{D} , and an independent variable λ :

$$\vec{P}(\lambda) = \vec{C} + \lambda \cdot \vec{D} \quad (16.3)$$

(ii) LIFT FORCE AXIS EQUATION : The lift force axis equation of a line doublet may be found by using the tunnel coordinates of the line doublet starting point in combination with the line doublet orientation angle φ_* (see also Appendix 4 and 15) . After the application of equations describing the support system kinematics, the line doublet starting point has moved to a location described by point vector \vec{E} . The line doublet orientation is given by a unit lift vector \vec{F} in the tunnel coordinate system :

$$\vec{F} = \begin{pmatrix} 0 \\ \sin \varphi_* \\ \cos \varphi_* \end{pmatrix} \quad (16.4)$$

For a left wing semispan model $\varphi_* = \pi/2$, for a right wing semispan model $\varphi_* = -\pi/2$. Similar to Eq. (16.3), a point \vec{Q} on the lift force axis may be described by using vectors \vec{E} , \vec{F} , and an independent variable μ :

$$\vec{Q}(\mu) = \vec{E} + \mu \cdot \vec{F} \quad (16.5)$$

(iii) PITCHING MOMENT LEVER ARM : The pitching moment lever arm of the selected line doublet is found by minimizing the square of the distance of points located on each axis (see Fig. 44). The square of the distance of two selected points may be computed using a scalar product :

$$D^2(\lambda, \mu) = [\vec{P}(\lambda) - \vec{Q}(\mu)] \circ [\vec{P}(\lambda) - \vec{Q}(\mu)] \quad (16.6)$$

Using Eqs. (16.3), (16.5) and applying the product rule to Eq. (16.6) we get :

$$\frac{\partial D^2(\lambda, \mu)}{\partial \lambda} = 2 \cdot [\vec{P}(\lambda) - \vec{Q}(\mu)] \circ \vec{D} \quad (16.7a)$$

$$\frac{\partial D^2(\lambda, \mu)}{\partial \mu} = 2 \cdot [\vec{P}(\lambda) - \vec{Q}(\mu)] \circ [-\vec{F}] \quad (16.7b)$$

The variables λ_{min} and μ_{min} of the two closest points are found by setting Eqs. (16.7a), (16.7b) to zero. We get :

$$[\vec{P}(\lambda_{min}) - \vec{Q}(\mu_{min})] \circ \vec{D} = 0 \quad (16.8a)$$

$$[\vec{P}(\lambda_{min}) - \vec{Q}(\mu_{min})] \circ \vec{F} = 0 \quad (16.8b)$$

Using Eqs. (16.3), (16.5), it is possible to write Eqs. (16.8a), (16.8b) as a 2×2 system of linear equations :

$$[\vec{D} \circ \vec{D}] \cdot \lambda_{min} + [-\vec{D} \circ \vec{F}] \cdot \mu_{min} = [\vec{E} - \vec{C}] \circ \vec{D} \quad (16.9a)$$

$$[\vec{D} \circ \vec{F}] \cdot \lambda_{min} + [-\vec{F} \circ \vec{F}] \cdot \mu_{min} = [\vec{E} - \vec{C}] \circ \vec{F} \quad (16.9b)$$

In general, $\vec{D} \perp \vec{F}$ or $\vec{D} \circ \vec{F} = 0$. Therefore, we get for λ_{min} and μ_{min} of the two closest points :

$$\lambda_{min} = \frac{[\vec{E} - \vec{C}] \circ \vec{D}}{\vec{D} \circ \vec{D}} \quad (16.10a)$$

$$\mu_{min} = \frac{[\vec{E} - \vec{C}] \circ \vec{F}}{-\vec{F} \circ \vec{F}} \quad (16.10b)$$

Finally, using Eq. (16.6), we get for the pitching moment lever arm :

$$D(\lambda_{min}, \mu_{min}) = \sqrt{ [\vec{P}(\lambda_{min}) - \vec{Q}(\mu_{min})] \circ [\vec{P}(\lambda_{min}) - \vec{Q}(\mu_{min})] } \quad (16.11)$$

The following two conditions may be used to determine the correct sign of the pitching moment caused by a line doublet :

$$[\vec{D} \times \vec{F}] \circ [\vec{P}(\lambda_{min}) - \vec{Q}(\mu_{min})] \geq 0 \implies "+"$$

$$[\vec{D} \times \vec{F}] \circ [\vec{P}(\lambda_{min}) - \vec{Q}(\mu_{min})] < 0 \implies "-"$$

These conditions ensure that the pitching moment is positive if the lift force axis of a line doublet is upstream of the pitching moment axis (see also Eq.(5.2) and Fig. 38) .

APPENDIX 17

INCLINATION OF FORCE AND MOMENT VECTORS

Corrections to the lift, drag, rolling moment, and yawing moment coefficient are caused by the wall interference induced inclination of corresponding force and moment vectors. These four corrections may be estimated by describing the inclination of the force and moment vectors using the induced mean angle of attack correction $\hat{\alpha}_i$ at the 1/4-chord line of the wing (see also Ref. [18], p.17).

LIFT AND DRAG COEFFICIENT CORRECTION

The lift and drag coefficient correction caused by the inclination of the lift and drag force may be estimated by using the resultant of the uncorrected lift and drag force vectors. Using Fig. 45a we get for the resultant vector in the x-z coordinate system :

$$\vec{S} = \vec{D}' + \vec{L}' = \begin{pmatrix} D' \\ L' \end{pmatrix} \quad (17.1)$$

where D' is the magnitude of the uncorrected drag force and L' is the magnitude of the uncorrected lift force experienced by the wind tunnel model.

Unit vectors \vec{i} , \vec{j} in the free-stream direction and perpendicular to the free-stream direction of the wind tunnel flow field have to be specified as they are used to define the lift and drag force. These unit vectors are a function of the mean angle of attack correction $\hat{\alpha}_i$ at the 1/4-chord of the wing. They may be written in the x-z coordinate system as :

$$\vec{i} = \begin{pmatrix} \cos \hat{\alpha}_i \\ \sin \hat{\alpha}_i \end{pmatrix} \quad (17.2a)$$

$$\vec{j} = \begin{pmatrix} -\sin \hat{\alpha}_i \\ \cos \hat{\alpha}_i \end{pmatrix} \quad (17.2b)$$

The mean angle of attack correction $\hat{\alpha}_i$ may be computed by calculating the local angle of attack correction at equally spaced reference points along the 1/4-chord line of the wing. We then get :

$$1/4 - \text{chord line} \implies \hat{\alpha}_i = \frac{\sum_{j=1}^N w(j) \cdot \alpha_i(j)}{\sum_{j=1}^N w(j)} \quad (17.2c)$$

where N is the number of reference points, w is the weighting factor of a reference point (a function of the lift distribution of the wing), and α_i is the local angle of attack correction at a reference point. Now it is possible to compute the lift and drag force vectors as :

$$\vec{L} = L \vec{j} = \left[\vec{R} \circ \vec{j} \right] \vec{j} \quad (17.3a)$$

$$\vec{D} = D \vec{i} = \left[\vec{R} \circ \vec{i} \right] \vec{i} \quad (17.3b)$$

where

$$L = \vec{R} \circ \vec{j} = -D' \cdot \sin \hat{\alpha}_i + L' \cdot \cos \hat{\alpha}_i \quad (17.4a)$$

$$D = \vec{R} \circ \vec{i} = D' \cdot \cos \hat{\alpha}_i + L' \cdot \sin \hat{\alpha}_i \quad (17.4b)$$

The lift and drag coefficient correction may now be written as :

$$\Delta c_L = c_L - c'_L = \frac{L - L'}{q_\infty \cdot \bar{S}} \quad (17.5a)$$

$$\Delta c_D = c_D - c'_D = \frac{D - D'}{q_\infty \cdot \bar{S}} \quad (17.5b)$$

where q_∞ is the free-stream dynamic pressure and \bar{S} is the reference area of the wind tunnel model. A first order approximation of the free-stream dynamic pressure may be obtained by using Eq. (1.15) in Appendix 1. Using the test section reference density, velocity, and Mach number we get :

$$\begin{aligned} q_\infty &= q_{ref} \cdot [1 + (2 - M_{ref}^2) \cdot \bar{\epsilon}] \\ &= \frac{\rho_{ref}}{2} \cdot U_{ref}^2 \cdot [1 + (2 - M_{ref}^2) \cdot \bar{\epsilon}] \end{aligned} \quad (17.6a)$$

The mean blockage factor $\bar{\epsilon}$ has to be computed as a weighted average of local blockage factors ϵ that are computed at a set of user selected reference points. We get :

$$\bar{\epsilon} = \frac{\sum_{j=1}^N w(j) \cdot \epsilon(j)}{\sum_{j=1}^N w(j)} \quad (17.6b)$$

where N is the number of reference points, w is the weighting factor of a reference point, and ϵ is the local blockage factor at a reference point.

Important remark: The reference points used to compute the mean blockage factor in Eq. (17.6b) are not necessarily identical with the reference points used to compute the mean angle of attack correction in Eq. (17.2c) !

Combining Eqs. (17.4a), (17.4b), (17.5a), and (17.5b) we get for the lift and drag coefficient correction :

$$\Delta c_L = \frac{-D' \cdot \sin \hat{\alpha}_i + L' \cdot [\cos \hat{\alpha}_i - 1]}{q_\infty \cdot \bar{S}} \quad (17.7a)$$

$$\Delta c_D = \frac{D' \cdot [\cos \hat{\alpha}_i - 1] + L' \cdot \sin \hat{\alpha}_i}{q_\infty \cdot \bar{S}} \quad (17.7b)$$

Finally, corrections have to be added to the uncorrected lift and drag coefficients. Then we get :

$$c_{L,c} = c_{L,unc} + \Delta c_L \quad (17.8a)$$

$$c_{D,c} = c_{D,unc} + \Delta c_D \quad (17.8b)$$

ROLLING AND YAWING MOMENT COEFFICIENT CORRECTION

The rolling and yawing moment coefficient correction caused by the inclination of the rolling and yawing moment vector may be computed by using the resultant of the uncorrected rolling and yawing moment vectors. Using Fig. 45b we get for the resultant vector in the x-z coordinate system :

$$\vec{S} = \vec{R}' + \vec{Y}' = \begin{pmatrix} -R' \\ -Y' \end{pmatrix} \quad (17.9)$$

where R' is the magnitude of the uncorrected rolling moment and Y' is the magnitude of the uncorrected yawing moment experienced by the wind tunnel model.

Similar to Eqs. (17.3a) and (17.3b), it is possible to combine Eqs. (17.2a),(17.2b) with Eq. (17.9) . Then, we get for the rolling and yawing moment vectors :

$$\vec{R} = -R \vec{i} = \left[\vec{S} \circ \vec{i} \right] \vec{i} \quad (17.10a)$$

$$\vec{Y} = -Y \vec{j} = \left[\vec{S} \circ \vec{j} \right] \vec{j} \quad (17.10b)$$

where

$$R = -\vec{S} \circ \vec{i} = R' \cdot \cos \hat{\alpha}_i + Y' \cdot \sin \hat{\alpha}_i \quad (17.11a)$$

$$Y = -\vec{S} \circ \vec{j} = -R' \cdot \sin \hat{\alpha}_i + Y' \cdot \cos \hat{\alpha}_i \quad (17.11b)$$

The rolling moment and yawing moment coefficient correction may now be written as :

$$\Delta \bar{c}_l = c_l - c'_l = \frac{R - R'}{q_\infty \cdot \bar{S} \cdot b/2} \quad (17.12a)$$

$$\Delta \bar{c}_n = c_n - c'_n = \frac{Y - Y'}{q_\infty \cdot \bar{S} \cdot b/2} \quad (17.12b)$$

where q_∞ is the free-stream dynamic pressure, \bar{S} is the reference area of the wind tunnel model, and b is the wing span.

Combining Eqs. (17.11a), (17.11b), (17.12a), and (17.12b) we get for the rolling and yawing moment coefficient correction :

$$\Delta \bar{c}_l = \frac{R' \cdot [\cos \hat{\alpha}_i - 1] + Y' \cdot \sin \hat{\alpha}_i}{q_\infty \cdot \bar{S} \cdot b/2} \quad (17.13a)$$

$$\Delta \bar{c}_n = \frac{-R' \cdot \sin \hat{\alpha}_i + Y' \cdot [\cos \hat{\alpha}_i - 1]}{q_\infty \cdot \bar{S} \cdot b/2} \quad (17.13b)$$

Finally, corrections have to be added to the uncorrected rolling and yawing moment coefficients. Then we get :

$$c_{l,c} = c_{l,unc} + \Delta \bar{c}_l \quad (17.14a)$$

$$c_{n,c} = c_{n,unc} + \Delta \bar{c}_n \quad (17.14b)$$

APPENDIX 18

PITCHING MOMENT COEFFICIENT CORRECTION

Wall interference induced angle of attack corrections are not constant in the test section of a wind tunnel (see Fig. 24c). Therefore, it is necessary to compute a pitching moment coefficient correction that will account for the difference between the mean and local angle of attack correction in the spanwise and chordwise direction of the wing of the test article.

In general, the corrected pitching moment coefficient $c_{M,c}$ of the complete test article configuration may be written as :

$$c_{M,c} = c_{M,unc} + \Delta c_{M1} + \Delta c_{M2} \quad (18.1)$$

where $c_{M,unc}$ is the uncorrected pitching moment coefficient, Δc_{M1} is the pitching moment coefficient correction due to the difference between the mean and local angle of attack correction in the spanwise direction of the wing, and Δc_{M2} is the pitching moment coefficient correction due to wall interference induced streamline curvature in the chordwise direction of the wing.

PITCHING MOMENT CORRECTION Δc_{M1} :

A pitching moment coefficient correction Δc_{M1} is due to the difference between the mean and local angle of attack correction in the spanwise direction of the wing. It may also be interpreted as a correction resulting from the lateral shift of the spanwise center of lift caused by wall interference effects.

The pitching moment coefficient correction Δc_{M1} may be computed by using Eq. (3.58) given in Ref. [10], which is essentially identical with Eq. (34) in Ref. [18] . Using the notation introduced in the WICS Theory Guide we get :

$$\Delta c_{M1} = F \cdot \int_0^1 \frac{\pi}{180} \cdot \left[\alpha_i(0.75, y) - \bar{\alpha}_i \right] \cdot w_w(y) \cdot \frac{2y}{b} \cdot d \left(\frac{2y}{b} \right) \quad (18.2a)$$

$$F = \frac{(\pi/2) \cdot \Lambda^2 \cdot (\partial c_L / \partial \alpha) \cdot \tan \varphi_{0.25}}{\pi \cdot \Lambda + 2 \cdot (\partial c_L / \partial \alpha)} \quad (18.2b)$$

where Λ is the aspect ratio of the wing, $\partial c_L / \partial \alpha$ is the lift curve slope in [1/rad], $\varphi_{0.25}$ is the sweep angle of the 1/4-chord line of the wing, $\alpha_i(0.75, y)$ is the local angle of attack

correction in [deg] along the 3/4-chord line of the wing, $\bar{\alpha}_i$ is the angle of attack correction in [deg] of the wing, w_w is a weighting factor derived from the lift distribution (see also Eq. (19.2c) in Appendix 19), y is the spanwise coordinate, and b is the span of the wing.

In general, Simpson's Rule may be applied to Eq. (18.2a) if Δc_{M1} has to be determined for a given wing. However, it is also possible to simply discretize Eq. (18.2a) as long as the local angle of attack correction $\alpha_i(0.75, y)$ is computed at a large number of equally spaced points along the 3/4-chord line of the wing. Assuming that a total number of N equally spaced reference points were selected along the semispan of the wing (i.e. $b/2 = N \cdot \Delta y$), we get the approximation :

$$d\left(\frac{2y}{b}\right) \approx \frac{2}{b} \cdot \Delta y = \frac{1}{N} \quad (18.3a)$$

Using the abbreviation $w_w(y(j)) \equiv w_w(j)$, Eq. (18.2a) may be discretized as :

$$\Delta c_{M1} \approx F \cdot \sum_{j=1}^N \frac{\pi}{180} \cdot \left[\alpha_i(0.75, j) - \bar{\alpha}_i \right] \cdot w_w(j) \cdot \frac{2y(j)}{b} \cdot \frac{1}{N} \quad (18.3b)$$

After rearranging terms we get :

$$\Delta c_{M1} \approx \frac{F \cdot \pi}{b \cdot 90} \cdot \frac{1}{N} \cdot \sum_{j=1}^N \left[\alpha_i(0.75, j) - \bar{\alpha}_i \right] \cdot w_w(j) \cdot y(j) \quad (18.3c)$$

Sometimes it is necessary to distribute a total number of M equally spaced reference points along the complete span of the wing (i.e. $b = M \cdot \Delta y$). Then, using the absolute value of $y(j)$, Eq. (18.3c) becomes :

$$\Delta c_{M1} \approx \frac{F \cdot \pi}{b \cdot 90} \cdot \frac{1}{M} \cdot \sum_{j=1}^M \left[\alpha_i(0.75, j) - \bar{\alpha}_i \right] \cdot w_w(j) \cdot |y(j)| \quad (18.4)$$

WICS uses Eq. (18.4) to determine the pitching moment coefficient correction Δc_{M1} that is caused by the wall interference induced shift of the center of pressure of the wing.

PITCHING MOMENT CORRECTION Δc_{M2} :

A pitching moment coefficient correction Δc_{M2} due to the streamline curvature along the chord of the wing has to be computed. Classical theory has shown that the magnitude of this correction may be approximated by the camber of a two-dimensional circularly cambered airfoil (see Ref. [18], p.17/18 and Ref. [28], p.91) .

In general, the angle of attack correction α_i is not constant along the chord of a wing. This phenomena may be described as a wall interference induced streamline curvature that is experienced by the wing. A constant streamline curvature may be found if we assume a linear change of the angle of attack correction along the chord (see Fig. 46a) . Then, a linear function $\delta\alpha_i$ may be defined as (see Fig. 46b) :

$$\delta\alpha_i(\xi) = [\alpha_i(\xi) - \alpha_i(0.50)] \cdot \frac{\pi}{180} \text{ [rad]} \quad (18.5)$$

The linear function $\delta\alpha_i$ may be related to a two-dimensional circularly cambered airfoil,[28], because its derivative with respect to ξ is the streamline curvature. The pitching moment coefficient about the 1/4-chord point of a circularly cambered airfoil is given in Ref. [28] as :

$$c_M(0.25) = -\pi \cdot \frac{f}{c} \quad (18.6)$$

where f/c is the camber of the airfoil (see Fig. 47). The camber is related to the slope of the circular arc at the 1/4 and 3/4-chord point. The slope is related to the upwash along the chord. Then, using Fig. 47, we get :

$$\begin{aligned} \tan \beta \approx \beta &= \frac{1}{2} \cdot \left[\left(\frac{dz}{d\xi} \right)_{0.25} - \left(\frac{dz}{d\xi} \right)_{0.75} \right] \\ &= \frac{1}{2} \cdot [\delta\alpha_i(0.25) - \delta\alpha_i(0.75)] \end{aligned} \quad (18.7a)$$

Using triangle ABC in Fig. 47 we also know that

$$\tan \beta \approx \beta = \frac{2 \cdot f}{c} \quad (18.7b)$$

Combining Eqs. (18.7a), (18.7b) we get for the camber as a function of the streamline curvature :

$$\frac{f}{c} = \frac{1}{4} \cdot [\delta\alpha_i(0.25) - \delta\alpha_i(0.75)] \quad (18.8)$$

Using Eq. (18.5) we also know :

$$\delta\alpha_i(0.25) = [\alpha_i(0.25) - \alpha_i(0.50)] \cdot \frac{\pi}{180} \text{ [rad]} \quad (18.9a)$$

$$\delta\alpha_i(0.75) = [\alpha_i(0.75) - \alpha_i(0.50)] \cdot \frac{\pi}{180} \text{ [rad]} \quad (18.9b)$$

Combining Eqs. (18.6), (18.8), (18.9a), (18.9b) we finally get for the pitching moment coefficient of the two-dimensional circularly cambered airfoil as a function of the difference between the angle of attack correction on the 1/4 and 3/4-chord point :

$$c_M(0.25) = \frac{\pi}{4} \cdot [\alpha_i(0.75) - \alpha_i(0.25)] \cdot \frac{\pi}{180} \quad (18.10)$$

In the next step, it is necessary to integrate the pitching moment coefficient in the spanwise direction of the wing. Assuming that the sweep angle φ of the wing is 0.0° (see Fig. 48), the local pitching moment coefficient of a wing segment of width dy about the 1/4-chord line may be written as

$$c_M(0.25, y) = \frac{d P(y)}{q_\infty \cdot c(y) \cdot d \bar{S}(y)} \quad (18.11)$$

where $d P(y)$ is the infinitesimal pitching moment acting on the wing segment, q_∞ is the free-stream dynamic pressure seen by the wing segment, $c(y)$ is the local chord, and $d \bar{S}(y)$ is the infinitesimal area of the wing segment. The infinitesimal area $d \bar{S}(y)$ of the wing segment is a trapezoid and may therefore be expressed as :

$$d \bar{S}(y) = c(y) \cdot dy \quad (18.12)$$

Introducing the mean geometric chord as a function of the wing reference area \bar{S} and the wing span b we know :

$$\bar{c} = \frac{\bar{S}}{b} \quad (18.13)$$

In the next step we combine Eqs. (18.11), (18.12), divide both sides of the resulting equation by the mean geometric chord \bar{c} and the mean aerodynamic chord c' , introduce Eq. (18.13) on the right hand side of the equation, and rearrange terms. Then, we get :

$$c_M(0.25, y) \cdot \frac{c^2(y)}{c' \cdot \bar{c}} \cdot \frac{1}{b} \cdot dy = \frac{d P(y)}{q_\infty \cdot c' \cdot \bar{S}} \quad (18.14)$$

The pitching moment coefficient correction Δc_{M2} for 0.0° sweep angle may be obtained by integrating both sides of Eq. (18.14) over the whole wing span :

$$\Delta c_{M2} = \int_{-b/2}^{b/2} c_M(0.25, y) \cdot \frac{c^2(y)}{c' \cdot \bar{c}} \cdot \frac{dy}{b} = \int_0^P \frac{d P(y)}{q_\infty \cdot c' \cdot \bar{S}} \quad (18.15)$$

The pitching moment coefficient of a swept wing may be approximated (see Ref. [29]) by using the product of the pitching moment coefficient of the unswept wing and the *cosine* of an average sweep angle φ . For a circular cambered airfoil the sweep angle at the 1/2-chord is selected. We get :

$$\Delta c_{M2}(\varphi \neq 0.0^\circ) = \cos \varphi_{0.50} \cdot \Delta c_{M2}(\varphi = 0.0^\circ) \quad (18.16)$$

Finally, combining Eqs. (18.10), (18.15), (18.16) we get for the pitching moment coefficient correction Δc_{M2} due to streamline curvature :

$$\Delta c_{M2} = \frac{\pi \cdot \cos \varphi_{0.50}}{4} \cdot \int_{-b/2}^{b/2} [\alpha_i(0.75, y) - \alpha_i(0.25, y)] \cdot \frac{\pi}{180} \cdot \frac{c^2(y)}{c' \cdot \bar{c}} \cdot \frac{d y}{b} \quad (18.17)$$

The variable transformation $\mu = 2y/b$ is introduced in an effort to compare Eq. (18.17) with an equation reported in the literature. Assuming that the lift distribution is symmetric, Eq. (18.17) may then be written as :

$$\Delta c_{M2} = \frac{\pi \cdot \cos \varphi_{0.50}}{4} \cdot \int_0^1 [\alpha_i(0.75, \mu) - \alpha_i(0.25, \mu)] \cdot \frac{\pi}{180} \cdot \frac{c^2(\mu)}{c' \cdot \bar{c}} d \mu \quad (18.18)$$

Equation (18.18) agrees with Eq. (35) in Ref. [18] .

Assuming that local angle of attack corrections are computed on a total of N equally spaced reference points along the 1/4-chord line of the wing and N equally spaced reference points along the 3/4-chord line of the wing (i.e. $b/2 = N \cdot \Delta y$), we get the approximation :

$$d \mu \approx \Delta \mu = \frac{2 \Delta y}{b} = \frac{1}{N} \quad (18.19)$$

Combining Eqs. (18.18), (18.19) we get an approximation of the pitching moment coefficient correction due to streamline curvature :

$$\Delta c_{M2} \approx \frac{\pi \cdot \cos \varphi_{0.50}}{4} \cdot \sum_{j=1}^N [\alpha_i(0.75, j) - \alpha_i(0.25, j)] \cdot \frac{\pi}{180} \cdot \frac{c^2(j)}{c' \cdot \bar{c}} \cdot \frac{1}{N} \quad (18.20a)$$

Sometimes it is required to distribute a total number of M equally spaced reference points along the 1/4- and 3/4-chord line of the complete span of the wing (i.e. $b = M \cdot \Delta y$).

Then Eq. (18.20a) becomes :

$$\Delta c_{M2} \approx \frac{\pi \cdot \cos \varphi_{0.50}}{4} \cdot \sum_{j=1}^M [\alpha_i(0.75, j) - \alpha_i(0.25, j)] \cdot \frac{\pi}{180} \cdot \frac{c^2(j)}{c' \cdot \bar{c}} \cdot \frac{1}{M} \quad (18.20b)$$

Finally, introducing compressibility effects in Eq. (18.20b) (see Ref. [10], Eq. (3.59)), we get :

$$\Delta c_{M2} \approx G \cdot \frac{1}{M} \cdot \sum_{j=1}^M \left[\alpha_i(0.75, j) - \alpha_i(0.25, j) \right] \cdot c^2(j) \quad (18.21a)$$

where

$$G = \frac{\pi \cdot \cos \varphi_{0.50}}{4 \cdot \sqrt{1 - M^2 \cdot \cos^2 \varphi_{0.50}}} \cdot \frac{\pi}{180} \cdot \frac{1}{c' \cdot \bar{c}} \quad (18.21b)$$

Equation (18.21a) and (18.21b) are used by WICS to determine a pitching moment correction due to streamline curvature.

CALCULATION OF PITCHING MOMENT COEFFICIENT CORRECTIONS :

WICS uses Eq. (18.4) and Eqs. (18.21a,b) to compute pitching moment coefficient corrections due to the difference between the mean and local wall interference corrections in the spanwise and chordwise direction of the wing of a wind tunnel model. Input variables required for the application of these equations are classified as follows : (1) variables that depend on the geometry of the test article (Λ , c , c' , \bar{c} , $\varphi_{0.25}$, $\varphi_{0.50}$), (2) variables that depend on the lift of the wing ($w_w(j)$, $\partial c_L / \partial \alpha$), and (3) variables that are a result of the calculation of mean and local wall interference corrections ($\bar{\alpha}_i$, $\alpha_i(j)$; $\alpha_i(0.25, j)$, $\alpha_i(0.75, j)$). For best results it is recommended to determine the lift curve slope $\partial c_L / \partial \alpha$ by using the experimental $c_L - \alpha$ curve.

APPENDIX 19

ROLLING MOMENT COEFFICIENT CORRECTION

An additional rolling moment coefficient correction Δc_l has to be found whenever wall interference effects are the result of a non-symmetric lift distribution on the wing. A non-symmetric lift distribution may be caused by deflected ailerons or non-zero sideslip angle of the wind tunnel model.

In general, the corrected rolling moment coefficient $c_{l,c}$ of the complete test article configuration may be written as :

$$c_{l,c} = c_{l,unc} + \Delta c_l \quad (19.1)$$

where $c_{l,unc}$ is the uncorrected rolling moment coefficient and Δc_l is the rolling moment coefficient correction due to wall interference effects.

The calculation of the rolling moment coefficient correction is done in three steps. At first, it is necessary to find a reasonable non-symmetric lift distribution and line doublet representation of the wing that satisfies the measured lift force, pitching moment, and rolling moment of the test article. Then, angle of attack corrections along the 3/4-chord of the wing are computed using the non-symmetric line doublet representation of the wing and the wall signature method. Finally, the rolling moment coefficient correction Δc_l is determined by integrating the angle of attack correction distribution.

LIFT DISTRIBUTION AND LINE DOUBLET REPRESENTATION :

The calculation of a rolling moment coefficient correction is only possible if a non-symmetric lift distribution of the wing is found that matches the measured lift force, pitching moment, and rolling moment of the test article. This lift distribution may be obtained in two steps by using results presented in Appendix 5.

At first, a symmetric lift distribution of the wing is assumed. The corresponding circulation Γ^* of the wing is written as (see Appendix 5 for more detail) :

$$\Gamma^*(y) = \Gamma_w \cdot w_w(y) \quad (19.2a)$$

where Γ_w is only a function of the lift force and pitching moment measurement on the test article and $w_w(y)$ is the weighting factor of the selected symmetric lift distribution. The

weighting factor $w_w(y)$ has to fulfill the condition :

$$\int_{-b/2}^{b/2} w_w(y) dy = b \quad (19.2b)$$

The weighting factor $w_w(y)$ of an elliptic lift distribution ($b \equiv$ wing span) is given as :

$$w_w(y) = \frac{4}{\pi} \cdot \sqrt{1 - \left[\frac{2 \cdot y}{b} \right]^2} \quad (19.2c)$$

The total lift caused by the symmetric lift distribution may be computed by integrating the circulation along the wing span. Using Eqs. (19.2a), (19.2b) we get :

$$L(\Gamma^*) = \rho_\infty \cdot u_\infty \cdot \int_{-b/2}^{b/2} \Gamma^*(y) dy = \rho_\infty \cdot u_\infty \cdot \Gamma_w \cdot b \quad (19.3a)$$

Similarly, we get for the total pitching moment caused by the symmetric lift distribution :

$$\begin{aligned} P(\Gamma^*) &= \rho_\infty \cdot u_\infty \cdot \int_{-b/2}^{b/2} \Delta x(y) \cdot \Gamma^*(y) dy \\ &= \rho_\infty \cdot u_\infty \cdot \Gamma_w \cdot \int_{-b/2}^{b/2} \Delta x(y) \cdot w_w(y) dy \end{aligned} \quad (19.3b)$$

where $\Delta x(y)$ is the pitching moment arm.

In a second step, a weighting factor Δw is applied to the symmetric lift distribution such that the total rolling moment caused by the resulting non-symmetric lift distribution equals the measured rolling moment R . The weighting factor Δw must be introduced such that the total lift force and pitching moment of the non-symmetric lift distribution equals the lift force and pitching moment of the symmetric lift distribution. This weighting factor Δw may be defined as follows (see Figure 49) :

$$\Gamma^{**}(y) = \Gamma^*(y) \cdot [1 + \Delta w] \quad ; \quad y < 0 \quad (19.4a)$$

$$\Gamma^{**}(y) = \Gamma^*(y) \quad ; \quad y = 0 \quad (19.4b)$$

$$\Gamma^{**}(y) = \Gamma^*(y) \cdot [1 - \Delta w] \quad ; \quad y > 0 \quad (19.4c)$$

where Γ^{**} is the circulation of the non-symmetric lift distribution of the wing.

Combining Eqs. (19.2a), (19.4a), (19.4b), and (19.4c) it is possible to express the non-symmetric lift distribution as a function of the symmetric lift distribution. Similar to Eq. (19.2a), we get for the circulation of the non-symmetric lift distribution :

$$\Gamma^{**}(y) = \Gamma_w \cdot \overline{w_w}(y) \quad (19.5a)$$

where

$$\overline{w_w}(y) = w_w(y) \cdot [1 + \Delta w] \quad ; \quad y < 0 \quad (19.5b)$$

$$\overline{w_w}(y) = w_w(y) \quad ; \quad y = 0 \quad (19.5c)$$

$$\overline{w_w}(y) = w_w(y) \cdot [1 - \Delta w] \quad ; \quad y > 0 \quad (19.5d)$$

In the next step it is necessary to show that the lift and pitching moment caused by the non-symmetric lift distribution Γ^{**} is identical with values obtained from the symmetric lift distribution Γ^* . Integrating the circulation Γ^{**} of the non-symmetric lift distribution along the wing span and introducing Eqs. (19.5a) we get :

$$\begin{aligned} L(\Gamma^{**}) &= \rho_\infty \cdot u_\infty \cdot \int_{-b/2}^{b/2} \Gamma^{**}(y) d y \\ &= \rho_\infty \cdot u_\infty \cdot \Gamma_w \cdot \int_{-b/2}^{b/2} \overline{w_w}(y) d y \end{aligned} \quad (19.6a)$$

Using Eqs. (19.2b),(19.5b),(19.5c),(19.5d) and knowing that $w_w(y)$ is symmetric to $y = 0$ we get :

$$\begin{aligned} &\int_{-b/2}^{b/2} \overline{w_w}(y) d y \\ &= \int_{-b/2}^0 \overline{w_w}(y) d y + \int_0^{b/2} \overline{w_w}(y) d y \\ &= \int_{-b/2}^0 w_w(y) \cdot [1 + \Delta w] d y + \int_0^{b/2} w_w(y) \cdot [1 - \Delta w] d y \quad (19.6b) \\ &= \int_{-b/2}^{b/2} w_w(y) d y + \Delta w \cdot \left[\int_{-b/2}^0 w_w(y) d y - \int_0^{b/2} w_w(y) d y \right] \\ &= b \end{aligned}$$

Thus, combining Eqs. (19.6a), (19.6b) and comparing the result with Eq. (19.3a) we conclude that :

$$L(\Gamma^{**}) = \rho_\infty \cdot u_\infty \cdot \Gamma_w \cdot b = L(\Gamma^*) \quad (19.6c)$$

Similarly, we get for the pitching moment of the non-symmetric lift distribution :

$$\begin{aligned}
 P(\Gamma^{**}) &= \rho_{\infty} \cdot u_{\infty} \cdot \int_{-b/2}^{b/2} \Delta x(y) \cdot \Gamma^{**}(y) d y \\
 &= \rho_{\infty} \cdot u_{\infty} \cdot \Gamma_w \cdot \int_{-b/2}^{b/2} \Delta x(y) \cdot \overline{w_w}(y) d y
 \end{aligned} \tag{19.7a}$$

Using Eqs. (19.5b),(19.5c),(19.5d) and knowing that $\Delta x(y) \cdot w_w(y)$ is symmetric to $y = 0$ we get :

$$\begin{aligned}
 &\int_{-b/2}^{b/2} \Delta x(y) \cdot \overline{w_w}(y) d y \\
 = &\int_{-b/2}^0 \Delta x(y) \cdot \overline{w_w}(y) d y + \int_0^{b/2} \Delta x(y) \cdot \overline{w_w}(y) d y \\
 = &\int_{-b/2}^0 \Delta x(y) \cdot w_w(y) \cdot [1 + \Delta w] d y \\
 &+ \int_0^{b/2} \Delta x(y) \cdot w_w(y) \cdot [1 - \Delta w] d y \\
 = &\int_{-b/2}^{b/2} \Delta x(y) \cdot w_w(y) d y \\
 &+ \Delta w \cdot \left[\int_{-b/2}^0 \Delta x(y) \cdot w_w(y) d y - \int_0^{b/2} \Delta x(y) \cdot w_w(y) d y \right] \\
 = &\int_{-b/2}^{b/2} \Delta x(y) \cdot w_w(y) d y
 \end{aligned} \tag{19.7b}$$

Thus, combining Eqs. (19.7a), (19.7b) and comparing the result with Eq. (19.3b) we conclude that :

$$P(\Gamma^{**}) = \rho_{\infty} \cdot u_{\infty} \cdot \Gamma_w \cdot \int_{-b/2}^{b/2} \Delta x(y) \cdot w_w(y) d y = P(\Gamma^*) \tag{19.7c}$$

In Eqs. (19.6c) and (19.7c) it was shown that the introduction of the weighting factor Δw does not change the lift force and pitching moment. It remains to determine Δw as a function of the rolling moment measurement. This may be done as follows :

The calculation of the angle of attack correction based on the wall signature method requires that the non-symmetric lift distribution of the wing has to be translated to a corresponding non-symmetric line doublet representation of the wing. We assume that a

total number of n_w equally spaced line doublets are selected along the 1/4-chord line of the wing. Then, the strength $\sigma_w^{**}(y(i))$ of a line doublet at the spanwise location $y(i)$ is defined as (see also Eq. (5.4a) in Appendix 5) :

$$\sigma_w^{**}(y(i)) = \Delta s_w \cdot \Gamma_w \cdot \overline{w_w}(y(i)) \quad (19.8a)$$

where $\overline{w_w}(y(i))$ is given by Eqs. (19.5b), (19.5c), (19.5d) and

$$\Delta s_w = \frac{b}{n_w} \quad (19.8b)$$

$$y(i) = \frac{-b}{2} + \Delta s_w \cdot \left[i - \frac{1}{2} \right] \quad (19.8c)$$

The total rolling moment caused by the non-symmetric line doublet representation of the wing may now be written as :

$$-R = \sum_{i=1}^{n_w} L_w(i) \cdot y(i) \quad (19.9a)$$

where $L_w(i)$ is the lift force caused by a single line doublet at the spanwise station $y(i)$. Equation (19.9a) may also be written as the sum of the contributions from the left and right wing. For an even number n_w of line doublets we then get :

$$-R = \sum_{i=1}^{n_w/2} L_w(i) \cdot y(i) + \sum_{i=n_w/2+1}^{n_w} L_w(i) \cdot y(i) \quad (19.9b)$$

Applying the Kutta/Joukowski formula to the wing span increment Δs_w , introducing Eq. (19.5a), and using the abbreviations $\Gamma^{**}(y(i)) \equiv \Gamma^{**}(i)$ and $\overline{w_w}(y(i)) \equiv \overline{w_w}(i)$ we get :

$$L_w(i) = \rho_\infty \cdot u_\infty \cdot \Delta s_w \cdot \Gamma^{**}(i) = \rho_\infty \cdot u_\infty \cdot \Delta s_w \cdot \Gamma_w \cdot \overline{w_w}(i) \quad (19.10)$$

Combining Eqs. (19.5b), (19.5c), (19.5d), (19.9b) and (19.10) we get :

$$\begin{aligned} \frac{-R}{\rho_\infty \cdot u_\infty \cdot \Delta s_w \cdot \Gamma_w} &= [1 + \Delta w] \cdot \sum_{i=1}^{n_w/2} w_w(i) \cdot y(i) \\ &+ [1 - \Delta w] \cdot \sum_{i=n_w/2+1}^{n_w} w_w(i) \cdot y(i) \end{aligned} \quad (19.11)$$

The weighting factor $w_w(i)$ of the symmetric lift distribution is symmetric to the root of the wing ($y = 0$). Therefore, we know :

$$\sum_{i=n_w/2+1}^{n_w} w_w(i) \cdot y(i) = - \sum_{i=1}^{n_w/2} w_w(i) \cdot y(i) \quad (19.12)$$

Combining Eqs. (19.11) and (19.12) we get :

$$\frac{-R}{\rho_\infty \cdot u_\infty \cdot \Delta s_w \cdot \Gamma_w} = 2 \cdot \Delta w \cdot \sum_{i=1}^{n_w/2} w_w(i) \cdot y(i) \quad (19.13)$$

After rearranging terms in Eq. (19.13) we get for the weighting factor Δw :

$$\Delta w = \frac{-R}{2 \cdot \rho_\infty \cdot u_\infty \cdot \Delta s_w \cdot \Gamma_w \cdot \sum_{i=1}^{n_w/2} w_w(i) \cdot y(i)} \quad (19.14a)$$

where the number n_w of line doublets of the wing is even. Assuming that the number n_w of line doublets of the wing is odd, we get :

$$\Delta w = \frac{-R}{2 \cdot \rho_\infty \cdot u_\infty \cdot \Delta s_w \cdot \Gamma_w \cdot \sum_{i=1}^{\frac{n_w+1}{2}-1} w_w(i) \cdot y(i)} \quad (19.14b)$$

Finally, non-symmetric line doublet strength values $\sigma_w^{**}(y(i))$ that satisfy the measured lift, pitching moment, and rolling moment may be determined by using Eqs. (19.5b), (19.5c), (19.5d), (19.8a), (19.14a) and (19.14b) .

The angle of attack correction α_i along the 3/4-chord line of the wing may now be computed by applying the wall signature method as the line doublet representation of the wing is known (for more detail see Chapter 2) .

ROLLING MOMENT COEFFICIENT CORRECTION :

It is now possible to compute a rolling moment coefficient correction due to wind tunnel wall interference effects as the angle of attack correction along the 3/4-chord line of the wing is known. Figure 50 shows the angle of attack correction distribution $\alpha_i(0.75, y)$ as a function of the spanwise coordinate y of the wing. Using Fig. 50, we get for the infinitesimal rolling moment of a wing span increment $d y$:

$$d R = (-1) \cdot y \cdot \frac{d c_L(y)}{d \alpha} \cdot \alpha_i(0.75, y) \cdot q_\infty \cdot d \bar{S} \quad (19.15)$$

The infinitesimal area $d\bar{S}$ of the wing span element may be written as :

$$d\bar{S} = c(y) \cdot dy \quad (19.16)$$

where $c(y)$ is the local chord of the wing. Combining Eqs. (19.15) and (19.16) and integrating the corresponding equation in the spanwise direction, we get for the rolling moment due to wall interference effects :

$$\Delta R = q_\infty \cdot \int_{-b/2}^{b/2} (-y) \cdot \frac{d c_L(y)}{d \alpha} \cdot \alpha_i(0.75, y) \cdot c(y) \cdot dy \quad (19.17)$$

The rolling moment coefficient correction Δc_l has to be added to the uncorrected rolling moment coefficient (see Eq. (19.1)). Therefore we get :

$$\Delta c_l \equiv (-1) \cdot \frac{\Delta R}{q_\infty \cdot \bar{S} \cdot b/2} \quad (19.18)$$

Finally, combining Eqs. (19.17), (19.18), the rolling moment coefficient correction is obtained as :

$$\Delta c_l = \frac{2}{\bar{S} \cdot b} \cdot \int_{-b/2}^{b/2} y \cdot \frac{d c_L(y)}{d \alpha} \cdot \alpha_i(0.75, y) \cdot c(y) \cdot dy \quad (19.19a)$$

In general, Simpson's Rule may be applied to Eq. (19.19a) if Δc_l has to be determined for a given wing. However, it is also possible to simply discretize Eq. (19.19a) as long as the local angle of attack correction α_i is computed at a large number of equally spaced points along the 3/4-chord line of the wing. Assuming that a total number of M equally spaced reference points were selected along the complete span of the wing (i.e. $b = M \cdot \Delta y$ and $dy \approx \Delta y = b/M$), we get the approximation :

$$\Delta c_l \approx \frac{2}{\bar{S}} \cdot \frac{1}{M} \cdot \sum_{j=1}^M y(j) \cdot \frac{d c_L(j)}{d \alpha} \cdot \alpha_i(0.75, j) \cdot c(j) \quad (19.19b)$$

where

$$y(j) = \frac{-b}{2} + \frac{b}{M} \cdot \left[j - \frac{1}{2} \right] \quad (19.19c)$$

The application of Eq. (19.19b) requires an estimate of the local lift curve slope $dc_L(j)/d\alpha$ at the spanwise station of a reference point. This estimate may be obtained by

using the Kutta/Joukowski formula. For an infinitesimal wing span increment dy we get for the lift dL using the non-symmetric lift distribution :

$$dL = \rho_{\infty} \cdot u_{\infty} \cdot \Gamma^{**}(y) \cdot dy \quad (19.20a)$$

The local lift coefficient is defined as :

$$c_L(y) = \frac{dL}{\rho_{\infty}/2 \cdot u_{\infty}^2 \cdot c(y) \cdot dy} \quad (19.20b)$$

Combining Eqs. (19.20a), (19.20b) we then get :

$$c_L(y) = \frac{2 \cdot \Gamma^{**}(y)}{u_{\infty} \cdot c(y)} \quad (19.21)$$

Combining Eq. (19.5a) with Eq. (19.21) and differentiating both sides of the resulting equation with respect to angle of attack α we get :

$$\frac{d c_L(y)}{d \alpha} = \frac{2 \cdot \overline{w_w}(y)}{u_{\infty} \cdot c(y)} \cdot \frac{d \Gamma_w}{d \alpha} \quad (19.22)$$

Introducing the abbreviation $y(j) \equiv j$, we get at the discrete spanwise position j :

$$\frac{d c_L(j)}{d \alpha} = \frac{2 \cdot \overline{w_w}(j)}{u_{\infty} \cdot c(j)} \cdot \frac{d \Gamma_w}{d \alpha} \quad (19.23)$$

Assuming that the total lift of the model is charged to the wing, we get from Eq. (19.6c) :

$$L = \rho_{\infty} \cdot u_{\infty} \cdot \Gamma_w \cdot b = c_L \cdot \frac{\rho_{\infty}}{2} \cdot u_{\infty}^2 \cdot \overline{S} \quad (19.24)$$

Differentiating both sides of Eq. (19.21) with respect to the angle of attack α and rearranging terms we get :

$$\frac{d \Gamma_w}{d \alpha} = \frac{u_{\infty} \cdot \overline{S}}{2 \cdot b} \cdot \frac{d c_L}{d \alpha} \quad (19.25)$$

Thus, combining Eqs. (19.23), (19.25) we get the following approximation of the local lift curve slope :

$$\frac{d c_L(j)}{d \alpha} \approx \frac{\overline{w_w}(j) \cdot \overline{S}}{c(j) \cdot b} \cdot \frac{d c_L}{d \alpha} \quad (19.26)$$

Finally, combining Eqs. (19.19b), (19.26) we get for the rolling moment coefficient correction due to wall interference effects :

$$\Delta c_l \approx \frac{2}{b} \cdot \frac{dc_L}{d\alpha} \cdot \frac{1}{M} \cdot \sum_{j=1}^M y(j) \cdot \overline{w_w}(j) \cdot \alpha_i(0.75, j) \quad (19.27)$$

where $dc_L/d\alpha$ is the lift curve slope of the wing in [1/deg], b is the wing span, M is the number of reference points in the spanwise direction of the wing, $y(j)$ is the spanwise coordinate of reference point "j", $\overline{w_w}(j)$ is the weighting factor of the non-symmetric lift distribution of the wing at reference point "j", and $\alpha_i(0.75, j)$ is the angle of attack correction at reference point "j" in [deg]. An interesting interpretation of Eq. (19.27) is possible if we introduce the absolute value of $y(j)$ and assume that $y(j) \neq 0$. Then Eq. (19.27) becomes :

$$\Delta c_l \approx \frac{1}{M} \cdot \sum_{j=1}^M \frac{y(j)}{|y(j)|} \cdot \frac{|y(j)|}{b/2} \cdot \left[\overline{w_w}(j) \cdot \frac{dc_L}{d\alpha} \cdot \alpha_i(0.75, j) \right] \quad (19.28)$$

Equation (19.28) may be interpreted as the arithmetic mean value of weighted rolling moment coefficient contributions along the 3/4-chord of the wing where

$$\frac{y(j)}{|y(j)|} \equiv \text{sign of the local rolling moment correction}$$

$$\frac{|y(j)|}{b/2} \equiv \text{dimensionless rolling moment arm}$$

$$\overline{w_w}(j) \cdot \frac{dc_L}{d\alpha} \cdot \alpha_i(0.75, j) \equiv \text{local lift coefficient}$$

Equation (19.27) is used by WICS to determine a rolling moment coefficient correction due to wind tunnel wall interference effects.

APPENDIX 20

SCALE FACTOR LAW

The minimum of the blockage factor of a wind tunnel model tested in a clean configuration (i.e. flaps, slats not extended and no landing gear) is more or less identical with the solid volume blockage contribution. This approximation is valid if such a model is tested in the vicinity of 0.0° angle of attack where solid volume blockage effects are significantly larger than corresponding separation wake blockage effects.

Solid volume blockage effects are a function of the volume displacement of the wind tunnel model. The solid volume blockage factor is proportional to the volume of the test article. Therefore, it is possible to develop a scale factor law, that relates the length scale of two models of different size but identical geometry to the observed minimum of the solid volume blockage. The scale factor law may be written as :

$$\epsilon_{min}(\psi_2) \approx \epsilon_{min}(\psi_1) \cdot \left[\frac{\psi_2}{\psi_1} \right]^3 \quad (20.1)$$

where ϵ_{min} is the minimum of the blockage factor as a function of the length scale of the model, ψ_1 is the length scale of the first model, and ψ_2 is the length scale of the second model.

The following example shows how this scale factor law may be applied to a test of two different sized Boeing 7J7 semispan models (see Chapter 3.3 for more detail). Both semispan models had identical geometry. The first model was a 8 % scale model, the second model was a 14 % scale model. Both models were tested in a cruise configuration. From Fig. 23a we estimate that the minimum of the blockage factor computed by WICS (wall signature method) and the two-variable method for the 8 % scale model is approximately 0.0030 . Now it is possible to predict the solid volume blockage factor of the 14 % model by applying the scale factor law. Using the blockage factor minimum of the 8 % model and the cube of the scale factor ratio we get the prediction :

$$\epsilon_{min}(14\%) \approx \epsilon_{min}(8\%) \cdot \left[\frac{14\%}{8\%} \right]^3 = 0.0030 \cdot 5.36 = 0.0160 \quad (20.2)$$

Comparing the predicted solid volume blockage factor, i.e. 0.0160, with the estimate of the solid volume blockage from Fig. 23b, i.e. 0.0155, we see that both values agree

fairly well. Therefore, it can be concluded that the wall pressure measurements used by WICS to determine blockage corrections and the corresponding description of the solid volume blockage effect by a source/sink pair is sufficiently accurate. The scale factor law also provides an additional absolute magnitude check of blockage corrections that are computed by using wall pressure measurements.

FIGURES

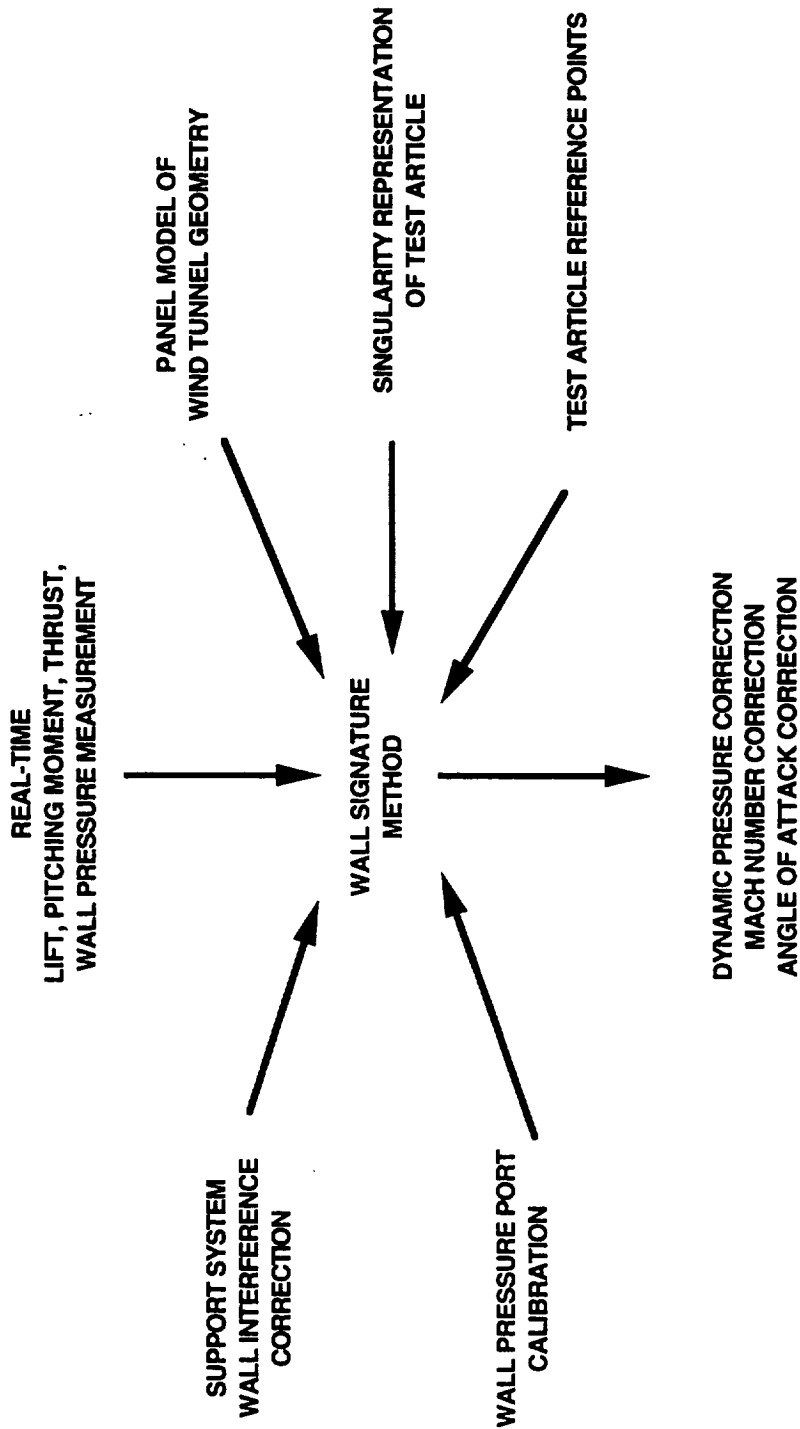


Fig. 1 Basic Elements of Wall Signature Method.

WIND TUNNEL WALL INTERFERENCE

=

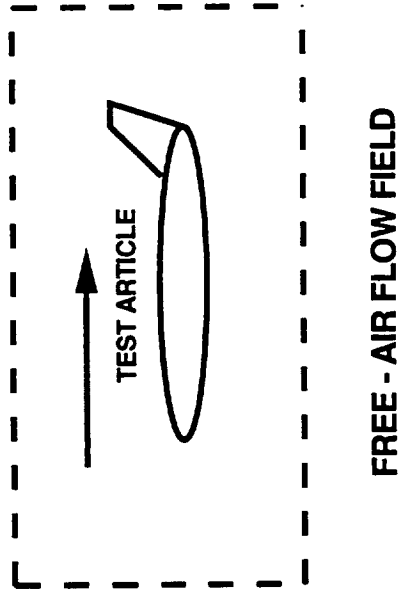
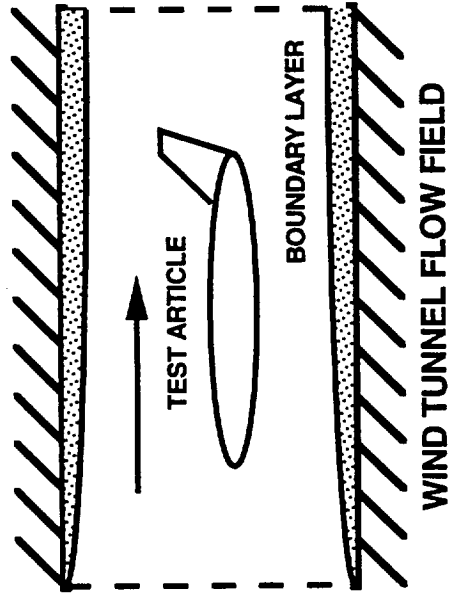


Fig. 2a Definition of Wind Tunnel Wall Interference Effects.

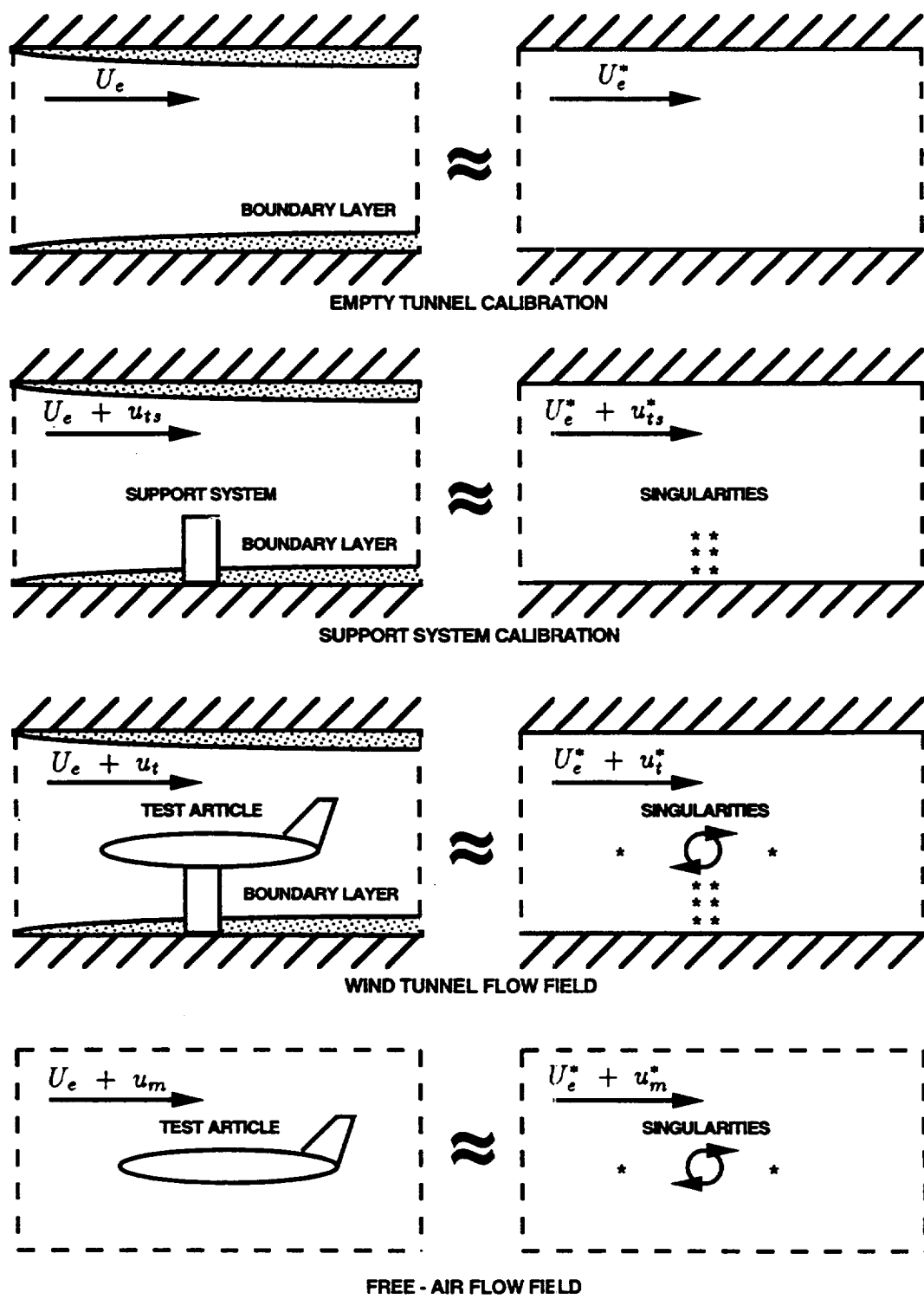


Fig. 2b Singularity Representation of Flow Field.

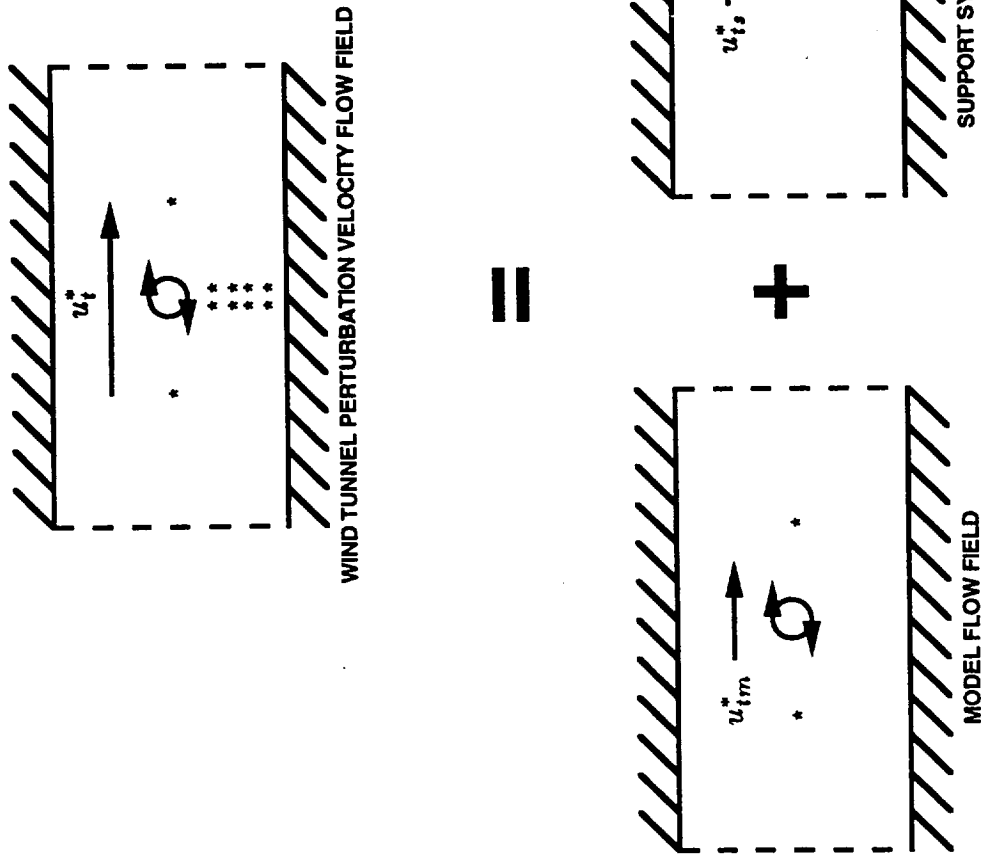


Fig. 2c Superposition of Model and Support System Flow Field.

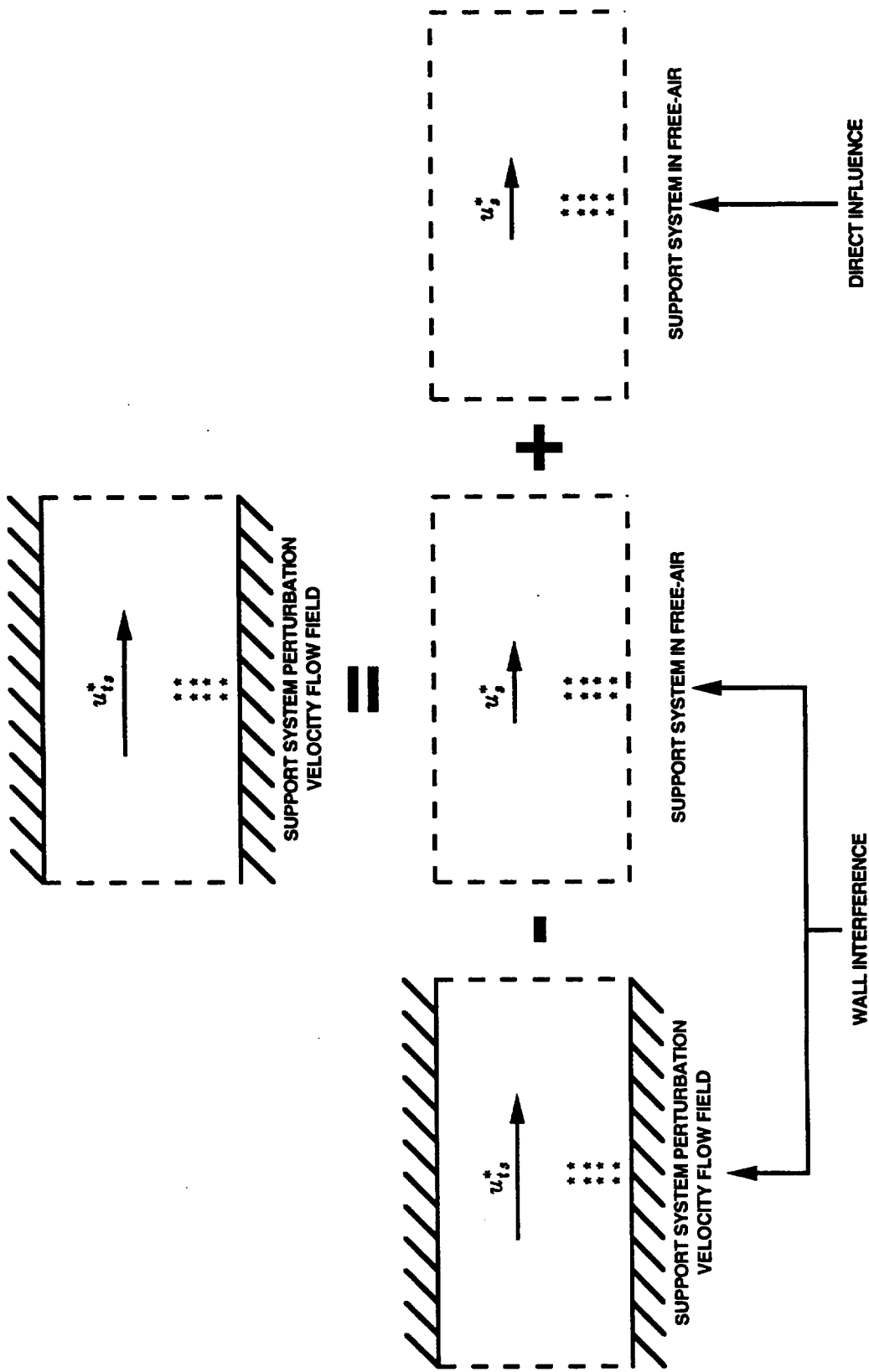


Fig. 2d Wall Interference and Direct Influence of Support System.

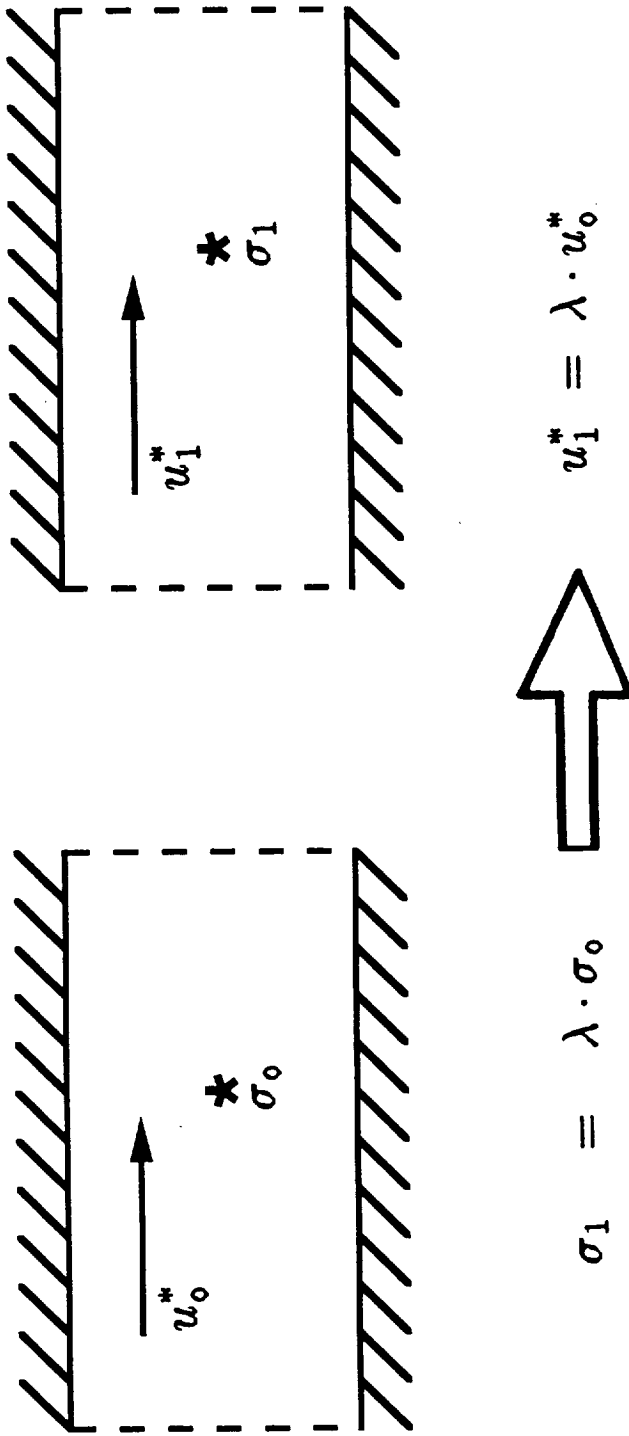


Fig. 3 Linear Property of Singularity Flow Field.

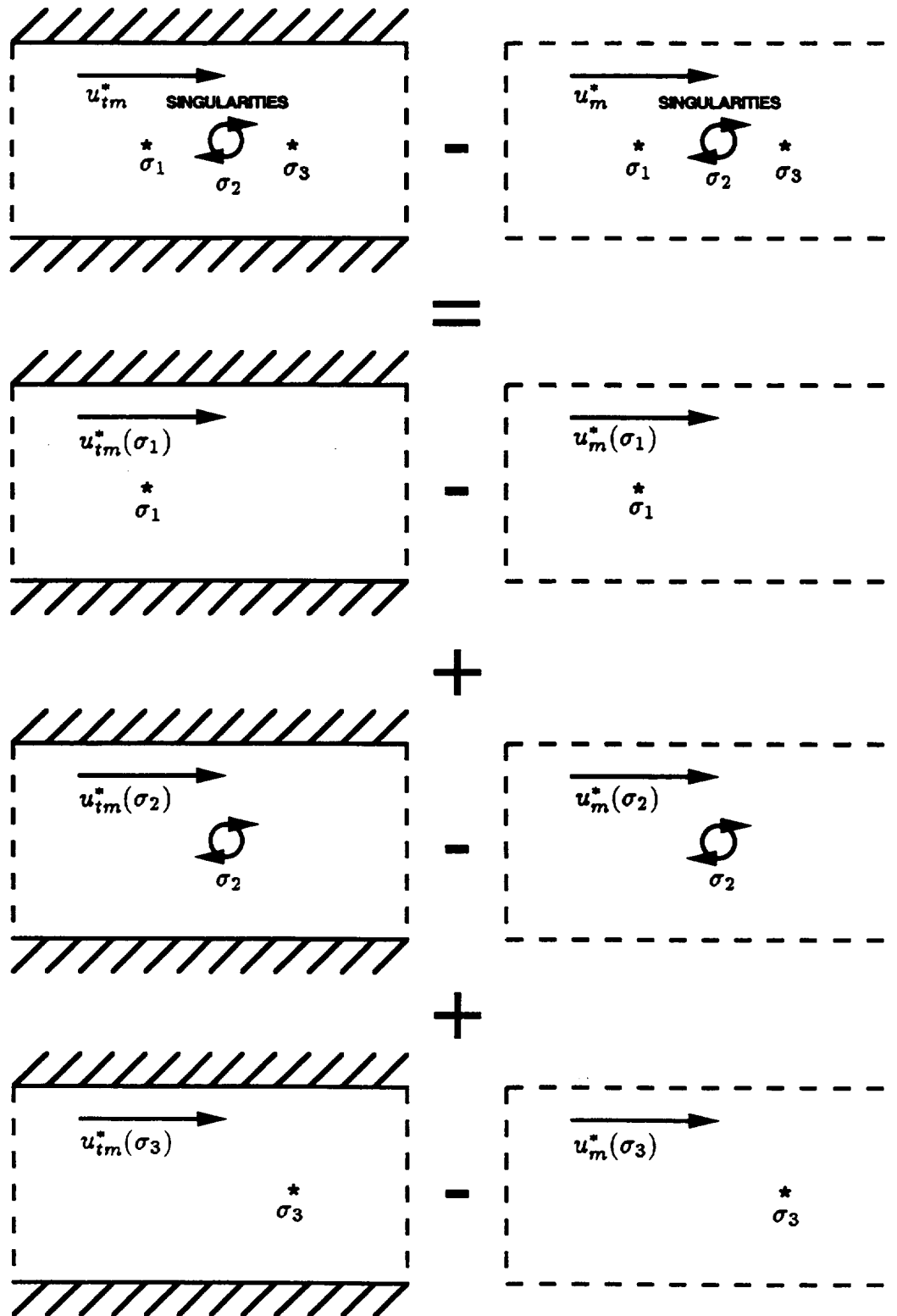


Fig. 4 Application of Principle of Superposition to Wall Interference Flow Field.

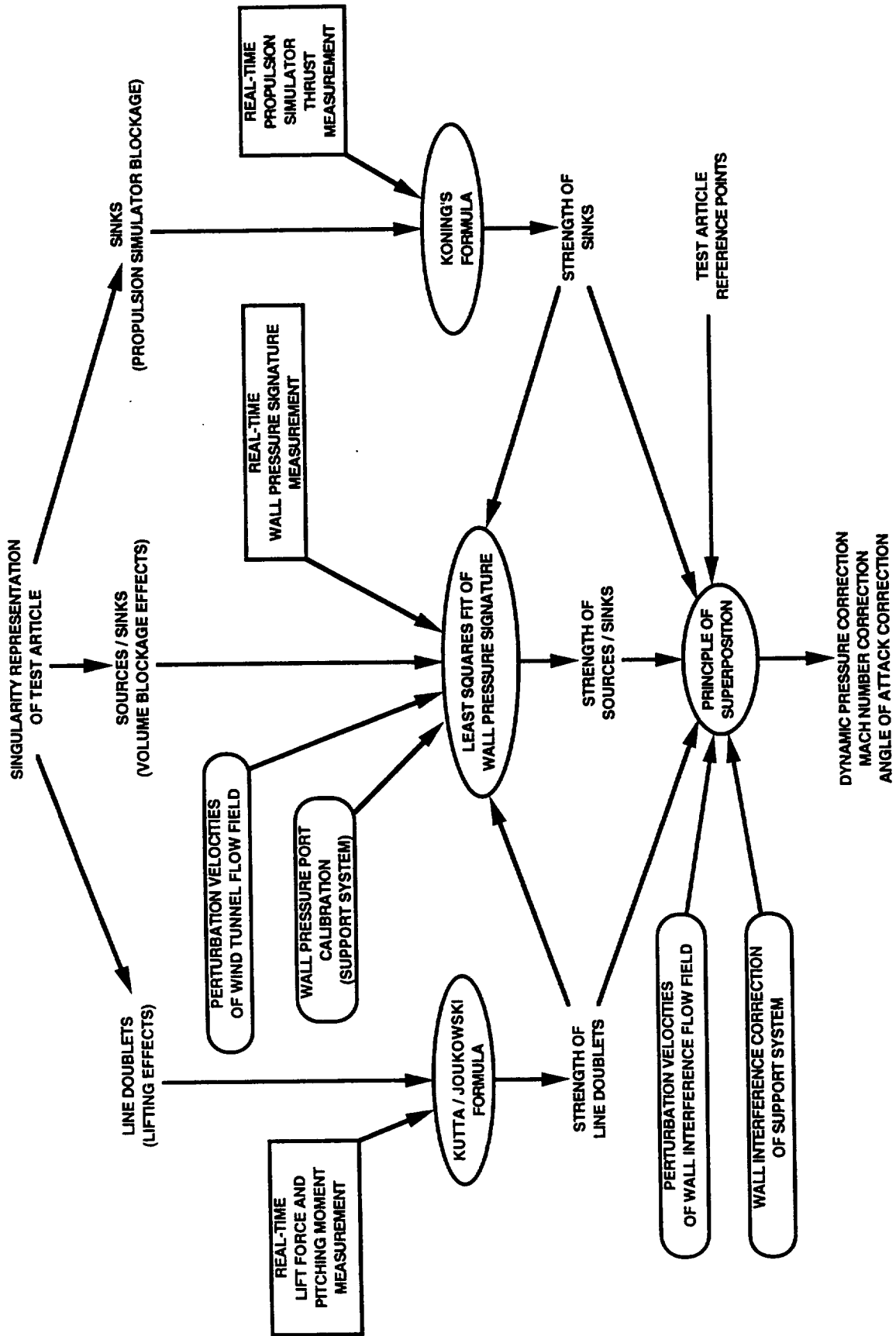


Fig. 5a Wall Interference Calculation of Fullspan Model.

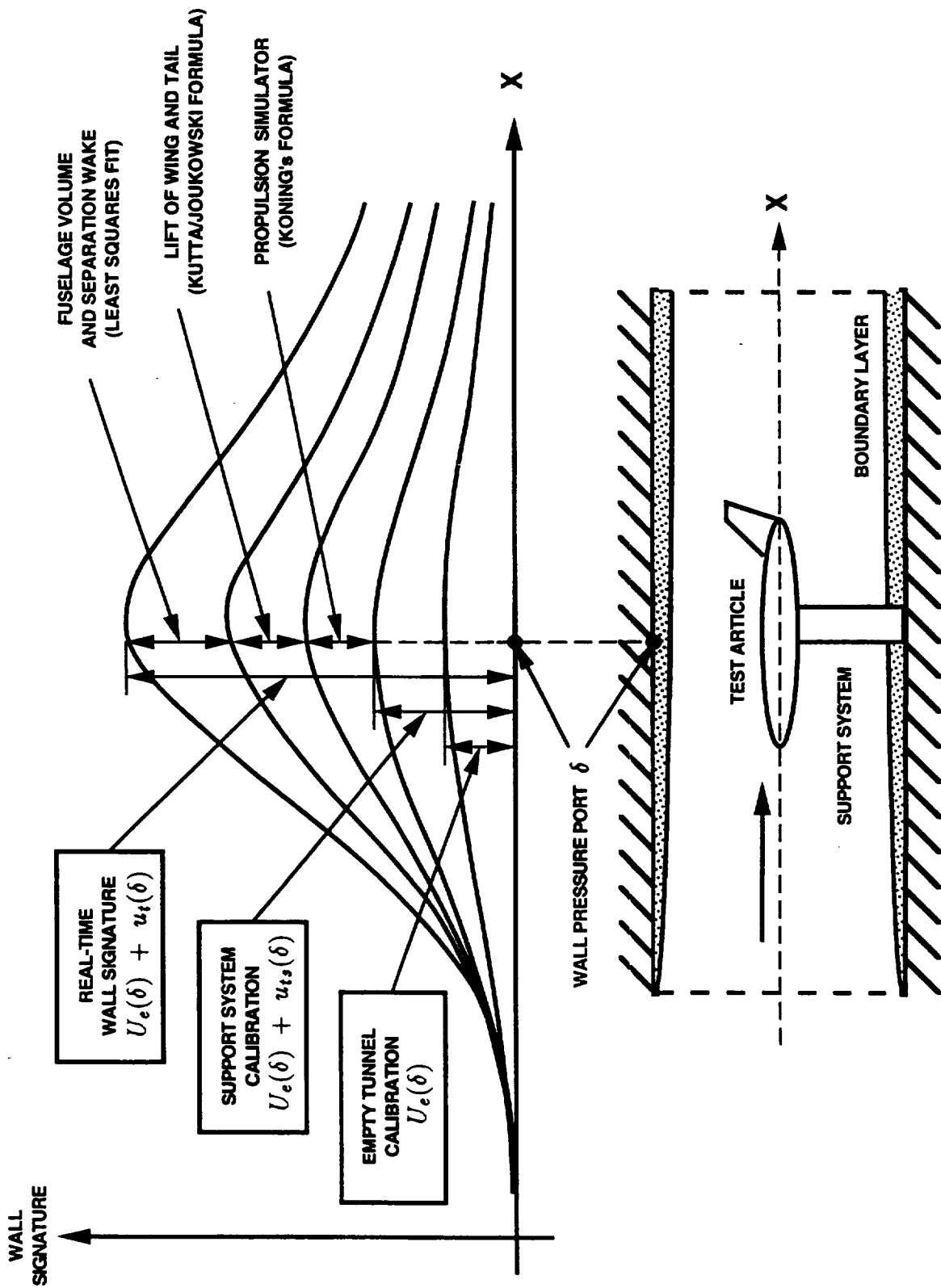


Fig. 5b Least Squares Fit of Wall Signature of Fullspan Model.

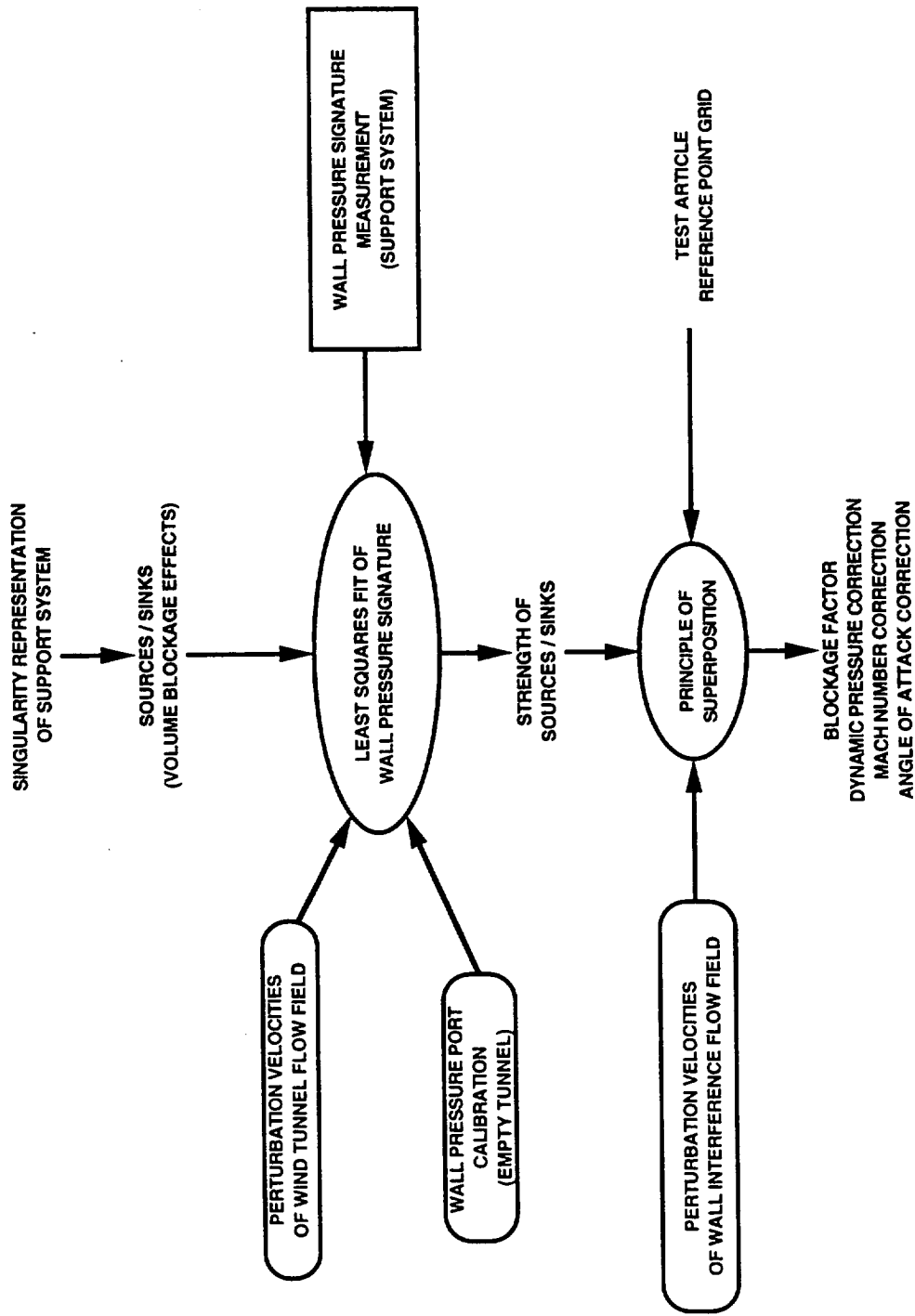


Fig. 6a Wall Interference Calculation of Support System.

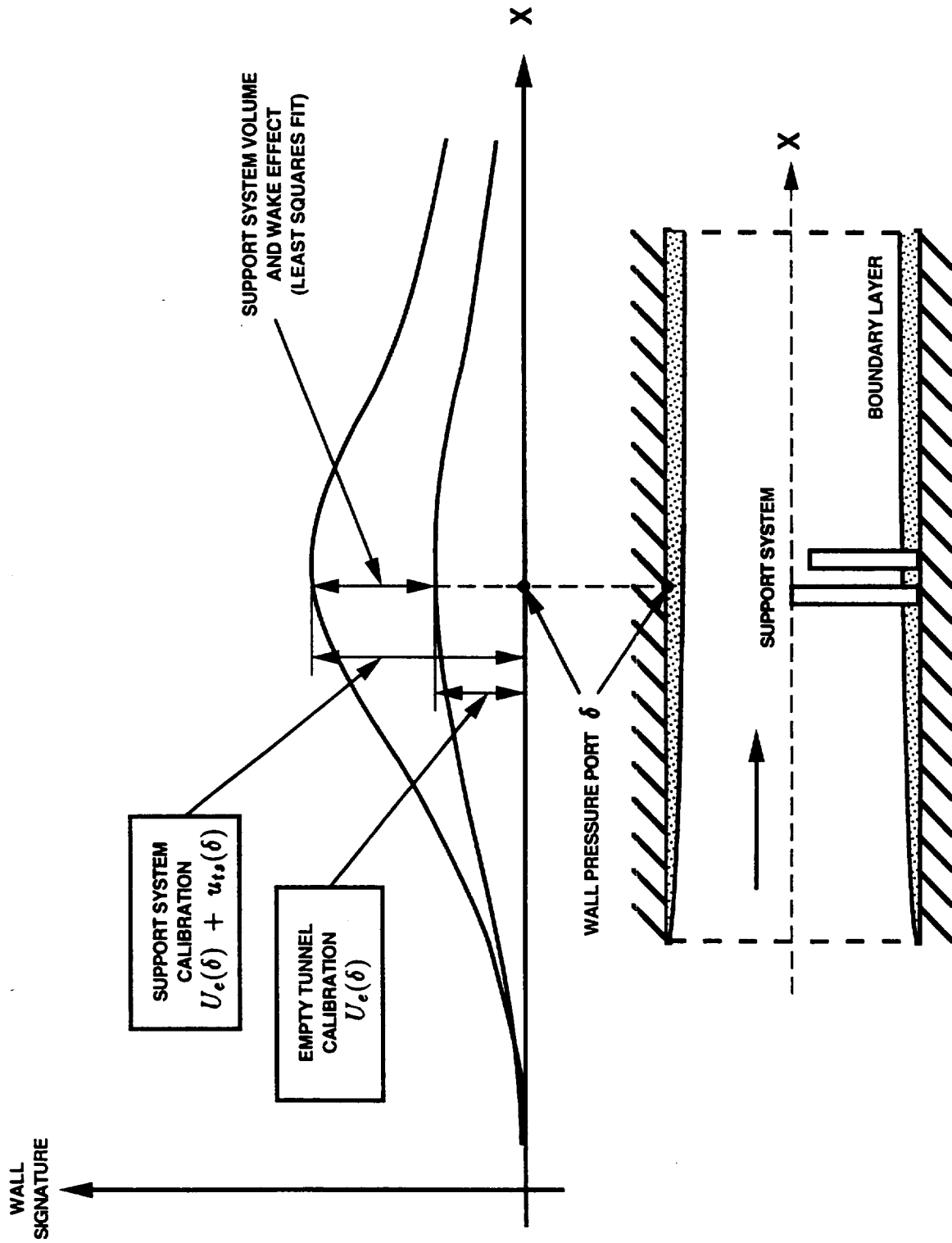


Fig. 6b Least Squares Fit of Wall Signature of Support System.

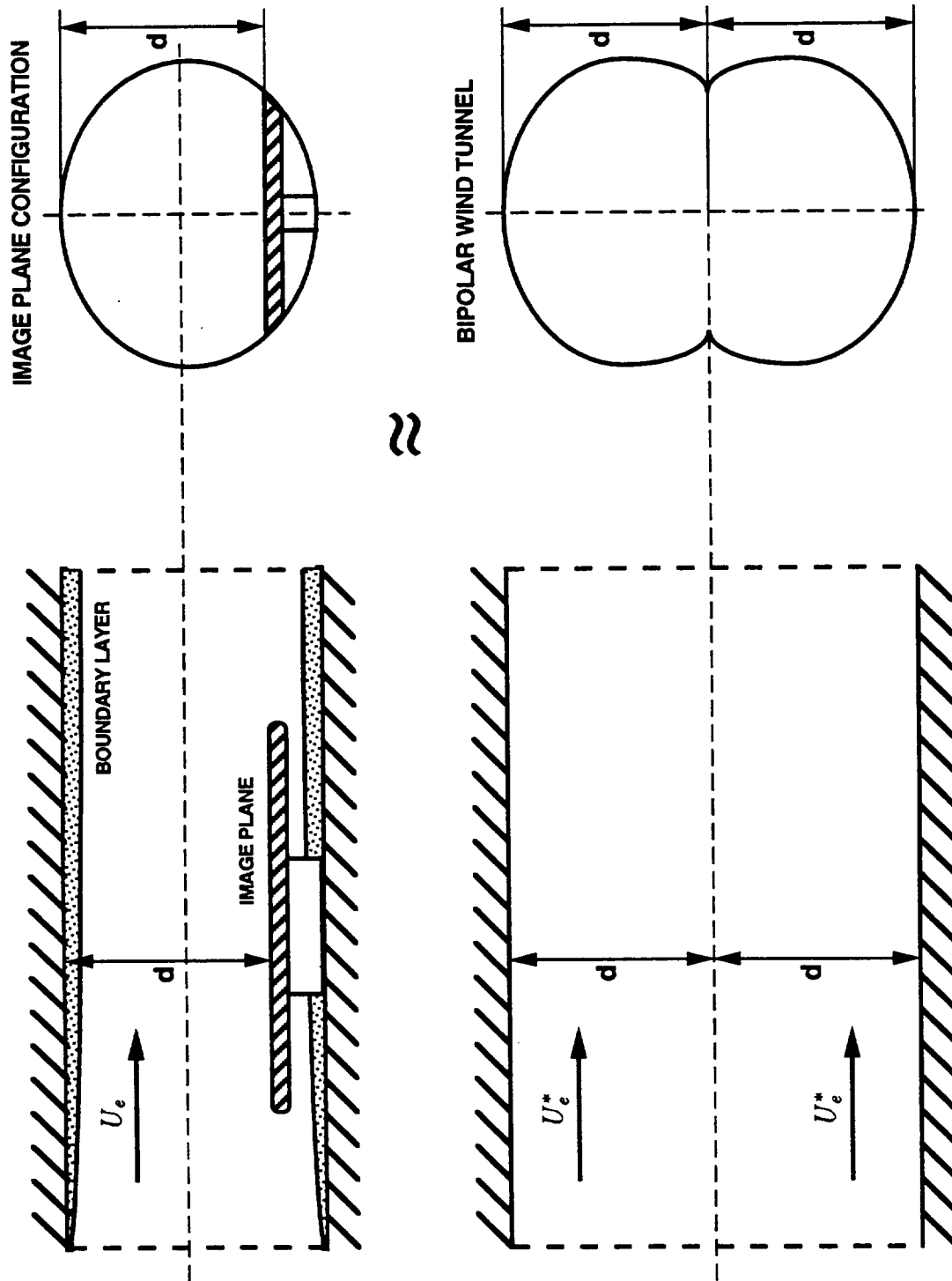


Fig. 7 Bipolar Wind Tunnel Approximation of Image Plane Configuration.

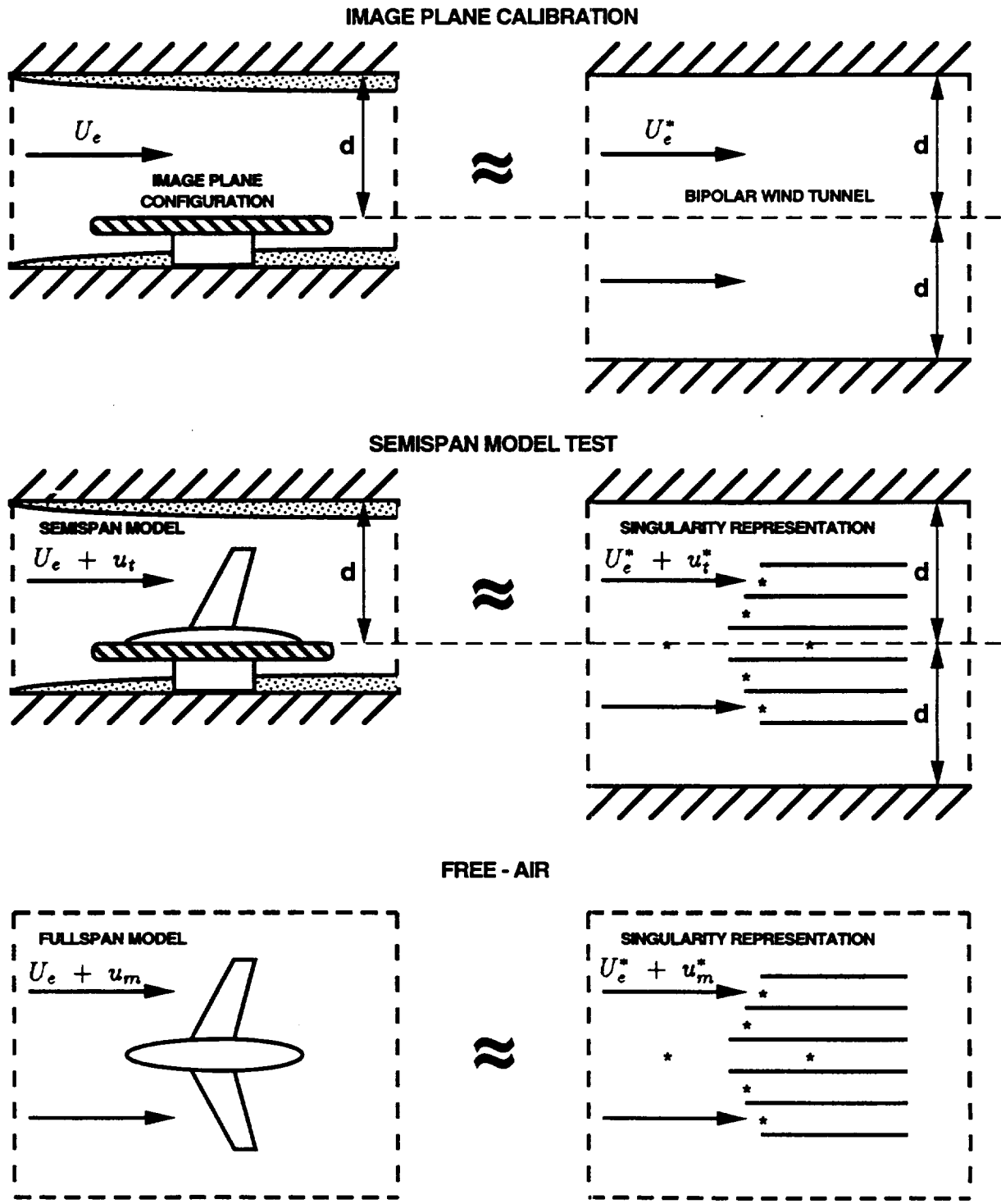


Fig. 8 Singularity Representation of Semispan Model.

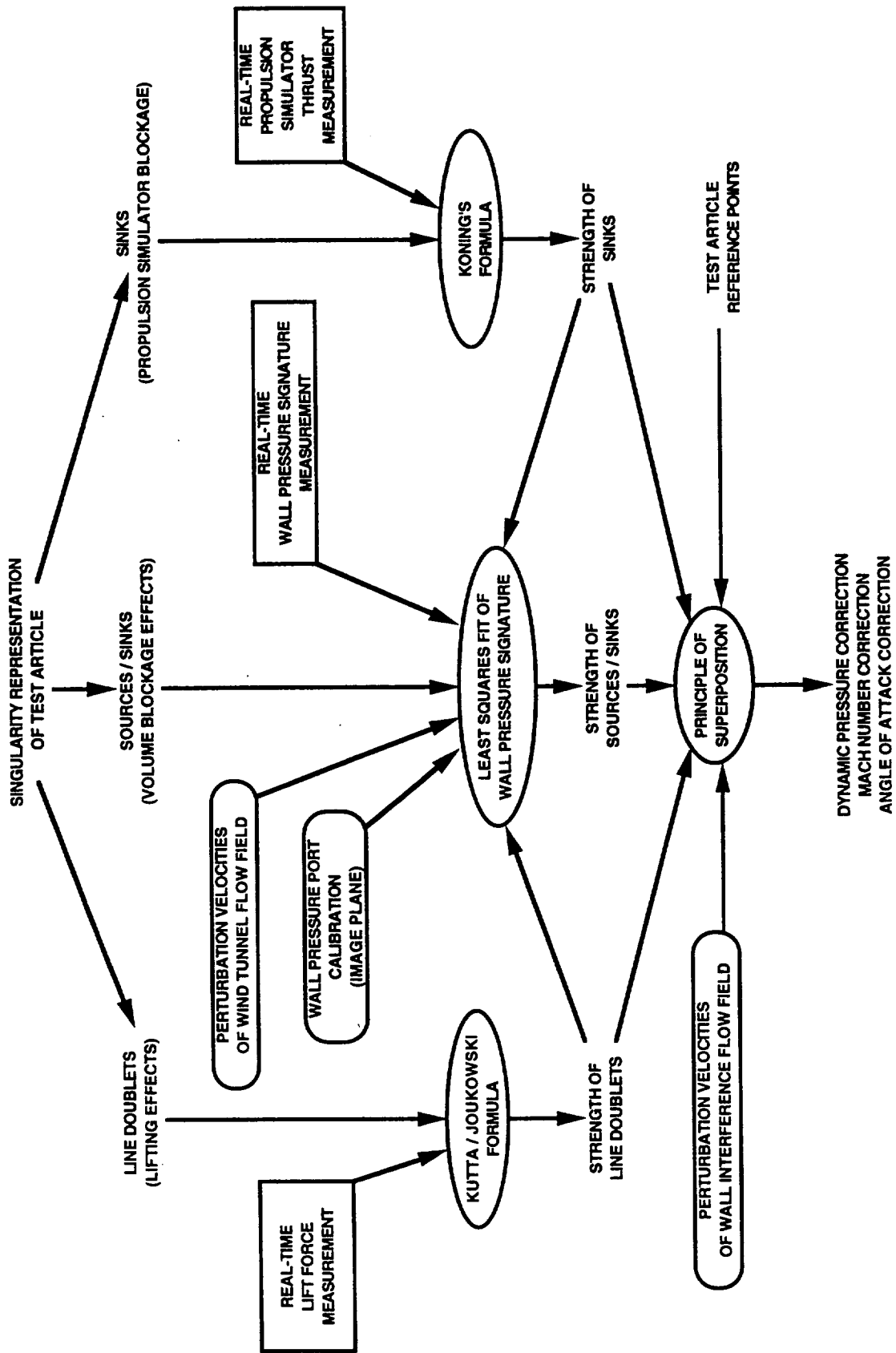


Fig. 9a Wall Interference Calculation of Semispan Model.

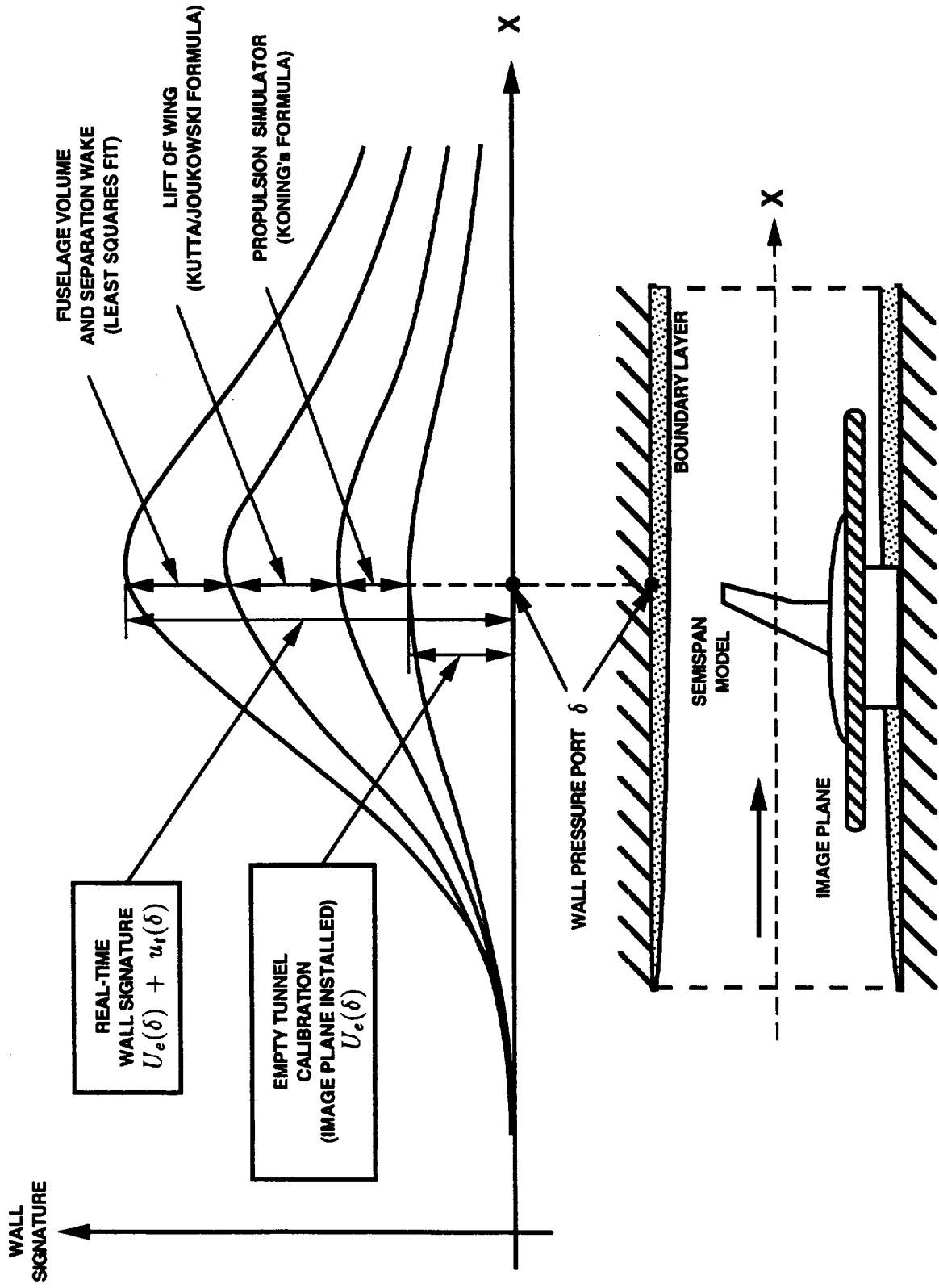


Fig. 9b Least Squares Fit of Wall Signature of Semispan Model.

Point Source at $x = 118.0$ [ft] , $y = 3.0$ [ft] , $z = 2.0$ [ft]

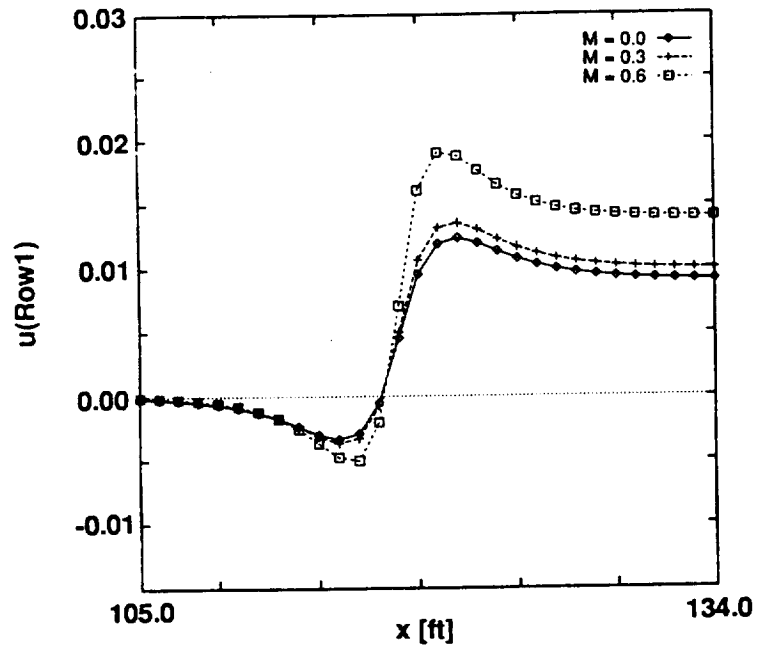


Fig. 10 Wall Signature of Point Source as Function of Mach Number.

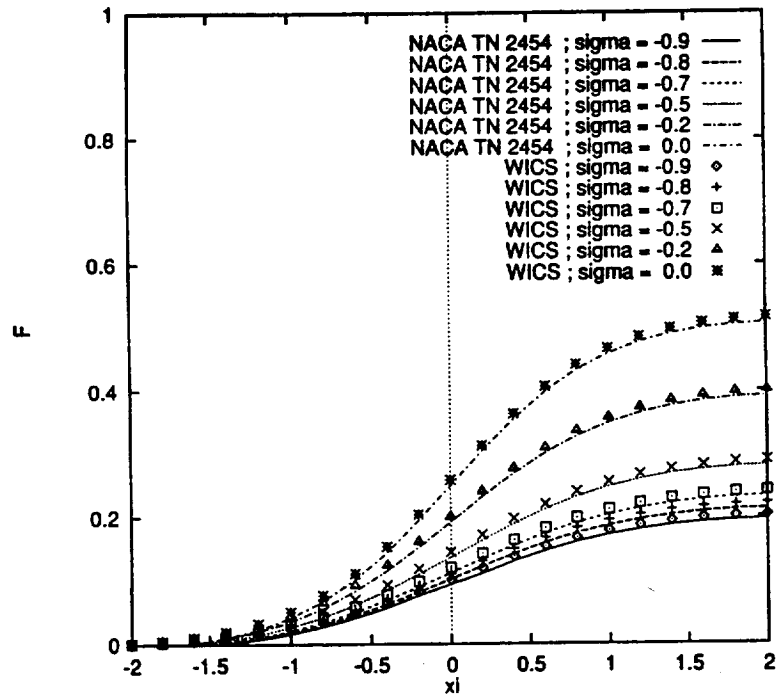


Fig. 11a Comparison Bessel Function Solution / Panel Code Solution (WICS).

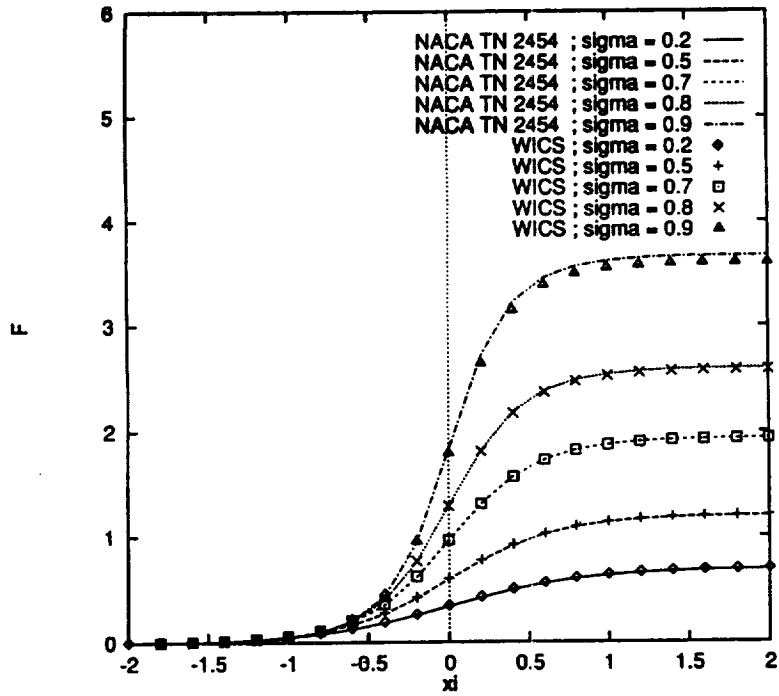


Fig. 11b Comparison Bessel Function Solution / Panel Code Solution (WICS).

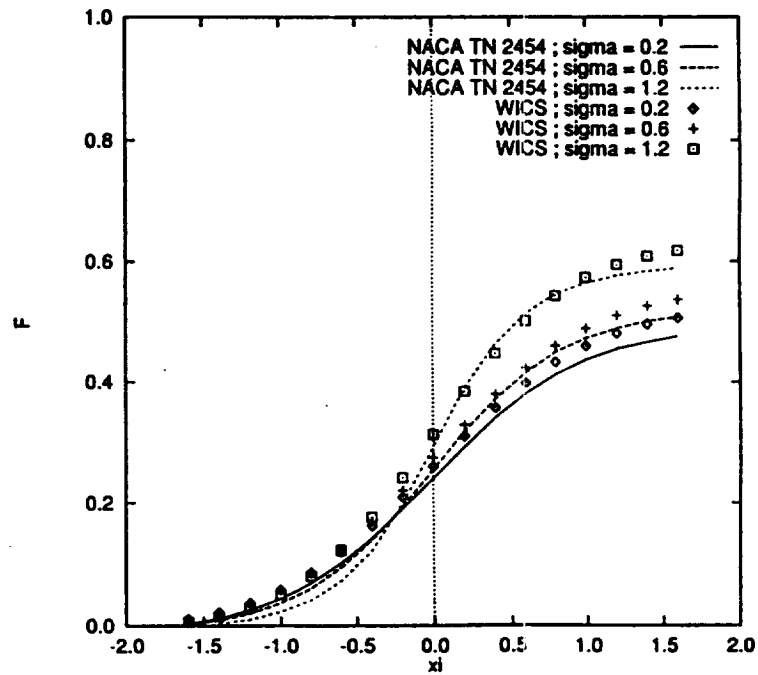


Fig. 11c Comparison NACA TN 2454 Approximation / Panel Code Solution (WICS).

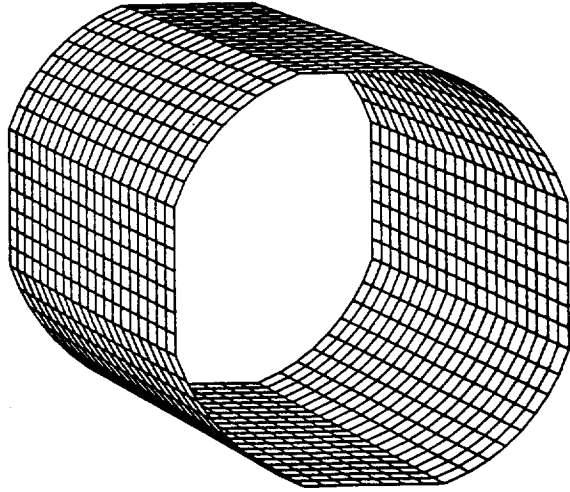


Fig. 12a Panel Model of Wind Tunnel Geometry / Fullspan Model Configuration.

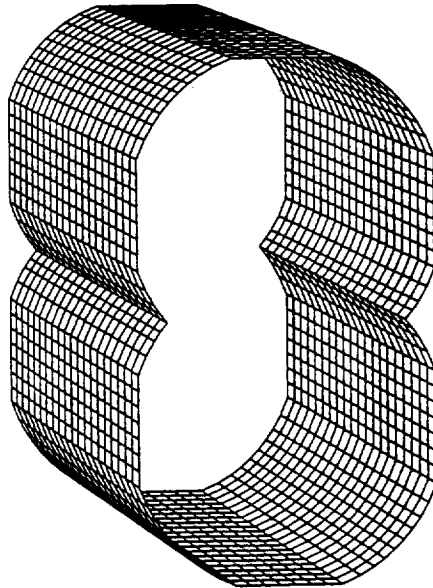


Fig. 12b Panel Model of Wind Tunnel Geometry / Semispan Model Configuration.

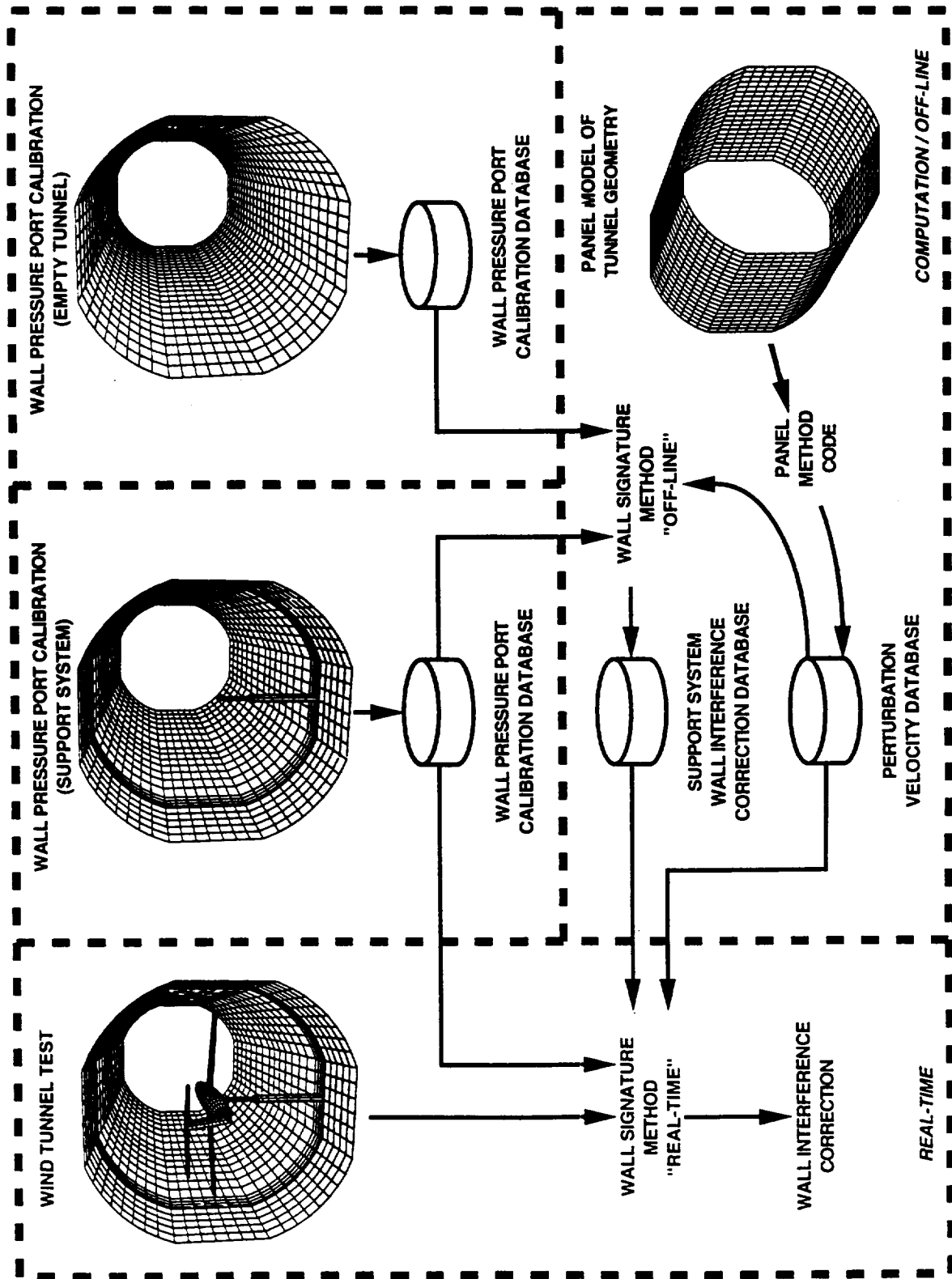


Fig. 13a Real-Time Wall Interference Correction System / Fullspan Model Configuration.

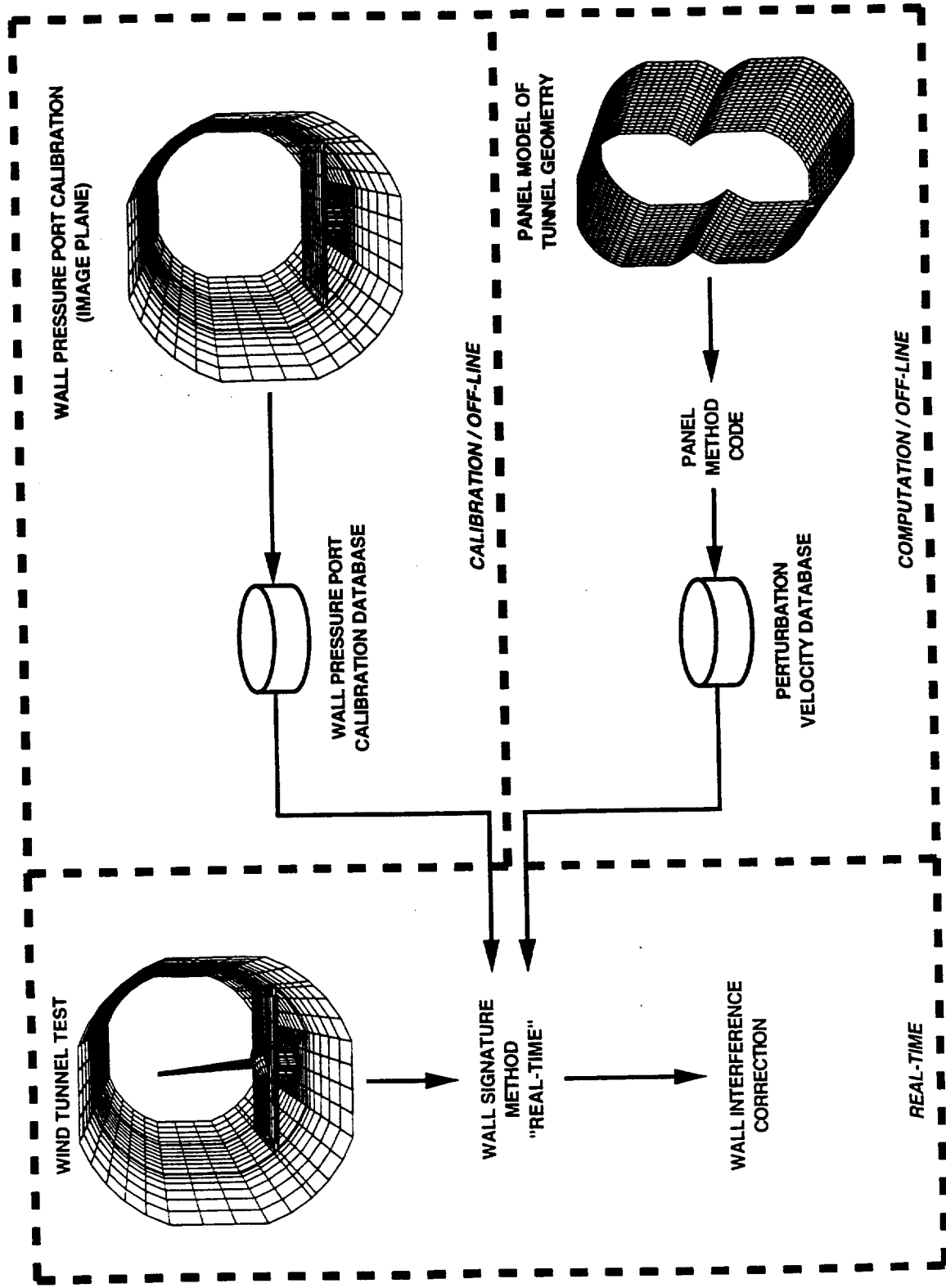


Fig. 13b Real-Time Wall Interference Correction System / Semispan Model Configuration.

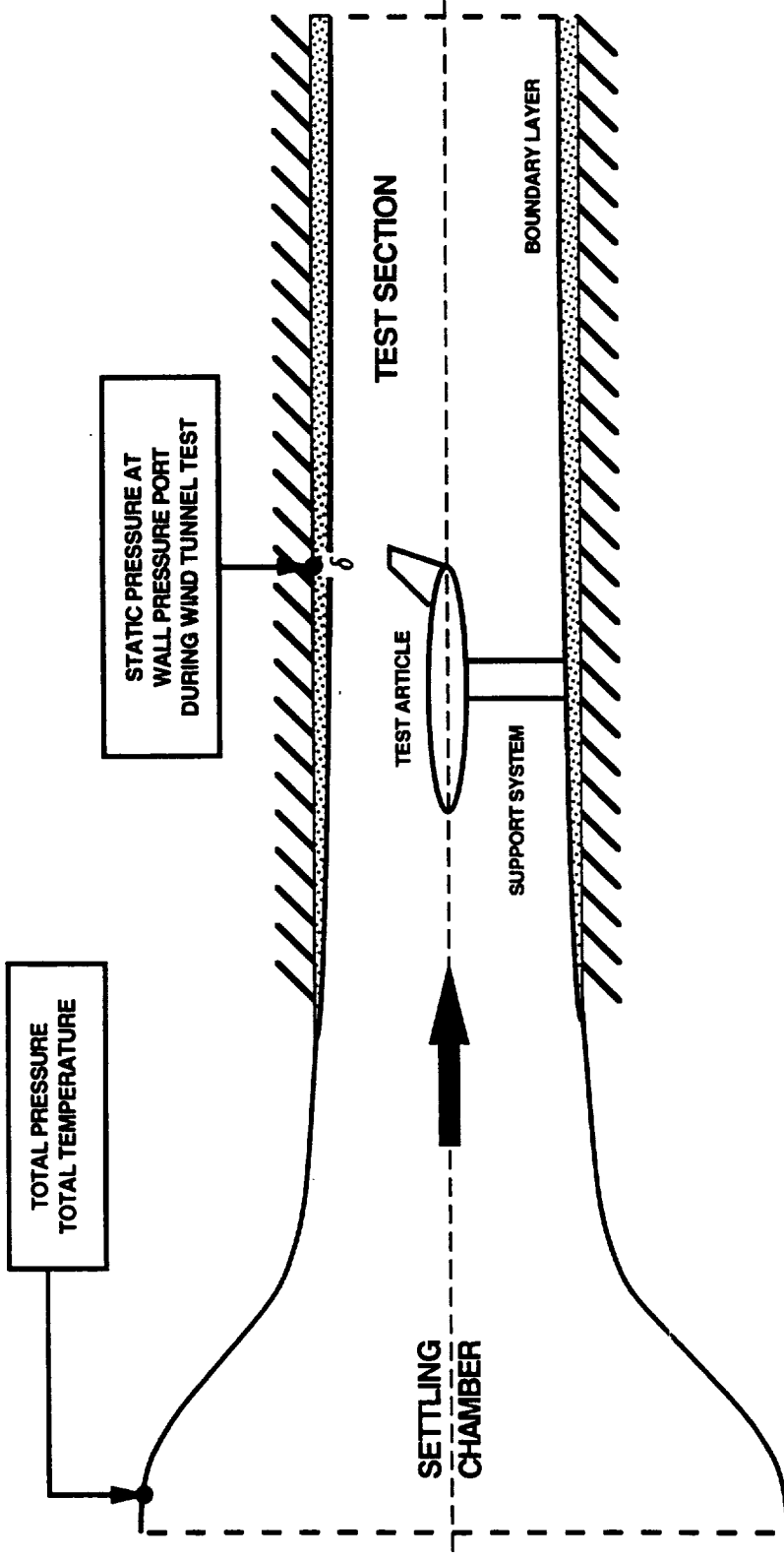


Fig. 14a Pressure / Temperature Measurement during Wind Tunnel Test.

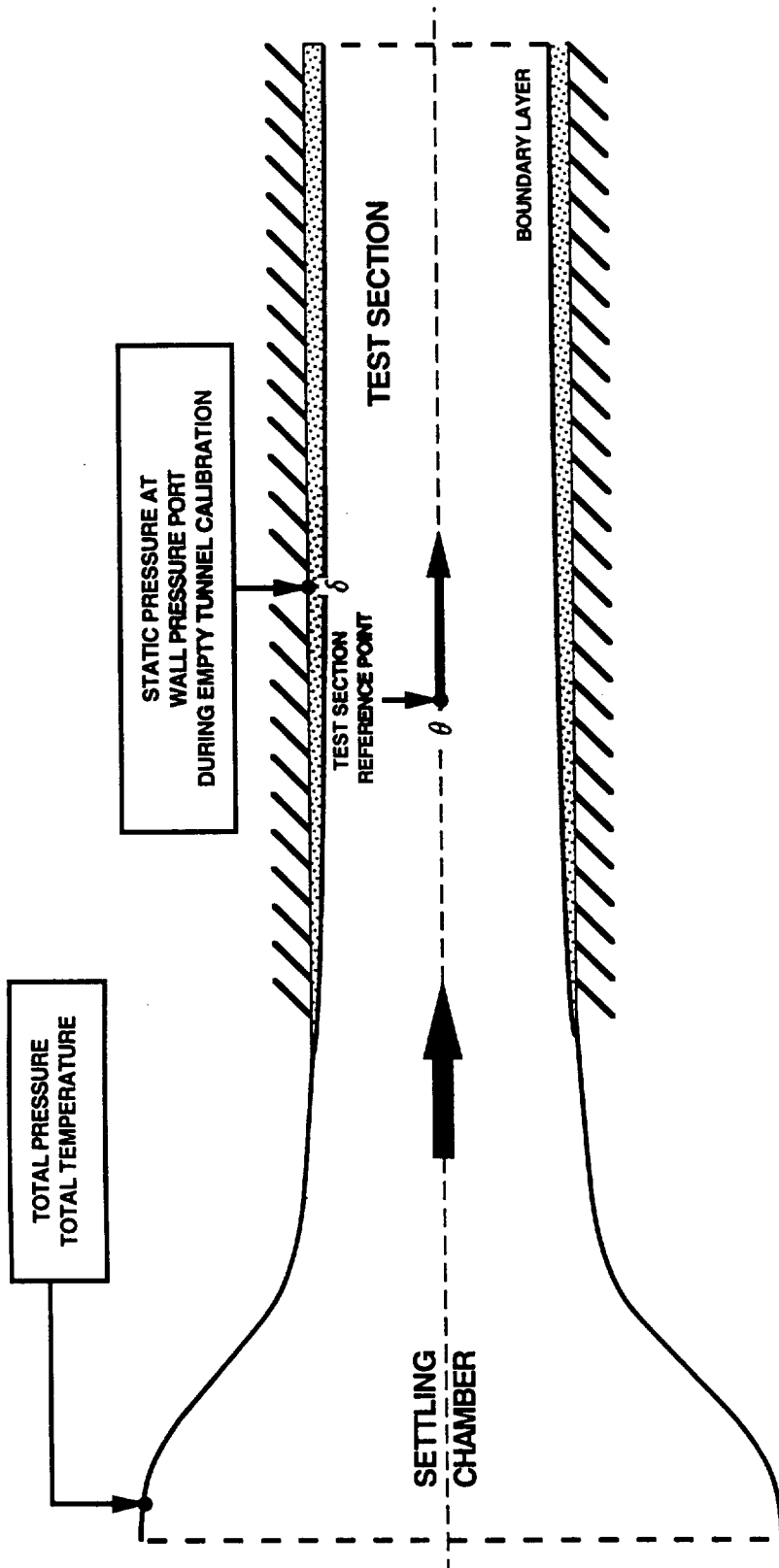


Fig. 14b Pressure / Temperature Measurement during Calibration.

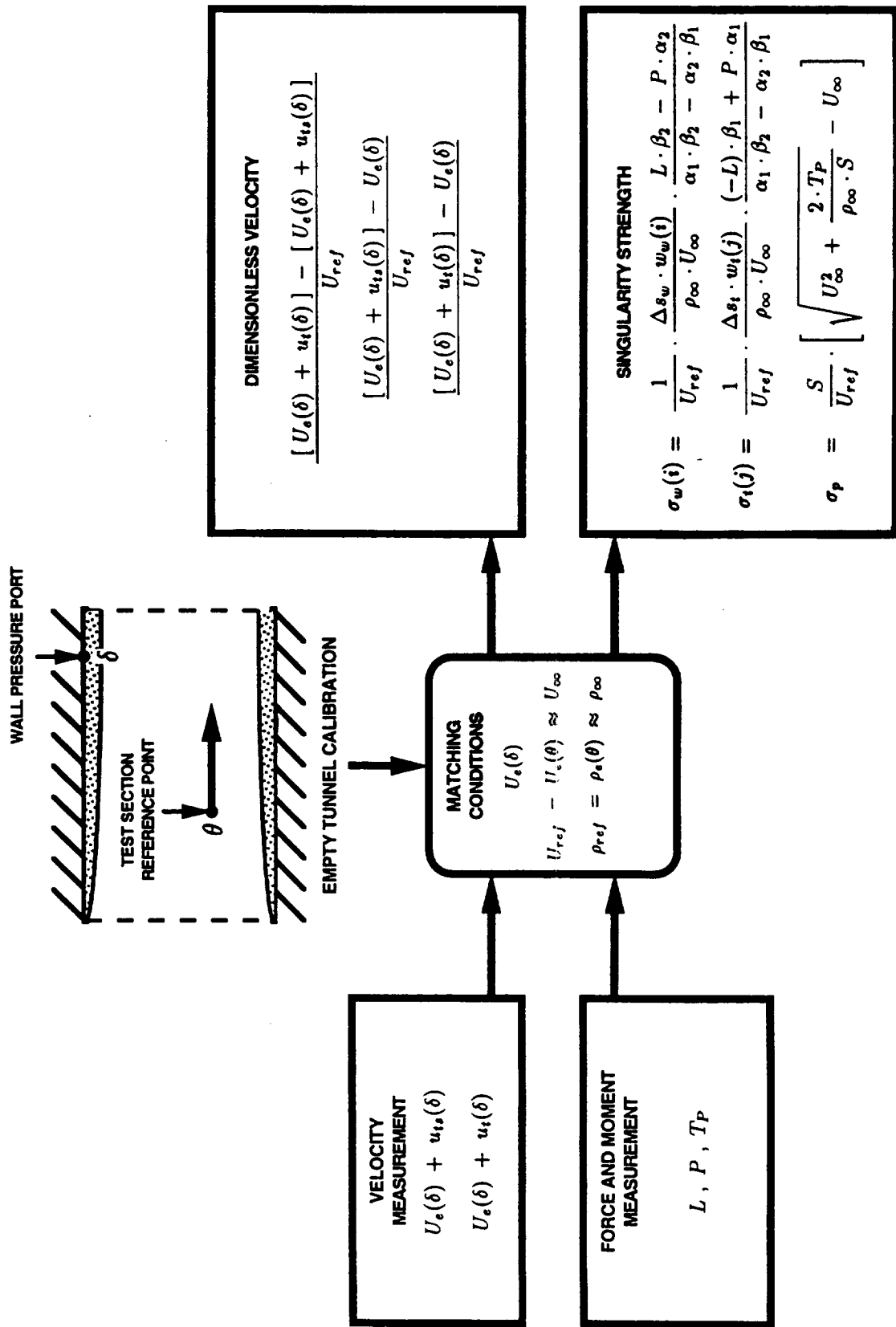


Fig. 14c Application of Matching Conditions to Velocity, Force, and Moment Measurements.

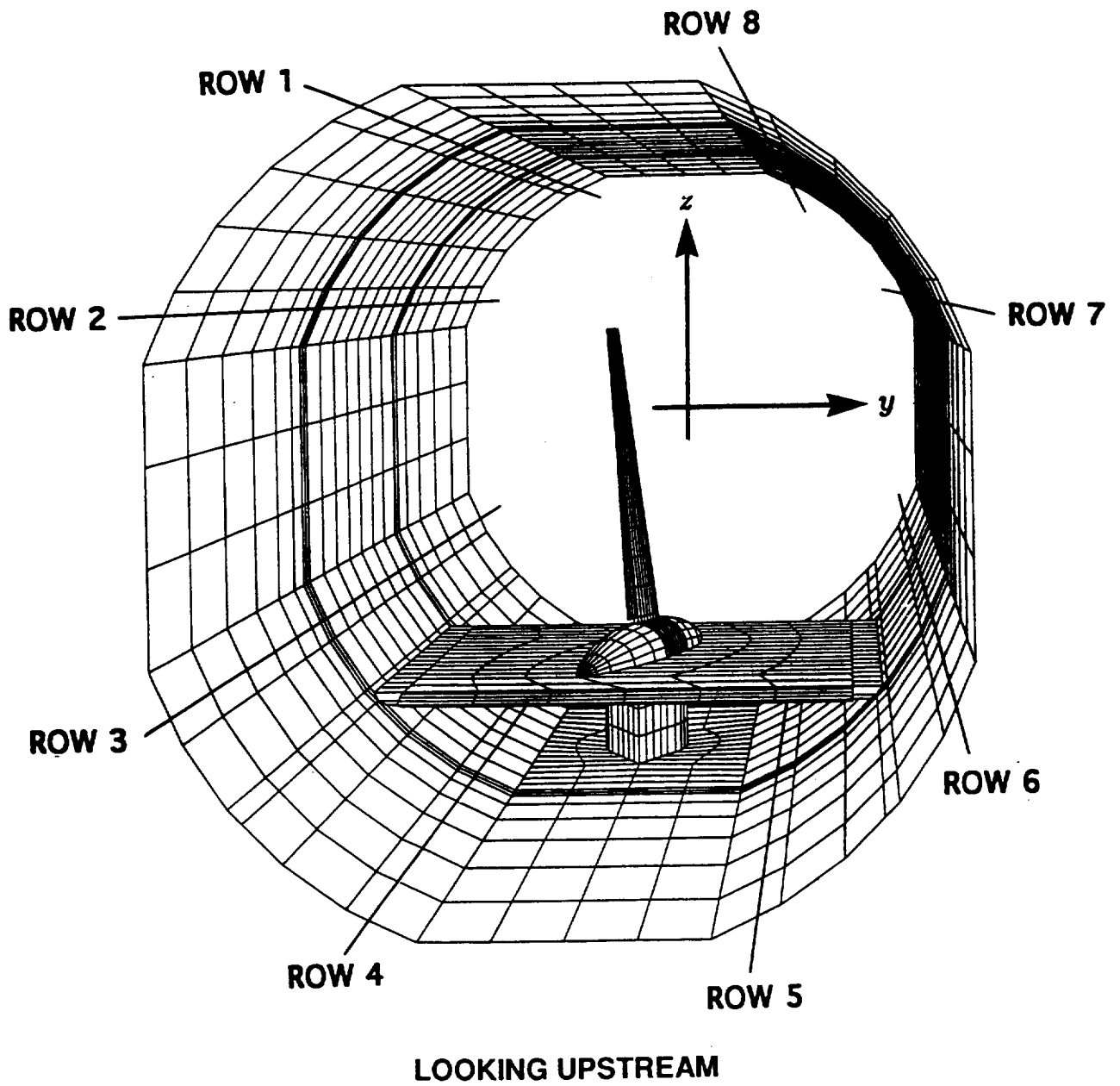
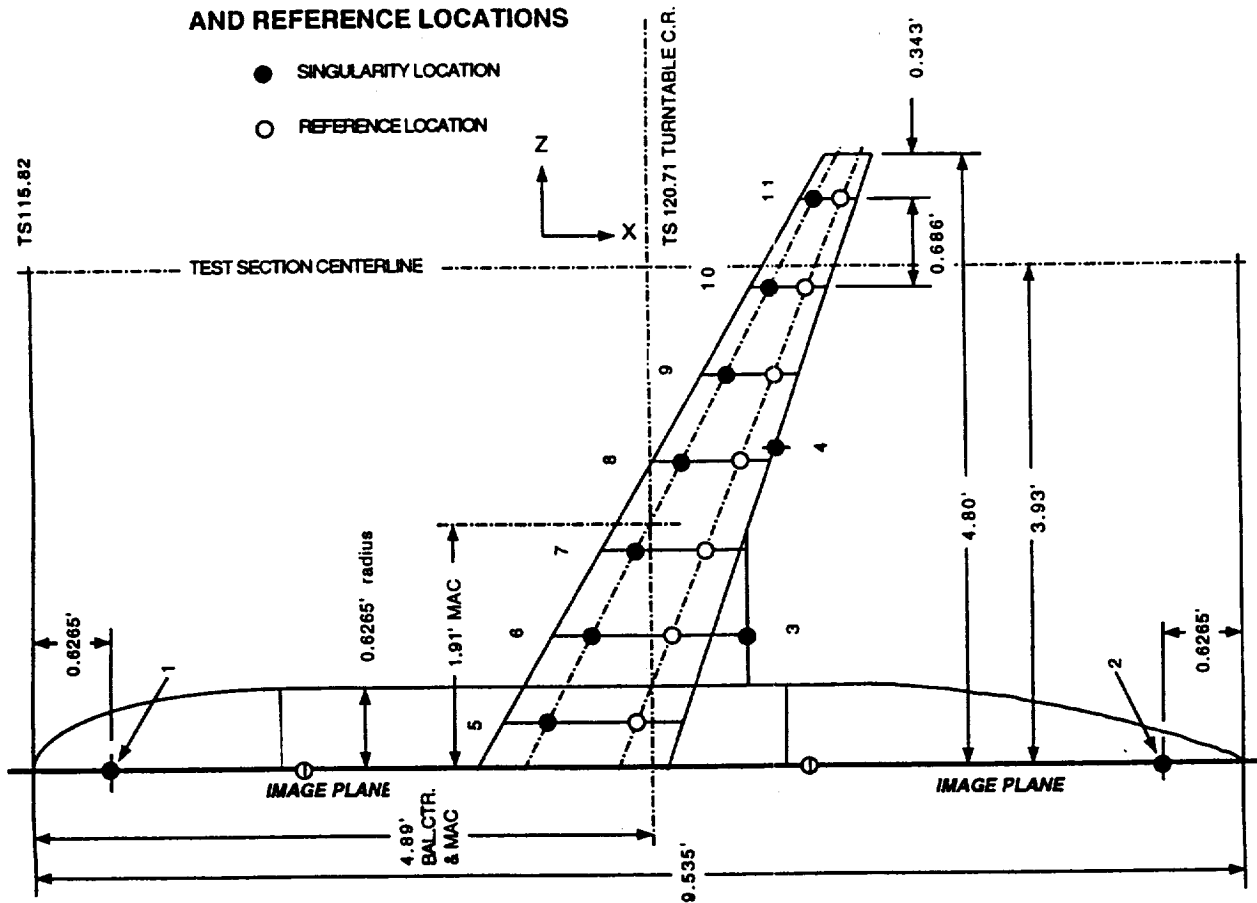


Fig. 15 Testsection, Semispan Model, and Image Plane Geometry.

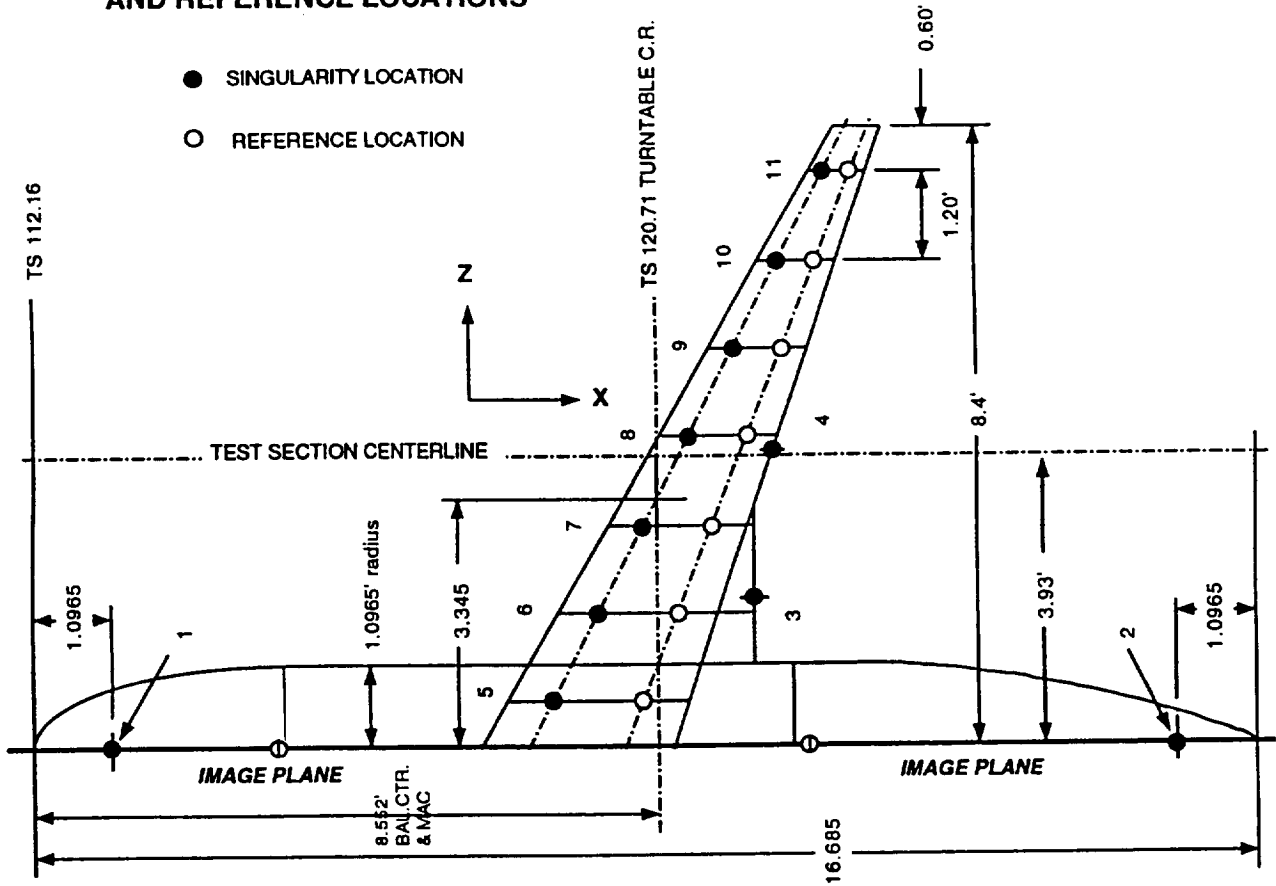
**7J7 8% SEMI-SPAN SINGULARITY
AND REFERENCE LOCATIONS**



No.	Type	x [ft]	y [ft]	z [ft]	Weight
1	SOURCE	116.45	0.000	-3.920	1.000
2	SINK	124.73	0.000	-3.920	-1.000
3	SOURCE	121.47	0.000	-2.930	1.000
4	SOURCE	121.69	0.000	-1.430	1.000
5	LINE DOUBLET	119.89	0.000	-3.587	0.997
6	LINE DOUBLET	120.25	0.000	-2.901	0.977
7	LINE DOUBLET	120.60	0.000	-2.216	0.934
8	LINE DOUBLET	120.96	0.000	-1.530	0.866
9	LINE DOUBLET	121.32	0.000	-0.844	0.766
10	LINE DOUBLET	121.68	0.000	-0.159	0.619
11	LINE DOUBLET	122.03	0.000	0.527	0.371

Fig. 16a Singularity Representation of Boeing 7J7 8% Scale Semispan Model.

7J7 14% SEMI-SPAN SINGULARITY AND REFERENCE LOCATIONS



No.	Type	x [ft]	y [ft]	z [ft]	Weight
1	SOURCE	113.26	0.000	-3.920	1.000
2	SINK	127.75	0.000	-3.920	-1.000
3	SOURCE	122.04	0.000	-1.930	1.000
4	SOURCE	122.31	0.000	0.070	1.000
5	LINE DOUBLET	119.28	0.000	-3.330	0.997
6	LINE DOUBLET	119.90	0.000	-2.130	0.977
7	LINE DOUBLET	120.53	0.000	-0.930	0.934
8	LINE DOUBLET	121.16	0.000	0.270	0.866
9	LINE DOUBLET	121.78	0.000	1.470	0.766
10	LINE DOUBLET	122.41	0.000	2.670	0.619
11	LINE DOUBLET	123.03	0.000	3.870	0.371

Fig. 16b Singularity Representation of Boeing 7J7 14% Scale Semispan Model.

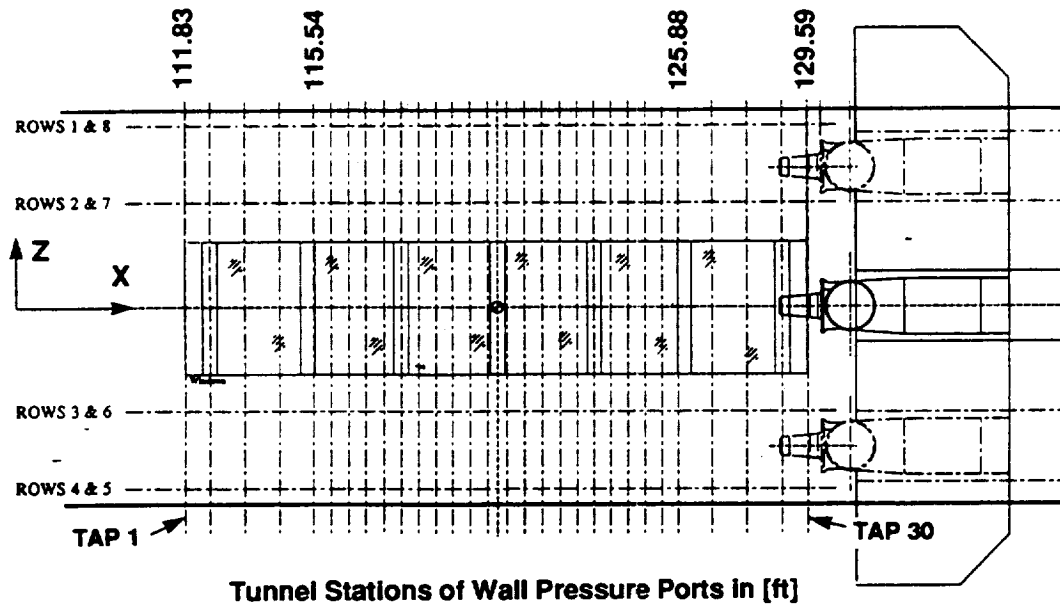


Fig. 17a Wall Pressure Port Location in 12ft Pressure Wind Tunnel.

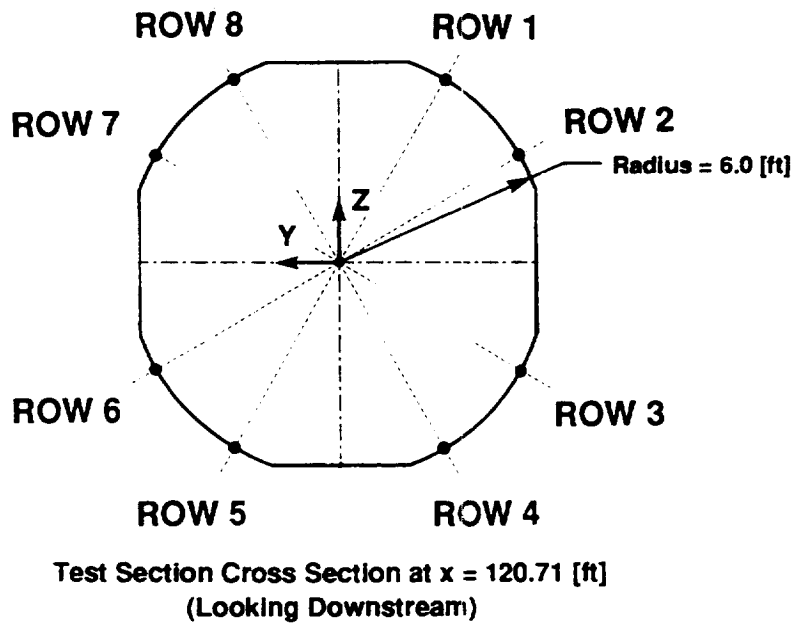


Fig. 17b Wall Pressure Port Row Definition in 12ft Pressure Wind Tunnel.

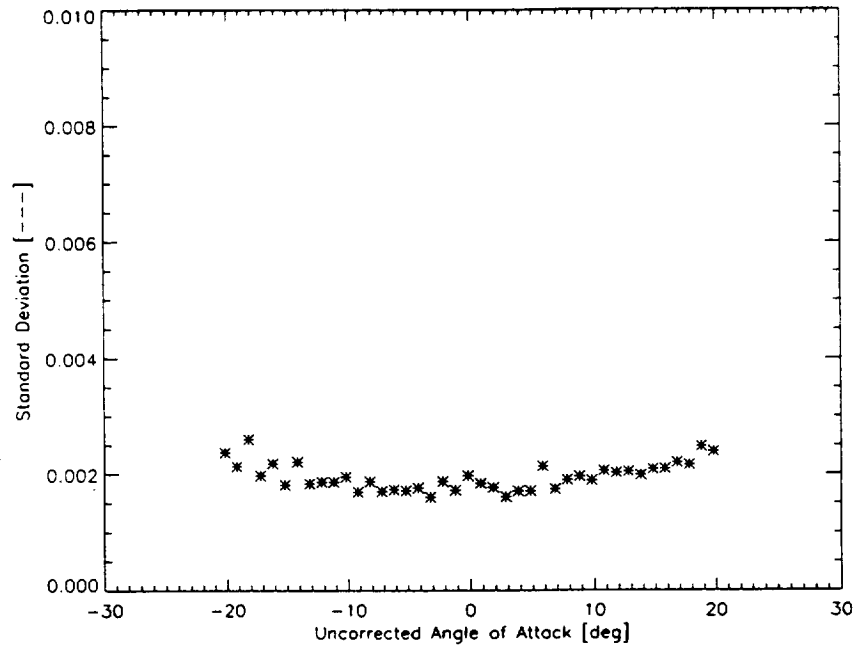


Fig. 18a Standard Deviation of Least Squares Fit of Wall Signature / 8% Scale Model.

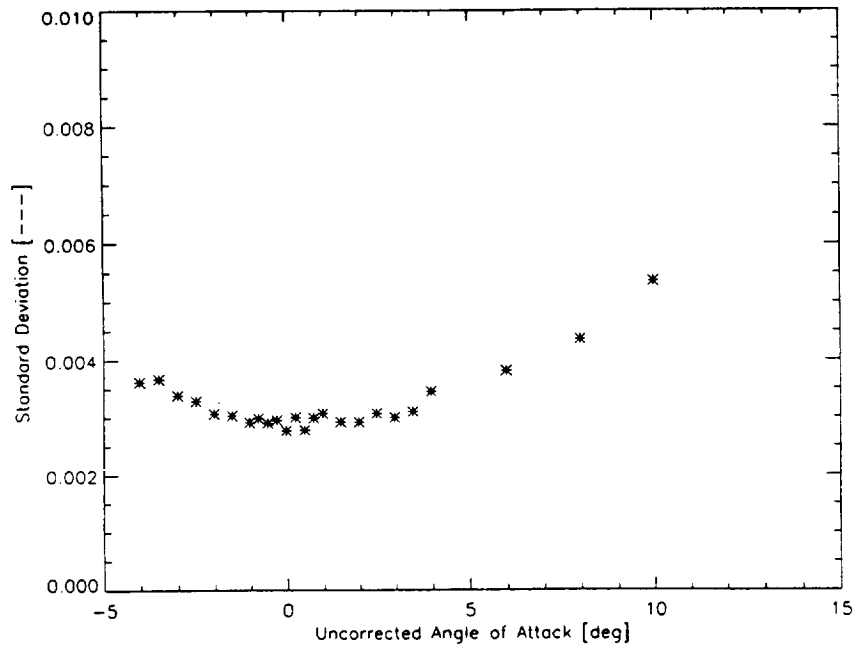


Fig. 18b Standard Deviation of Least Squares Fit of Wall Signature / 14% Scale Model.

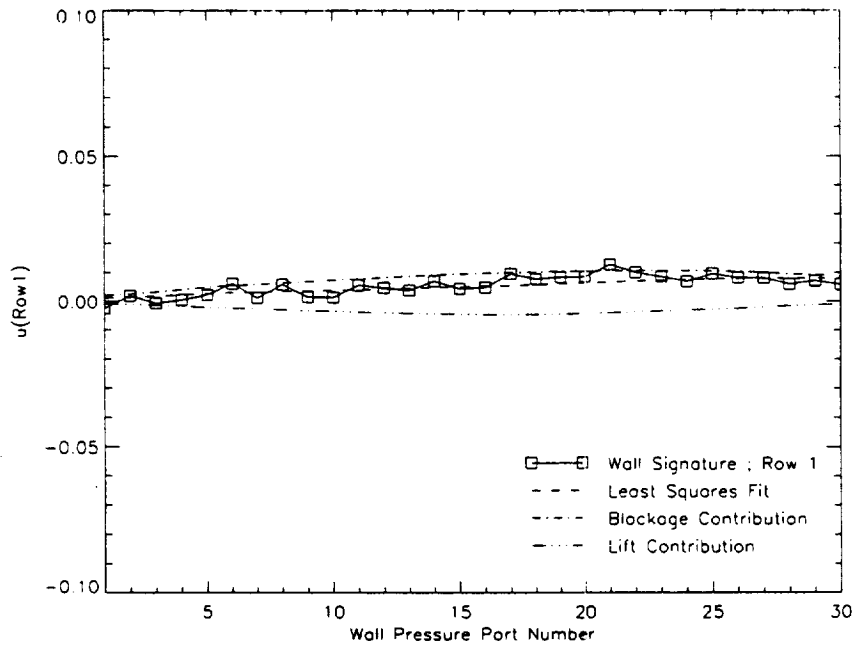


Fig. 19a Wall Signature at Row 1 / 8% Scale Model at 19.82[deg] Angle of Attack.

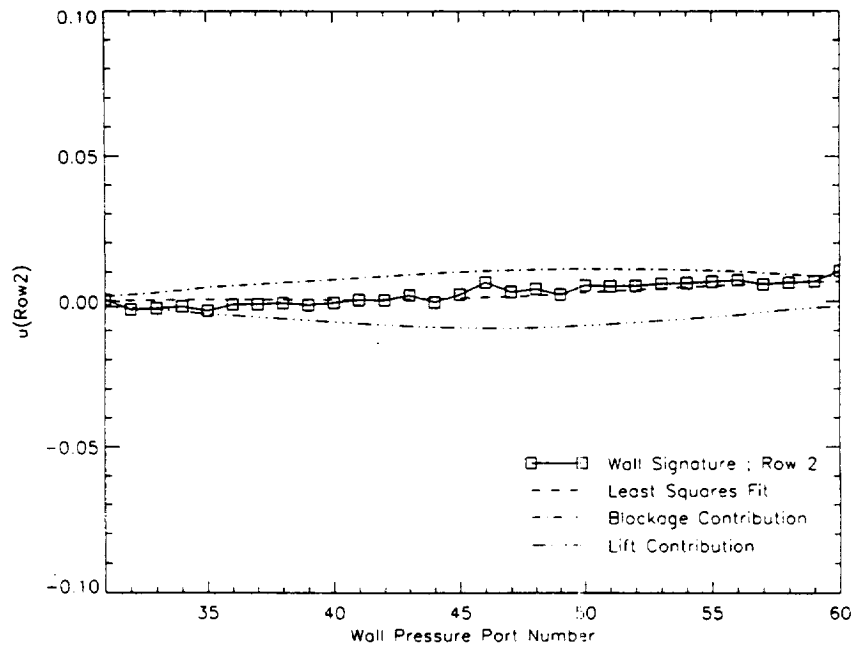


Fig. 19b Wall Signature at Row 2 / 8% Scale Model at 19.82[deg] Angle of Attack.

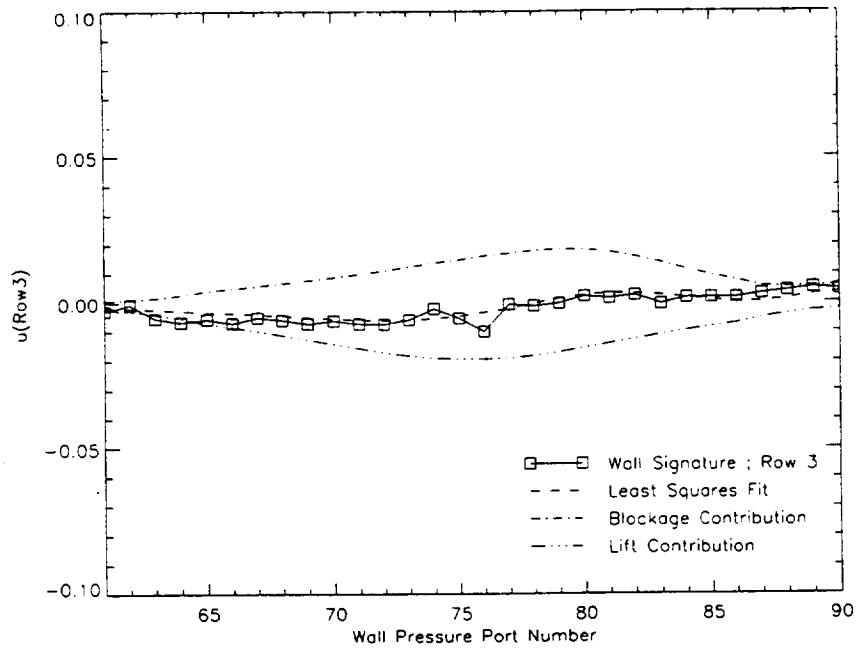


Fig. 19c Wall Signature at Row 3 / 8% Scale Model at 19.82[deg] Angle of Attack.

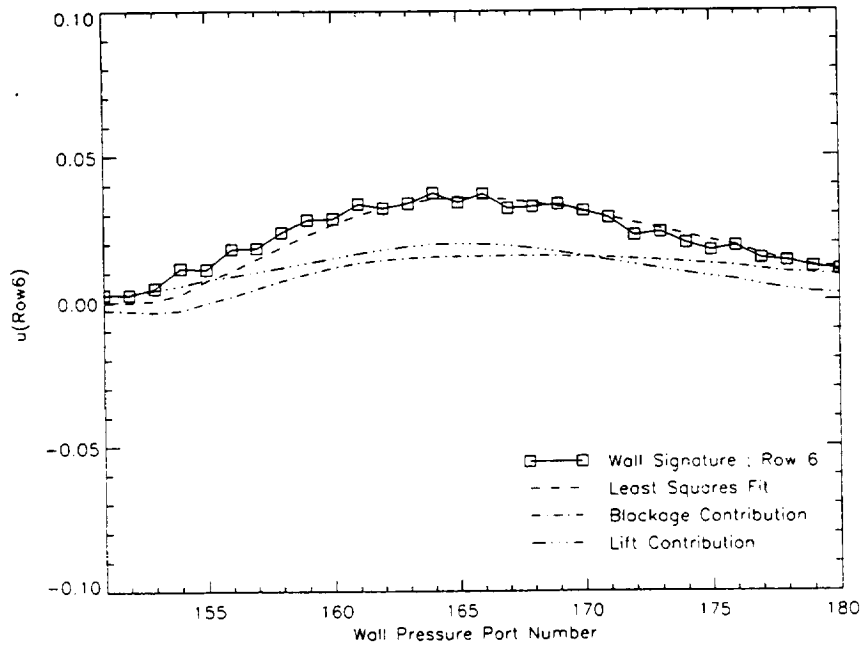


Fig. 19d Wall Signature at Row 6 / 8% Scale Model at 19.82[deg] Angle of Attack.

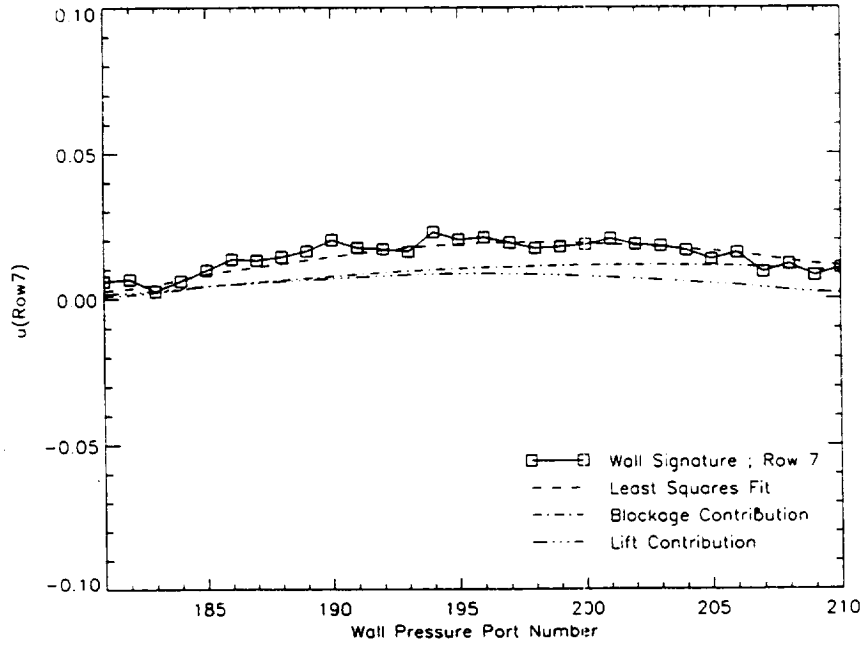


Fig. 19e Wall Signature at Row 7 / 8% Scale Model at 19.82[deg] Angle of Attack.

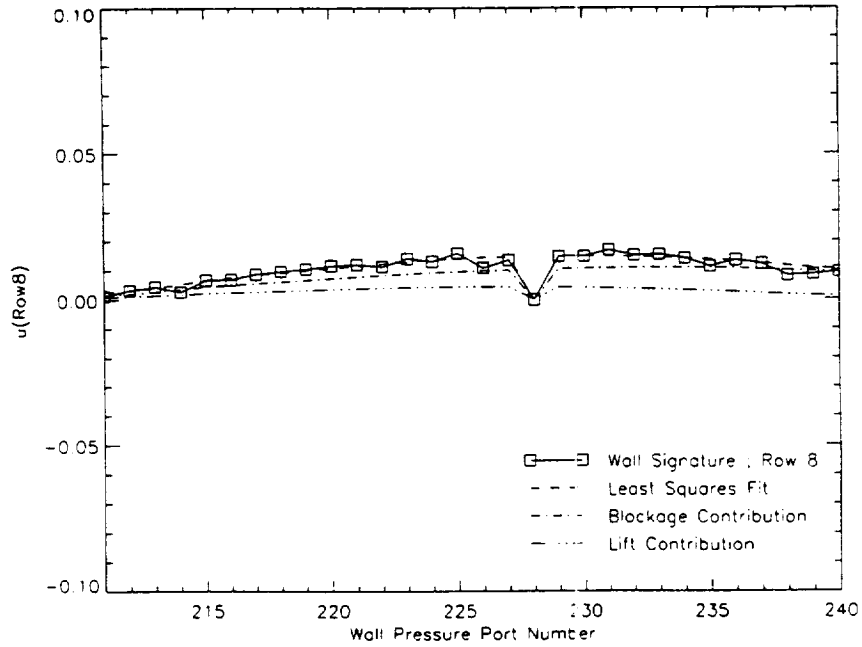


Fig. 19f Wall Signature at Row 8 / 8% Scale Model at 19.82[deg] Angle of Attack.

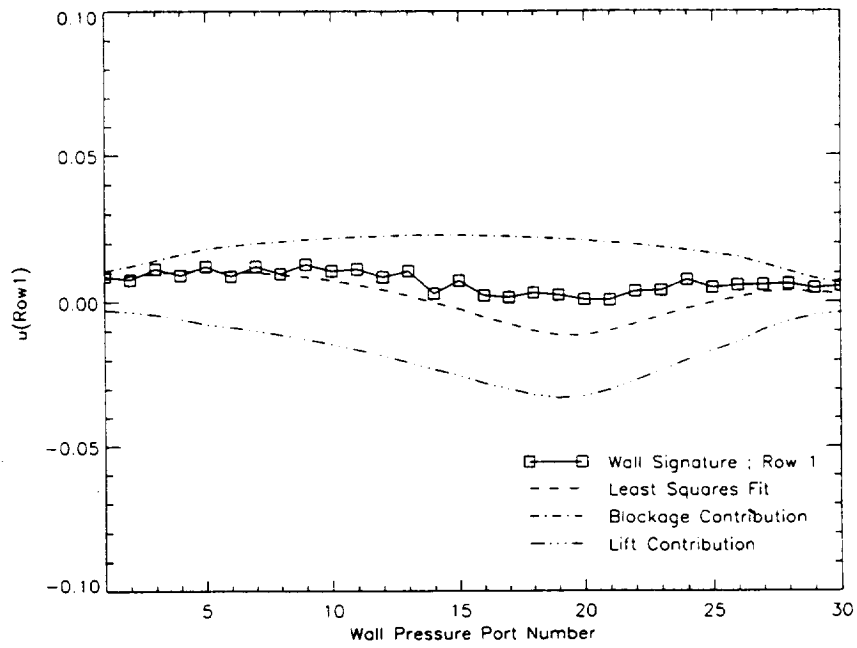


Fig. 20a Wall Signature at Row 1 / 14% Scale Model at 9.98[deg] Angle of Attack.

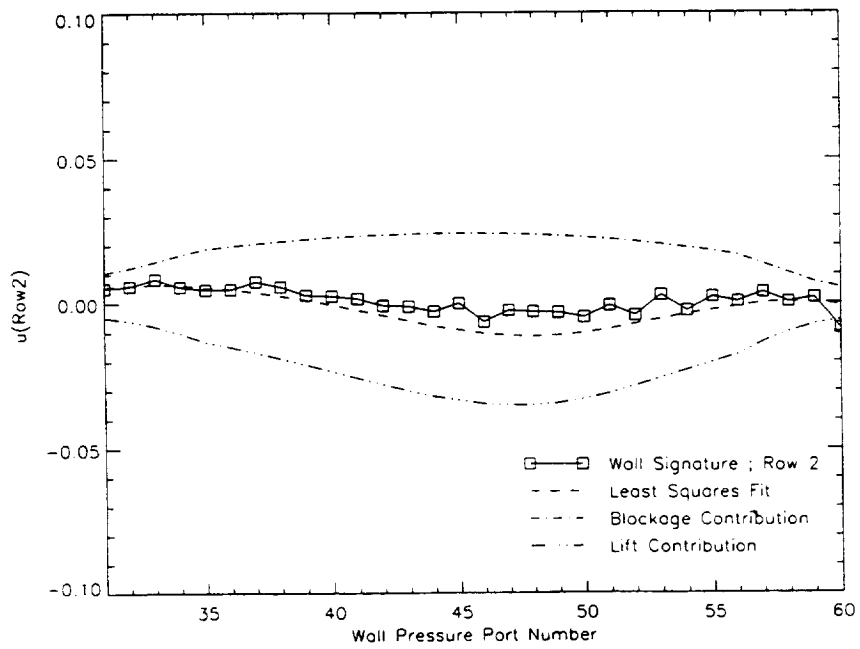


Fig. 20b Wall Signature at Row 2 / 14% Scale Model at 9.98[deg] Angle of Attack.

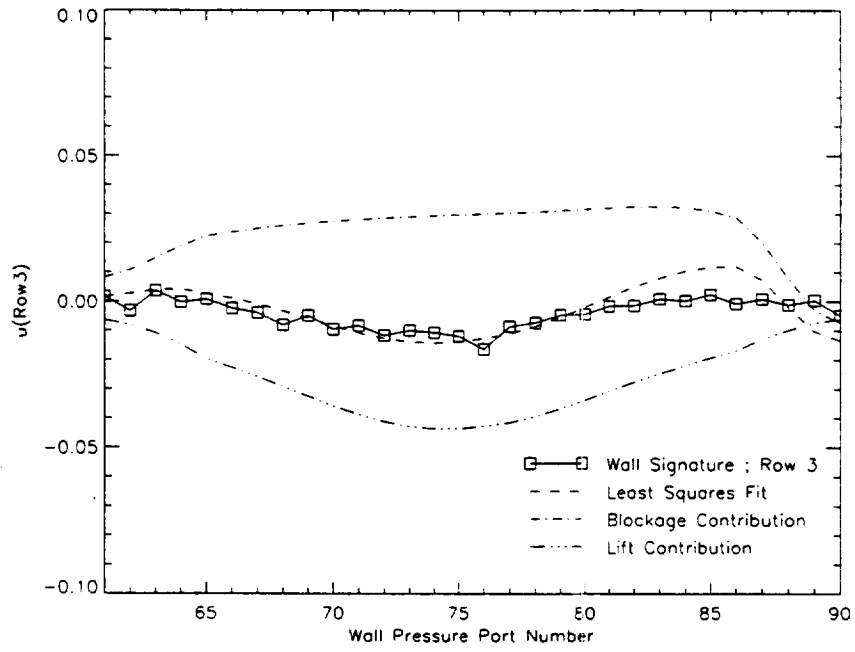


Fig. 20c Wall Signature at Row 3 / 14% Scale Model at 9.98[deg] Angle of Attack.

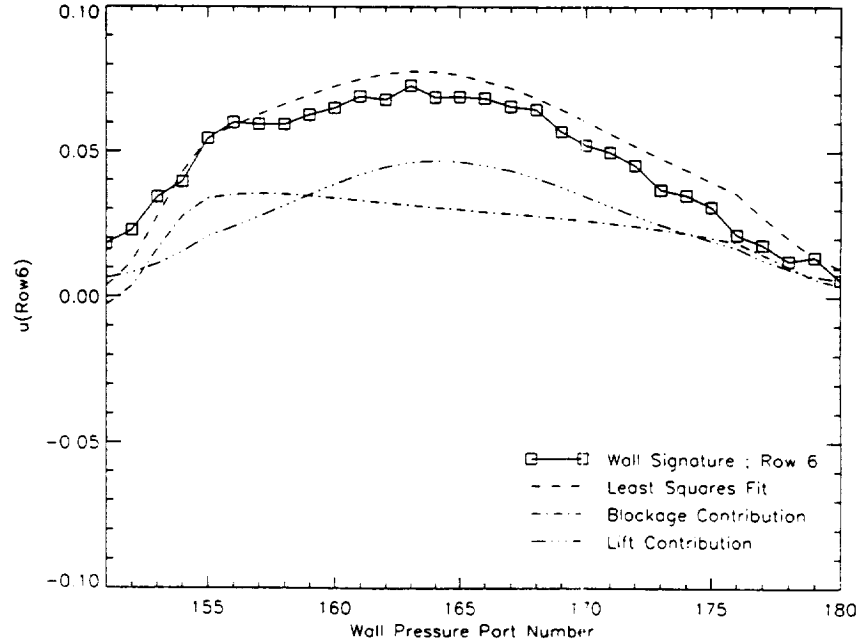


Fig. 20d Wall Signature at Row 6 / 14% Scale Model at 9.98[deg] Angle of Attack.

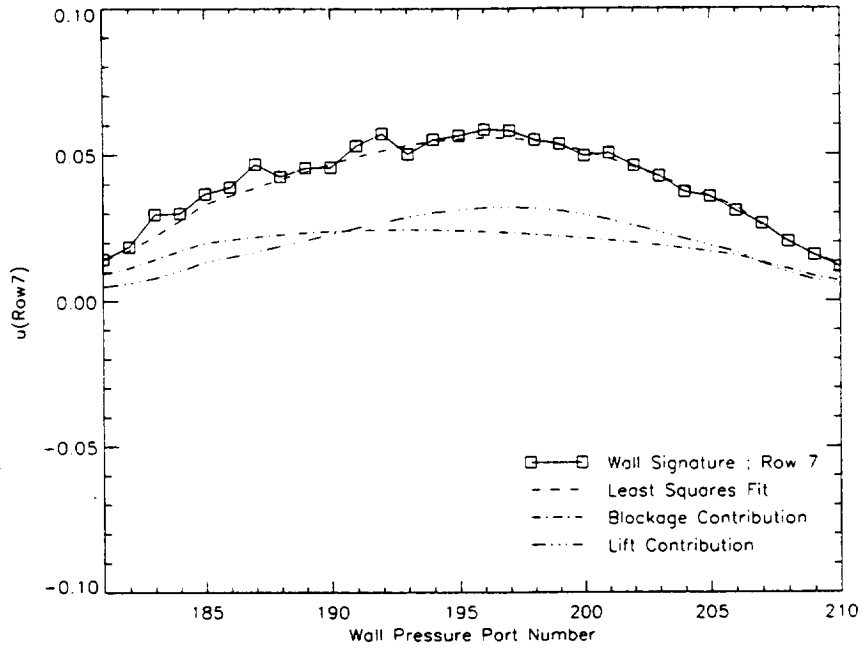


Fig. 20e Wall Signature at Row 7 / 14% Scale Model at 9.98[deg] Angle of Attack.

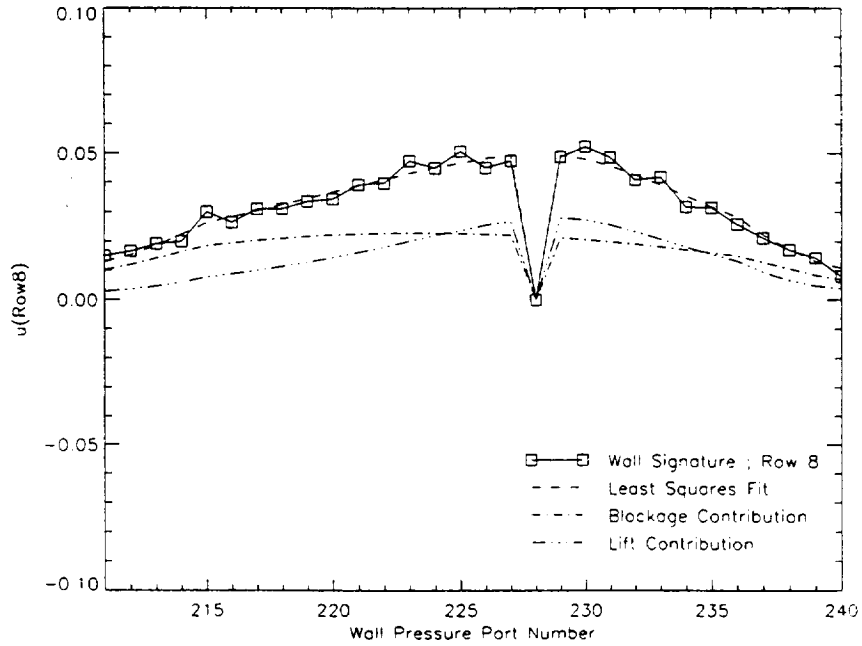


Fig. 20f Wall Signature at Row 8 / 14% Scale Model at 9.98[deg] Angle of Attack.

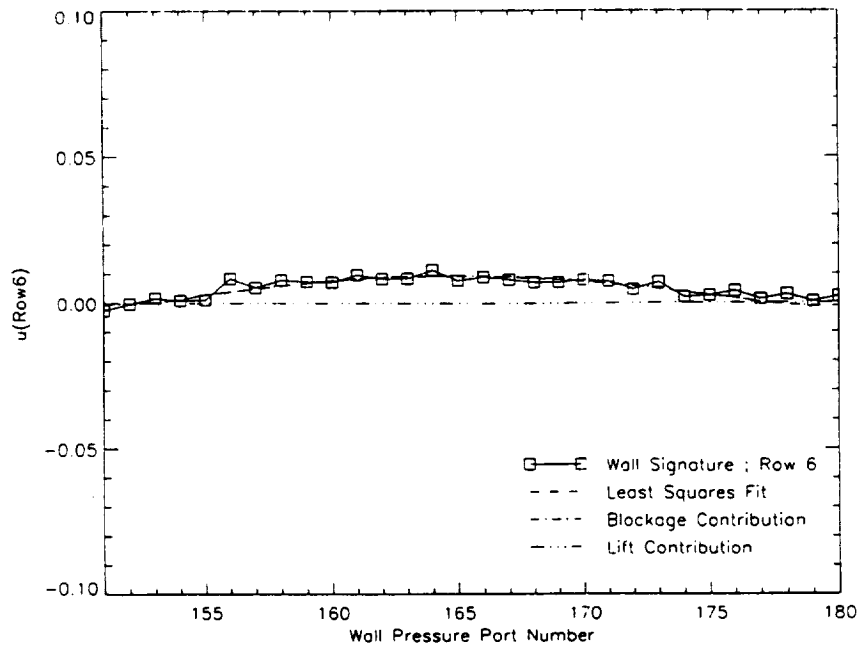


Fig. 21a Wall Signature at Row 6 / 8% Scale Model at -0.18 [deg] Angle of Attack.

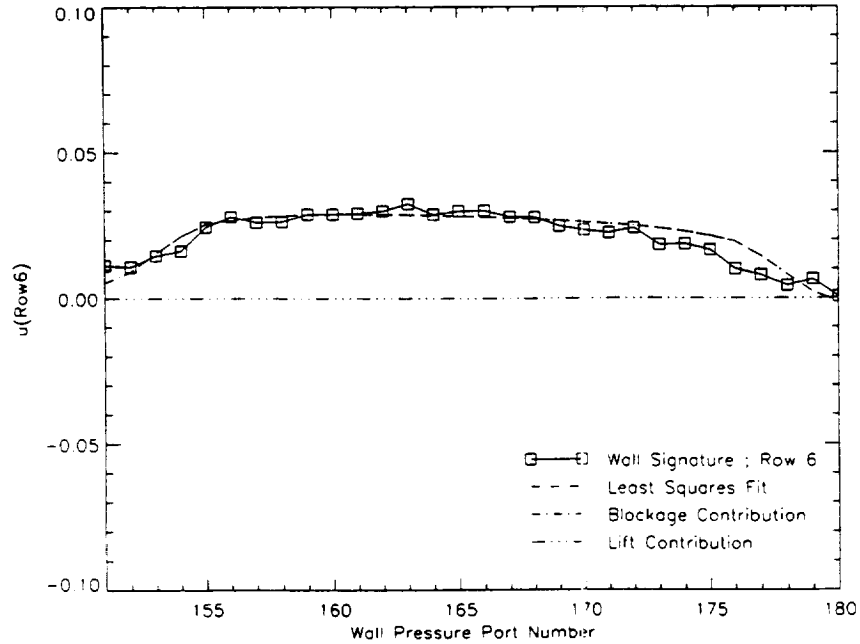


Fig. 21b Wall Signature at Row 6 / 14% Scale Model at -0.02 [deg] Angle of Attack.

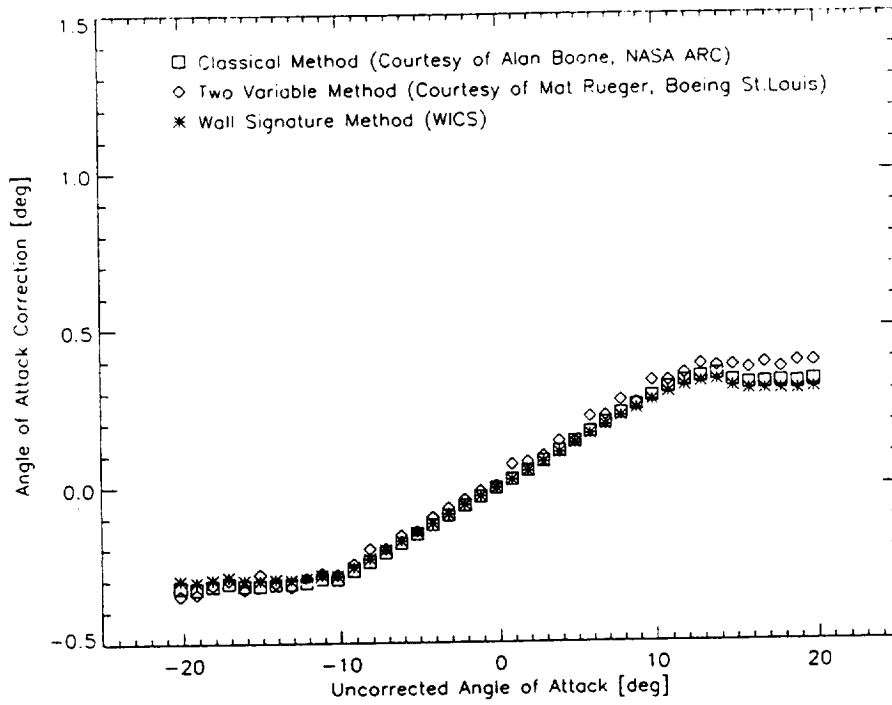


Fig. 22a Comparison of Angle of Attack Correction / 8% Scale Model.

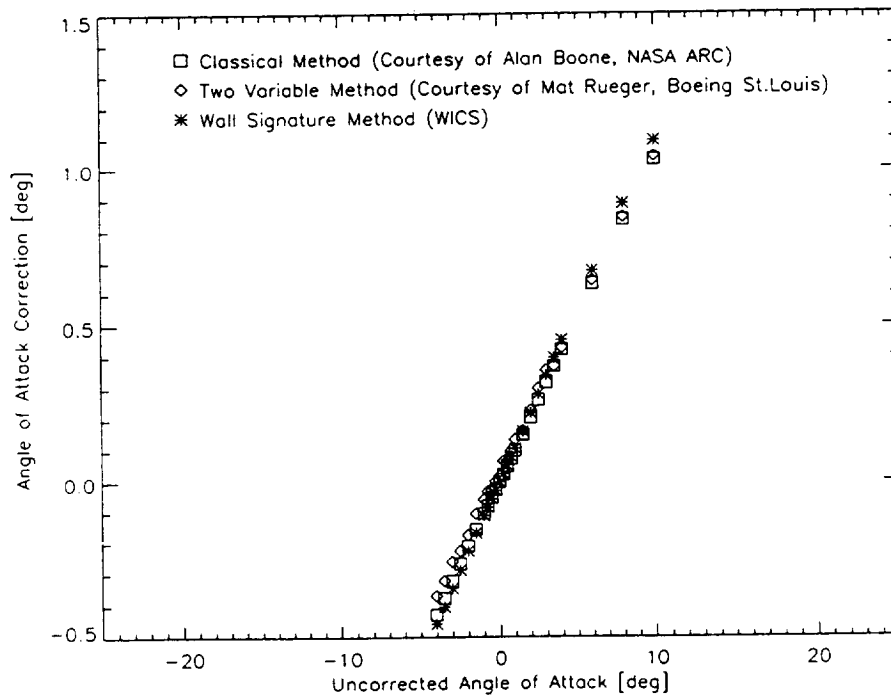


Fig. 22b Comparison of Angle of Attack Correction / 14% Scale Model.

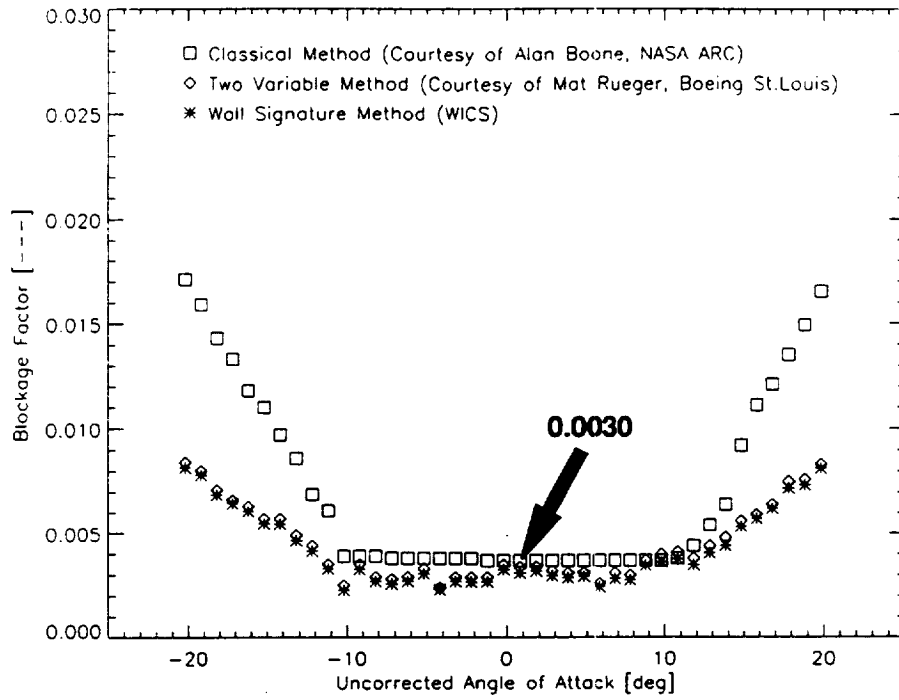


Fig. 23a Comparison of Blockage Factor / 8% Scale Model.

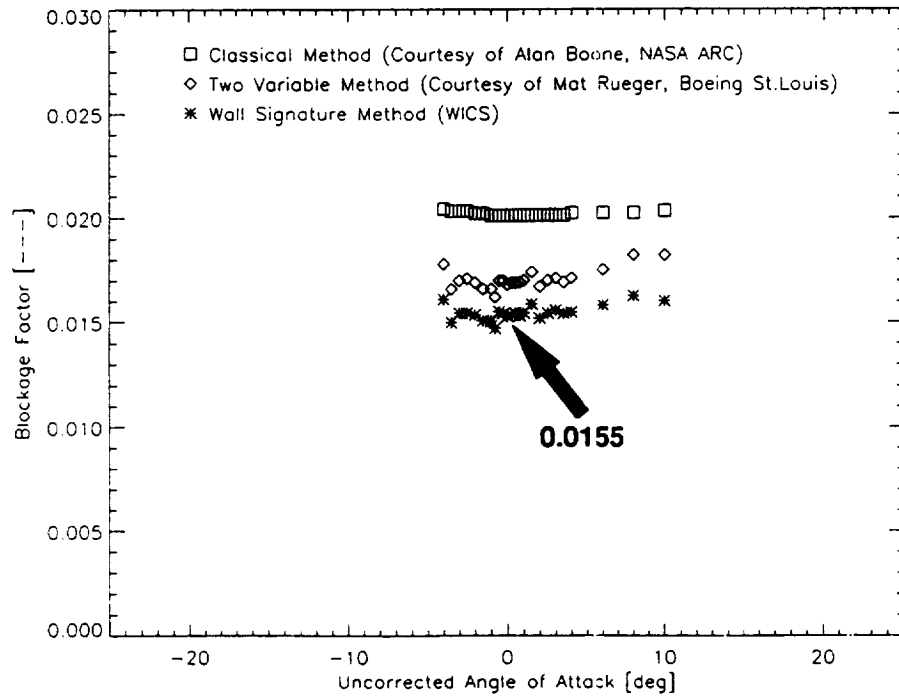


Fig. 23b Comparison of Blockage Factor / 14% Scale Model.

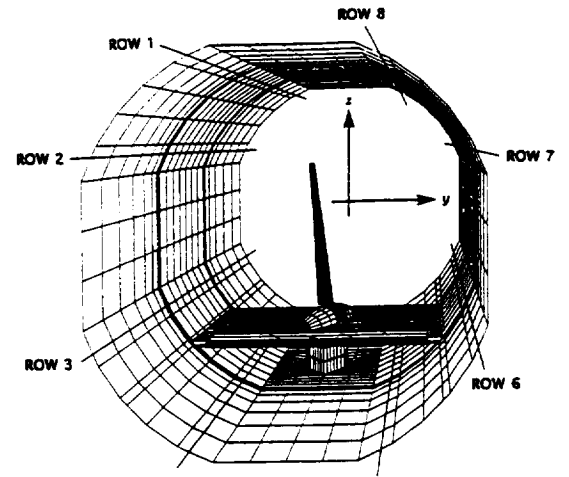
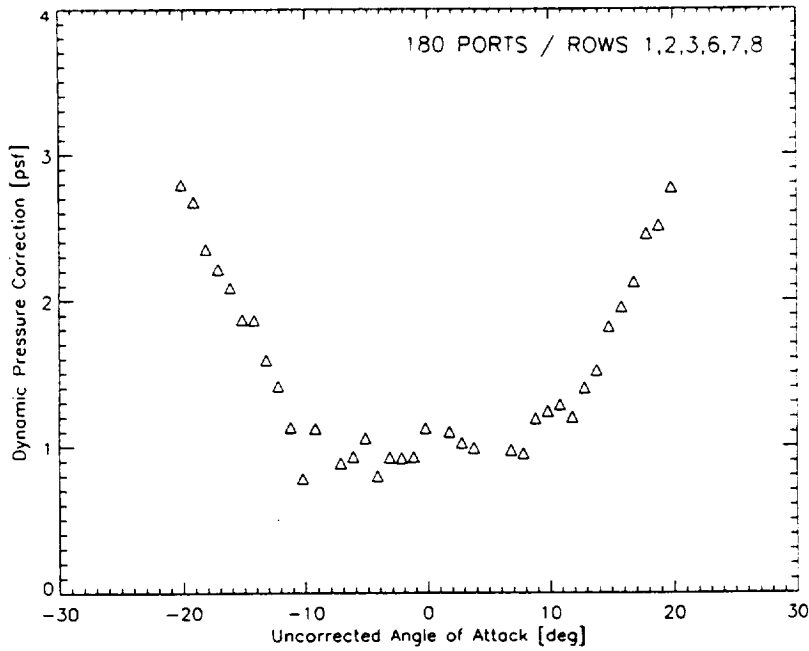


Fig. 23c Dynamic Pressure Correction of 8% Scale Model using 180 Ports.

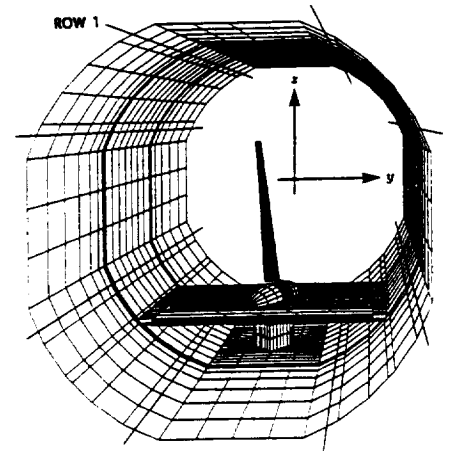
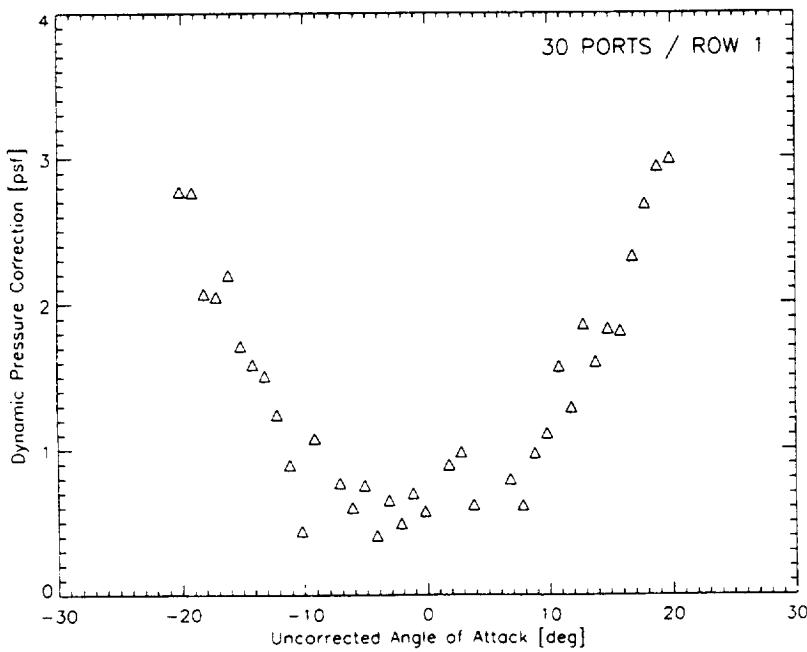
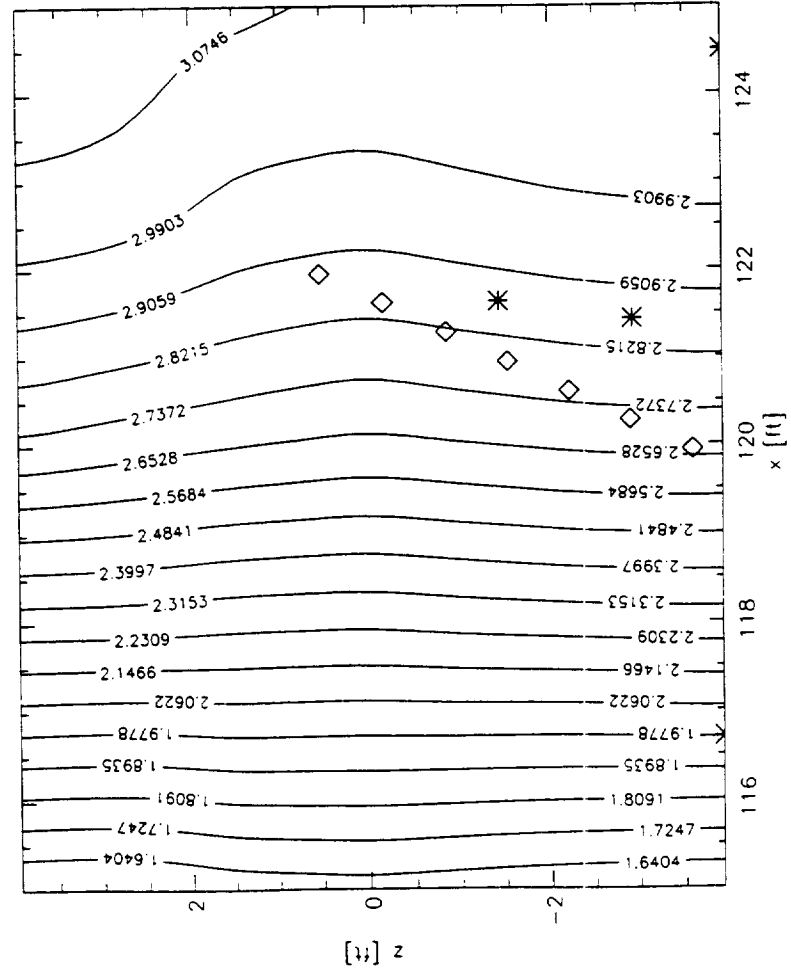


Fig. 23d Dynamic Pressure Correction of 8% Scale Model using 30 Ports.

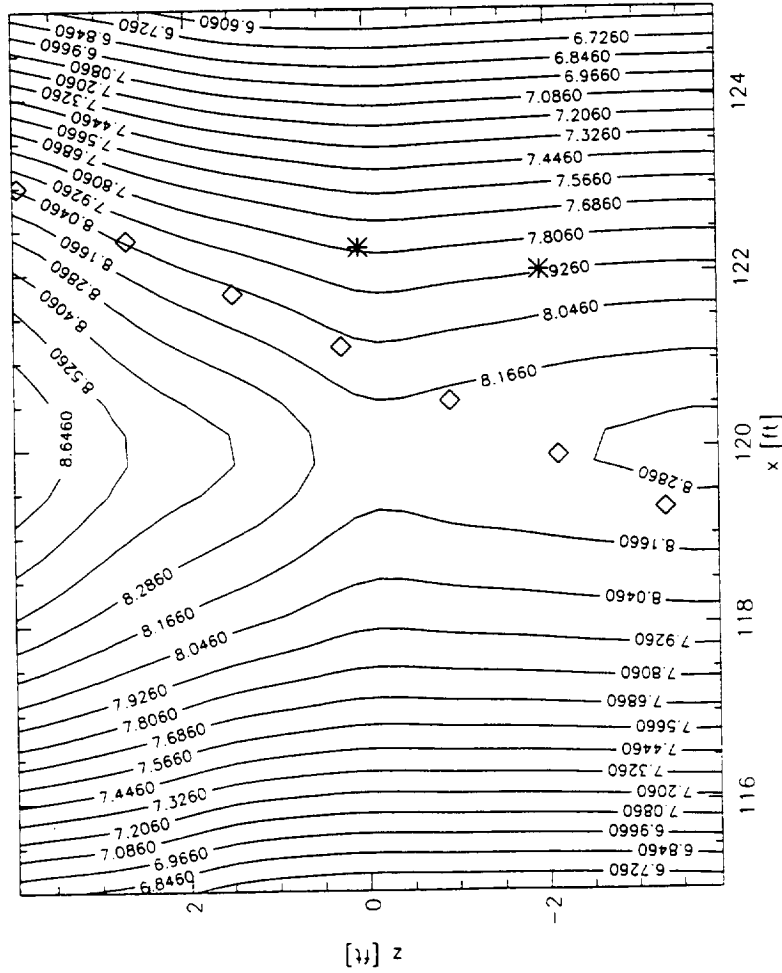
DYNAMIC PRESSURE CORRECTION [PSF]
 Boeing 7J7 Model / 8 Percent Scale
 RUN:SEQ = 0154.0000:041.0000 ; TUNNEL PLANE Y = 0.00 [FT]
 pto = 2.00 [atm] ; mach = 0.25 ; alpha = 19.82 [deg]



NO	SINGULARITY REPRESENTATION				STRENGTH
	* SOURCE	x [ft]	y [ft]	z [ft]	
1	SOURCE	116.7023	1.4444	-3.9258	1.0020
2	SOURCE	124.4919	-1.3630	-3.9258	-1.0020
3	SOURCE	121.4250	-0.2577	-2.9300	0.3731
4	SOURCE	121.6320	-0.3323	-1.4300	0.3731
5	DOUBLET	119.9386	0.2780	-3.5870	0.4462
6	DOUBLET	120.2772	0.1580	-2.9010	0.4372
7	DOUBLET	120.6065	0.0373	-2.2160	0.4180
8	DOUBLET	120.9452	-0.0848	-1.5300	0.3875
9	DOUBLET	121.2839	-0.2068	-0.8440	0.3428
10	DOUBLET	121.6225	-0.3289	-0.1590	0.2770
11	DOUBLET	121.9518	-0.4475	0.5270	0.1860

Fig. 24a Singularity Representation and Dynamic Pressure Correction of 8% Scale Model at 19.82 [deg] Angle of Attack / Tunnel Plane Y=0.0.

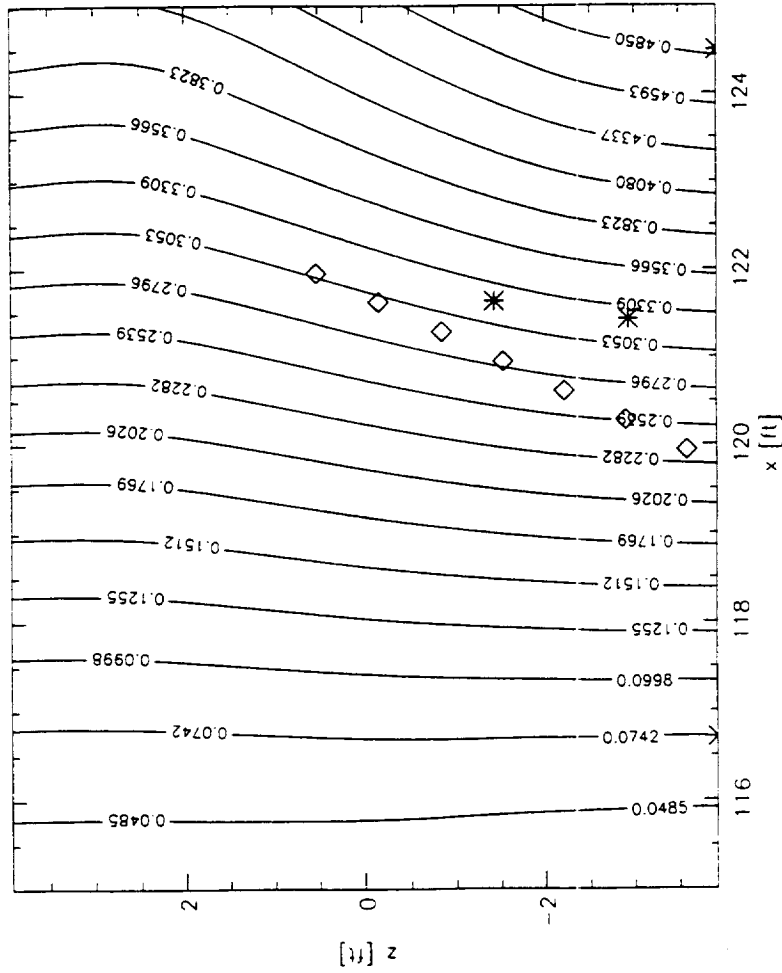
DYNAMIC PRESSURE CORRECTION [PSF]
 Boeing 7J7 Model / 14 Percent Scale
 RUN:SEQ = 0219.0000:024.0000 ; TUNNEL PLANE Y = 0.00 [FT]
 ptot = 2.00 [atm] ; mach = 0.30 ; alpha = 9.98 [deg]



NO.	SINGULARITY REPRESENTATION			STRENGTH	
	* SOURCE	o DOUBLET	z [ft]		
1	SOURCE	113.3726	1.2806	-3.9258	2.4936
2	SOURCE	127.6436	-1.2195	-3.9258	-2.4936
3	SOURCE	122.0199	-0.2304	-1.9300	-0.1243
4	SOURCE	122.2856	-0.2772	0.0700	-0.1243
5	DOUBLET	119.3016	0.2477	-3.3300	1.2987
6	DOUBLET	119.9122	0.1403	-2.1300	1.2726
7	DOUBLET	120.5327	0.0312	-0.9300	1.2166
8	DOUBLET	121.1532	-0.0780	0.2700	1.1280
9	DOUBLET	121.7638	-0.1854	1.4700	0.9978
10	DOUBLET	122.3843	-0.2945	2.6700	0.8063
11	DOUBLET	122.9949	-0.4019	3.8700	0.4833

Fig. 24b Singularity Representation and Dynamic Pressure Correction of 14% Scale Model at 9.98 [deg] Angle of Attack / Tunnel Plane Y=0.0 .

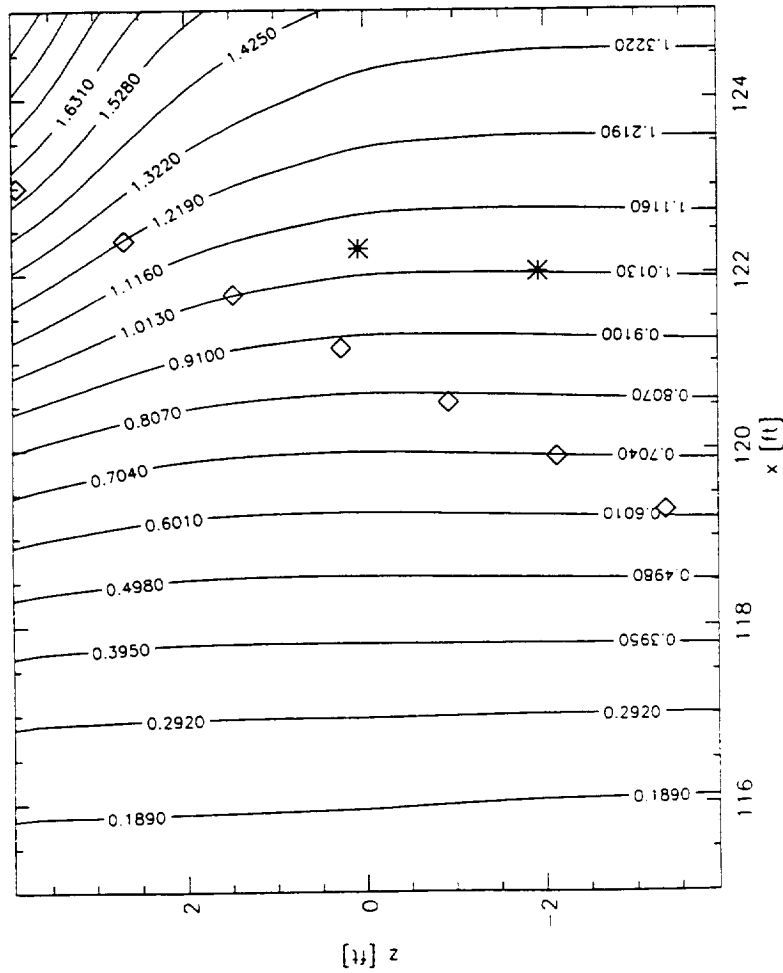
ANGLE OF ATTACK CORRECTION [DEG]
 Boeing 7J7 Model / 8 Percent Scale
 RUN:SEQ = 0154.0000:041.0000 ; TUNNEL PLANE Y = 0.00 [FT]
 ptot = 2.00 [atm] ; mach = 0.25 ; alpha = 19.82 [deg]



NO	SINGULARITY REPRESENTATION			STRENGTH	
	* SOURCE	◇ DOUBLET	Z [ft]		
1	SOURCE	116 7023	1.4444	-3.9258	1.0020
2	SOURCE	124 4919	-1.3630	-3.9258	-1.0020
3	SOURCE	121 4250	-0.2577	-2.9300	0.3731
4	SOURCE	121 6320	-0.3323	-1.4300	0.3731
5	DOUBLET	119 9386	0.2780	-3.5870	0.4462
6	DOUBLET	120 2772	0.1560	-2.9010	0.4372
7	DOUBLET	120 6065	0.0373	-2.2160	0.4180
8	DOUBLET	120 9452	-0.0848	-1.5300	0.3875
9	DOUBLET	121 2839	-0.2068	-0.8440	0.3428
10	DOUBLET	121 6225	-0.3289	-0.1590	0.2770
11	DOUBLET	121 9518	-0.4475	0.5270	0.1660

Fig. 24c Singularity Representation and Angle of Attack Correction of 8% Scale Model at 19.82 [deg] Angle of Attack / Tunnel Plane Y=0.0 .

ANGLE OF ATTACK CORRECTION [DEG]
 Boeing 7J7 Model / 14 Percent Scale
 RUN:SEQ = 0219.0000:024.0000 ; TUNNEL PLANE Y = 0.00 [FT]
 plot = 2.00 [atm] ; mach = 0.30 ; alpha = 9.98 [deg]



NO.	SINGULARITY REPRESENTATION				STRENGTH
	TYPE	* SOURCE x [FT]	o DOUBLET y [FT]	z [FT]	
1	SOURCE	113.3726	1.2906	-3.9258	2.4936
2	SOURCE	127.6436	-1.2195	-3.9258	-2.4936
3	SOURCE	122.0199	-0.2304	-1.9300	-0.1243
4	SOURCE	122.2858	-0.2772	0.0700	-0.1243
5	DOUBLET	119.3016	0.2477	-3.3300	1.2987
6	DOUBLET	119.9122	0.1403	-2.1300	1.2726
7	DOUBLET	120.5327	0.0312	-0.9300	1.2166
8	DOUBLET	121.1532	-0.0780	0.2700	1.1280
9	DOUBLET	121.7638	-0.1854	1.4700	0.9978
10	DOUBLET	122.3843	-0.2945	2.6700	0.8063
11	DOUBLET	122.9949	-0.4019	3.8700	0.4633

Fig. 24d Singularity Representation and Angle of Attack Correction of 14% Scale Model at 9.98 [deg] Angle of Attack / Tunnel Plane Y=0.0.

Initial Singularity Representation of Ames Bipod

No.	Type	x [ft]	y [ft]	z [ft]	Weight
1	SOURCE	120.5	0.0	-4.0	1.0
2	SOURCE	120.5	0.0	-3.5	1.0
3	SOURCE	120.5	0.0	-3.0	1.0
4	SOURCE	120.5	0.0	-2.5	1.0
5	SOURCE	120.5	0.0	-2.0	1.0
6	SOURCE	120.5	0.0	-1.5	1.0
7	SOURCE	120.5	0.0	-1.0	1.0
8	SOURCE	120.5	0.0	-0.5	1.0
9	SOURCE	120.5	0.0	-0.0	1.0
10	SINK	121.5	0.0	-4.0	-1.0
11	SINK	121.5	0.0	-3.5	-1.0
12	SINK	121.5	0.0	-3.0	-1.0
13	SINK	121.5	0.0	-2.5	-1.0
14	SINK	121.5	0.0	-2.0	-1.0
15	SINK	121.5	0.0	-1.5	-1.0
16	SINK	121.5	0.0	-1.0	-1.0
17	SINK	121.5	0.0	-0.5	-1.0
18	SINK	121.5	0.0	-0.0	-1.0
19	SOURCE	121.0	0.0	-4.0	1.0
20	SOURCE	121.0	0.0	-3.5	1.0
21	SOURCE	121.0	0.0	-3.0	1.0
22	SOURCE	121.0	0.0	-2.5	1.0
23	SOURCE	121.0	0.0	-2.0	1.0
24	SOURCE	121.0	0.0	-1.5	1.0
25	SOURCE	121.0	0.0	-1.0	1.0
26	SOURCE	121.0	0.0	-0.5	1.0
27	SOURCE	121.0	0.0	-0.0	1.0

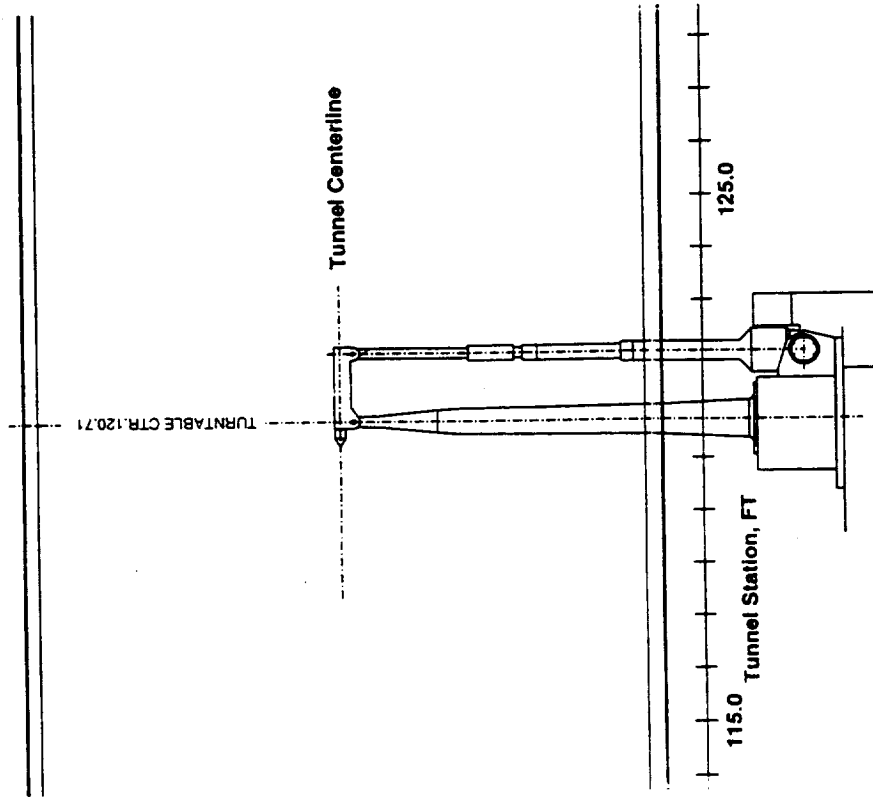


Fig. 25a Singularity Representation of Ames Bipod.

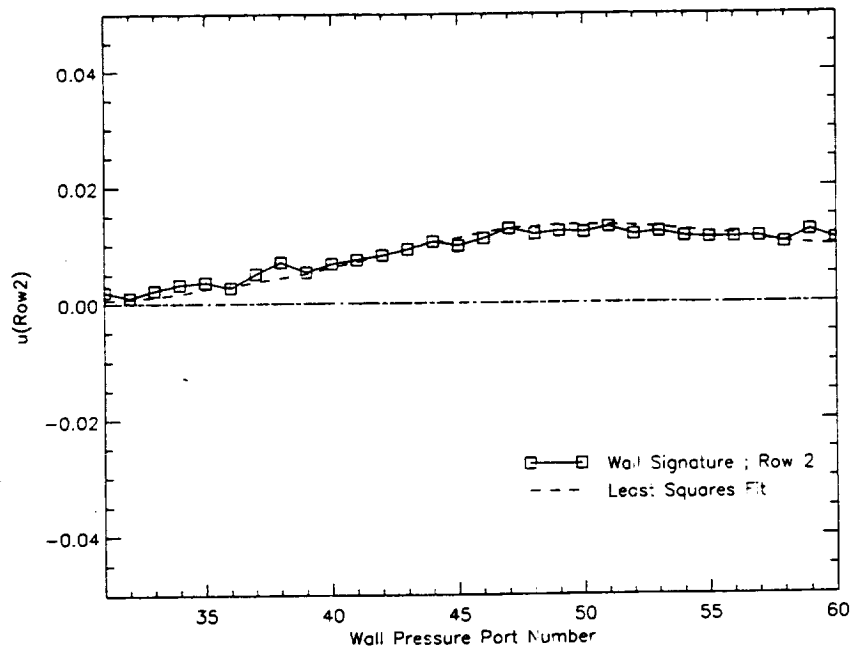


Fig. 25b Wall Signature of Ames Bipod ; Row 2 .

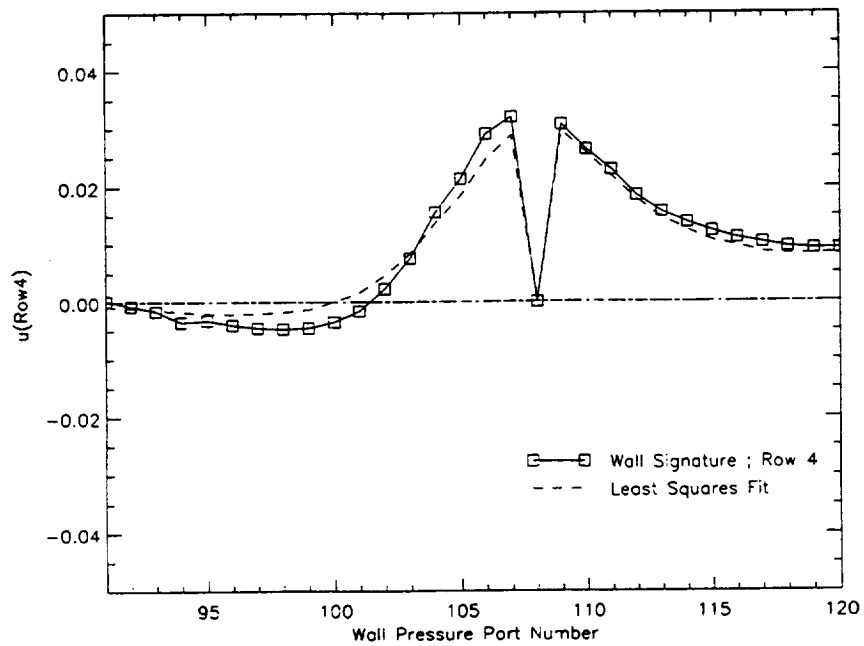
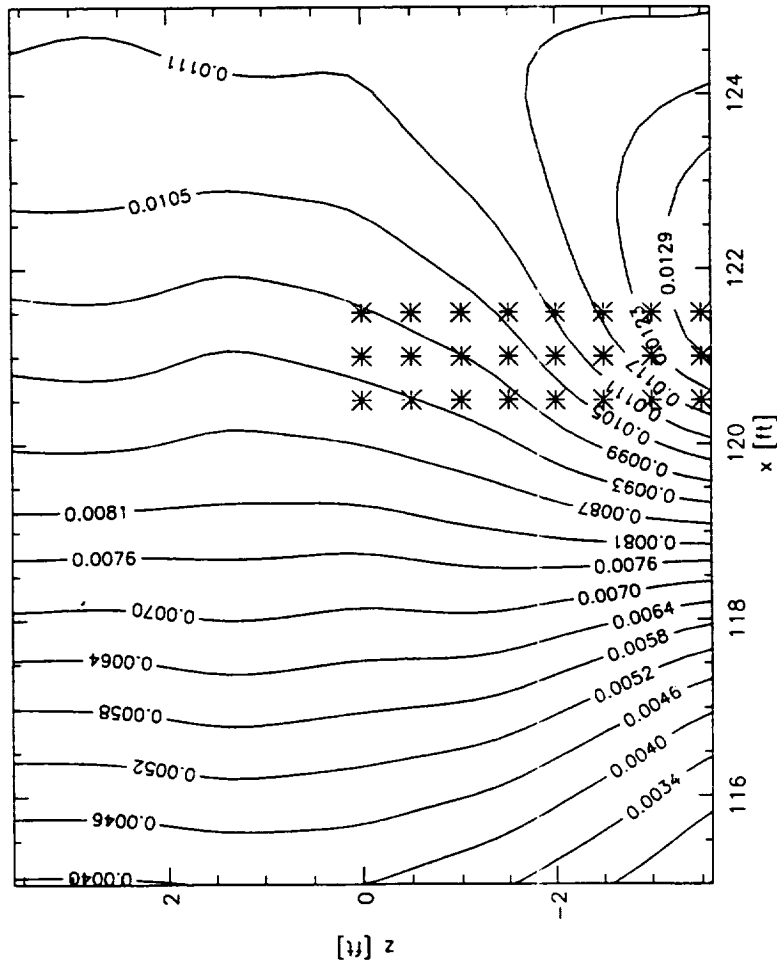


Fig. 25c Wall Signature of Ames Bipod ; Row 4 .

BLOCKAGE FACTOR [---]
 AMES_BIPOD
 RUN:SEQ = 0000.0000:011.0000 ; TUNNEL PLANE Y = 0.00 [FT]
 plot = 4.00 [atm] ; mach = 0.29 ; alpha = 0.00 [deg]
 NO OPTIMIZATION OF SINGULARITY LOCATION

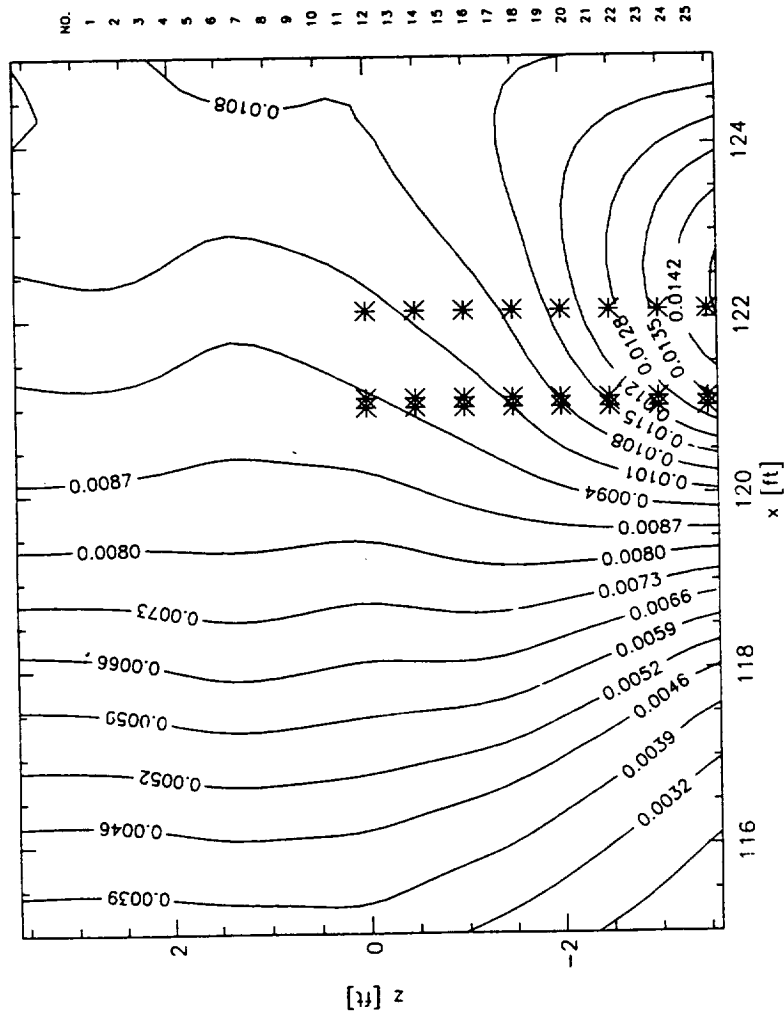


NO.	SINGULARITY REPRESENTATION				
	TYPE	x [FT]	y [FT]	z [FT]	STRENGTH
1	SOURCE	120.5000	0.0000	-4.0000	0.8757
2	SOURCE	120.5000	0.0000	-3.5000	0.8757
3	SOURCE	120.5000	0.0000	-3.0000	0.8757
4	SOURCE	120.5000	0.0000	-2.5000	0.8757
5	SOURCE	120.5000	0.0000	-2.0000	0.8757
6	SOURCE	120.5000	0.0000	-1.5000	0.8757
7	SOURCE	120.5000	0.0000	-1.0000	0.8757
8	SOURCE	120.5000	0.0000	-0.5000	0.8757
9	SOURCE	120.5000	0.0000	0.0000	0.8757
10	SOURCE	121.5000	0.0000	-4.0000	-0.8757
11	SOURCE	121.5000	0.0000	-3.5000	-0.8757
12	SOURCE	121.5000	0.0000	-3.0000	-0.8757
13	SOURCE	121.5000	0.0000	-2.5000	-0.8757
14	SOURCE	121.5000	0.0000	-2.0000	-0.8757
15	SOURCE	121.5000	0.0000	-1.5000	-0.8757
16	SOURCE	121.5000	0.0000	-1.0000	-0.8757
17	SOURCE	121.5000	0.0000	-0.5000	-0.8757
18	SOURCE	121.5000	0.0000	0.0000	-0.8757
19	SOURCE	121.0000	0.0000	-4.0000	0.1242
20	SOURCE	121.0000	0.0000	-3.5000	0.1242
21	SOURCE	121.0000	0.0000	-3.0000	0.1242
22	SOURCE	121.0000	0.0000	-2.5000	0.1242
23	SOURCE	121.0000	0.0000	-2.0000	0.1242
24	SOURCE	121.0000	0.0000	-1.5000	0.1242
25	SOURCE	121.0000	0.0000	-1.0000	0.1242

>>> NOT ALL SINGULARITIES ARE LISTED <<<

Fig. 25d Blockage Factor of Ames Bipod ; Tunnel Plane Y = 0.0 [FT] .
 (No Optimization of Singularity Location)

BLOCKAGE FACTOR [---]
 AMES_BIPOD
 RUN:SEQ = 0000,0000;011.0000 ; TUNNEL PLANE Y = 0.00 [FT]
 plot = 4.00 [atm] ; mach = 0.29 ; alpha = 0.00 [deg]
 OPTIMIZATION OF SINGULARITY LOCATION



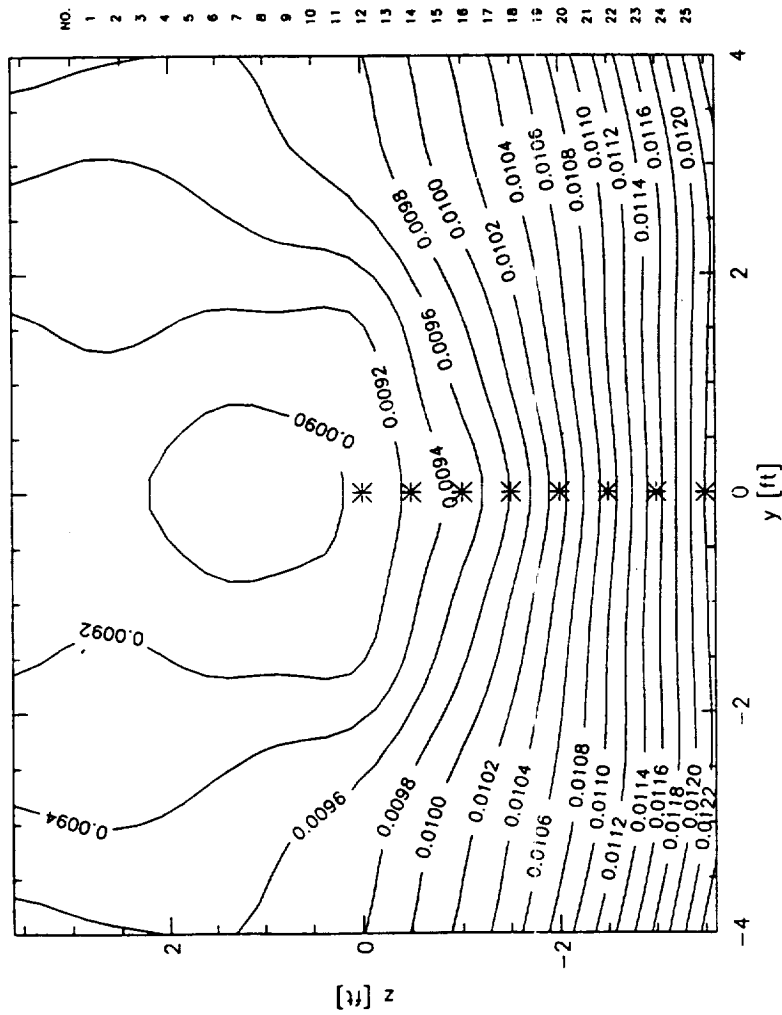
SINGULARITY REPRESENTATION

NO.	TYPE	X [FT]	Y [FT]	Z [FT]	STRENGTH
1	SOURCE	121.0000	0.0000	-4.0000	0.7730
2	SOURCE	121.0000	0.0000	-3.5000	0.7730
3	SOURCE	121.0000	0.0000	-3.0000	0.7730
4	SOURCE	121.0000	0.0000	-2.5000	0.7730
5	SOURCE	121.0000	0.0000	-2.0000	0.7730
6	SOURCE	121.0000	0.0000	-1.5000	0.7730
7	SOURCE	121.0000	0.0000	-1.0000	0.7730
8	SOURCE	121.0000	0.0000	-0.5000	0.7730
9	SOURCE	121.0000	0.0000	0.0000	0.7730
10	SOURCE	122.1000	0.0000	-4.0000	-0.7730
11	SOURCE	122.1000	0.0000	-3.5000	-0.7730
12	SOURCE	122.1000	0.0000	-3.0000	-0.7730
13	SOURCE	122.1000	0.0000	-2.5000	-0.7730
14	SOURCE	122.1000	0.0000	-2.0000	-0.7730
15	SOURCE	122.1000	0.0000	-1.5000	-0.7730
16	SOURCE	122.1000	0.0000	-1.0000	-0.7730
17	SOURCE	122.1000	0.0000	-0.5000	-0.7730
18	SOURCE	121.0000	0.0000	0.0000	-0.7730
19	SOURCE	121.0000	0.0000	-4.0000	0.1015
20	SOURCE	121.0000	0.0000	-3.5000	0.1015
21	SOURCE	121.0000	0.0000	-3.0000	0.1015
22	SOURCE	121.0000	0.0000	-2.5000	0.1015
23	SOURCE	121.0000	0.0000	-2.0000	0.1015
24	SOURCE	121.0000	0.0000	-1.5000	0.1015
25	SOURCE	121.0000	0.0000	-1.0000	0.1015

>>> NOT ALL SINGULARITIES ARE LISTED <<<

Fig. 25e Blockage Factor of Ames Bipod ; Tunnel Plane Y = 0.0 [FT] .
 (Optimization of Singularity Location)

BLOCKAGE FACTOR [---]
 AMES-BIPOD
 RUN:SEQ = 0000.0000:011.0000 ; TUNNEL PLANE X = 120.71 [FT]
 plot = 4.00 [atm] ; mach = 0.29 ; alpha = 0.00 [deg]
 OPTIMIZATION OF SINGULARITY LOCATION



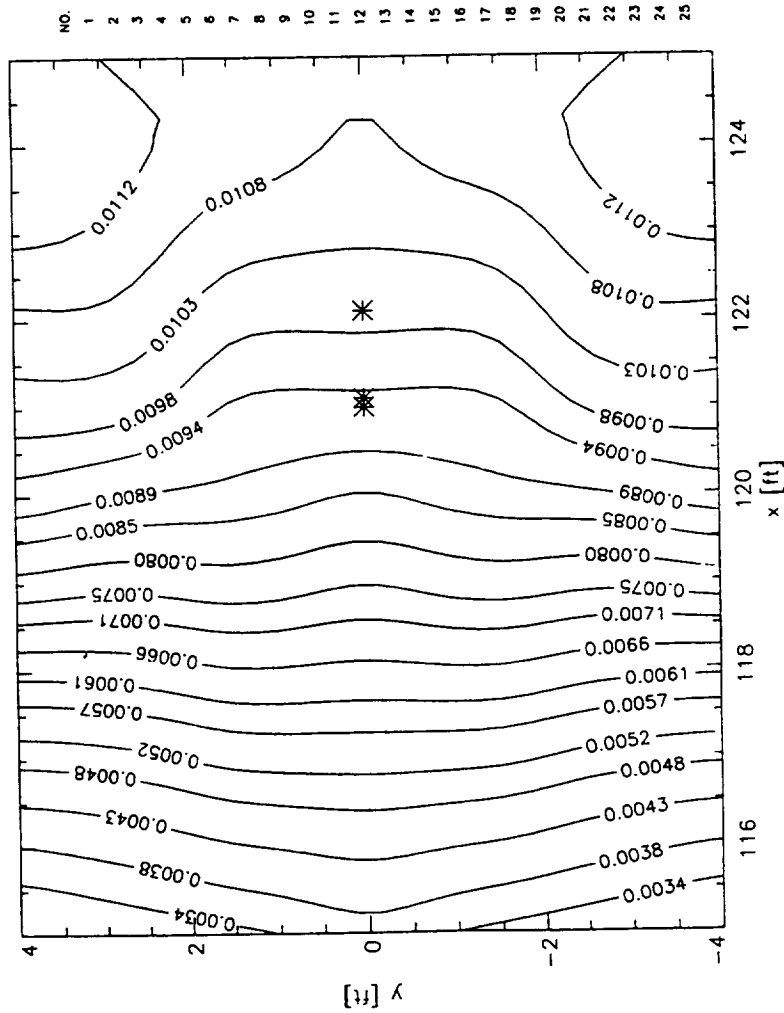
SINGULARITY REPRESENTATION

NO.	TYPE	X [FT]	Y [FT]	Z [FT]	STRENGTH
1	SOURCE	121.0000	0.0000	-4.0000	0.7730
2	SOURCE	121.0000	0.0000	-3.5000	0.7730
3	SOURCE	121.0000	0.0000	-3.0000	0.7730
4	SOURCE	121.0000	0.0000	-2.5000	0.7730
5	SOURCE	121.0000	0.0000	-2.0000	0.7730
6	SOURCE	121.0000	0.0000	-1.5000	0.7730
7	SOURCE	121.0000	0.0000	-1.0000	0.7730
8	SOURCE	121.0000	0.0000	-0.5000	0.7730
9	SOURCE	121.0000	0.0000	0.0000	0.7730
10	SOURCE	122.1000	0.0000	-4.0000	-0.7730
11	SOURCE	122.1000	0.0000	-3.5000	-0.7730
12	SOURCE	122.1000	0.0000	-3.0000	-0.7730
13	SOURCE	122.1000	0.0000	-2.5000	-0.7730
14	SOURCE	122.1000	0.0000	-2.0000	-0.7730
15	SOURCE	122.1000	0.0000	-1.5000	-0.7730
16	SOURCE	122.1000	0.0000	-1.0000	-0.7730
17	SOURCE	122.1000	0.0000	-0.5000	-0.7730
18	SOURCE	122.1000	0.0000	0.0000	-0.7730
19	SOURCE	121.1000	0.0000	0.0000	0.1015
20	SOURCE	121.1000	0.0000	-3.5000	0.1015
21	SOURCE	121.1000	0.0000	-3.0000	0.1015
22	SOURCE	121.1000	0.0000	-2.5000	0.1015
23	SOURCE	121.1000	0.0000	-2.0000	0.1015
24	SOURCE	121.1000	0.0000	-1.5000	0.1015
25	SOURCE	121.1000	0.0000	-1.0000	0.1015

>>> NOT ALL SINGULARITIES ARE LISTED <<<

Fig. 25f Blockage Factor of Ames Bipod ; Tunnel Plane X = 120.71 [FT].

BLOCKAGE FACTOR [---]
 AMES_BIPOD
 RUN:SEQ = 0000,0000;011.0000 ; TUNNEL PLANE Z = 0.00 [FT]
 plot = 4.00 [atm] ; mach = 0.29 ; alpha = 0.00 [deg]
 OPTIMIZATION OF SINGULARITY LOCATION



SINGULARITY REPRESENTATION		◇ DOUBLET		STRENGTH
* SOURCE	x [FT]	y [FT]	z [FT]	
SOURCE	121.0000	0.0000	-4.0000	0.7730
SOURCE	121.0000	0.0000	-3.5000	0.7730
SOURCE	121.0000	0.0000	-3.0000	0.7730
SOURCE	121.0000	0.0000	-2.5000	0.7730
SOURCE	121.0000	0.0000	-2.0000	0.7730
SOURCE	121.0000	0.0000	-1.5000	0.7730
SOURCE	121.0000	0.0000	-1.0000	0.7730
SOURCE	121.0000	0.0000	-0.5000	0.7730
SOURCE	121.0000	0.0000	0.0000	0.7730
SOURCE	122.1000	0.0000	-4.0000	-0.7730
SOURCE	122.1000	0.0000	-3.5000	-0.7730
SOURCE	122.1000	0.0000	-3.0000	-0.7730
SOURCE	122.1000	0.0000	-2.5000	-0.7730
SOURCE	122.1000	0.0000	-2.0000	-0.7730
SOURCE	122.1000	0.0000	-1.5000	-0.7730
SOURCE	122.1000	0.0000	-1.0000	-0.7730
SOURCE	122.1000	0.0000	-0.5000	-0.7730
SOURCE	122.1000	0.0000	0.0000	-0.7730
SOURCE	121.1000	0.0000	-4.0000	0.1015
SOURCE	121.1000	0.0000	-3.5000	0.1015
SOURCE	121.1000	0.0000	-3.0000	0.1015
SOURCE	121.1000	0.0000	-2.5000	0.1015
SOURCE	121.1000	0.0000	-2.0000	0.1015
SOURCE	121.1000	0.0000	-1.5000	0.1015
SOURCE	121.1000	0.0000	-1.0000	0.1015
SOURCE	121.1000	0.0000	-0.5000	0.1015
SOURCE	121.1000	0.0000	0.0000	0.1015

>>> NOT ALL SINGULARITIES ARE LISTED <<<

Fig. 25g Blockage Factor of Ames Bipod ; Tunnel Plane Z = 0.0 [FT] .

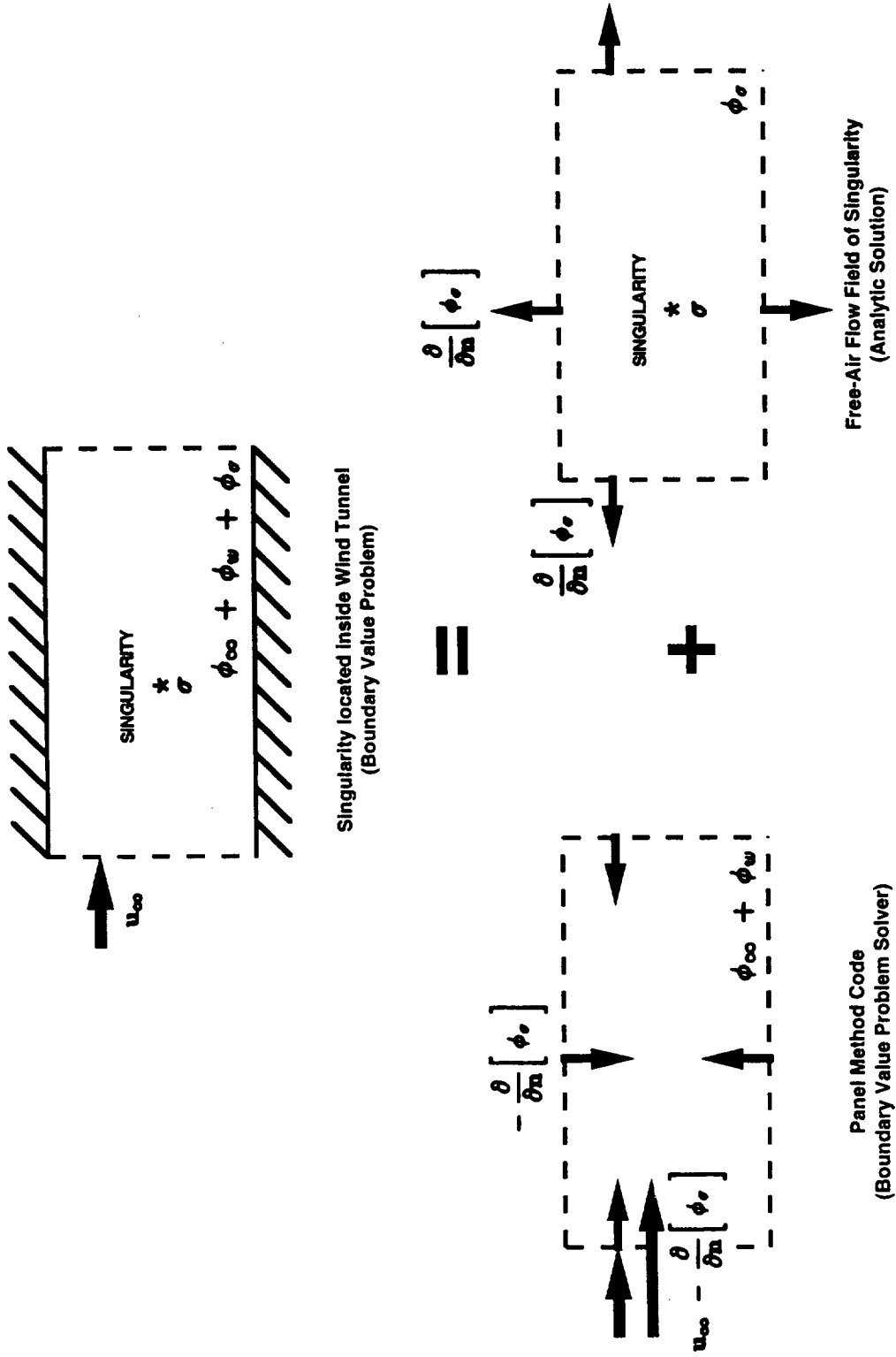


Fig. 26 Superposition of Boundary Value Problem Solutions.

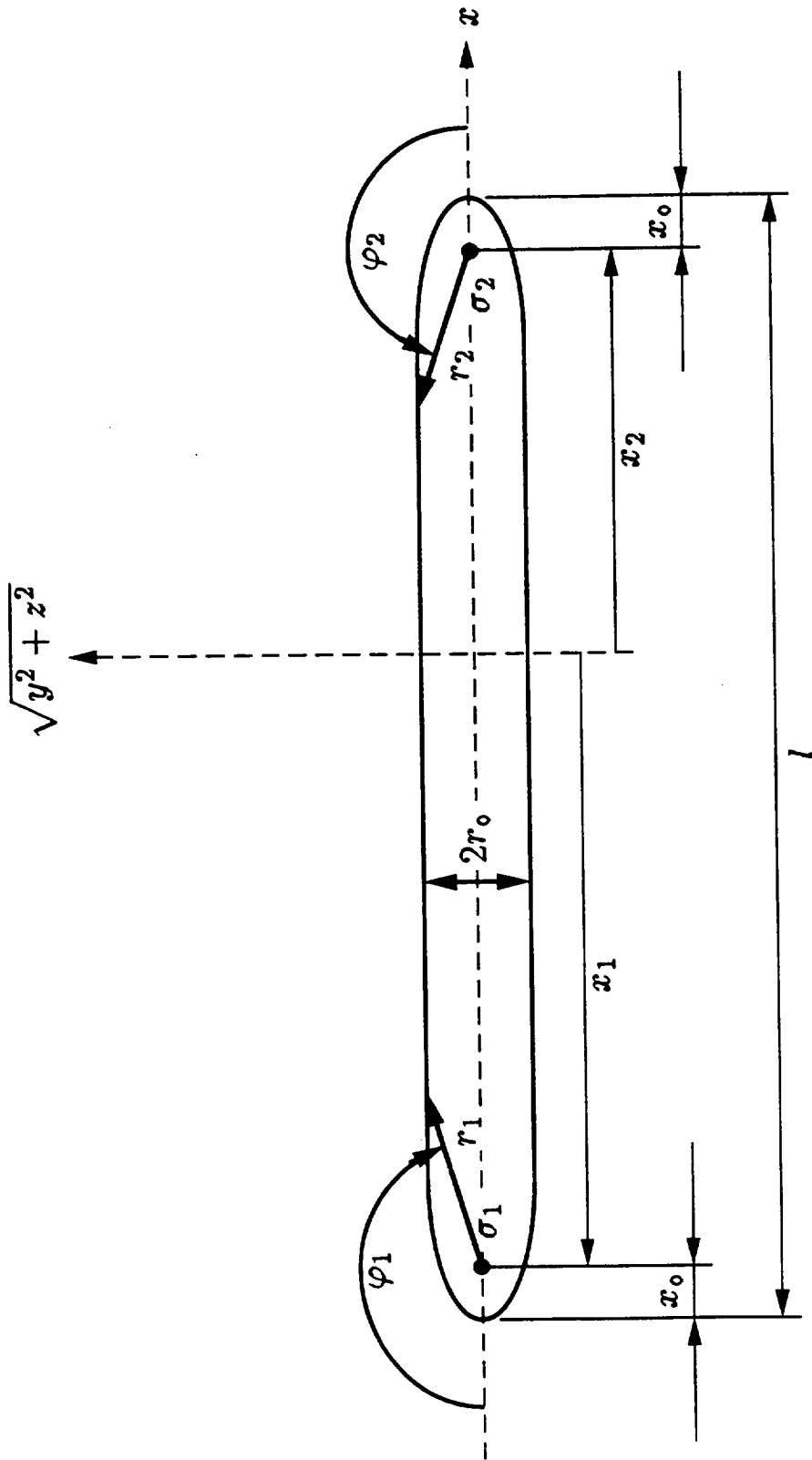


Fig. 27a Geometry of Rankine Body of Example.

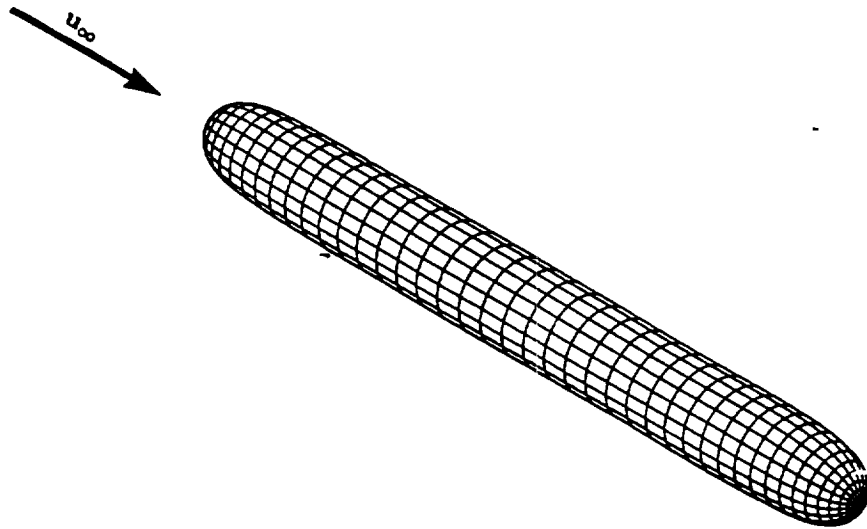


Fig. 27b Panel Representation of Rankine Body Geometry.

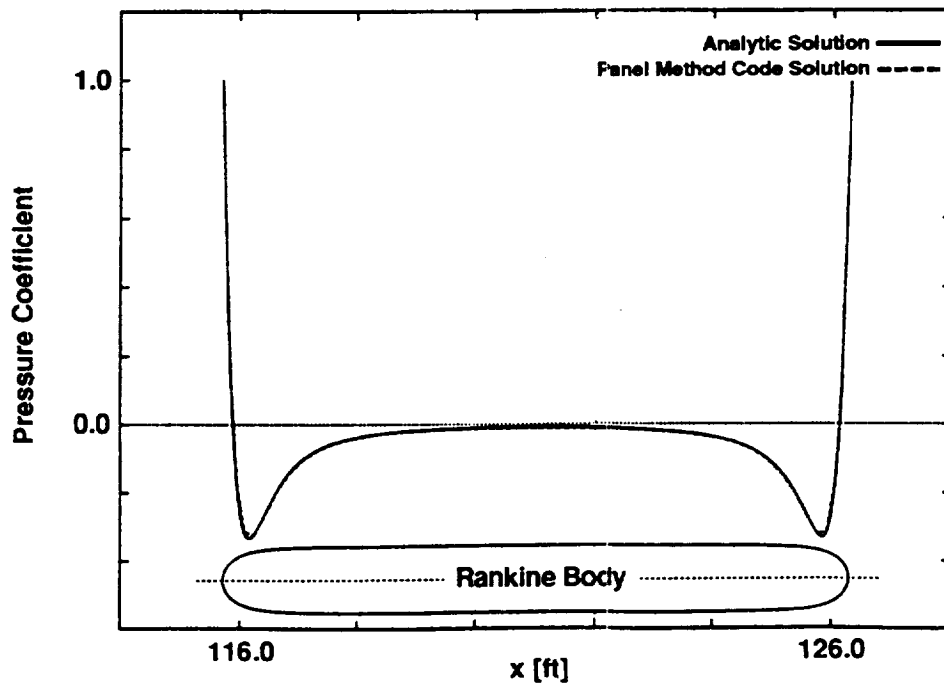


Fig. 28 Comparison of Surface Pressure Distribution of Rankine Body.

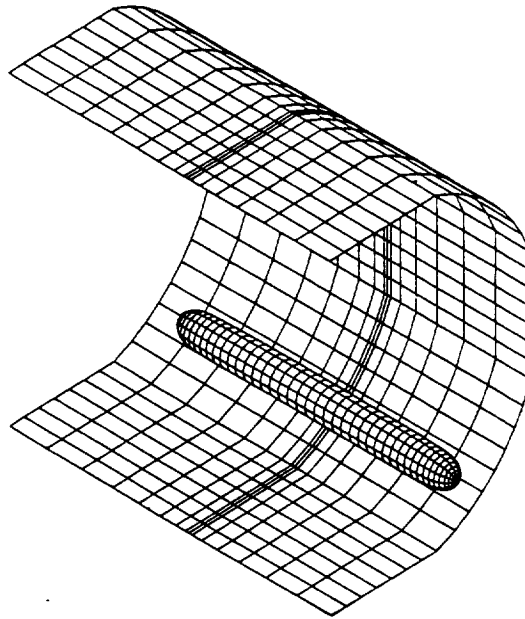


Fig. 29 Panel Model of Rankine Body inside Test Section.

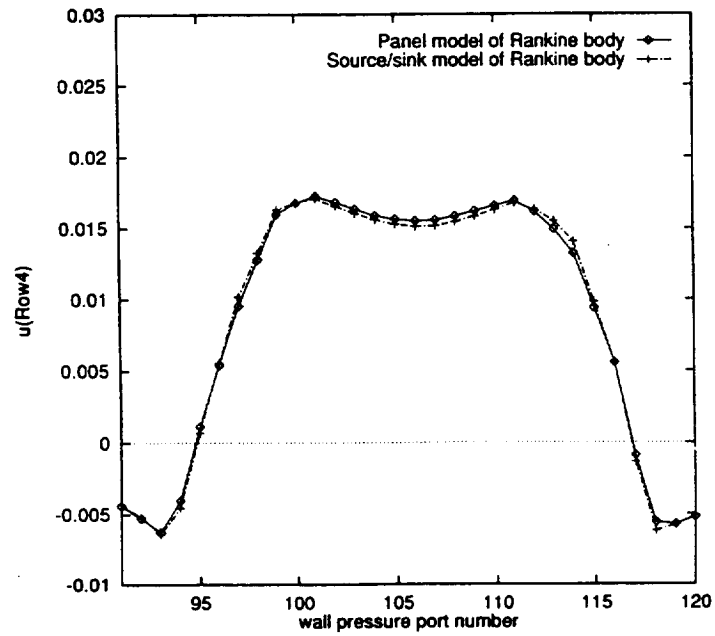


Fig. 30 Comparison of Wall Signature of Rankine Body with equivalent Source-Sink Representation.

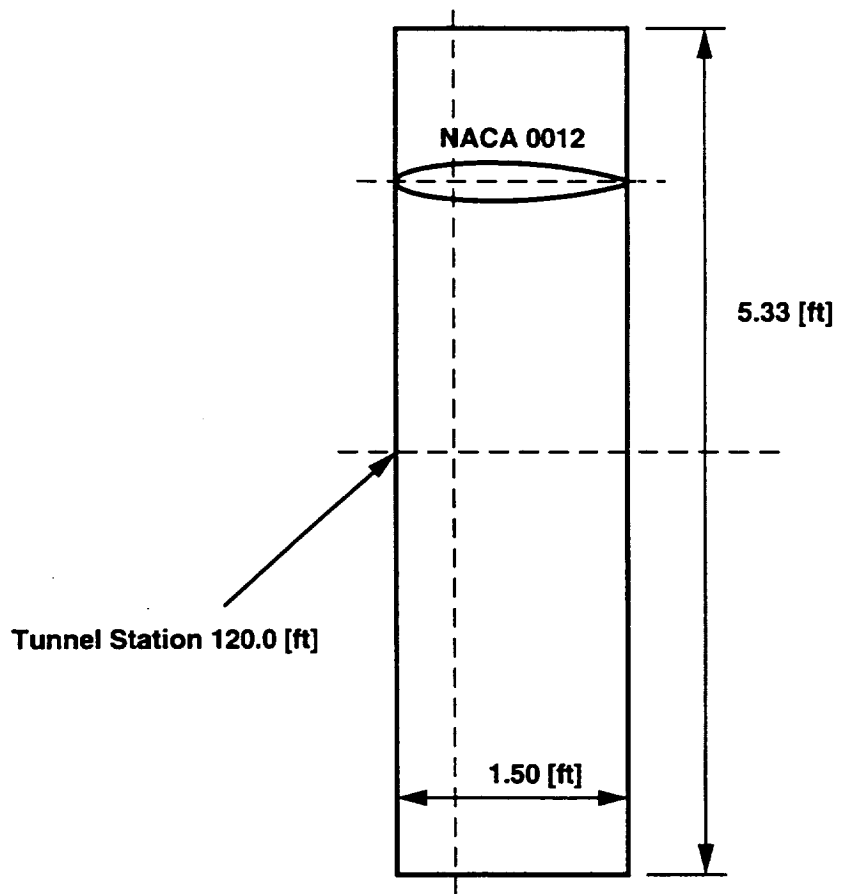


Fig. 31 Geometry of Rectangular Wing.

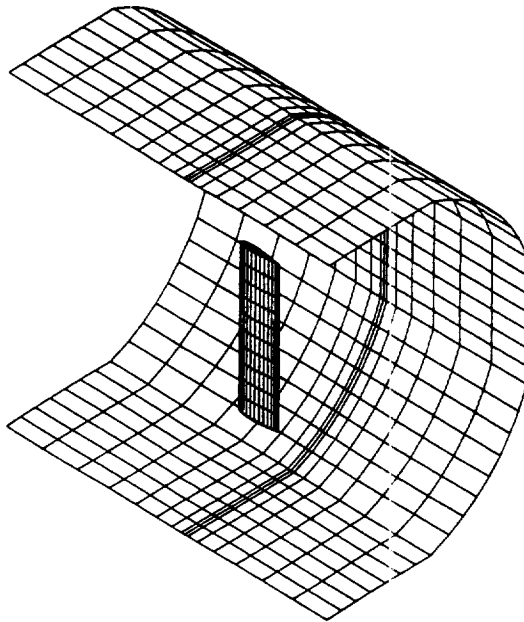


Fig. 32 Panel Model of Wing inside Test Section.

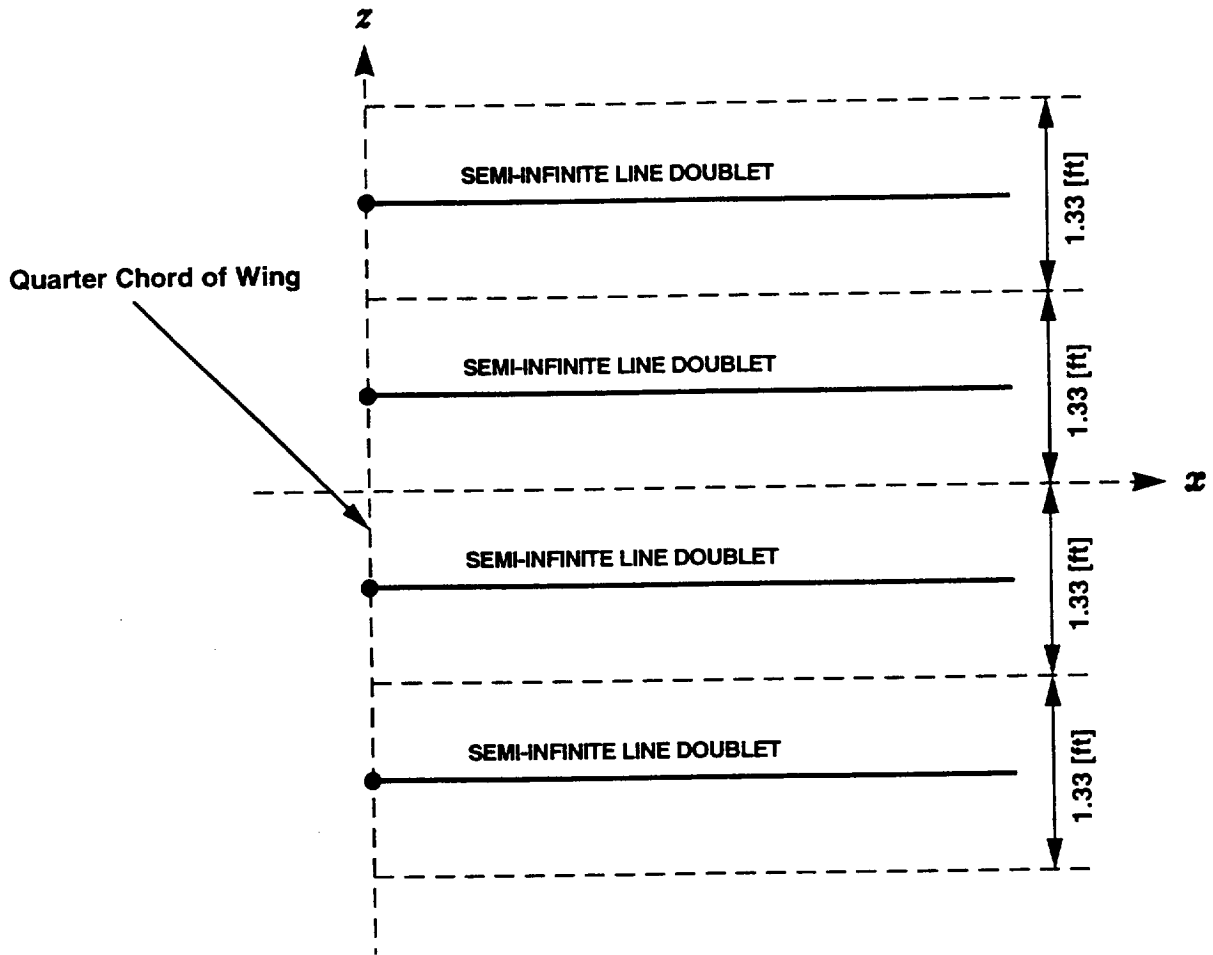


Fig. 33 Singularity Representation of Rectangular Wing.

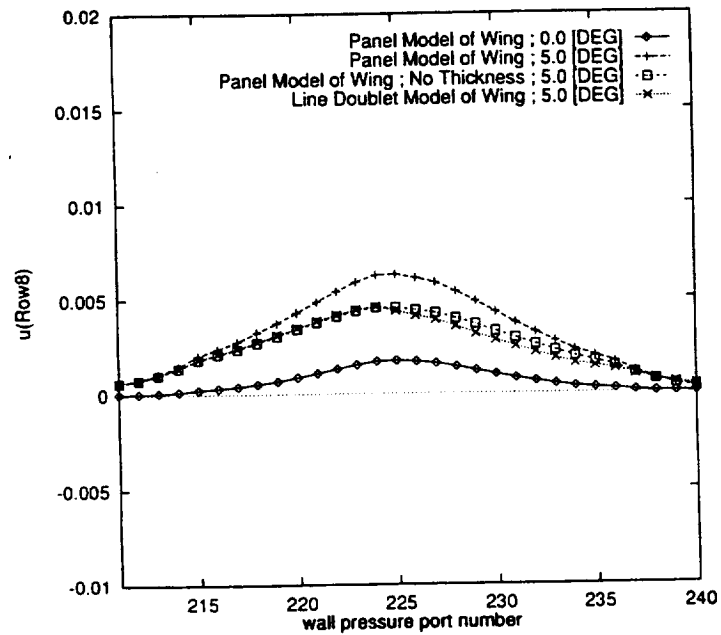
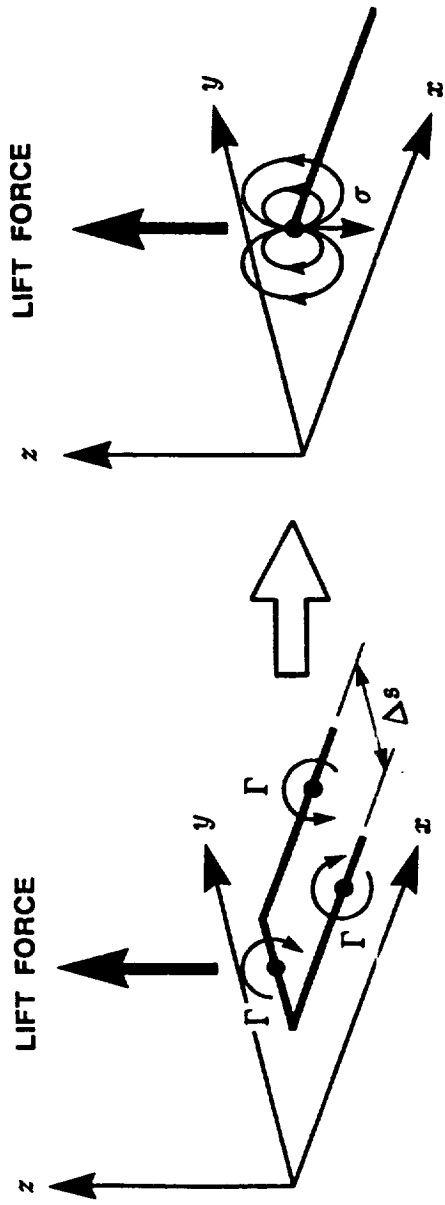


Fig. 34 Comparison of Wall Signature of Wing with equivalent Line Doublet Representation.



HORSESHOE VORTEX

LINE DOUBLET

Fig. 35 Comparison of Horseshoe Vortex with Line Doublet.

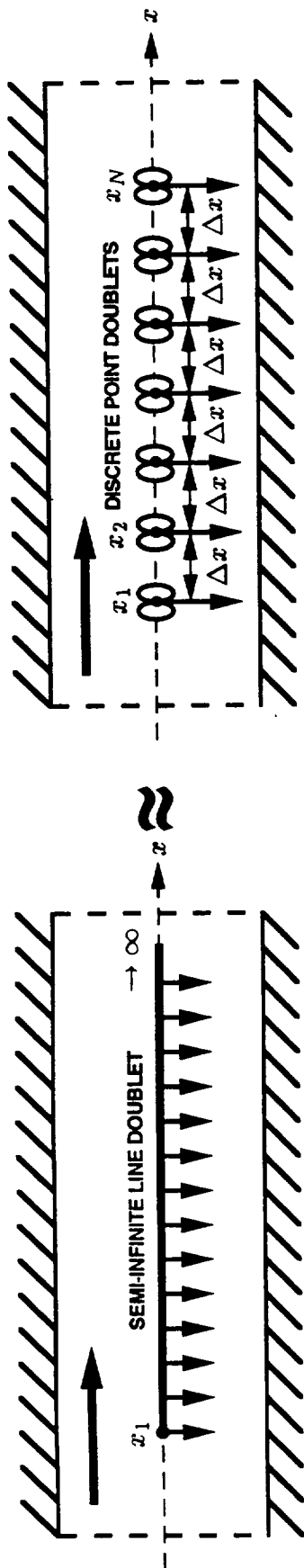


Fig. 36a Approximation of Line Doublet using Point Doublets.

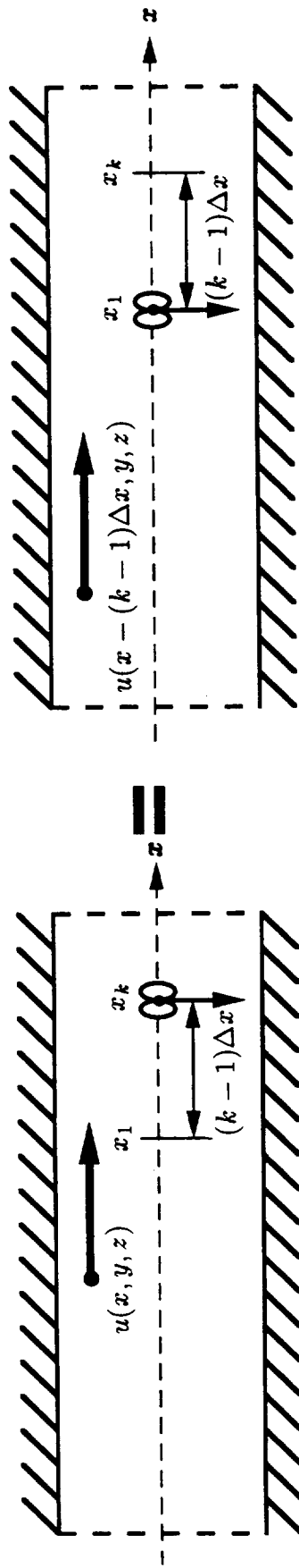


Fig. 36b Shift of Point Doublet Solution.

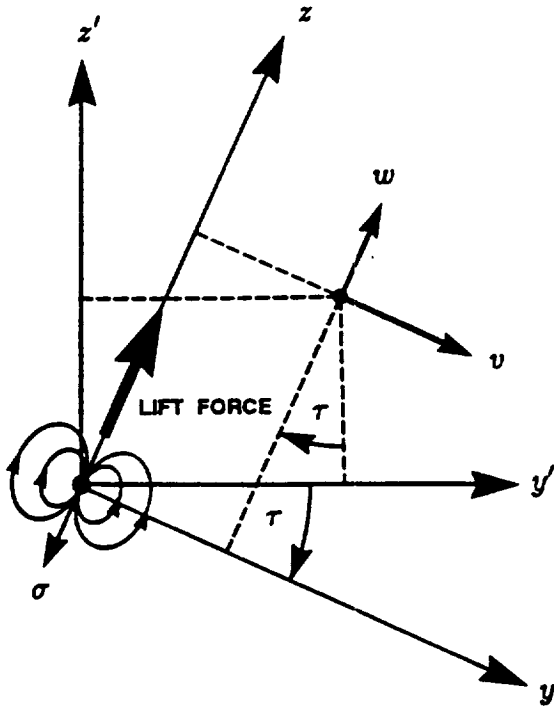


Fig. 37 Line Doublet Flow Field as a Function of Orientation Angle.

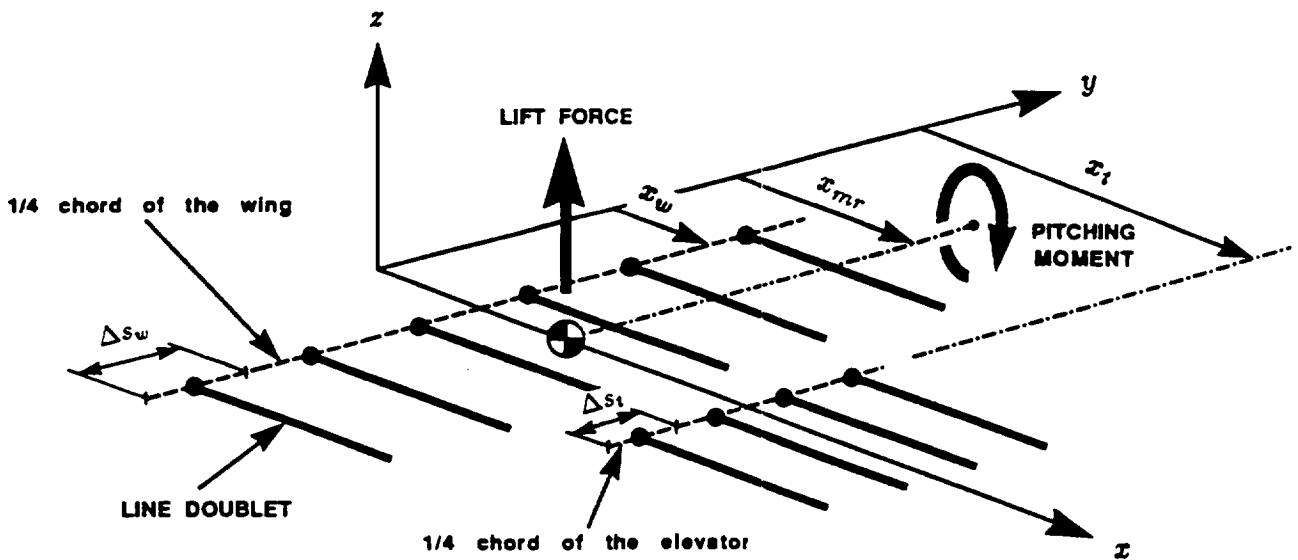


Fig. 38 Calculation of Line Doublet Strength using Lift Force and Pitching Moment.

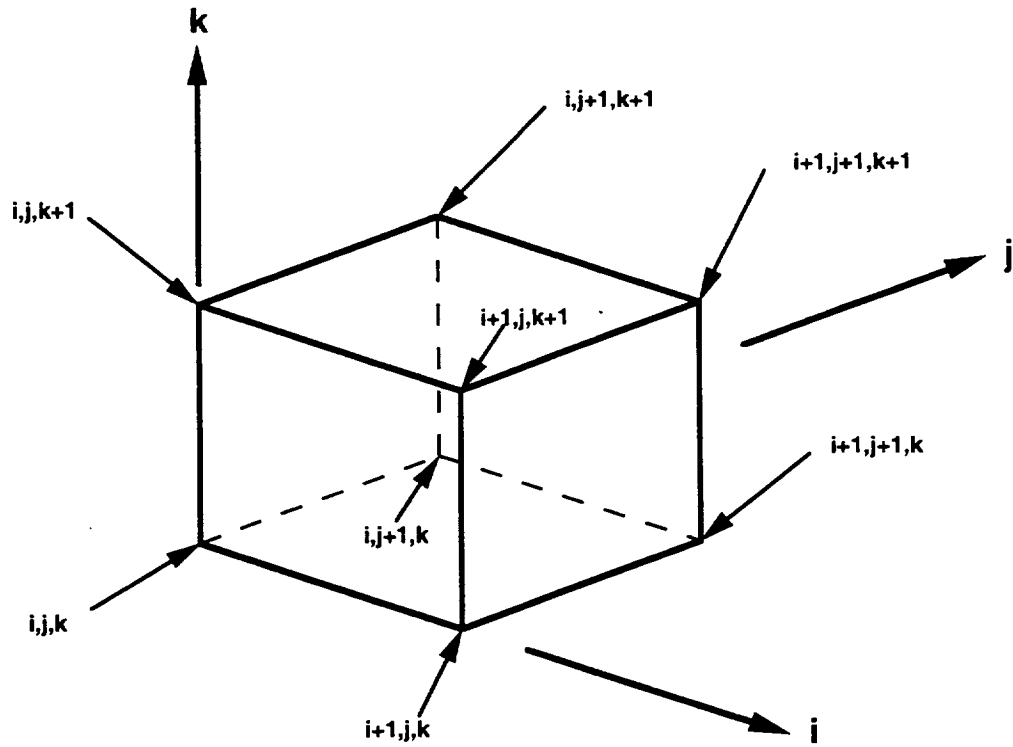


Fig. 39 Grid Cell Indices.

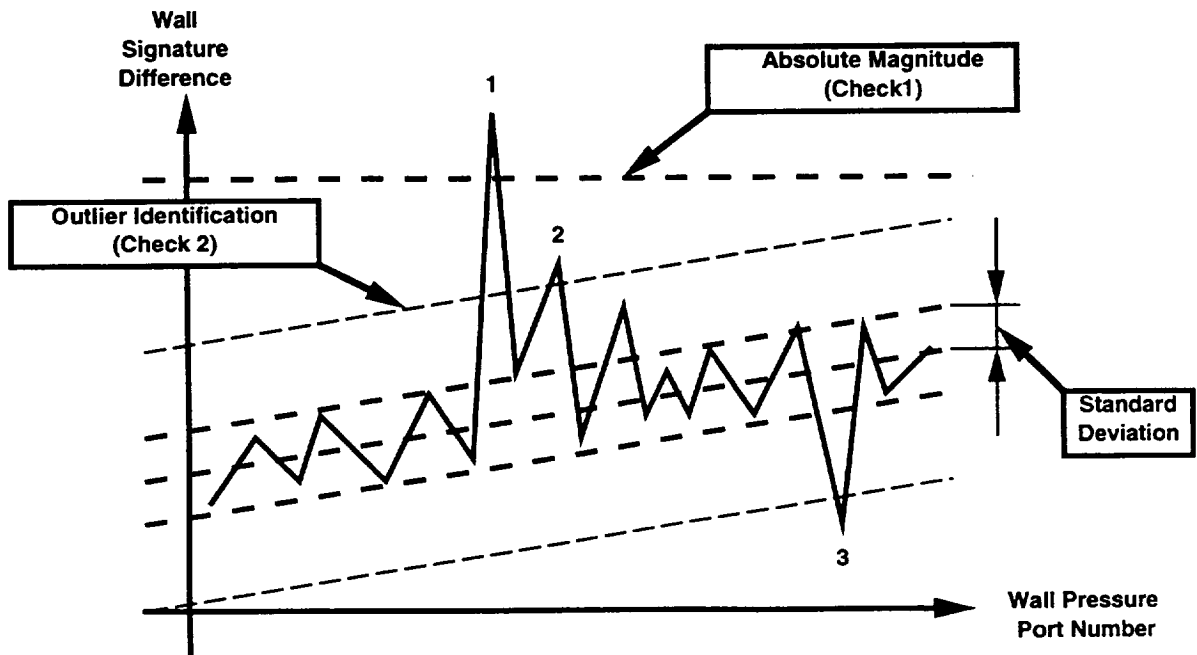


Fig. 40 Quality Check of Least Squares Fit of Wall Signature.

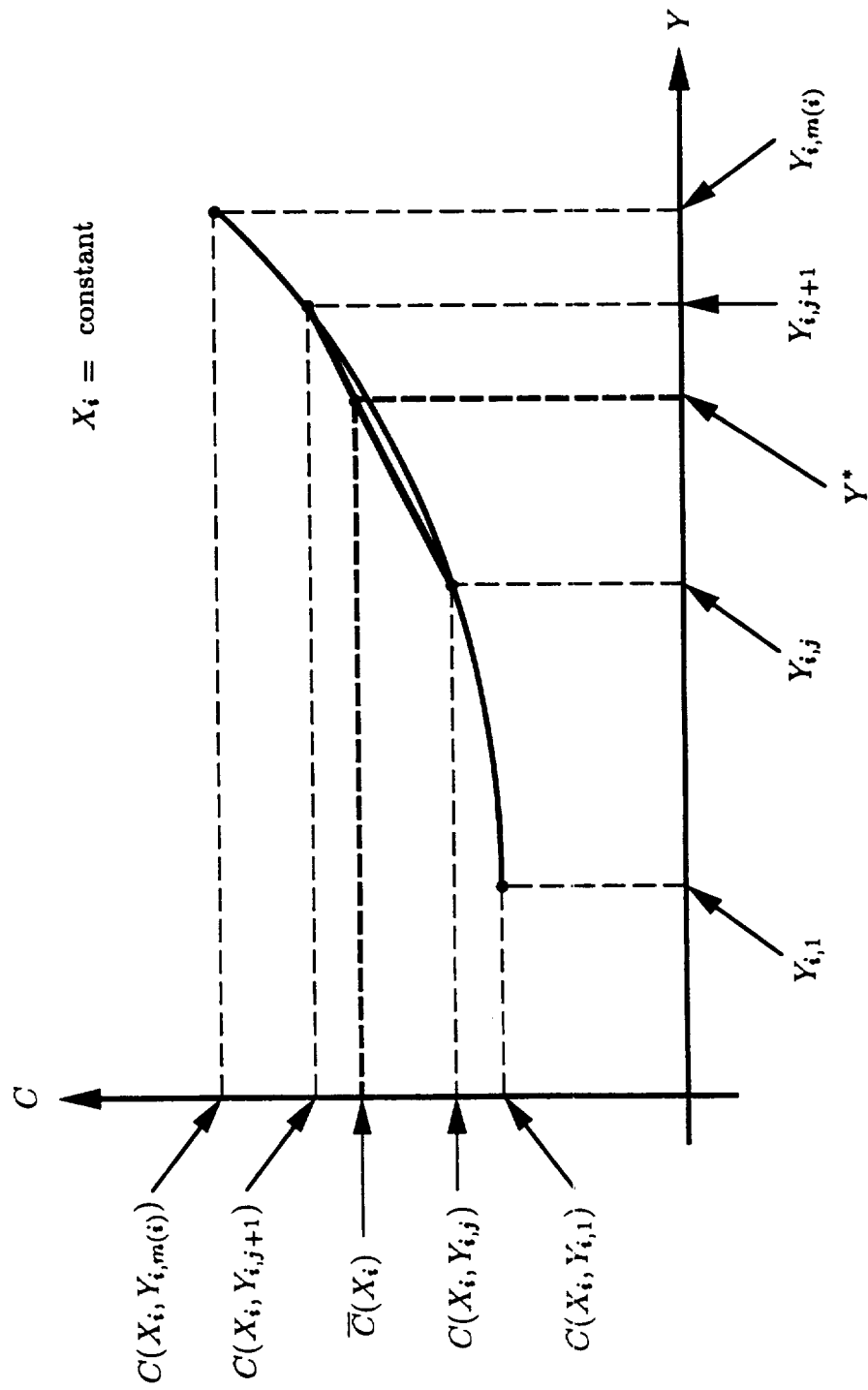


Fig. 41a Linear Interpolation of Wall Pressure Port Calibration (Second Variable).

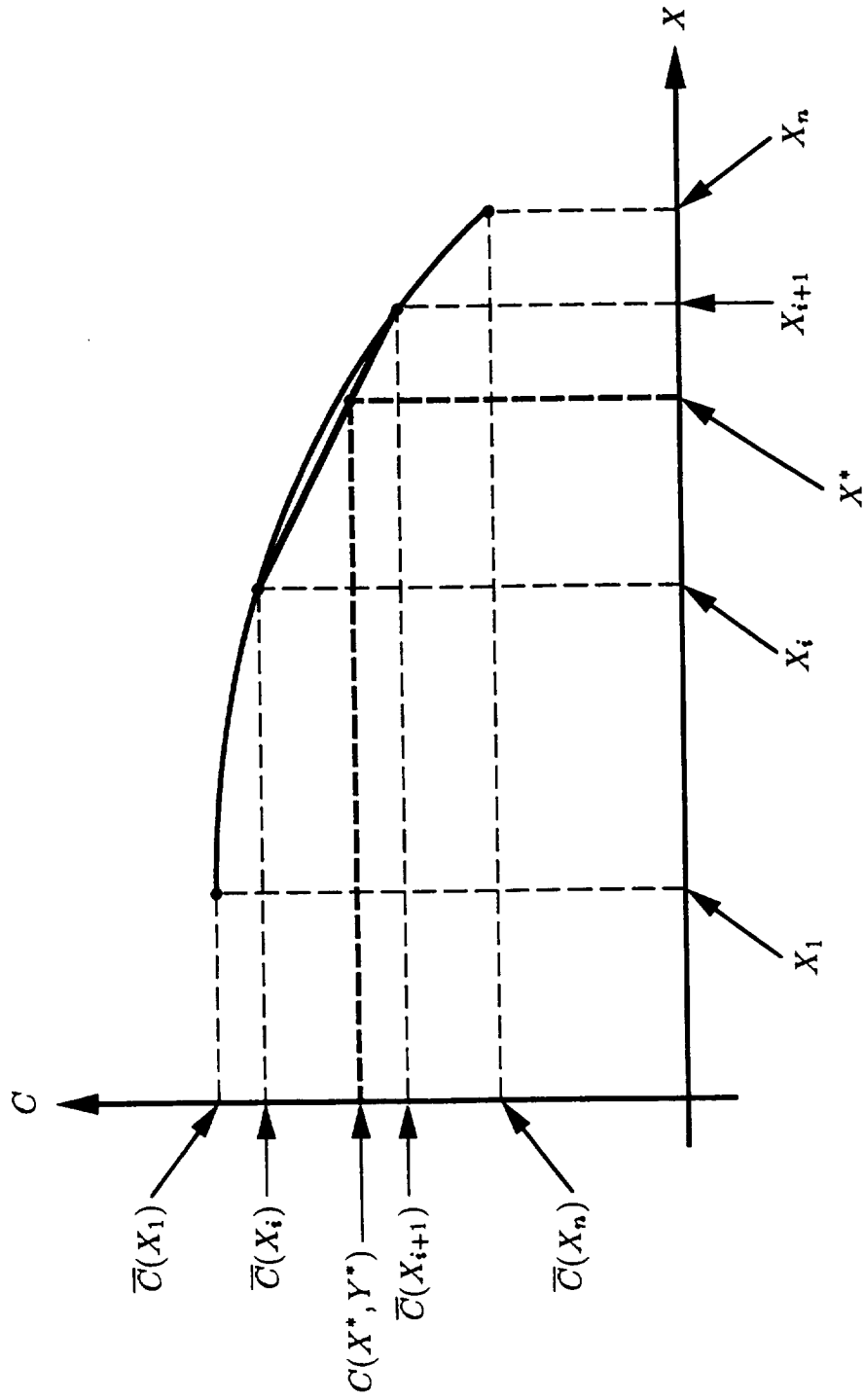


Fig. 41b Linear Interpolation of Wall Pressure Port Calibration (First Variable).

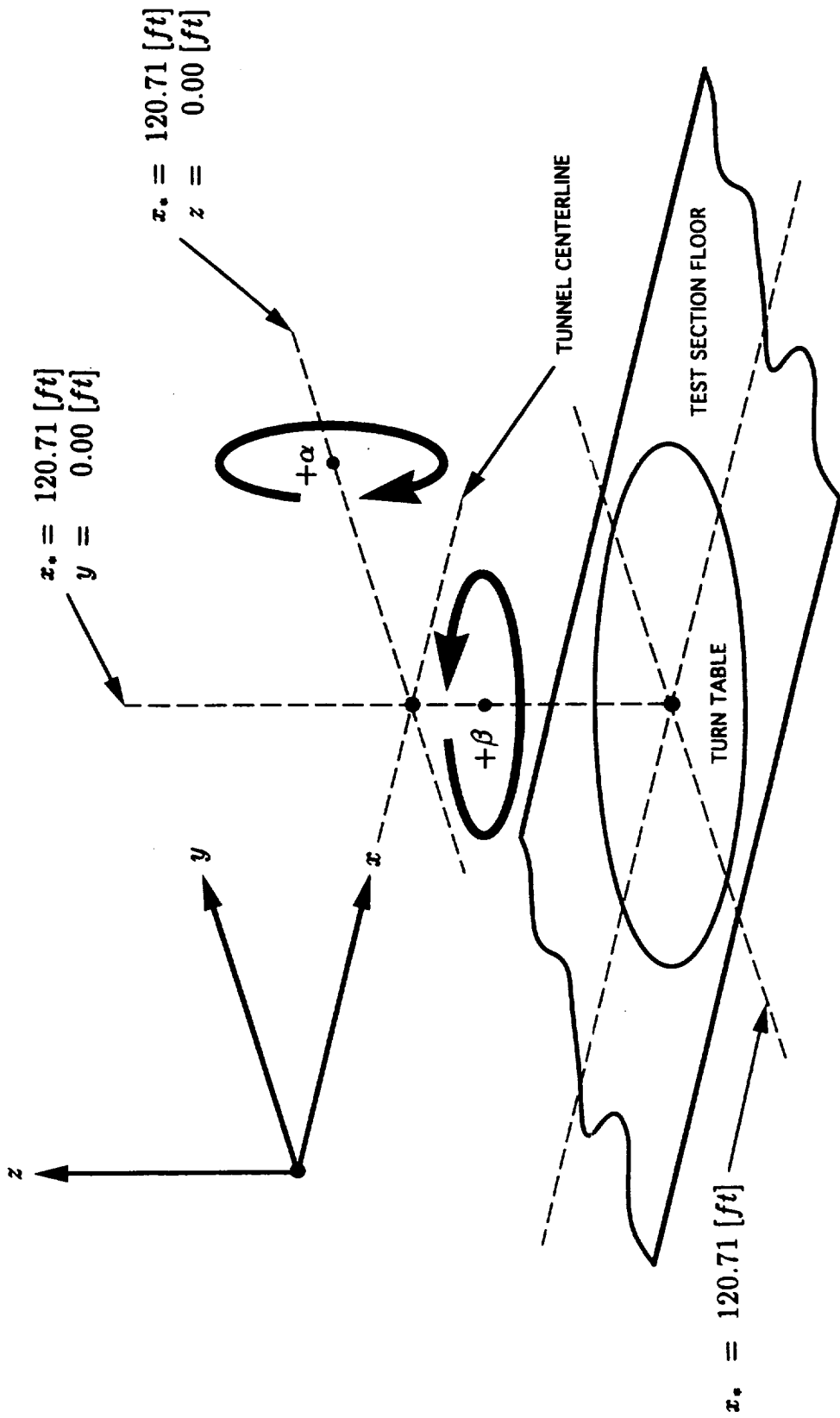


Fig. 42a Axis of Rotation of Ames Bipod and High Angle of Attack Sting.

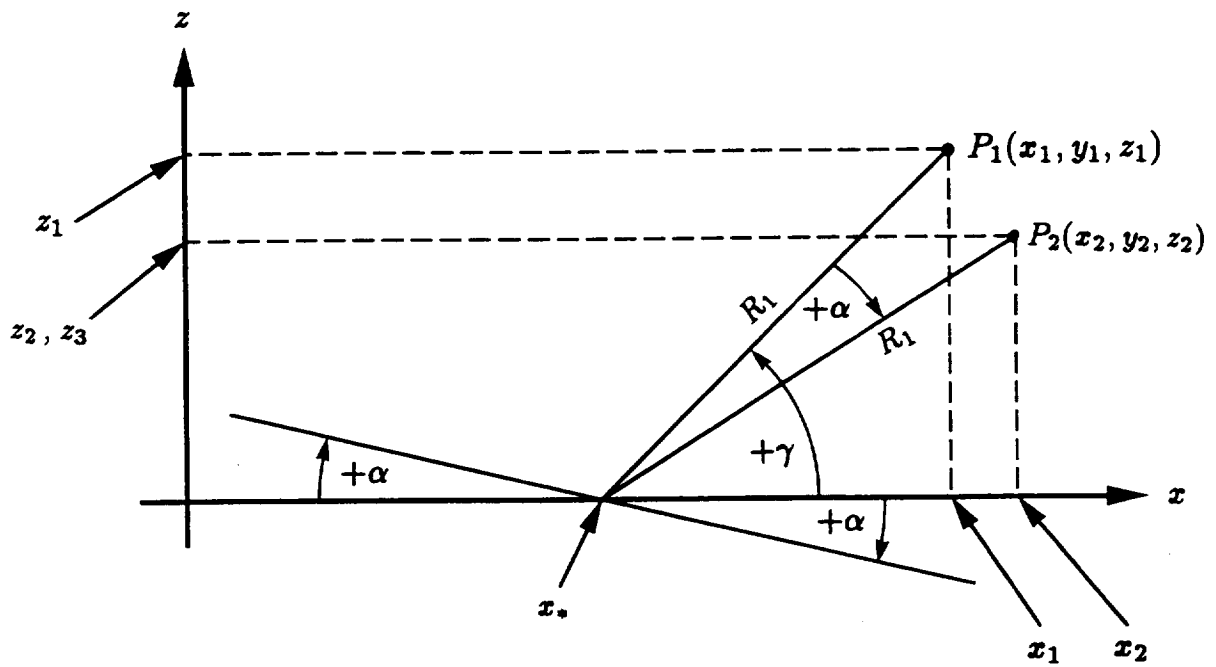


Fig. 42b Rotation No.1 ($x=120.71$ [ft]; $z=0.00$ [ft]).

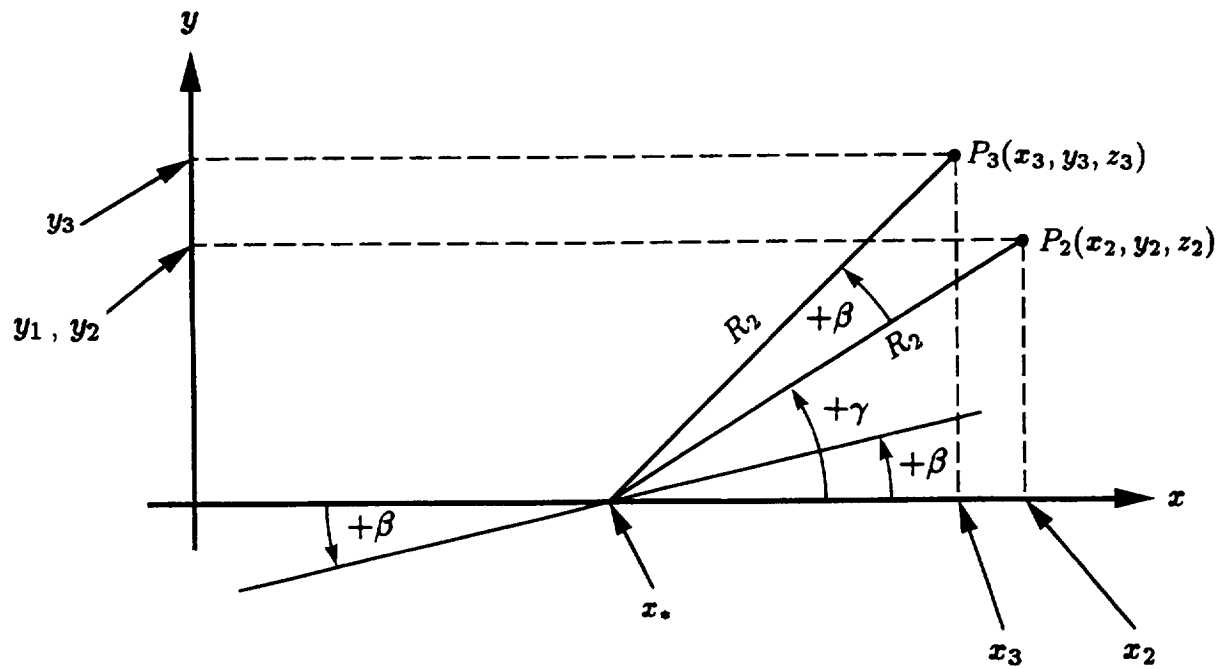


Fig. 42c Rotation No.2 ($x=120.71$ [ft]; $y=0.00$ [ft]).

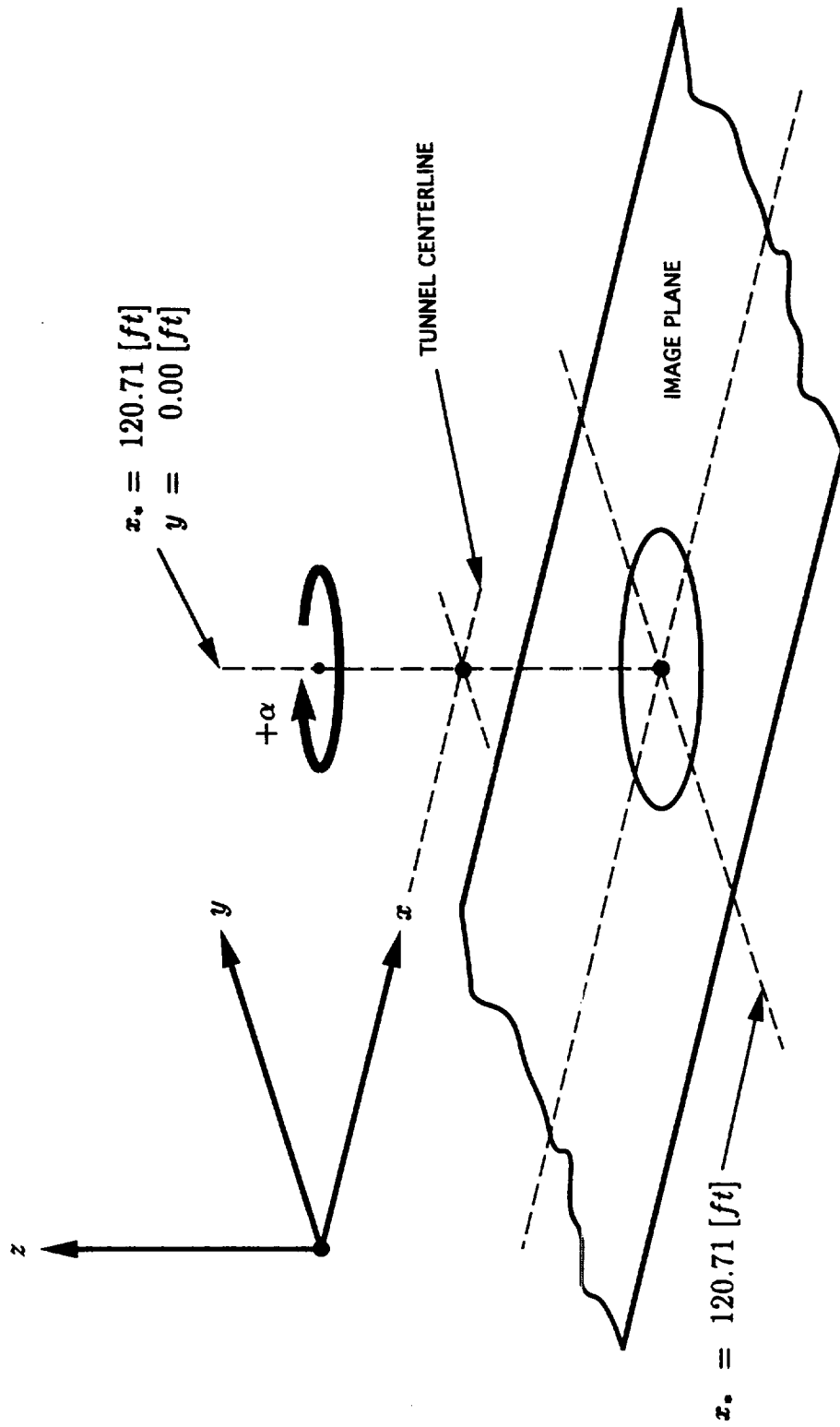


Fig. 42d Axis of Rotation of Semispan Model.

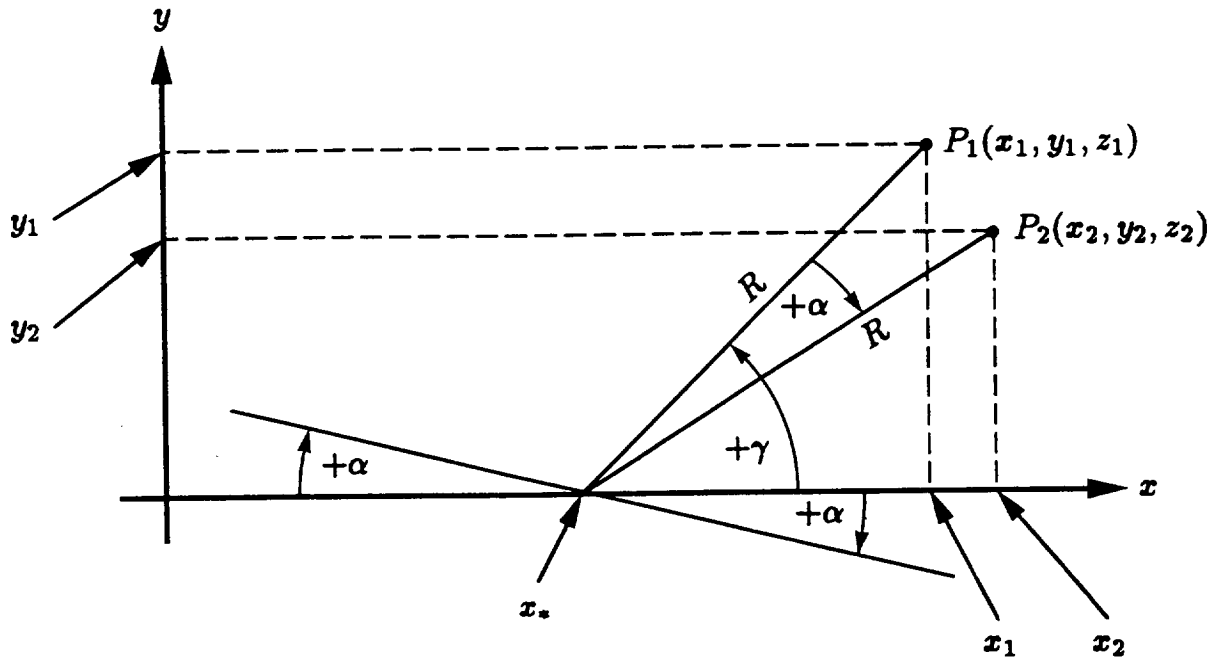


Fig. 42e Left Wing Semispan Model.

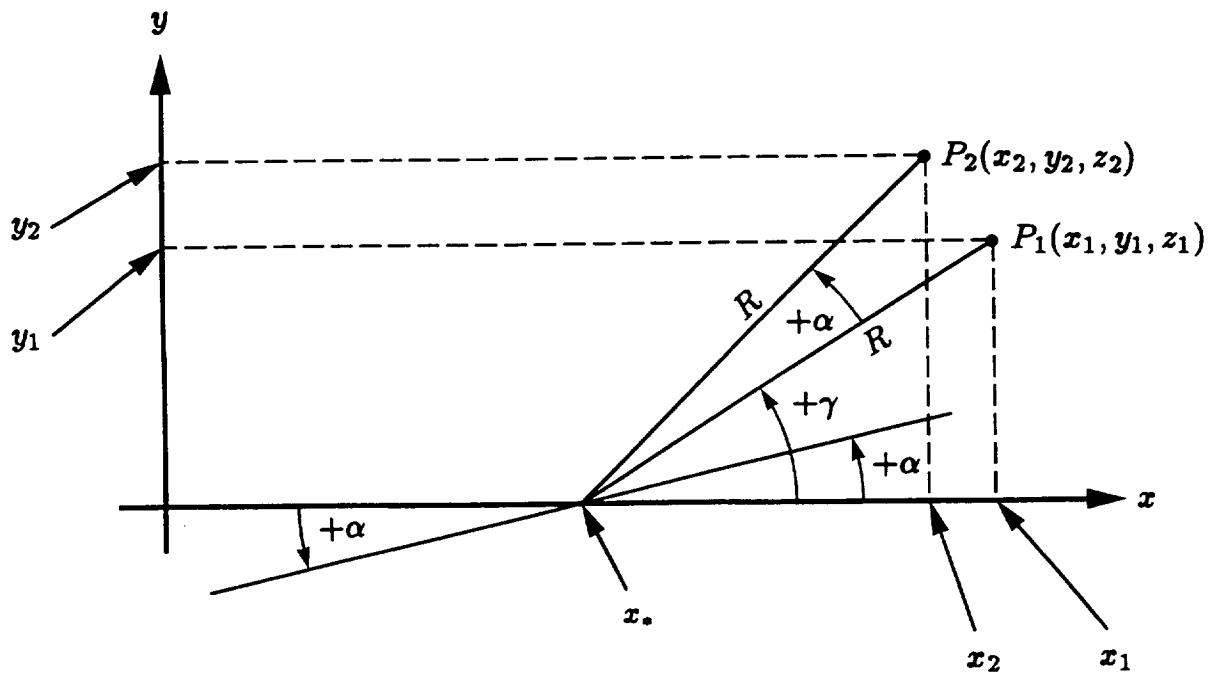


Fig. 42f Right Wing Semispan Model.

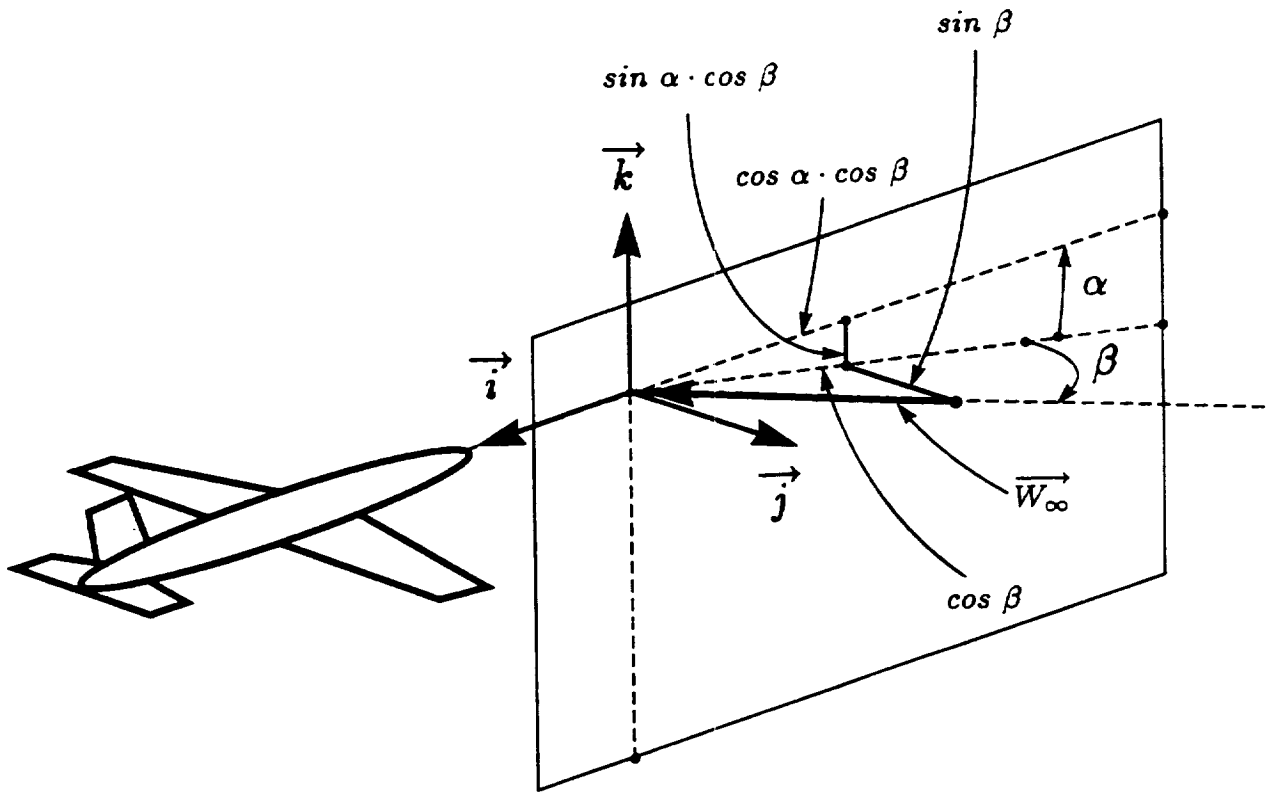


Fig. 43a Unit Wind Vector in Model Coordinate System.

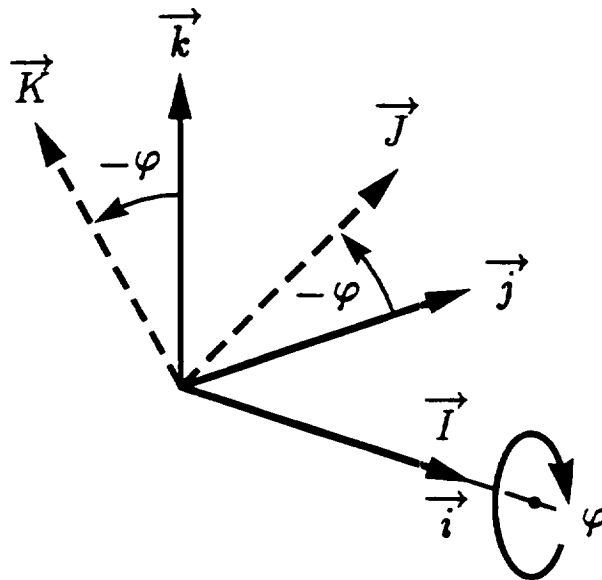


Fig. 43b Reversal of Roll Axis Rotation.

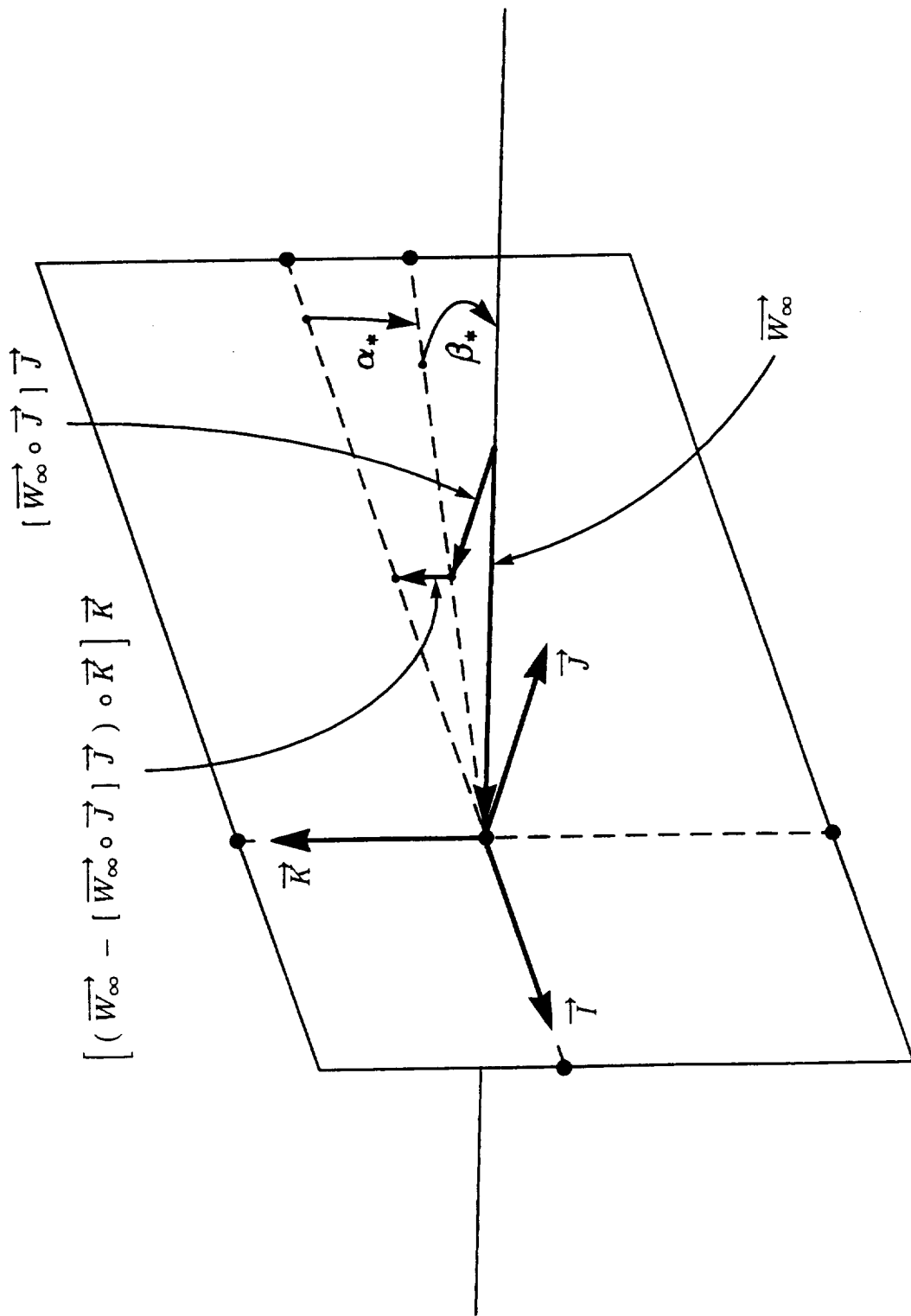


Fig. 43c Pitch and Yaw Angle of High Angle of Attack Sting.

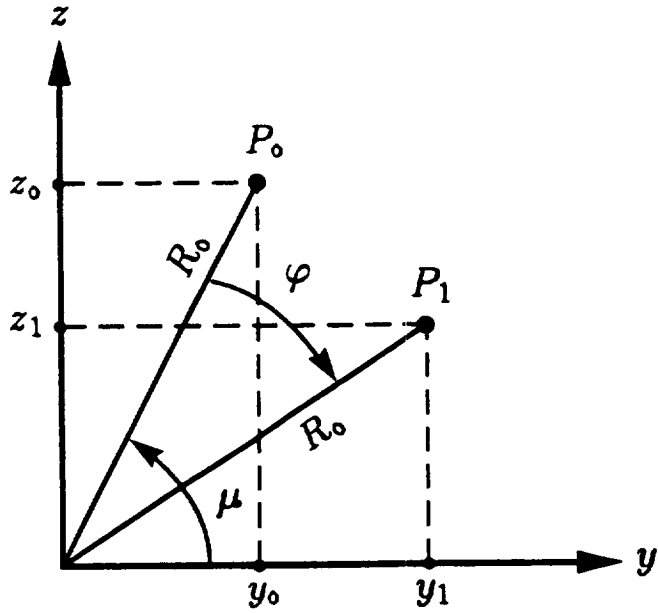


Fig. 43d Singularity or Reference Point Location as a Function of Test Article Roll Angle.

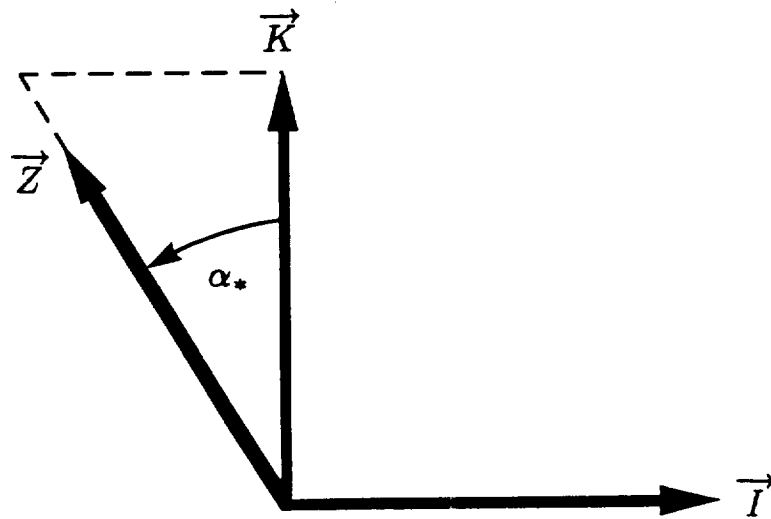


Fig. 43e Pitch Rotation of Unit Vector \vec{K} .

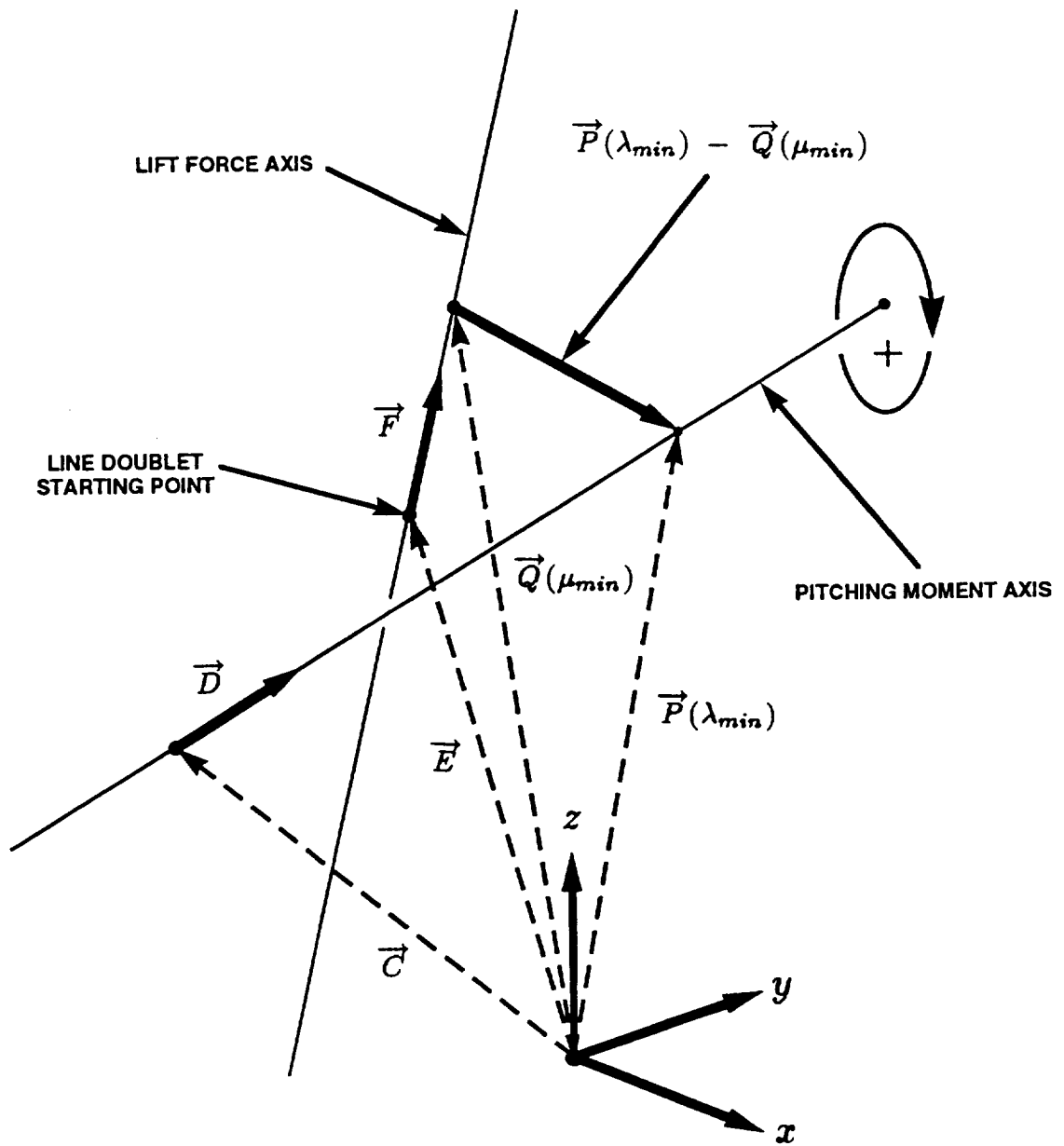


Fig. 44 Pitching Moment Lever Arm Calculation.

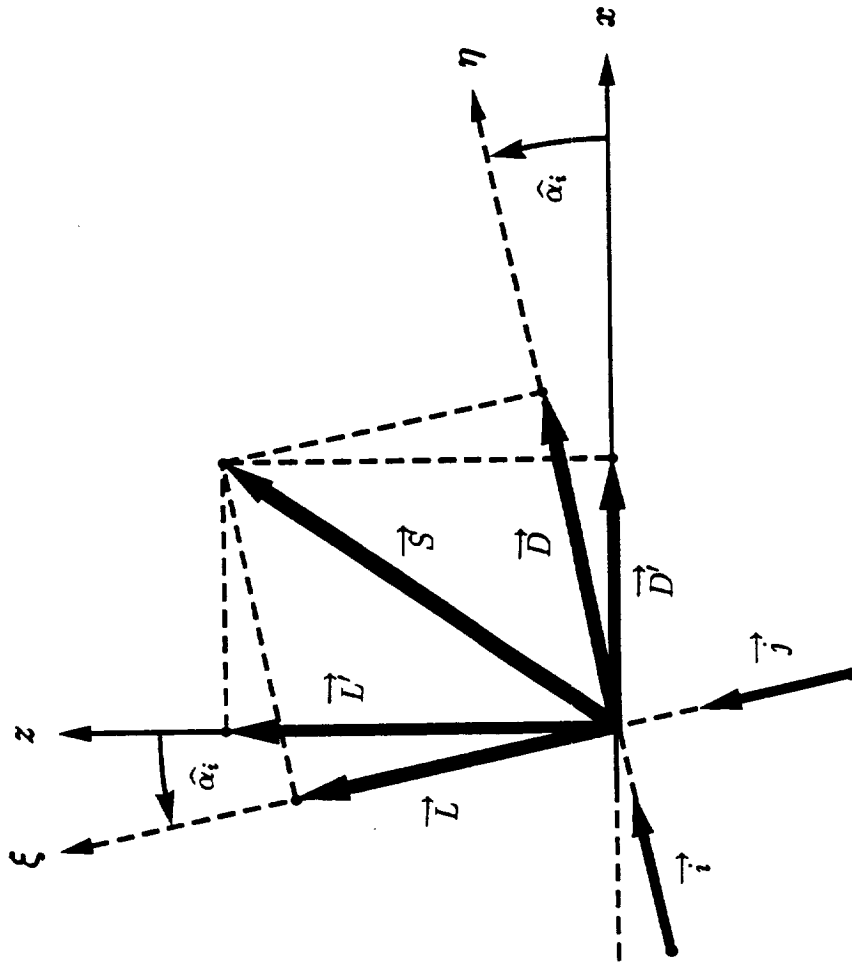


Fig. 45a Inclination of Lift and Drag Force.

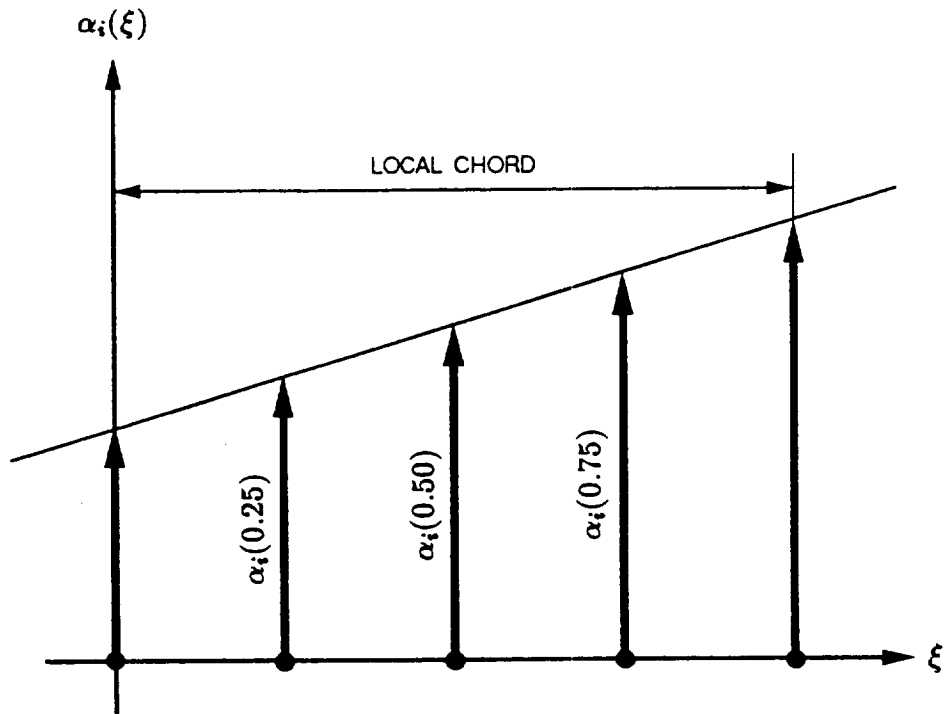


Fig. 46a Angle of Attack Correction at Wing Chord.

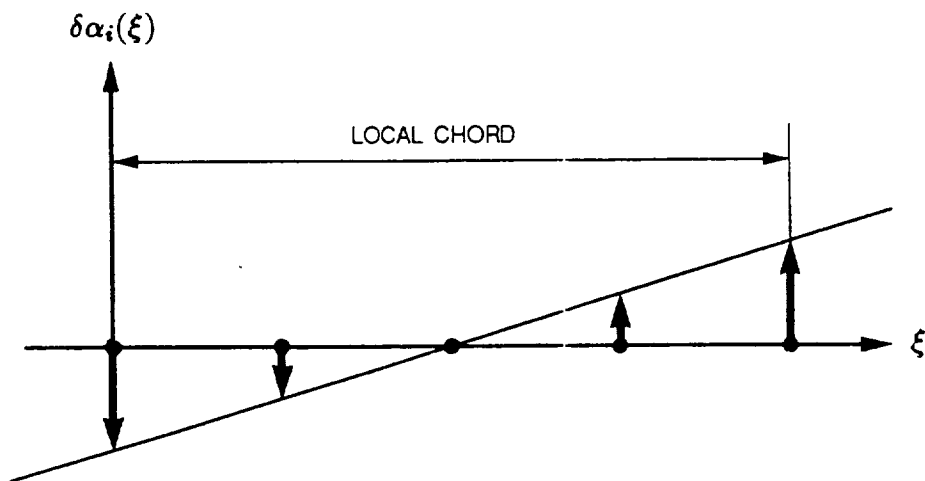


Fig. 46b Change of Angle of Attack Correction at Wing Chord.

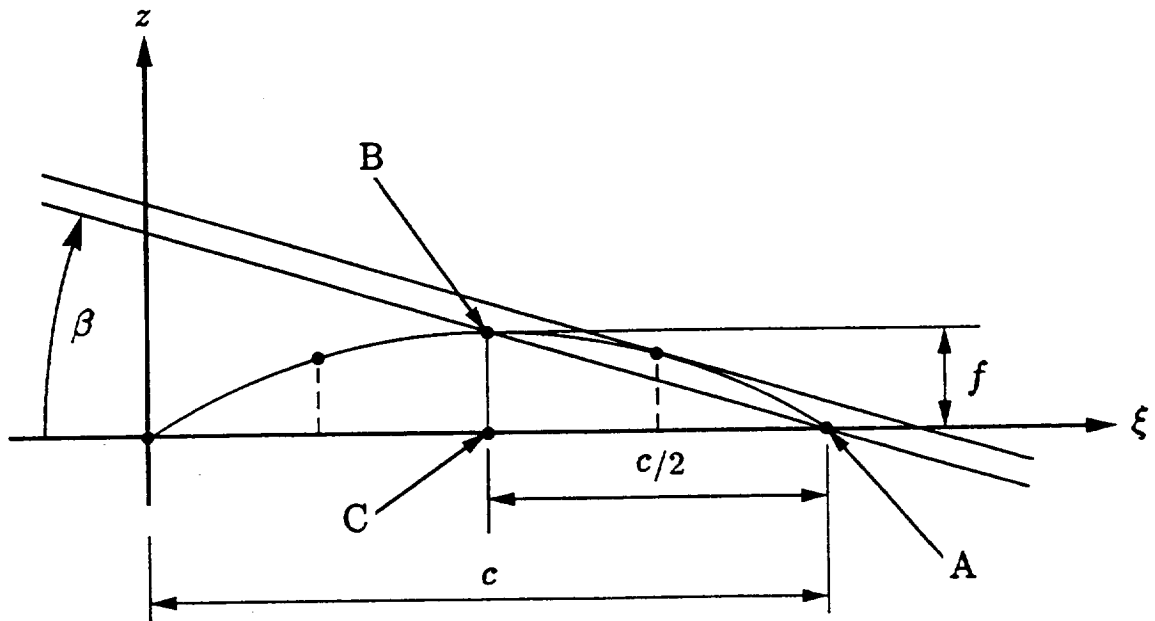


Fig. 47 Geometry of Circular Arc Airfoil.

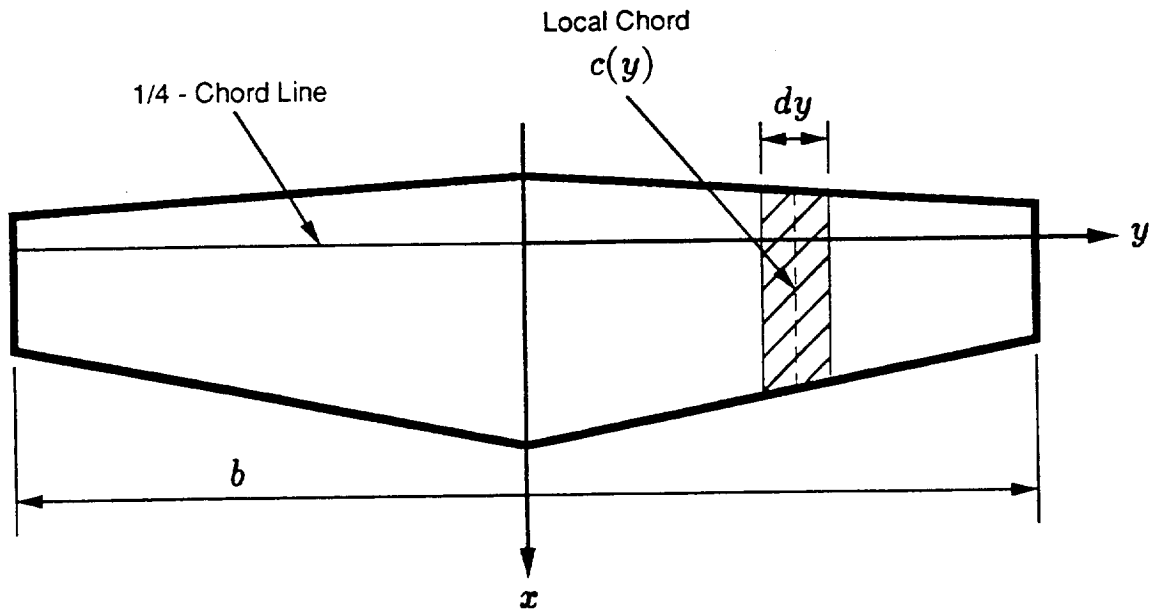


Fig. 48 Geometry of Wing with 0.0 [deg] Sweep Angle.

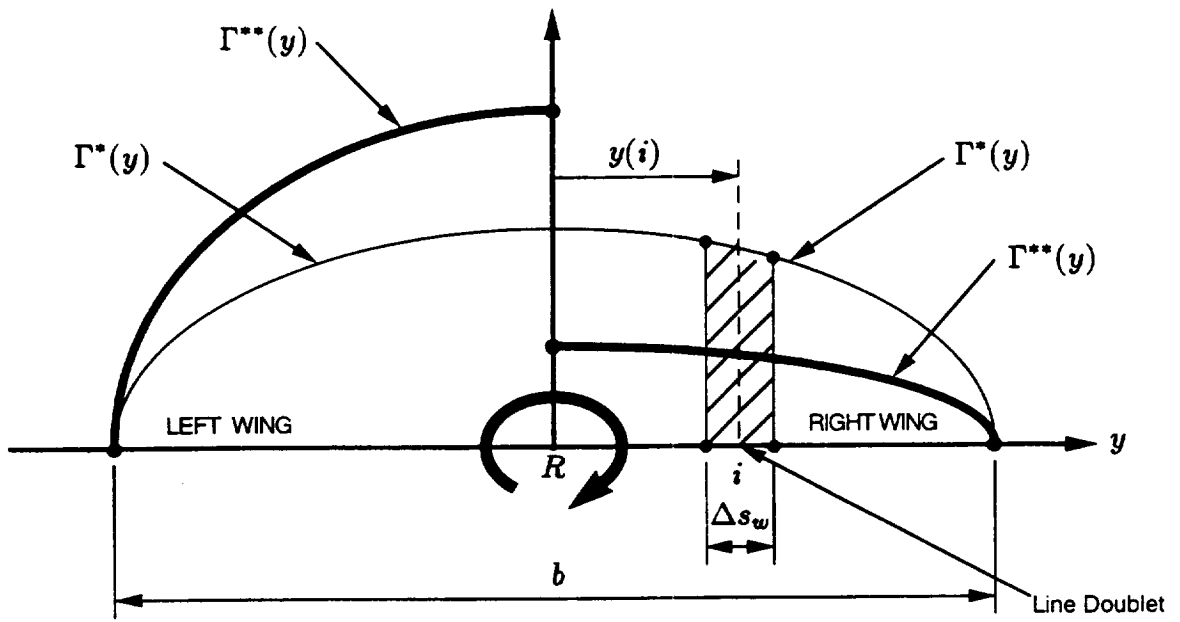


Fig. 49 Non-symmetric Lift Distribution.

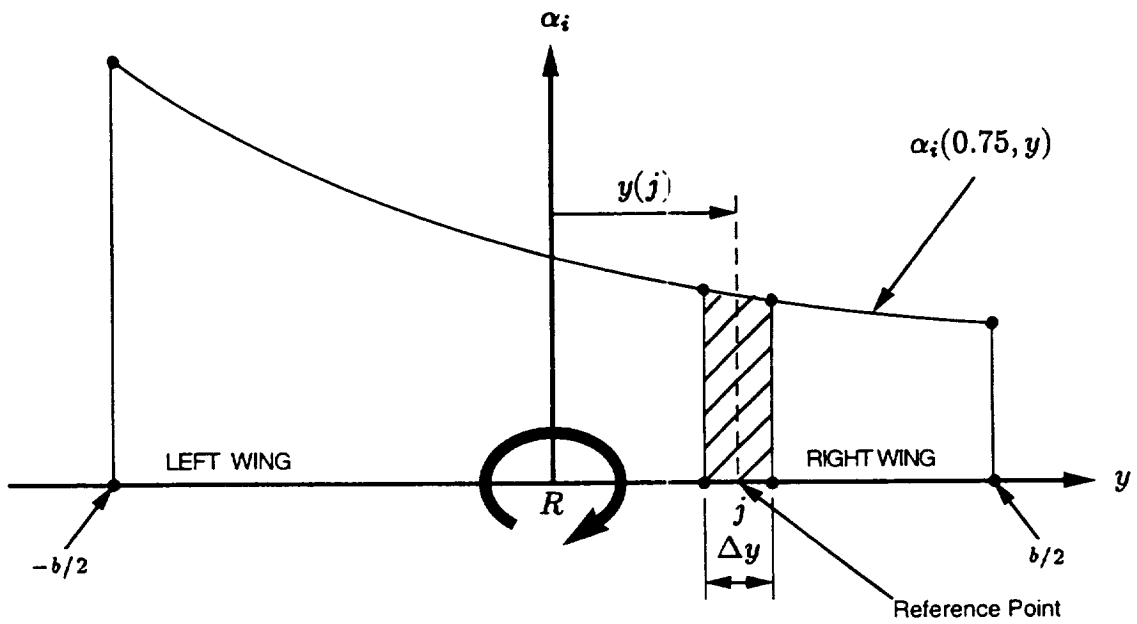


Fig. 50 Angle of Attack Correction Distribution.

REPORT DOCUMENTATION PAGE

Form Approved
OMB No. 0704-0188

Public reporting burden for this collection of information is estimated to average 1 hour per response, including the time for reviewing instructions, searching existing data sources, gathering and maintaining the data needed, and completing and reviewing the collection of information. Send comments regarding this burden estimate or any other aspect of this collection of information, including suggestions for reducing this burden, to Washington Headquarters Services, Directorate for Information Operations and Reports, 1215 Jefferson Davis Highway, Suite 1204, Arlington, VA 22202-4302, and to the Office of Management and Budget, Paperwork Reduction Project (0704-0188), Washington, DC 20503.

1. AGENCY USE ONLY (Leave blank)		2. REPORT DATE July 1998	3. REPORT TYPE AND DATES COVERED Contractor Report	
4. TITLE AND SUBTITLE The Real-Time Wall Interference Correction System of the NASA Ames 12-Foot Pressure Wind Tunnel			5. FUNDING NUMBERS NAS2-13605	
6. AUTHOR(S) Norbert Ulbrich				
7. PERFORMING ORGANIZATION NAME(S) AND ADDRESS(ES) VERIDIAN/Calspan Operations NASA Ames Research Center P.O. Box 7 Moffett Field, California 94035-0007			8. PERFORMING ORGANIZATION REPORT NUMBER A-98-11989	
9. SPONSORING/MONITORING AGENCY NAME(S) AND ADDRESS(ES) National Aeronautics and Space Administration Washington, DC 20546-0001			10. SPONSORING/MONITORING AGENCY REPORT NUMBER NASA/CR—1998-208537	
11. SUPPLEMENTARY NOTES Point of Contact: Norbert Ulbrich, Ames Research Center, MS 227-3, Moffett Field, CA 94035-1000; (415) 604-6893				
12a. DISTRIBUTION/AVAILABILITY STATEMENT Unclassified — Unlimited Subject Category 09			12b. DISTRIBUTION CODE	
13. ABSTRACT (Maximum 200 words) An improved version of the Wall Signature Method was developed to compute wall interference effects in three-dimensional subsonic wind tunnel testing of aircraft models in real-time. The method may be applied to a fullspan or a semispan model. A simplified singularity representation of the aircraft model is used. Fuselage, support system, propulsion simulator, and separation wake volume blockage effects are represented by point sources and sinks. Lifting effects are represented by semi--infinite line doublets. The singularity representation of the test article is combined with the measurement of wind tunnel test reference conditions, wall pressure, lift force, thrust force, pitching moment, rolling moment, and precomputed solutions of the subsonic potential equation to determine first order wall interference corrections. Second order wall interference corrections for pitching and rolling moment coefficient are also determined. A new procedure is presented that estimates a rolling moment coefficient correction for wings with non-symmetric lift distribution. Experimental data obtained during the calibration of the Ames Bipod model support system and during tests of two semispan models mounted on an image plane in the NASA Ames 12ft Pressure Wind Tunnel are used to demonstrate the application of the wall interference correction method.				
14. SUBJECT TERMS Subsonic flow, Wind tunnel wall interference, Wall pressure measurements			15. NUMBER OF PAGES 202	
			16. PRICE CODE A10	
17. SECURITY CLASSIFICATION OF REPORT Unclassified	18. SECURITY CLASSIFICATION OF THIS PAGE Unclassified	19. SECURITY CLASSIFICATION OF ABSTRACT	20. LIMITATION OF ABSTRACT	